Evaluation of uncertainty in the vibration attenuation with shunted piezoelectric transducers integrated in a beam-column support

vom Fachbereich Maschinenbau
der Technischen Universität Darmstadt

zur Erlangung des Grades
Doktor-Ingenieur (Dr.-Ing.)

Dissertation
von Benedict Götz

Erstgutachter: Prof. Dr.-Ing. Tobias Melz
Zweitgutachter: Prof. Dr.-Ing. Dipl.-Wirtsch.-Ing. Peter Groche

Darmstadt 2018

Götz, Benedict: Evaluation of uncertainty in the vibration attenuation with shunted piezoelectric transducers integrated in a beam-column support

Darmstadt, Technische Universität Darmstadt,
Jahr der Veröffentlichung der Dissertation auf TUprints: 2019
Tag der mündlichen Prüfung: 28.11.2018

Veröffentlicht unter CC BY-NC-ND 4.0 International
https://creativecommons.org/licenses/

Acknowledgments

Die vorliegende Arbeit entstand während meiner Tätigkeit als wissenschaftlicher Mitarbeiter am Fachgebiet Systemzuverlässigkeit, Adaptronik und Maschinenakustik SAM an der Technischen Universität Darmstadt und am Fraunhofer-Institut für Betriebsfestigkeit und Systemzuverlässigkeit LBF. Der Deutschen Forschungsgemeinschaft (DFG) danke ich für die finanzielle Förderung meiner Arbeit im Rahmen des Sonderforschungsbereichs (SFB) 805 „Beherrschung von Unsicherheit in lasttragenden Systemen des Maschinenbaus“.

Meinem Doktorvater, Herrn Prof. Tobias Melz, gilt mein herzlicher Dank für die Betreuung meiner Arbeit. Herrn Prof. Peter Groche, Leiter des Fachgebiets für Produktionstechnik und Umformmaschinen PtU, danke ich für die freundliche Übernahme des Korreferats. Besonderer Dank gilt Herrn Dr.-Ing. Roland Platz für die intensiven fachlichen Gespräche, die zum Gelingen der Arbeit beigetragen haben.

Den Kollegen im SFB 805 und am Fraunhofer LBF sowie meinen Studenten danke ich sehr herzlich für das angenehme Arbeitsumfeld, die vielen anregenden Gespräche und ihr tatkräftiges Mitwirken. Bei Oliver Heuss und Rogério Salloum möchte ich mich besonders für den konstruktiven Austausch bedanken. Ferner gilt mein spezieller Dank meinen Freunden und Kollegen Christopher Gehb und Max Schäffner für die vielen intensiven, produktiven und humorvollen Gespräche.

Darüber hinaus danke ich meiner Familie und meinen Freunden für ihre nicht endenden Ermutigungen. Schließlich, aber nicht zuletzt, danke ich meiner liebsten Marie für ihre bedingungslose Unterstützung und stete Aufmunterung.

Abstract

Vibrations in mechanical lightweight beam and truss-type structures are often related to several detrimental effects such as diminished durability, unwanted noise and safety issues. By integration of two piezoelectric transducers connected to RL- and RLC-shunts into a beam-column support with rotational elasticity as presented in this work, vibrations of a beam-column with circular cross-section is significantly attenuated in various lateral directions. In contrast to other measures for vibration attenuation, the advantages of the piezoelectric transducer with shunt circuit are the possibility of integrating the transducer into the structure's mechanical load path and the precise vibration attenuation adjustment. In this work, on the one hand, the capability of the proposed piezo-elastic support to attenuate lateral beam-column vibrations with shunted transducers is investigated experimentally and numerically. On the other hand, uncertainty in the vibration attenuation is quantified and evaluated by experiments and simulation to reduce uncertainty in the application of the piezo-elastic support.

It is shown numerically and experimentally that the proposed concept of the piezo-elastic support attenuates beam-column vibrations in various lateral directions by 89 % with RL-shunts and by 96 % with RLC-shunts compared to vibrations without attenuation through shunts. However, uncertainty caused by manufacturing, assembly and static axial beam-column load variations affects the lateral beam-column vibration attenuation during operation. As an approach for uncertainty quantification, a model-based uncertainty analysis with parameter uncertainty assumed from own experiments and literature is performed. Own experiments are performed to quantify uncertainty due to spring element manufacturing variations, a key element of the piezo-elastic support, and due to static beam-column load variations. It is shown that both sources significantly affect the vibration attenuation with RL- and RLC-shunts. So far, uncertainty due to static beam-column load variations has not been subject of research for resonant shunted transducers. Numerical results of the model-based uncertainty analysis with uncertainty assumed from own experiments and literature combined show that vibration attenuation with RL- and RLC-shunts is significantly affected by all three sources of uncertainty but still adequate vibration attenuation is achieved. More specifically, vibration attenuation with RLC-shunts is only little affected by static load variations.

The novelty of this work is the use of resonant shunted piezoelectric transducers integrated in a beam-column support for vibration attenuation. Furthermore, the evaluation of uncertainty by probabilistic measures of the maximum vibration amplitude of the uncertain vibration behavior is new.

Contents

Nomenclature

Acronyms

FE	finite element
GEMCC	general electromechanical coupling coefficient
MCS	MONTE-CARLO-Simulation
NRMSE	normalized root mean square error
oc	open circuited transducer electrodes
ol	open-loop transducer electrodes
OpAmp	operational amplifier
opt	optimal value
P	piezoelectric transducer
pdf	probability density function
PZT	lead zirconate titanate
RL-shunt	electric shunt circuit consisting of a resistor and an inductor
RLC-shunt	RL-shunt with additional negative capacitance
sc	short circuited transducer electrodes
SFB	Sonderforschungsbereich (Collaborative Research Center)
SPIF	single point incremental forming
TVA	tuned vibration absorber

Latin Letters

f	frequency in Hz
A	cross-section area in m^2, or iterations of system assembly
a	lateral acceleration in m/s^2
$\widehat{a}$	peak acceleration m/s^2
$\underline{\boldsymbol{A}}$	state space system matrix
$\boldsymbol{b}_s$	displacement extraction matrix, non-dimensional
$\boldsymbol{b}_A$	support A transducer positioning matrix, non-dimensional
$\boldsymbol{b}_B$	support B transducer positioning matrix, non-dimensional
$\underline{\boldsymbol{B}}$	state space input matrix
C	electric capacitance in μF

C^{n}	negative capacitance in µF
C^{s}	static transducer capacitance in µF
$\underline{\boldsymbol{C}}$	state space output matrix
D	electric displacement in C/m^2
d	piezoelectric constant in m/V, or diameter in m
$\boldsymbol{D}$	damping matrix in N/(sm)
E	Young's modulus in N/m^2, or electric field in V/m
err	relative deviation of numerical from experimental value in %
e	axial transducer elongation in 3-direction in m
F	force in N
G	frequency transfer function in m/(s^2 V)
$\boldsymbol{G}$	frequency transfer function matrix in m/(s^2 V)
$p_{\mathscr{G}}(X)$	GUMBEL probability density function, unit of related quantity X
$\widehat{G}$	peak gain of frequency transfer function in m/(s^2 V)
h	height in m
$\boldsymbol{I}$	identity matrix, non-dimensional
j	index variable
$\boldsymbol{k}$	transducer stiffness matrix in N/m
$\boldsymbol{K}$	stiffness matrix in N/m
k_{φ}	rotational stiffness in Nm/rad
L	inductance in H
l	length in m
M	number of lateral vibration modes
m	mass in kg, or index of lateral vibration mode
N	number of averages, or number of piezoelectric layers, or number of FE nodes
n	index of summation, or index of FE node
$p_{\mathscr{N}}(X)$	normal probability density fuction, unit of related quantity X
P	cross power spectral density, unit of related quantities
p	probability density with unit of related quantity X, or modal displacement, non-dimensional
$\boldsymbol{P}$	model parameter vector
q	electric charge in C
Q_X^{95}	95$^{\mathrm{th}}$ percentile in m/(s^{2}V)
R	electric resistance in Ohm
r	lateral displacement in m, or radius in m
$\widehat{\boldsymbol{r}}$	eigenvector, non-dimensional
$\boldsymbol{r}$	FE lateral beam-column displacement vector in m
s	LAPLACE variable in 1/s

S	mechanical transducer strain in m/m, or number of spring elements
T	mechanical transducer stress in N/m^2, or kinetic energy in J
t	time in s
$\widehat{N}$	number of averages
$\boldsymbol{t}_\mathrm{r}$	displacement transformation matrix, non-dimensional
$\boldsymbol{t}_\mathrm{u}$	voltage transformation matrix, non-dimensional
U	potential energy in J
u	electric voltage in V
$\underline{\boldsymbol{u}}$	state space input vector
v	nodal dispalcement in y-direction in m
w	nodal dispalcement in z-direction in m
X	arbitrary (random) quantity, unit of related quantity
x	x-direction
$\underline{\boldsymbol{x}}$	state vector
y	lateral y-direction, or output signal
Y	dynamic transducer capacitance in µF
$\widetilde{Y}$	modal transducer capacitance in µF
$\underline{\boldsymbol{y}}$	state space output vector
$\underline{Z}$	impedance in Ohm
z	lateral z-direction

Greek Letters

α	angle in °
δ	negative capacitance ratio, non-dimensional
δ_crit	stability limit of negative capaticance ratio, non-dimensional
Δf	frequency resolution in Hz
ε	electrical permitivity in F/m
γ	general lectromechanical coupling coefficient (GEMCC), non-dimensional
μ_X	mean of normal distribution, unit of related quantity X
Ω	excitation angular frequency in rad/s
ω	angular eigenfrequency in rad/s
$\boldsymbol{\Phi}$	modal matrix, non-dimensional
φ	rotation in rad
Ψ	shape function of beam-column deflection, non-dimensional
Δ_X	scale parameter of GUMBEL distribution, unit of related quantity X
σ_X	standard deviation of normal distribution, unit of related quantity X
Θ	pieoelectric transducer force constant in N/V

ζ	modal damping ratio, non-dimensional

Subscripts

3	transducer 3-direction, short for index 33
A	support A
aa	input acceleration, output acceleration
α	in α-direction
$\alpha^{\perp}$	orthogonal to α-direction
au	input voltage, output acceleration
B	support B
b	beam-colum
c	cutoff
el	elastic
exp	experimental
ext	axial extension
g	geometric
m	modal
num	numerical
p	refers to piezeoelectric transducer
φ	in φ-direction
$\dot{q}$u	input voltage, output current
r$\dot{q}$	input current, output displacement
ru	input voltage, output displacement
s	position of acceleration sensor, or sampling
TVA	with tuned vibration absorber
u$\dot{q}$	input current, output voltage
uu	input voltage, output voltage
x	x-direction
y	y-direction
Z	impedance
z	z-direction

Superscripts

0	unloaded
c	compressive force
D	damping resistance
L	inductance

N	negative capacitance
t	tensile force
e	element
−	lower limit of interval
oc	open circuited transducer electrodes
ol	open loop transducer electrodes
+	upper limit of interval
RL	transducer connected to RL-Shunt
RLC	transducer connected to RLC-Shunt
s	static
sc	short circuited transducer electrodes
TVA	with tuned vibration absorber

Other mathematical symbols

$\mathscr{F}$	FOURIER transform
$\mathscr{I}\{\}$	imaginary part
$\mathscr{L}\{\}$	LAPLACE transform
$()'$	first derivative with respect to location ($= \frac{d}{dx}$)
$()''$	second derivative with respect to location ($= \frac{d^2}{dx^2}$)
$\mathscr{R}\{\}$	real part
$\dot{()}$	first derivative with respect to time ($= \frac{d}{dt}$)
$\ddot{()}$	second derivative with respect to time ($= \frac{d^2}{dt^2}$)

1 Introduction

1.1 Motivation

Modern mobile structures are increasingly benefiting from the effort of lightweight design that is to bear and withstand loads with minimum material usage over a defined life time without failure, [97]. Mechanical lightweight structures such as frames and struts in cars, airplanes or space structures are dynamic systems with inertia, stiffness and damping properties that respond to external time-varying disturbances such as road surfaces, aerodynamic forces and varying operation loads. Although lighter structures reduce energy consumption, they are susceptible to vibration issues due to low inherent damping. As a result, time-varying disturbances, such as external cyclic forces, can cause undesired structural vibrations that may lead to fatigue, reduced durability or undesirable noise.

Truss-type structures are a widely used approach for designing especially lightweight structures in mechanical and civil engineering, [32, 79, 96]. In the research framework of the Collaborative Research Center (SFB) 805 "Control of Uncertainty in Load-Carrying Structures in Mechanical Engineering", a truss-type structure is the main characteristic of the SFB-Demonstrator. The research program of the SFB 805 focuses on a holistic approach in order to control uncertainty along all phases of the product life: from product development to production to usage. In this context, the SFB-Demonstrator serves as a platform to all subprojects in the SFB 805 to test the developed methods and technologies for reducing or compensating uncertainty on real load carrying systems in order to control uncertainty. As typical for truss-type structures, the truss in the SFB-Demonstrator comprises truss members such as beam-columns with circular cross-section that are connected to each other via the relatively stiff truss nodes, [17, 52]. In the truss, beam-columns are subject to axial compression or tension and time-varying bending due to static and cyclic truss loads. Consequently, lightweight structures, such as truss-type structures, with little inertia or damping and high stiffness are prone to high vibration amplitudes when excited by a range of frequencies that induce resonance. Furthermore, the static truss loads may lead to axial compressive and tensile beam-column loads that detune the lateral beam-column resonance behavior, which is often neglected.

Vibration attenuation of truss-type structures may be achieved by stiffening, using supports for vibration isolation, increasing the structural damping or by using compensating forces, [77]. To this end, passive, semi-active and active measures such as viscous damping elements, mechanical tuned vibration absorbers (TVA) and active feedback control are used. Especially TVAs are widely applied for the attenuation of structural resonance modes. Typically, a TVA comprises a mass, stiffness and damping element, [95]. This vibratory system is added to a host structure, in this case to the truss, and usually tuned to a selected host structure resonance mode, thereby attenuating host structure vibrations in a narrow frequency range. With resonant shunted piezoelectric transducers, [47, 63], vibration attenuation is achieved in a comparable manner to a TVA, but several advantages become noticeable. Piezoelectric transducers convert mechanical energy into electrical energy, and vice versa. By connecting the piezoelectric transducer electrodes to an electrical circuit with resistance and inductance, the RL-shunt, an electrical tunable oscillation circuit with the inherent capacitance of the transducer is created. In contrast to a TVA that is additionally attached to a host structure, a piezoelectric transducer connected to an RL-shunt can be integrated into the axial or lateral mechanical load path where it becomes a load-carrying element in the host structure itself. Lightweight design benefits from load path integrated piezoelectric transducers thanks to less additional mass and also the load-carrying capability of stiff piezoceramic materials. Furthermore, the shunted transducer does not rely on a moving mass and, hence, no complex mechanical stiffness and damping elements are required. Instead, the dynamic properties such as damping and stiffness are precisely manipulated by the connected shunt circuit.

In this work, the advantages of compact integration and precise tuning for shunted transducers are used in a novel beam-column support concept called the piezo-elastic support [16, 25, 85], which has two shunted piezoelectric stack transducers integrated in the beam-column support. The piezo-elastic support is capable of attenuating vibrations in all lateral directions of a beam-column with circular cross-section when connected to RL-shunts without manipulating the beam-column's surface, and can also be used in the SFB-Demonstrator truss for vibration attenuation. This technical solution has not been published by other authors yet. In order to increase the performance of vibration attenuation with RL-shunts and as an enhancement in this work, RL-shunts with additional negative capacitances called the RLC-shunts are used, [6, 65]. However, in contrast to the RL-shunt, the negative capacitance can cause stability problems of the structural vibration, which has to be considered when setting the shunt values.

Despite the advantages of piezoelectric transducers in lightweight structures that have been named in the last paragraph, the vibration attenuation with resonant

shunted piezoelectric transducers is sensitive to variations in the tuning of shunt and host structure, [56, 73]. If not tuned optimally, host structure vibrations may not be attenuated adequately. In real lightweight structures, system properties and states vary due to manufacturing, assembly and load variations, and deterministic values usually cannot be predicted. Consequently, non-optimally tuned shunted piezoelectric transducers due to non-deterministic system property variations cause uncertainty in the vibration attenuation that may involve significantly reduced vibration attenuation performance or may even cause unstable vibrations, as in case of the RLC-shunt. In this context, a model-based uncertainty prediction is often used to estimate the discrepancy in vibration attenuation and its probability of occurrence, [3, 84]. So far, model-based prediction of uncertainty in the vibration attenuation with resonant shunted transducers is mainly limited to parameter uncertainty assumptions made from literature without experimental validation. However, a complete and consistent uncertainty quantification is only achieved by validation of the simulation model with experimental data, [81].

The main objectives of this work are:

- Quantification of the vibration attenuation of a beam-column with circular cross-section in arbitrary lateral direction using a novel beam-column support with rotational elasticity and integrated piezoelectric stack transducers connected to resonant shunts with and without negative capacitance.
- Numerical and experimental quantification of uncertainty in the vibration attenuation arising from static axial tensile and compressive load variations, manufacturing variations and system assembly variations.

Both objectives are necessary to evaluate the vibration attenuation capability of the piezo-elastic support.

1.2 Approach and scope of work

Lateral vibration attenuation of a beam-column with circular cross-section by a piezo-elastic support with integrated and resonant shunted piezoelectric transducers is investigated in two steps by using simulations and experiments:

1. Investigation of the deterministic lateral vibration attenuation with optimally tuned RL- and RLC-shunts.
2. Investigation of the non-deterministic and uncertain lateral vibration attenuation with RL- and RLC-shunts.

To quantify optimal vibration attenuation in (1.), the maximum lateral beam-column vibration amplitudes with RL- and RLC-shunts are compared to amplitudes when no shunts are connected. Uncertainty in the vibration attenuation in (2.) is quantified by probabilistic and non-probabilistic variations of the maximum amplitudes with shunts. Uncertainty in vibration attenuation with RL- and RLC-shunts is evaluated by the discrepancy of the uncertain and the optimal maximum vibration amplitudes and compared for the two shunt concepts.

Uncertainty in the vibration attenuation in (2.) is assumed to result from non-deterministic input parameter variations caused by the following and interacting sources of uncertainty:

- static axial tensile and compressive beam-column load variations and
- manufacturing and system assembly variations.

During operation, a static axial tensile or compressive force is assumed to act along the beam-column axis. For static axial tensile and compressive loading, non-probabilistic uncertainty is assumed by a force interval with lower and upper limit, but with unknown variability. Manufacturing and assembly variations are assumed to cause parameter value scattering about a mean value and, therefore, are quantified by probability density functions with known variability.

In this work, uncertain lateral vibration attenuation with RL- and RLC-shunts is numerically predicted by taking into account uncertainty assumed from own experiments and literature as well as disregarded uncertainty. In a case study, uncertainty from own experiments and literature is first analyzed individually and then combined.

Uncertainty assumed from own experiments:

- Non-probabilistic uncertainty in the vibration attenuation is derived from experimental static axial tensile and compressive load variations within the assumed load interval limits.
- Probabilistic uncertainty in the vibration attenuation is derived from interacting experimental variations of the manufacturing of the membrane-like spring element, which is a key element of the piezo-elastic support, and system assembly.

Uncertainty assumed from literature:

- Probabilistic parameter uncertainty due to manufacturing variations of the piezoelectric transducer properties and the electrical shunt components is derived from manufacturing tolerances.

The investigated systems consist of a beam-column with circular cross-section embedded in two piezo-elastic supports A and B, which are used for vibration excitation and attenuation, refer to figures 3.1 and 3.2. In support A, two piezoelectric transducers are used to apply broad-band vibration excitation in lateral directions in the frequency range of the first beam-column resonance mode. In support B, two piezoelectric transducers are either connected to RL- or RLC-shunts for vibration attenuation of the first resonance mode in lateral directions or the transducer electrodes are short circuited to account for vibration without shunts connected.

The structure of this work is as follows:

Chapter 2 classifies vibration attenuation with shunted piezoelectric transducers in general into state-of-art vibration attenuation approaches and explains vibration attenuation with resonant shunted transducers, which are also used in this work. Furthermore, the advantages of the piezo-elastic support are compared to existing technical approaches for vibration attenuation of beam-column and truss-type structures are discussed. The classification of uncertainty used in this work is presented and the state of research of uncertainty in vibration attenuation with resonant shunted transducers is discussed.

Chapter 3 presents the investigated beam-column system. The dynamic models of the beam-column system without and with shunts used for numerical analyses are derived by the use of a linear finite element (FE) beam-column model, linear piezoelectric transducer models and linear electrical shunt models. The model with shunts is used to optimally tune shunts for vibration attenuation in simulation and experiments.

Chapter 4 presents the experimental realization of the investigated beam-column system and shunt circuits. The experimental setup is used to measure the beam-column system's dynamic behavior with and without shunts in order to quantify the vibration attenuation capability of the piezo-elastic support with shunted transducers and to quantify uncertainty in the vibration attenuation due to membrane-like spring element and static axial load variations.

Chapter 5 presents numerical and experimental results of the deterministic lateral beam-column vibration attenuation with optimally tuned shunts when uncertainty is disregarded. Furthermore, the effect of excitation applied at oblique angles on the plane lateral beam-column vibration is investigated and studied via orbit plots and frequency transfer function.

Chapter 6 presents the general concept to assume and quantify uncertainty from own experiments. A case study is performed to quantify and compare uncertainty in vibration attenuation with RL- and RLC-shunts.

Chapter 7 summarizes the presented work and gives an outlook on future research objectives.

2 Background and state of research

Vibrations are a structure's response to dynamic excitation forces or displacements and depend on the excited frequency range. Especially lightweight structures, such as truss-type structures, with little inertia or damping and high stiffness, are prone to high vibration amplitudes when excited by a range of frequencies that induce resonance. High structural vibration amplitudes are related to several detrimental effects, such as diminished durability, unwanted noise, reduced operation precision and safety issues. Therefore, different technical vibration attenuation approaches such as shunted piezoelectric transducers have been developed to influence the structure's dynamic behavior in order to reduce undesired effects of high vibration levels.

In this chapter, resonant shunted piezoelectric transducers are classified into the general context of vibration attenuation approaches and other available shunt concepts. The principle of vibration attenuation with resonant shunted transducers is explained and their attenuation capability is compared to that of tuned vibration absorbers. A state-of-art classification of uncertainty used in this work is given and the state of research of uncertainty in vibration attenuation with resonant shunted transducers is discussed.

2.1 Vibration attenuation of mechanical structures

Different approaches to achieve vibration attenuation of mechanical structures exist and they can be characterized by their amount of additional energy that is necessary to achieve vibration attenuation.

Technical approaches for vibration attenuation

The most common approaches rely on stiffening, damping, compensation and isolation, [42, 77]. By stiffening, the resonance frequencies of a structure are shifted up beyond the frequency band of excitation. By damping, the resonance vibration peaks are reduced by dissipation of vibration energy. By compensation, forces of opposite phase to the vibration are applied to the structure. By isolation, the propagation of vibration to the structure is prevented.

Characterization of vibration attenuation approaches

Vibration attenuation, in context of the named approaches, is achieved by passive, semi-active or active methods. In this context, the classification passive, semi-active or active results from the amount of additional energy that is put into the structure and that is necessary to achieve vibration attenuation, [20, 78, 94]. Passive vibration attenuation does not rely on additional energy and can be achieved by a variety of technical approaches, e.g. TVAs. A TVA is an auxiliary vibratory system comprising a mass, stiffness and damping element that is attached to the host structure, [95]. The TVA is tuned to a host structure resonance frequency thereby attenuating vibrations in a narrow frequency range. While the host structure's vibration is reduced, the vibration amplitudes of the TVA mass can be significantly high. For semi-active vibration attenuation, additional energy is used to change or control passive mechanical properties, such as stiffness or damping [61]. For active vibration attenuation, additional energy is used to provide active forces, such as position-, velocity- or acceleration-proportional forces [77]. Although effective and powerful, active vibration attenuation always needs power supply and computational controller performance.

In this work, shunted piezoelectric transducers are used for vibration attenuation. In general, a shunted piezoelectric transducer achieves passive, semi-active or active vibration attenuation through damping and compensation depending on the used shunt concept.

2.2 Vibration attenuation with shunted piezoelectric transducers

Among the numerous technical possibilities to attenuate vibrations, one well-known technique for passive, semi-active or active vibration attenuation uses piezoelectric transducers coupled with the host structure and an electric circuit that is connected to the transducer electrodes. This approach was first proposed in [19] and has been subject to research in many publications, [6, 9, 18, 28, 32, 34, 50, 59, 61, 65, 66, 76, 83, 92, 93, 99].

Piezoelectric transducers

A piezoelectric transducer coupled to a host structure converts mechanical deformations of the host structure into electrical charges, using the piezoelectric effect. Furthermore, when applying electrical voltages to the transducer electrodes the transducer deforms, according to the inverse piezoelectric effect. The latter enables

the transducer to generate actuating forces that act on the host structure and can attenuate vibrations. The piezoelectric effect and the inverse piezoelectric effect combined characterize the sensing and actuating behavior of a piezoelectric transducer. The conversion of mechanical to electrical energy, and vice versa, depends on the material electromechanical coupling coefficient of the piezoelectric material used in the transducer, [44]. Vibration attenuation with piezoelectric transducers is suitable for lightweight structures as the transducers can be integrated into the mechanical axial or lateral load path where they become load-carrying elements in the host structure itself, thereby reducing the effect of additional masses, [83].

For practical applications, various shapes of piezoelectric transducer are commercially available, e.g. patches, blocks, tubes or multilayer stack transducers, often made of the piezoceramic material lead zirconate titanate also called PZT, [44]. In this work, piezoelectric multilayer stack transducers made of PZT are used as PZT achieves an adequate material electromechanical coupling coefficient and the stack transducer design allows a compact integration in the piezo-elastic support.

Shunt concepts

In [59] and [99], an overview of available shunt circuit designs to achieve passive, semi-active and active vibration attenuation is given. Resistive and resonant shunts for passive vibration attenuation, [9, 32, 65, 83], work comparable to mechanical viscous damping elements and TVAs. But like TVAs, resonant shunts are sensitive to an imprecise tuning of host structure and shunt as a result of model inaccuracies or system property variations, [73]. To overcome this drawback and to improve vibration attenuation, more complex shunts have been presented and investigated, e.g. switching and adaptive shunts for semi-active vibration attenuation, [28, 34, 50, 61, 66, 92], and shunts with negative capacitances or additional power supplies for active vibration attenuation, [6, 7, 18, 65, 76].

The variety of presented shunt concepts shows a trend of increasing shunt complexity in order to pursue vibration attenuation improvements and robustness. However, adaptive and switching shunts become more complex as additional components and electric energy for sensors and control loops are needed. In contrast to that, resonant shunted piezoelectric transducers with optimally tuned RL- or RLC-shunt values can still highly attenuate host structure vibration with no additional sensors needed. In order to evaluate the suitability of resonant shunted piezoelectric transducers for lateral beam-column vibration attenuation with the piezo-elastic support, numerical and experimental deterministic and uncertain nondeterministic vibration attenuation analyses are performed in this work.

2.2.1 Resonant shunted piezoelectric transducer

By connecting the electrodes of a piezoelectric transducer coupled to a host structure with a series circuit of inductance L and resistance R^{D}, the RL-shunt [32], an electrical tunable oscillation circuit with the inherent piezoelectric transducer capacitance C is created. When the host structure vibrates, mechanical vibratory energy is converted into electrical energy in the piezoelectric transducer due to the piezoelectric effect and stored in the oscillating circuit. The electrical energy partly dissipates in the resistor R^{D}, thus increasing damping and generating forces to counteract the vibration due to the inverse piezoelectric effect. Because of this, the transducer connected to an RL-shunt achieves vibration attenuation via both damping and compensation, and is well suited for vibration attenuation of host structure resonances. The performance of vibration attenuation with shunted transducers depends on the dimensionless piezoelectric general electromechanical coupling coefficient (GEMCC) γ of the transducer and the structure, [33]. The GEMCC is a modal quantity that is related to the host structure's resonance modes. It indicates the amount of mechanical vibratory energy converted into electrical energy and depends on the used piezoelectric material as well as on the position on the host structure where the transducer is coupled. The maximization of the GEMCC is usually attempted during the design process, [13]. However, the GEMCC only indicates the vibration attenuation potential and, eventually, the vibration attenuation depends on the tuning of the shunt values of R^{D} and L.

The piezoelectric transducer mainly behaves as a capacitor with inherent capacitance C due to the unbalanced electric charges that appear on its electrodes when a mechanical strain is applied. This results in an increase in the mechanical stiffness of the transducer. In order to counteract this effect and to increase vibration attenuation with resonant shunted transducers, a capacitor with a negative capacitance C^{n} can be connected in series to the transducer to reduce the mechanical transducer stiffness. The negative capacitance behaves as a spring element with negative stiffness, as evidenced by [12], where the elasticity of piezoelectric polymer films is adjusted using a variable negative capacitance. This is also valid for piezoceramic materials. By adding a negative capacitance C^{n} to the RL-shunt, the RLC-shunt, a higher effective coupling is achieved and the vibration attenuation performance of the resonant shunted transducer is increased significantly. Furthermore, the effective piezoelectric transducer capacitance increases and smaller values for the inductance L are needed, [55]. In theory, the vibration attenuation performance increases monotonically and non-linearly with the negative capacitance ratio $\delta = C/C^{\mathrm{n}}$ approaching the stability limit $\delta_{\mathrm{crit}} = -1 + \gamma^2$, [65]. In

experiments, instability usually occurs earlier for $\delta < \delta_{\text{crit}}$ due to imprecise system parameter knowledge, [55].

Vibration attenuation with resonant shunted piezoelectric transducers and comparison to TVAs

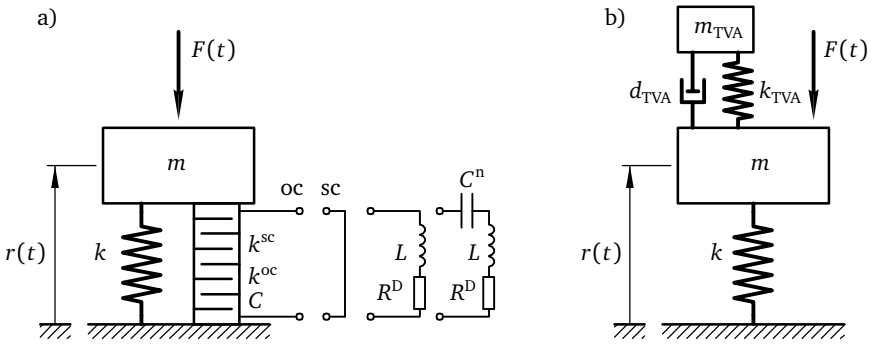

Figure 2.1: a) host structure with piezoelectric transducer and shunts, b) host structure with tuned vibration absorber (TVA)

Figure 2.1 shows the principles of vibration attenuation with a resonant shunted transducer and with a TVA for an undamped mechanical host structure. For both concepts, the host structure is represented by a mass m and a stiffness k. Mostly and also in this work, vibration attenuation analyses with shunted transducers and TVAs are based on the frequency transfer behavior in a frequency range that contains host structure resonances. In figure 2.1, the host structure's mass is excited by the periodic force $F(t)$, which leads to the periodic displacement response $r(t)$. To obtain the frequency transfer behavior of excitation force to displacement response, the host structure's equation of motion is transformed into the frequency domain by using the LAPLACE transform, chapter 3. The frequency transfer behavior is described by

$$F(\Omega)\,G(\Omega) = r(\Omega) \tag{2.1}$$

with the excitation force $F(\Omega)$, the frequency transfer function $G(\Omega)$ and displacement response $r(\Omega)$, which are all functions of the excitation frequency Ω.

In figure 2.1a, the piezoelectric transducer with electrical capacitance C is assumed to be without mass and is connected in parallel to the host structure stiffness k. When the transducer is not connected to a shunt and vibrations are not attenuated, the two states of transducer electrodes

- short circuited transducer electrodes (sc) with associated mechanical transducer stiffness k^{sc} and

- open circuited transducer electrodes (oc) with associated mechanical transducer stiffness k^{oc}, whereby $k^{oc} > k^{sc}$ due to the piezoelectric effect,

are distinguished, [65]. With sc or oc electrodes, the new host structure stiffness becomes $K^{sc} = k + k^{sc}$ or $K^{oc} = k + k^{oc}$. In consequence of the sc and oc transducer stiffness, the two host structure eigenfrequencies $\omega^{sc} = \sqrt{K^{sc}/m}$ and $\omega^{oc} = \sqrt{K^{oc}/m}$ can be calculated, which are often used to estimate the GEMCC via

$$\gamma = \sqrt{\frac{(\omega^{oc})^2 - (\omega^{sc})^2}{(\omega^{oc})^2}}. \tag{2.2}$$

For vibration attenuation, the transducer electrodes are connected to a series RL- or RLC-shunt, figure 2.1a. For vibration attenuation with TVAs, the TVA with mass m_{TVA}, stiffness k_{TVA} and damping d_{TVA} is attached to the host structure's mass m not affecting the host structure stiffness in figure 2.1b.

For optimal vibration attenuation with resonant shunted transducers, appropriate values for R^D, L and C^n have to be selected. Typically, the shunt values are selected to achieve minimum vibration amplitudes through the balanced calibration method. This is an analytical method presented in [36] for the tuning of TVAs and has been adapted to resonant shunted piezoelectric transducers, [39, 64]. Balanced calibration is shown in figure 2.2a by the amplitude response $|G^{RL}(\Omega)| = |r(\Omega)/F(\Omega)|$ of the host structure frequency transfer function (2.1) with the piezoelectric transducer connected to an RL-shunt, red lines. The balanced calibration imposes two fixed points P and Q on the amplitude response function $|G^{RL}(\Omega)|$ in figure 2.2a. The inductance L is determined to get approximate equal heights of amplitudes in P and Q for $R^D = 0$, this is indicated by the curve with a low value of R^D shown with a dashed red line. Then, resistance R^D is obtained to lead to a flat plateau with minimal broadband amplitudes shown with a solid red line in figure 2.2a and maximum remaining peak gain $\widehat{G}^{RL} = \max\{|G^{RL}(\Omega)|\}$. By comparing the peak gain $\widehat{G}^{RL}$ to the peak gain $\widehat{G}^{sc}$ of the short circuited normalized amplitude response $|G^{sc}(\Omega)|$, i.e. no shunt is connected to the piezoelectric transducer and where small damping has been added in the simulation, vibrations are reduced thanks to optimally tuned values for R^D and L. However, the vibration attenuation with resonant shunts is sensitive to imprecise tuning. Consequently, not optimally tuned shunt parameters reduce the capability of vibration attenuation, as shown by the red dotted line in figure 2.2a.

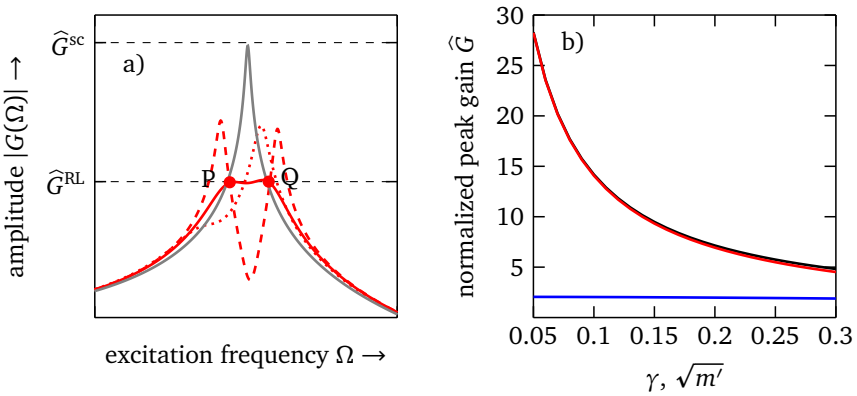

Figure 2.2: a) amplitude responses with RL-shunt $|G^{RL}(\Omega)|$: optimally tuned (——), low value of R^D (– –), not optimally tuned (·····), short circuited amplitude response $|G^{sc}(\Omega)|$ (——), b) normalized peak gains: with RL-shunt $\widehat{G}^{RL}$ (——), with RLC-shunt $\widehat{G}^{RLC}$ (——), with TVA $\widehat{G}^{TVA}$ (——)

Vibration attenuation with piezoelectric transducers shunted to an RL- and RLC-shunt is compared to vibration attenuation with a TVA, figure 2.1, by comparing peak gains of the attenuated host structure amplitude responses. In [65], the normalized peak gains

$$\widehat{G}^{RL} = \sqrt{\frac{2}{\gamma^2+\gamma^4}}, \quad \widehat{G}^{RLC} = \sqrt{\frac{2(1+\delta)}{\gamma^2+\gamma^4}} \quad \text{and} \quad \widehat{G}^{TVA} = \sqrt{1+\frac{2}{m'}} \tag{2.3}$$

for optimally tuned shunts and TVA have been derived as functions on the dimensionless parameters γ and δ and m'. In (2.3), γ and δ are respectively the already introduced GEMCC and negative capacitance ratio and $m' = m_{TVA}/m$ is the mass ratio of host structure mass and TVA mass. Figure 2.2b compares the peak gains $\widehat{G}^{RL}$, $\widehat{G}^{RLC}$ and $\widehat{G}^{TVA}$ for optimally tuned shunts and TVAs for different values of γ and m'. Both the peak gains $\widehat{G}^{RL}$ and $\widehat{G}^{TVA}$ reduce asymptotically for increasing values of γ and m'. For $\gamma \approx \sqrt{m'}$, similar peak gains are achieved and, hence, the transducer with RL-shunt and the TVA lead to similar host structure vibration attenuation. Additionally, figure 2.2b shows further reduced and almost constant host structure peak gains $\widehat{G}^{RLC}$ when a negative capacitance is included in the RL-shunt.

General aspects for experimental implementation

In experimental implementation, inductance values L in the range of millihenry to several henry may be required in combination with the demand for a precisely tunable inductance. Therefore, the inductance is often synthesized by electrical circuits with resistors, a capacitor and two operational amplifiers, [4, 41, 57]. This circuit creates an electrical impedance that behaves like an electromagnetic coil and for that, a power supply is required. Nevertheless, vibration attenuation with an RL-shunt and synthetic inductance can still be considered to be passive, because the energy used for vibration attenuation only results from the piezoelectric effect. Moreover, a negative capacitance C^{n} as required in the RLC-shunt does not exist in the form of passive electrical components. Therefore, a negative capacitance for vibration attenuation is also realized by an active electrical circuit with operational amplifiers. This circuit changes the sign of the impedance of a passive capacitor whose value can be adjusted by resistors in the circuit. A negative capacitance behaves like a charge source and provides electrical charges when a voltage is applied. Because of this, additional energy is used in the RLC-shunt to generate actuating forces. The authors in [6, 7, 38] define the RLC-shunt as active vibration attenuation. The characterization of passive and active vibration attenuation with RL- and RLC-shunt is also used in this work.

2.2.2 Truss-type structures with resonant shunted transducers

As stated in the last section, vibration attenuation with shunted piezoelectric transducers has been the subject of research for several decades. However, most of the investigations focus on academic structures, such as cantilever beams with rectangular cross-section, [6, 31, 47, 49, 60], or plates, [7, 9, 87], with piezoelectric patch transducers. These structures are subject to periodic forces that lead to vibration. What is more, vibration attenuation is only investigated in one lateral direction. In contrast, a beam-column with circular cross-section and vibration excitation due to periodic forces applied in various lateral directions is investigated in this work. A novel technical concept called the piezo-elastic support, [16, 25], is used for lateral vibration attenuation of a beam-column in various lateral directions, which has two shunted piezoelectric stack transducers integrated in the beam-column support.

Contrary to single beams and plates, truss-type structures under real conditions bear and withstand constant and cyclic loads. As an example, figure 2.3 shows the SFB-Demonstrator introduced in section 1.1 that carries a payload (1) on an upper beam-column truss (2) and that is connected to the lower truss (3) via guidance links and a spring-damper component (4), [52]. The guidance link enables the

kinematic motion between the lower and upper truss structures. The elastic foot (5) acts as an impact absorption element that introduces transient axial and lateral impact forces when releasing the SFB-Demonstrator from a specified drop height. Furthermore, cyclic forces are introduced at the elastic foot (5) in the case of cyclic base excitation. Both load scenarios may lead to upper truss vibrations. Due to a truss structure's design, which include many assembled components, such as beams, rods and supports, truss structures, as in the SFB-Demonstrator, show local and global vibration modes, [96]. Global vibration modes are characterized by the lateral or rotating movement of the truss supports, whereas local modes are dominated by the lateral vibration behavior of each beam-column.

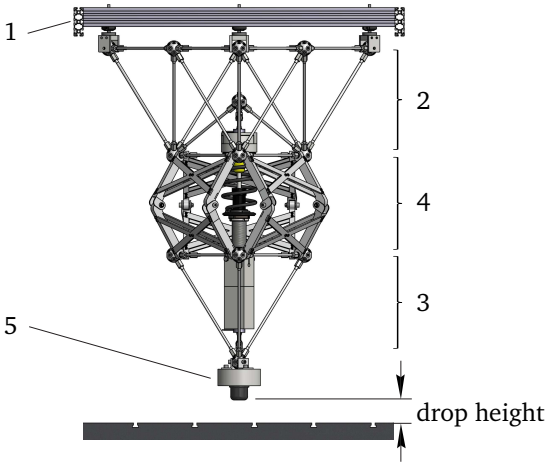

Figure 2.3: CAD illustration of SFB-Demonstrator, [52]

Only a few studies have investigated vibration attenuation with resonant shunted piezoelectric transducers for lightweight truss-type structures, [2, 55, 58, 79]. In [2], supports of a tripod beam-column truss of the ASTREX precision space structure use piezoelectric washers that are strained in shear under dynamic loading connected to RL-shunts. Due to the planar washer design, only one bending direction of the beam-columns with circular cross-section could be attenuated with RL-shunts in experiments. In [55, 58, 79], a piezoelectric stack transducer is integrated in a truss beam-column and compressed or elongated in the axial direction when the structure vibrates. RL- and RLC-shunts are connected to the transducer and the vibration attenuation of one global truss bending mode is experimentally

investigated. The piezo-elastic support with shunted transducers investigated in this work is capable of attenuating lateral beam-column vibration modes, chapter 5, as well as global truss vibration modes, [40].

Furthermore, in the SFB-Demonstrator and truss-type structures, variations in the static payloads may result in axial tensile and compressive loading of the truss beam-columns. This affects the resulting lateral bending stiffness of the beam-columns leading to changes in the beam-column and truss resonance frequencies, [71]. For vibration attenuation with resonant shunted piezoelectric transducers, a change of the resonance frequencies can reduce the achievable vibration attenuation capability due to detuned shunted piezoelectric transducers. Contributions that investigated the effect of additional static loads on the vibration attenuation with resonant shunted transducers are not known to the author of this dissertation. In this work, the vibration attenuation of a single beam-column with the novel piezo-elastic support is investigated when the beam-column is axially loaded. Besides vibration attenuation with shunted transducers, the piezo-elastic support additional allows a new concept of active buckling stabilization, [85].

2.3 Uncertainty

Uncertainty in design and application of resonant shunted transducers leads to non-deterministic vibration attenuation variations caused by non-deterministic varying system properties and operating conditions. Consequently, during operation, uncertainty may result in a detuned shunted piezoelectric transducer and loss of attenuation performance, which is comparable to the non-optimal tuning in figure 2.2a. In order to classify and describe uncertainty, section 2.3.1 presents the state-of-art in uncertainty classifications with mathematical distribution functions and measures to quantify uncertainty, which are used in this work. Afterwards, section 2.3.2 provides the state of research on uncertainty in vibration attenuation with shunted transducers.

2.3.1 Uncertainty classification and description

There are different ways to classify uncertainty. In this work, the holistic approach developed by SFB 805 is used in order to classify and evaluate uncertainty in the vibration attenuation with resonant shunted piezoelectric transducers. According to the SFB 805 in [14, 35], uncertainty in vibration attenuation occurs because properties of a system cannot or can only partially be determined. Furthermore,

uncertainty occurs along all phases of the product life: development, production and usage. The approach developed by the SFB 805 distinguishes data or parameter uncertainty and model uncertainty:

- Data uncertainty refers to uncertainty in the system parameters or states. The system parameters and states include quantities such as geometry, material properties, initial conditions or boundary conditions and system excitation, e.g., mechanical forces or moments acting on the system. Uncertainty in these quantities can originate from a range of sources including manufacturing tolerances, measurement uncertainty, changing boundary conditions or approximate numerical solutions of differential equation-based models, which are often used in mechanical engineering.

- Model uncertainty results from all assumptions, conceptualizations, abstractions, approximations, and mathematical formulations on which the model relies and the functional relation of data.

Uncertainty in the vibration attenuation with resonant shunted transducers due to parameter uncertainty, as part of data uncertainty, arising from manufacturing, system assembly and static load variations is investigated in this work. Model uncertainty is disregarded and not taken into account. Instead, state of research models are used and validated for uncertainty prediction.

Data uncertainy for each property of the investigated beam-column with piezoelastic supports and shunted transducers may be divided into the three categories probabilistic, non-probabilistic and disregarded uncertainty, [15, 69]:

- Probabilistic uncertainty is given if a non-deterministic value of an arbitrary property is approximated by probability measures and known or assumed probability distribution functions.

- Non-probabilistic uncertainty is given if a non-deterministic value of an arbitrary property is approximated by known or assumed membership function or interval. For each value, a lower limit and an upper limit can be specified.

- Disregarded uncertainty is given if no declaration regarding any uncertainty is made and the property is considered deterministic.

The mathematical description of probabilistic and non-probabilistic uncertainty is given in the following section.

Description of probabilistic uncertainty

The variation of an arbitrary system property X represented by a sample is often depicted graphically by empirical histograms. Histograms show the frequencies of observations occurring within a specified range of values (bins). Furthermore, the sample data can be used to calculate probabilistic measures such as arithmetic means, modes or percentiles that are used to characterize the central tendency and the dispersion of the sample. In some cases, it is reasonable to approximate empirical samples by continuous parametric distribution functions. In this work, the normal distribution is used for properties of the beam-column system without shunts, such as the short circuited resonance frequency, and GUMBEL distribution is used for the peak gains with shunt.

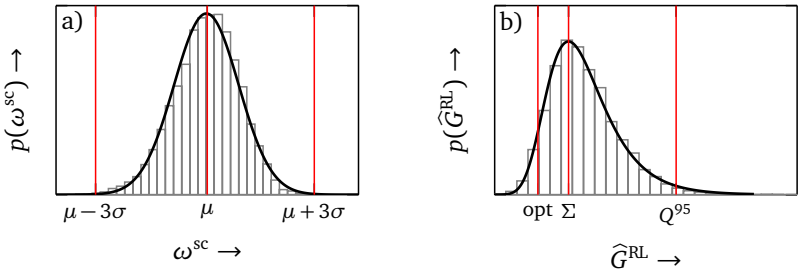

Figure 2.4: Histograms and fitted parametric distribution functions to represent probabilistic uncertainty, a) normal distribution, b) GUMBEL distribution

Figure 2.4a shows a histogram plot and the fitted normal distribution probability density function (pdf) (2.4) of the short circuited resonance frequency ω^{sc}, which has been introduced in section 2.2.1 and which varies due to uncertainty as investigated in section 6.3.1. For comparison with the pdf, the histogram is normalized to also obtain probability densities with the sum of the bar areas equal to 1. The general equation of the continuous normal pdf is

$$p_{\mathcal{N}}(X) = \frac{1}{\sigma_X \sqrt{2\pi}} e^{-\frac{(X-\mu_X)^2}{2\sigma_X^2}} \tag{2.4}$$

with a mean μ_X and a standard deviation σ_X

$$\mu_X = \frac{1}{N}\sum_{n=1}^{N} X_n \quad \text{and} \quad \sigma_X^2 = \frac{1}{N-1}\sum_{n=1}^{N}(X_n - \mu_X)^2 \tag{2.5}$$

calculated for N samples, [10]. The mean is a measure of the central tendency, and the standard deviation is a measure of the dispersion, which both are used to characterize the distribution.

Figure 2.4b shows a normalized histogram plot of the peak gain with RL-shunt $\widehat{G}^{\mathrm{RL}}$. As introduced in section 2.2.1, the peak gain represents the maximum attenuated amplitude response. Hence, the distribution of the peak gain values in figure 2.4b represents the distribution of the maximum of the attenuated amplitude response, which varies due to uncertainty as investigated in section 6.3.3. The central tendency of the distribution of peak gain values is represented by Σ, which represents the peak gain value that appears most likely. Additionally and as measure of dispersion, the 95$^{\mathrm{th}}$ percentile Q^{95} is used. Q^{95} represents the limit below which 95% of the peak gains in the sample may be found, and is used as a measure for the maximum occurring peak gain value in this work. Additionally, figure 2.4b shows qualitatively the optimal (opt) peak gain value of the attenuated amplitude response when uncertainty is disregarded. Probabilistic uncertainty in the vibration attenuation in this work is quantified by the most likely peak gain Σ_X and maximum peak gain Q_X^{95}. By comparing Σ_X and Q_X^{95} to opt_X, uncertainty in the vibration attenuation is evaluated.

The distribution of extreme values can be approximated by extreme value distributions, such as the Gumbel distribution in figure 2.4b. The general equation of the Gumbel pdf is given by

$$p_{\mathscr{G}}(X) = \frac{1}{\Delta_X} e^{-(\beta + e^{-\beta})} \quad \text{with} \quad \beta = \frac{X - \Sigma_X}{\Delta_X} \tag{2.6}$$

with location parameter Σ_X and scale parameter Δ_X, [10]. If the assumption of Gumbel is justified, then the pdf's location parameter is equal to the most likely peak gain. Furthermore, the Gumbel parameters can be used to calculate Q_X^{95} according to

$$Q^{95} = 100[\Sigma_X - \Delta_X \ln(-\ln(0.95))] \tag{2.7}$$

Description of non-probabilistic uncertainty

The variation of the property X in case of non-probabilistic uncertainty is described by the interval $X = [X^-, X^+]$ with lower limit X^- and upper limit X^+. No declaration about its probability distribution is made.

2.3.2 Uncertainty in vibration attenuation with resonant shunted transducers

Uncertainty in vibration attenuation with resonant shunted transducers can be caused by data and model uncertainty, compare to section 2.3.1. So far, research studies the aspects of uncertainty reduction and uncertainty quantification:

- For uncertainty reduction, technical and mathematical approaches are used with the purpose to reduce uncertainty in the vibration attenuation prediction and application.
- For uncertainty quantification, probabilistic and non-probabilistic approaches are used to predict variations in the vibration attenuation due to parametric uncertainty in the host structure, transducer and shunt properties.

Uncertainty reduction

In the context of uncertainty reduction, different approaches, such as controlled shunts, [34, 50, 61, 66, 92], and robust shunt value optimization, [48, 62, 92], are applied. As mentioned in section 2.2, controlled shunt circuits such as switching and adaptive shunts attempt to compensate the effect of an imprecise tuning by vibration synchronized switching and feedback adaptation strategies, [28, 34, 50, 61, 66, 92]. For example, in the experimental investigations in [61], artificially induced host structure resonance frequency changes are sensed and compensated by an adaptive inductance using a phase lock loop control. However, additional sensors, circuit elements and control loops are required that lead to additional costs and higher system complexity.

In robust shunt value optimization, host structure variations are included in the optimization process in order to ensure that vibration attenuation still performs as specified, [48, 62, 92]. In [48], host structure resonance frequency variations of $\pm 10\,\%$ have been taken into account in the robust optimization of an RL-shunt resulting in less variation in the host structure vibration attenuation for GEMCCs $\gamma \leq 0.15$ when compared to the non-robust optimized RL-shunt. For $\gamma > 0.15$, no advantage by robust optimization is observed. Furthermore, for the RLC-shunt no significant advantage of robust optimization is observed.

Uncertainty quantification

In the context of uncertainty quantification, mainly simulation models of the host structure with resonant shunted piezoelectric transducers are used to predict uncer-

tainty in the vibration attenuation via forward uncertainty propagation of uncertain input parameters, [81]. In order to make use of the deterministic simulation models that are common in the mechanical engineering, MONTE-CARLO-Simulation is often applied in the simulation-based uncertainty prediction, [27]. Parameter uncertainy for each property may be divided into the three categories: probabilistic, non-probabilistic and disregarded uncertainty, refer section 2.3.1.

In [3, 84, 87], uncertainty quantification in the vibration attenuation of resonant shunted piezoelectric transducers due to probabilistic parameter uncertainty caused by manufacturing variations of host structure and RL-shunt components is performed via MONTE-CARLO-Simulation. In [3, 84], cantilever beams with piezoelectric patch transducers and different GEMCCs are investigated and manufacturing variations in inductance L and resistance R^{D} are assumed with normal distribution. For other parameters, uncertainty is disregarded. For the example in [3] with $\gamma = 0.09$, variations of 10 % in L and R^{D} decrease the vibration attenuation by 50 % compared to the nominal case. For the example in [84] with $\gamma = 0.16$, variations of 5 % and 20 % in L and R^{D} decrease the attenuation performance by 30 % and 70 % compared to the nominal case. Comparing the results from [3, 84, 87] shows that uncertainty in the vibration attenuation depends on the considered variation range and the GEMCC. With increasing GEMCC, uncertainty in the vibration attenuation decreases, which has also been observed in an own numerical study, [21]. However, a system-specific uncertainty analysis is generally recommended.

In [87], probabilistic uncertainty in the host structure resonance frequencies and GEMCCs of a clamped shell structure with piezoelectric patch transducer results from forming process manufacturing variations and variability in the clamping stiffness is investigated. Therefore, a finite element shell model is calibrated by deterministic experimental results and the probability distribution functions for the resonance frequencies and GEMCCs are obtained with parametric uncertainty in the shell geometry, the transducer position and clamp stiffness, all with the assumed normal distribution. For other parameters uncertainty is disregarded, e.g. the transducer properties. However, no investigations on uncertainty in the vibration attenuation are performed.

As part of uncertainty quantification, other contributions focus on numerical vibration attenuation sensitivity analyses with RL- and RLC-shunt in order to identify parameters that should be taken into account in uncertainty analyses and to identify parameters that can be neglected with disregarded uncertainty. The numerical studies in [21, 56, 73] showed that the piezoelectric transducer properties, the shunt inductance L and the shunt negative capacitance C^{n} mainly affect the vibration attenuation. Variations in the host structure material properties and the

damping resistance R^{D} showed minor effects. Furthermore, in [30] and [23], the vibration attenuation sensitivity to variations in the host structure boundary support conditions has been evidenced.

As part of probabilistic uncertainty quantification in general, uncertain static loads with assumed logarithmic normal distribution have been taken into account in the structural analysis of a truss in [70]. However, vibration attenuation with resonant shunted piezoelectric transducers was not part of the study.

2.4 Conclusion of state of research

Resonant shunted piezoelectric transducers attenuate vibrations comparably to TVAs, [65]. In contrast to a TVA that is additionally attached to a host structure, a resonant shunted piezoelectric transducer can be integrated into the axial or lateral mechanical load path where it becomes a load-carrying element in the host structure itself. This allows novel technical approaches for vibration attenuation of lightweight structures, such as the piezo-elastic support.

However, vibration attenuation with resonant shunted piezoelectric transducers is sensitive to variations in the tuning of shunt and host structure, [56, 73], which leads to uncertainty in the vibration attenuation. So far, research studies mainly focused on numerical uncertainty quantification with parameter uncertainty assumed from literature, [3, 84]. Furthermore, a transfer of the results from available uncertainty analyses to the application of the piezo-elastic support is not straightforward since the effects of uncertainty on the vibration attenuation are influenced by system specific properties, such as the GEMCC.

Uncertainty in vibration attenuation with resonant shunted transducers due to static loading of beam-columns, which may occur in truss-type structures, has not been investigated numerically or experimentally in research studies. The beam-column in this work is subject to static tensile and compressive loading.

The main difference to existing works is the combination of uncertainty assumed from own experiments and literature to quantify uncertainty in the vibration attenuation with RL- and RLC-shunts. Additionally, uncertainty analyses of application-related piezoelectric structures, such as the used piezo-elastic support, is not performed often.

3 Vibration attenuation with a shunted piezo-elastic support

This chapter introduces the beam-column system consisting of a beam-column embedded in two piezo-elastic supports that are used for vibration excitation and attenuation. The beam-column system is used to investigate the capability of vibration attenuation of the piezo-elastic support with shunts, and to study uncertainty in the vibration attenuation due to static beam-column load, manufacturing and system assembly variations in chapters 5 and 6.

After presenting the general concept of the beam-column system, the mathematical electromechanical models of the beam-column system without shunts and with shunts are derived. In this work, the models are used to quantify the beam-column system's dynamic behavior in the frequency domain without and with attenuation through shunts for deterministic and uncertain system parameters. Furthermore, the models are used to numerically tune the shunts for optimal vibration attenuation of the first lateral beam-column mode in simulation and experiment. The frequency transfer functions and their related characteristic quantities to describe the dynamic behavior used in chapters 5 and 6 are summarized in the last section of this chapter.

3.1 General concept

Figure 3.1 presents the general concept of the beam-column with circular cross-section and with piezo-elastic supports used in this work to investigate lateral beam-column vibration attenuation in the y-z-plane.

At the beam-column's ends, pinned supports laterally support the beam-column and allow for rotation in case of bending. Additionally, in each support A and B, lateral transducer forces F_y and F_z act on the beam-column via relatively stiff axial extensions in order to affect the lateral beam-column dynamics. Particularly in support A, piezoelectric transducer forces $F_{y,\mathrm{A}}$ and $F_{z,\mathrm{A}}$ additionally support the beam-column in lateral y- and z-direction due to the transducer's elastic behavior

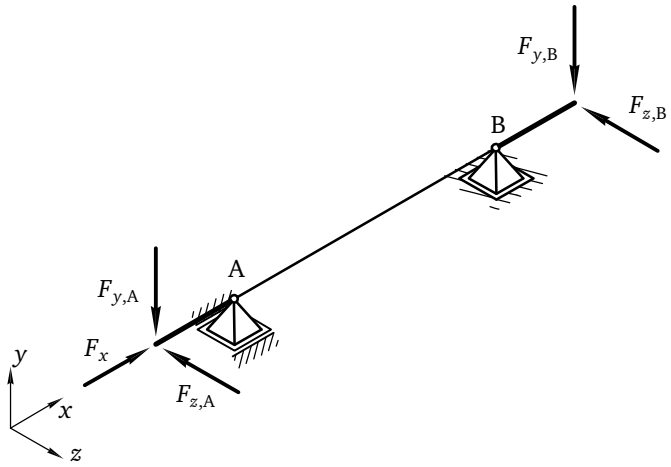

Figure 3.1: General concept of the beam-column with piezo-elastic supports

and laterally excite the beam-column to vibrate in the y-z-plane due to the inverse piezoelectric effect, section 2.2. In support B, piezoelectric transducer forces $F_{y,\mathrm{B}}$ and $F_{z,\mathrm{B}}$ additionally support the beam-column in lateral y- and z-direction due to the transducer's elastic behavior and laterally attenuate beam-column vibrations in the y-z-plane when connected to electrical shunt circuits due to the direct and the inverse piezoelectric effect, section 2.2. The static force F_x acts on the beam-column in axial direction to account for static truss loads as motivated in section 2.2.2. To sum up, support A is used to apply excitation, whereas support B provides the investigated vibration attenuation by shunted transducers.

3.2 System description

In this section, a detailed sketch of the beam-column with piezo-elastic supports as introduced in figure 3.1 with all relevant coordinates, directions, displacements and mechanical as well as electromechanical properties is given.

In figure 3.2a, the slender beam-column has a length l_b and a circular solid cross-section of radius r_b. The beam-column properties bending stiffness EI_b and density ϱ_b are assumed constant across the entire beam-column length. The beam-column is embedded in two piezo-elastic supports A and B at location $x = 0\,\mathrm{m}$ and location $x = l_\mathrm{b}$. The support B is fixed in axial and lateral directions. The support A is also fixed laterally, but is free to move in axial direction so that a static axial force F_x at

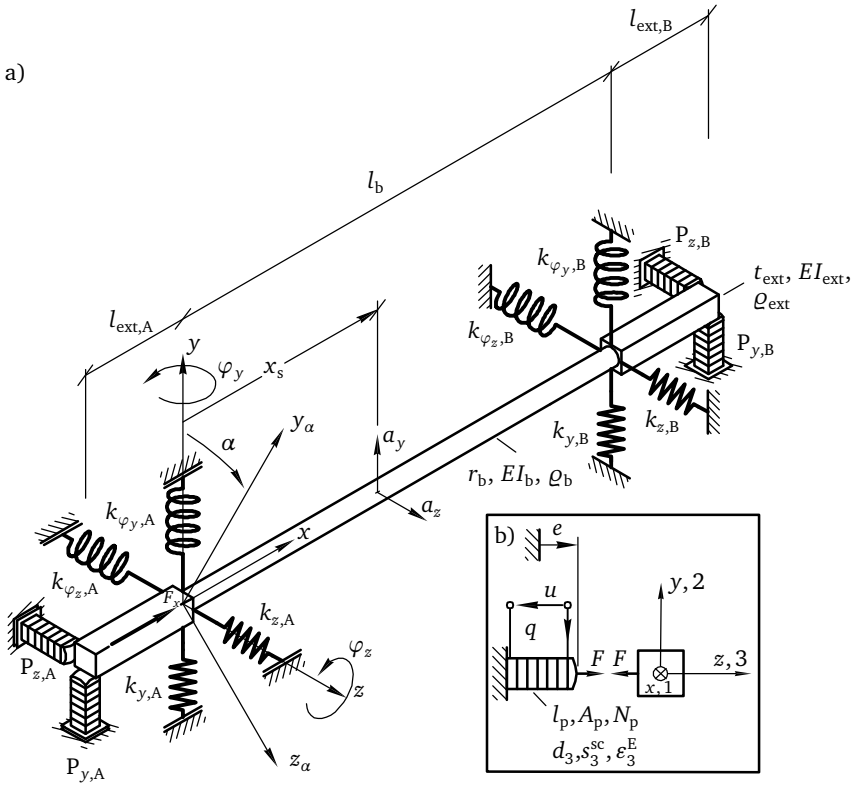

Figure 3.2: a) beam-column system, b) transducer acting on the beam-column

$x = 0\,\mathrm{m}$ may be applied. In figure 3.2a, the ideal hinged supports from figure 3.1 are replaced by discrete helical and torsional spring elements in both piezo-elastic supports A and B at locations $x = 0\,\mathrm{m}$ and $x = l_b$ to account for more realistic support stiffness conditions. The helical and torsional spring elements bear lateral and axial forces at the beam-column's ends in fixed x-, y- and z-direction, and allow rotation φ_y and φ_z in any plane perpendicular to the x-axis. The support stiffness properties are given by the axial support stiffness $k_{x,A}$ and $k_{x,B}$, not shown in the figure 3.2a, lateral support stiffness $k_{y,A}$, $k_{z,A}$, $k_{y,B}$ and $k_{z,B}$ in y- and z-direction and rotational support stiffness $k_{\varphi_y,A}$, $k_{\varphi_z,A}$, $k_{\varphi_y,B}$ and $k_{\varphi_z,B}$ around the y- and z-axes.

In each piezo-elastic support A and B at $x = -l_{ext}$ and $x = l_b + l_{ext}$, two piezoelectric multilayer stack transducers $P_{y,A}$ and $P_{z,A}$ as well as $P_{y,B}$ and $P_{z,B}$ in lateral

y- and z-direction are arranged in the support housing at an angle of 90° to each other orthogonal to the beam-column's x-axis. In general, the transducers are of length l_p with square cross-section A_p and are composed of N_p layers of piezoelectric material. The electromechanical transducer properties are the piezoelectric constant d_3, compliance s_3^sc when the transducer electrodes are short circuited (sc), section 2.2.1, and permittivity ε_3^T under constant mechanical stress, all valid in axial transducer 3-direction of the 1-, 2- and 3-transducer-coordinates, see figure 3.2b. When the transducer is compressed or elongated by $e(t)$ in its axial direction, charges $q(t)$ and voltages $u(t)$ are generated at the transducer electrodes due to the piezoelectric effect. When applied to the electrodes, $q(t)$ and $u(t)$ generate actuating forces $F(t)$ due to the inverse piezoelectric effect. The transducers are connected to the beam-column via a relatively stiff axial extension with length l_ext, bending stiffness EI_ext, density ϱ_ext and square cross-section with edge length t_ext constant across l_ext.

In support A, the transducer $\mathrm{P}_{y,\mathrm{A}}$ excites the beam-column to vibrate in y-direction and $\mathrm{P}_{z,\mathrm{A}}$ excites the beam-column to vibrate in z-direction, as introduced in section 3.1. Accelerations $a_y(t)$ and $a_z(t)$ in y- and z-direction at the sensor position $x = x_\mathrm{s}$ are used to describe the lateral beam-column vibration. The circular cross-section has no preferred direction of lateral deflection, so the beam-column may vibrate in any plane lateral to the longitudinal x-axis. To investigate the beam-column's vibrations in any plane lateral to the longitudinal x-axis, the excitation of the transducers $\mathrm{P}_{y,\mathrm{A}}$ and $\mathrm{P}_{z,\mathrm{A}}$ is superposed in order to apply excitation in y_α-direction at an oblique angle α measured from positive y-direction. The tilted y_α-z_α-coordinate system due to the tilt angle α is used to describe beam-column's vibrations in and orthogonal to the direction of excitation.

The transducers $\mathrm{P}_{y,\mathrm{B}}$ and $\mathrm{P}_{z,\mathrm{B}}$ attenuate lateral beam-column vibrations when connected to RL- or RLC-shunts, as introduced in section 2.2.1 in figure 2.1. To evaluate vibration attenuation, the beam-column vibrations without shunts connected to $\mathrm{P}_{y,\mathrm{B}}$ and $\mathrm{P}_{z,\mathrm{B}}$, and short circuited electrodes are compared to beam-column vibrations with shunts connected.

3.3 Models of beam-column with piezo-elastic supports without shunts

In this section, the mathematical electromechanical models of the beam-column with piezo-elastic supports in figure 3.2 used to describe the beam-column system's lateral dynamic behavior without shunts are derived. The models without shunts need to describe the lateral mechanical dynamic behavior of the elastically supported and axially loaded beam-column as well as the electromechanical dynamic

transducer behavior when coupled to the beam-column with sufficient accuracy in order to perform model-based shunt tuning and vibration simulations without and with shunts in the frequency domain, section 2.2.1.

In total, three models without shunts connected to the transducers in support B are derived for the beam-column with piezo-elastic supports: models with open-loop, short circuited and open circuited transducers in support B.

- The **open-loop model** has appropriate electrical inputs and outputs to allow connection of shunts for vibration attenuation. Furthermore, the open-loop model is used to calibrate and simulate the dynamic transducer transfer behavior that contains information about the actual transducer capacitance and electromechanical coupling. As explained in section 2.2.1, both are needed to optimally tune shunts and are also used to analyze the tuning of shunts in this work in chapters 5 und 6.

- The **short circuited model** only takes into account elastic mechanical transducer behavior with short circuited transducer stiffness and vibrations are not attenuated, section 2.2.1. In chapter 5, beam-column vibrations without attenuation through shunts are compared to beam-column vibrations with shunts in order to quantify the vibration attenuation capability of the shunts.

- The **open circuited model** with open circuited transducers in support B only takes into account elastic mechanical transducer behavior with open circuited transducer stiffness and vibrations are not attenuated, section 2.2.1.

The eigenvalue problems of the short and open circuited models are solved to calculate short circuited and open circuited beam-column resonance frequencies and the GEMCCs (2.2) of transducers in support B, which are analyzed in chapters 5 und 6.

To obtain the three models, open-loop, short circuited and open circuited equations of motion are derived. First, the lateral beam-column's inertia and axial force dependent stiffness properties of the elastically supported beam-column without transducers are derived by finite elements. Secondly, the equation of motion of the FE beam-column is extended with piezoelectric transducer models to simulate vibration excitation with transducers in support A, to allow for the connection of shunts to transducers in support B for vibration attenuation, section 3.4, and to simulate beam-column vibrations when no shunts are connected. Finally, the equations of motion are transferred into state space representations and solved in

the frequency domain in order to simulate the frequency transfer behavior of the beam-column system.

3.3.1 Beam-column modeling with FE

Figure 3.3 shows the FE model of the beam-column with piezo-elastic supports from figure 3.2. The FE model is used to obtain the lateral beam-column's inertia and stiffness properties when damping is neglected, section 3.3.2. This is justified, because of the small damping properties of the experimental beam-column system without shunts, section 5.1.1. To account for small damping properties, damping is approximated by the inertia and stiffness properties in section 3.3.8 and included in the dynamic beam-column system behavior in section 3.3.5.

The beam-column and the axial extensions are divided into $N-1$ one-dimensional EULER-BERNOULLI beam elements with N nodes. At node 1 and N, the discrete

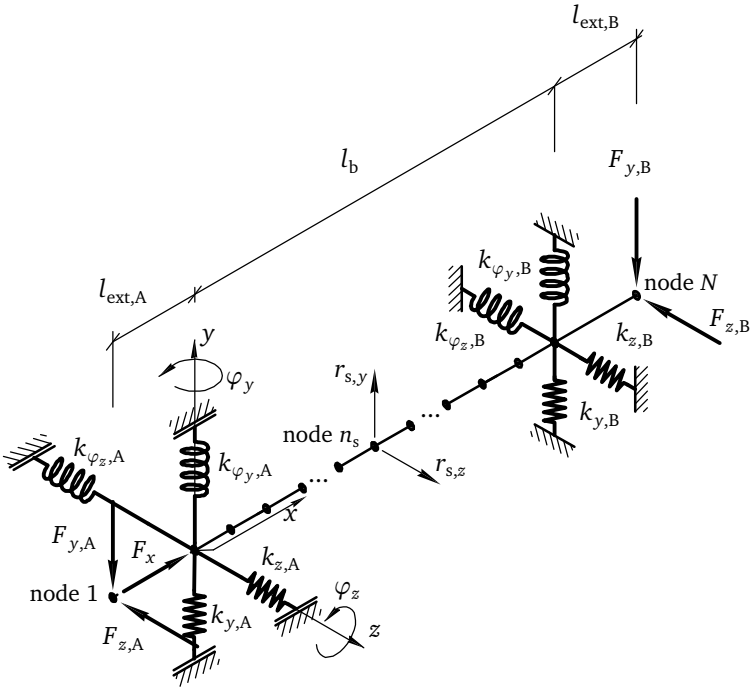

Figure 3.3: FE model of beam-column system

transducer forces $F_{y,\mathrm{A}}(t)$, $F_{z,\mathrm{A}}(t)$, $F_{y,\mathrm{B}}(t)$ and $F_{z,\mathrm{B}}(t)$, figure 3.1, act on the beam-column. At node 2 and $N-1$, the beam-column is elastically supported by the discrete lateral and rotational support stiffness $k_{y,\mathrm{A}}$, $k_{z,\mathrm{A}}$, $k_{y,\mathrm{B}}$, $k_{z,\mathrm{B}}$ and $k_{\varphi_y,\mathrm{A}}$, $k_{\varphi_z,\mathrm{A}}$, $k_{\varphi_y,\mathrm{B}}$, $k_{\varphi_z,\mathrm{B}}$. The static axial forces F_x acts on the beam-column at node 2 and the lateral beam-column accelerations $a_y(t)$ and $a_z(t)$ are later derived via time differentiation of the lateral displacements $r_{\mathrm{s},y}(t)$ and $r_{\mathrm{s},z}(t)$ of node n_s.

In the modeling process, the following assumptions are made:

- the lateral dynamic behavior of the beam-column is linear and independent in y- and z-direction,
- EULER-BERNOULLI beam theory is applied for the beam-column with axial extensions, lateral displacements due to shear deformation are neglected,
- inertia properties of the lateral and rotational beam-column support stiffness are neglected,
- even though axial loads are present axial beam-column displacements are neglected,
- axial loads linearly affect the beam-column's lateral stiffness,
- small-signal piezoelectric transducer properties are assumed that are independent from operating the transducers shunted or as actuators for vibration excitation.

Figure 3.4 shows a finite beam-column element e with node n and $n+1$, cross-section area A^e, bending stiffness EI^e and density ϱ^e. Each node n has four degrees of freedom, two translational displacements v_n and w_n in y- and z-direction and two rotational displacements $\varphi_{y,n}$ and $\varphi_{z,n}$ around the y- and z-axis, and may deflect in the x-y- and x-z-plane. The nodal displacements of each element are summarized in the $[8 \times 1]$ element displacement vector

$$\boldsymbol{r}^e(t) = \left[\, v_n(t),\, w_n(t),\, \varphi_{y,n}(t),\, \varphi_{z,n}(t),\, v_{n+1}(t),\, w_{n+1}(t),\, \varphi_{y,n+1}(t),\, \varphi_{z,n+1}(t) \right]^{\mathrm{T}} \tag{3.1}$$

with nodal rotations

$$\varphi_{y,n}(t) = -w_n'(t) \quad \text{and} \quad \varphi_{z,n}(t) = v_n'(t) \tag{3.2}$$

according to first-order theory that is valid without shear deformation or without slope deflections.

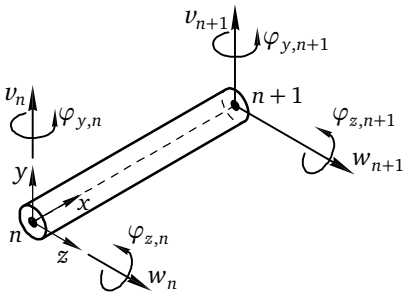

Figure 3.4: Finite EULER-BERNOULLI beam-column element e of length l^e between node n and $n+1$

The lateral displacements along each finite element e are given by

$$\begin{aligned} v^e(t,x) &\approx v_n(t)\,\psi_1(x) + \varphi_{z,n}(t)\,\psi_2(x) + v_{n+1}(t)\,\psi_3(x) + \varphi_{z,n+1}(t)\,\psi_4(x) \\ w^e(t,x) &\approx w_n(t)\,\psi_1(x) - \varphi_{y,n}(t)\,\psi_2(x) + w_{n+1}(t)\,\psi_3(x) - \varphi_{y,n+1}(t)\,\psi_4(x) \end{aligned} \tag{3.3}$$

and are functions of the local coordinate x and time t. They depend on the four cubic deflection beam shape functions, [1],

$$\begin{aligned} \psi_1(x) &= 1 - 3\left(\frac{x}{l}\right)^2 + 2\left(\frac{x}{l}\right)^3, & \psi_2(x) &= x - 2\frac{x^2}{l} + 3\frac{x^3}{l^2} \\ \psi_3(x) &= 3\left(\frac{x}{l}\right)^2 - 2\left(\frac{x}{l}\right)^3 & \text{and} \quad \psi_4(x) &= \frac{x^2}{l}\left(\frac{x}{l} - 1\right) \end{aligned} \tag{3.4}$$

where the superscript e in the element length l^e is omitted for the purpose of clarity ($l = l^e$). Thus, the beam-column element velocities can be expressed as

$$\begin{aligned} \dot{v}^e(t,x) &\approx \dot{v}_n(t)\,\psi_1(x) + \dot{\varphi}_{z,n}(t)\,\psi_2(x) + \dot{v}_{n+1}(t)\,\psi_3(x) + \dot{\varphi}_{z,n+1}(t)\,\psi_4(x) \\ \dot{w}^e(t,x) &\approx \dot{w}_n(t)\,\psi_1(x) - \dot{\varphi}_{y,n}(t)\,\psi_2(x) + \dot{w}_{n+1}(t)\,\psi_3(x) - \dot{\varphi}_{y,n+1}(t)\,\psi_4(x). \end{aligned} \tag{3.5}$$

3.3.2 FE beam-column matrices

In this section, the FE mass matrix and axial force dependent stiffness matrix of the beam-column in figure 3.3 without transducers are derived by the LAGRANGE approach, [1], with EULER-BERNOULLI finite elements from last section. The element mass and stiffness matrices are assembled in the global $[4N \times 4N]$ beam-column mass and stiffness matrices $\boldsymbol{M}$ and $\boldsymbol{K}(F_x)$. The global beam-column damping is

approximated by use of $\boldsymbol{M}$ and $\boldsymbol{K}(F_x)$ in the proportional damping approach in section 3.3.8.

LAGRANGE approach

The FE matrices are derived according to the LAGRANGE approach (3.6) by taking into account the static axial beam-column force F_x. The $j = 1,...,8$ rows of the $[8 \times 8]$ beam-column element matrices are derived from equating of coefficients of the LAGRANGIAN equation

$$\frac{d}{dt}\left(\frac{\partial T^e}{\partial \dot{r}_j^e}\right) - \frac{\partial T^e}{\partial r_j^e} + \frac{\partial U^e}{\partial r_j^e} = \left[\boldsymbol{M}^e \ddot{\boldsymbol{r}}^e + \left(\boldsymbol{K}_{\text{el}}^e - F_x \boldsymbol{K}_{\text{g}}^e\right)\boldsymbol{r}^e\right]_{j^{\text{th}}\text{ row}}, \tag{3.6}$$

where T^e is the kinetic energy, U^e is the potential energy and r_j^e and $\dot{r}_j^e$ are the j^{th} components of the element displacement $\boldsymbol{r}^e$ and the element velocity vector $\dot{\boldsymbol{r}}^e$ at nodes n and $n+1$. The matrices $\boldsymbol{M}^e$, $\boldsymbol{K}_{\text{el}}^e$ and $\boldsymbol{K}_{\text{g}}^e$ are the element mass matrix, the element elastic (el) stiffness matrix and the element geometric (g) stiffness matrix. The element geometric stiffness matrix describes the linear influence of the axial load F_x on the lateral element stiffness properties.

Element mass matrix

The element mass matrix is derived from the total beam-column kinetic energy with neglected effect of rotational and gyroscopic inertia by plugging (3.5) in

$$T^e = \frac{1}{2}\varrho A \int_0^l \left(\dot{v}^e(t,x)\right)^2 + \left(\dot{w}^e(t,x)\right)^2 \, dx. \tag{3.7}$$

In (3.7) and in the following, superscript e is omitted for the element properties l^e, A^e, EI^e and ϱ^e. By substitution of (3.7) in (3.6), the element mass matrix

$$\boldsymbol{M}^e = \frac{\varrho A l}{420}\begin{bmatrix} 156 & 0 & 0 & 22l & 54 & 0 & 0 & -13l \\ & 156 & -22l & 0 & 0 & 54 & 13l & 0 \\ & & 4l^2 & 0 & 0 & -13l & -3l^2 & 0 \\ & & & 4l^2 & 13l & 0 & 0 & -3l^2 \\ & & & & 156 & 0 & 0 & -22l \\ & & & & & 156 & 22l & 0 \\ & & \text{symmetric} & & & & 4l^2 & 0 \\ & & & & & & & 4l^2 \end{bmatrix} \tag{3.8}$$

results from equating of the coefficients of the acceleration part.

Element elastic stiffness and geometric stiffness matrices

The beam-column stiffness property is derived from the total beam-column potential energy in bending

$$\begin{aligned} U^e = &\frac{EI}{2}\int_0^l \left(v^{e\prime\prime}(t,x)\right)^2 + \left(w^{e\prime\prime}(t,x)\right)^2 dx \\ &+\frac{F_x}{2}\int_0^l \left(v^{e\prime}(t,x)\right)^2 + \left(w^{e\prime}(t,x)\right)^2 dx \end{aligned} \tag{3.9}$$

including the effect of the static axial force F_x, [80]. By substitution of (3.9) in (3.6) and equating coefficients, the element elastic stiffness matrix results in

$$\boldsymbol{K}^e_{\mathrm{el}} = \frac{EI}{l^3}\begin{bmatrix} 12 & 0 & 0 & 6l & -12 & 0 & 0 & 6l \\ & 12 & -6l & 0 & 0 & -12 & -6l & 0 \\ & & 4l^2 & 0 & 0 & 6l & 2l^2 & 0 \\ & & & 4l^2 & -6l & 0 & 0 & 2l^2 \\ & & & & 12 & 0 & 0 & -6l \\ & & & & & 12 & 6l & 0 \\ & & \text{symmetric} & & & & 4l^2 & 0 \\ & & & & & & & 4l^2 \end{bmatrix} \tag{3.10}$$

and the element geometric stiffness matrix results in

$$\boldsymbol{K}^e_{\mathrm{g}} = \frac{1}{10l}\begin{bmatrix} 12 & 0 & 0 & l & -12 & 0 & 0 & l \\ & 12 & -l & 0 & 0 & -12 & -l & 0 \\ & & 4/3\,l^2 & 0 & 0 & l & -l^2/3 & 0 \\ & & & 4/3\,l^2 & -l & 0 & 0 & -l^2/3 \\ & & & & 12 & 0 & 0 & -l \\ & & & & & 12 & l & 0 \\ & & \text{symmetric} & & & & 4/3\,l^2 & 0 \\ & & & & & & & 4/3\,l^2 \end{bmatrix}. \tag{3.11}$$

Elastic beam-column support

The lateral and rotational support stiffness at nodes 2 and $N-1$ in figure 3.3 are modeled as

$$\begin{aligned} k_{y,\mathrm{A/B}}(F_x) &= k_{y,\mathrm{A/B,el}} + F_x k_{y,\mathrm{A/B,g}}, \\ k_{z,\mathrm{A/B}}(F_x) &= k_{z,\mathrm{A/B,el}} + F_x k_{z,\mathrm{A/B,g}}, \\ k_{\varphi_y,\mathrm{A/B}}(F_x) &= k_{\varphi_y,\mathrm{A/B,el}} + F_x k_{\varphi_y,\mathrm{A/B,g}}, \\ k_{\varphi_z,\mathrm{A/B}}(F_x) &= k_{\varphi_z,\mathrm{A/B,el}} + F_x k_{\varphi_z,\mathrm{A/B,g}}, \end{aligned} \tag{3.12}$$

with elastic (el) and geometric (g) portions to account for an assumed linear stiffening and softening behavior of the elastic beam-column support that was observed experimentally for an increasing tensile and compressive axial force F_x, section 6.2. These additional stiffness terms are added to the diagonal elements of the lateral and rotational degrees of freedom in the element elastic stiffness matrix $\boldsymbol{K}_{\mathrm{el}}^{e}$ (3.10) and element geometric stiffness matrix $\boldsymbol{K}_{g}^{e}$ (3.11) at nodes $n = 2$ and $n = N-1$.

Assembly of FE beam-column mass and stiffness matrices

The inertia and stiffness properties of the elastically supported beam-column in figure 3.3 without transducers are represented by the global mass, elastic stiffness and geometrical stiffness matrices $\boldsymbol{M}$, $\boldsymbol{K}_{\mathrm{el}}$ and $\boldsymbol{K}_{g}$, all of the dimension $[4N \times 4N]$. The global system matrices for $N = 43$ nodes are assembled according to figure 3.5 from the local element beam-column matrices (3.8), (3.10) and (3.11) for the degrees of freedom in the $[4N \times 1]$ global displacement vector

$$\boldsymbol{r}(t) = \left[v_1(t), w_1(t), \varphi_{y,1}(t), \varphi_{z,1}(t), \ldots, v_N(t), w_N(t), \varphi_{y,N}(t), \varphi_{z,N}(t) \right]^{\mathrm{T}}. \tag{3.13}$$

The global stiffness matrix

$$\boldsymbol{K}(F_x) = \boldsymbol{K}_{\mathrm{el}} - F_x \boldsymbol{K}_{\mathrm{g}} \tag{3.14}$$

is formed by the global elastic and the global geometric stiffness matrix and takes into account the linear effect of the static axial force F_x on the lateral beam-column stiffness. This effect on the beam-column system's dynamic behavior without and with shunts is investigated in chapter 6 as part of the uncertainty analysis. For all investigations in this work, F_x is small compared to beam-column's buckling load, [91], and yield strength, which is why these effects are not discussed.

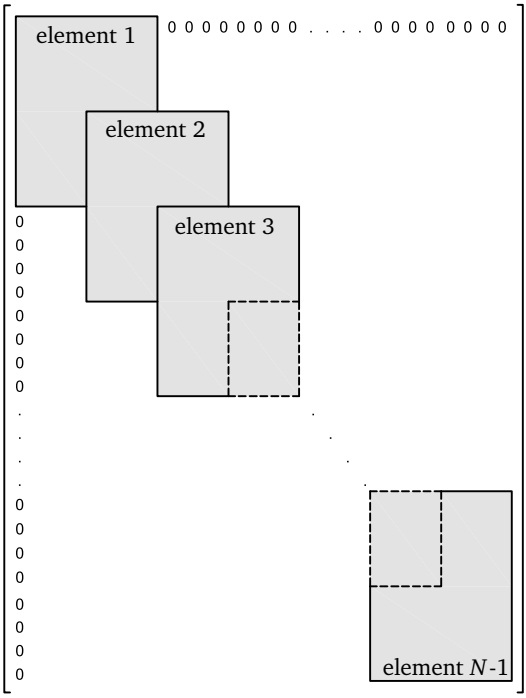

Figure 3.5: Assembly of the $[4N \times 4N]$ global mass and stiffness matrices

3.3.3 Piezoelectric transducer models

The forces $F_{y,\mathrm{A}}$, $F_{z,\mathrm{A}}$, $F_{y,\mathrm{B}}$ and $F_{z,\mathrm{B}}$ of the multilayer stack transducers $\mathrm{P}_{y,\mathrm{A}}$, $\mathrm{P}_{z,\mathrm{A}}$, $\mathrm{P}_{y,\mathrm{B}}$ and $\mathrm{P}_{z,\mathrm{B}}$ in the FE beam-column model in figure 3.3 are represented by different transducer models in support A and B to model vibration excitation, vibration attenuation with shunts and elastic transducer behavior with short circuited and open circuited transducer electrodes, section 2.2.1. For transducers in support A, an actuating transducer model with voltage driven electrodes is used to simulate vibration excitation due to the inverse piezoelectric effect. For transducers in support B, an actuating transducer model with charge and current driven electrodes together with a sensing transducer model due to the direct and the inverse piezoelectric effect are derived to later connect shunts. The actuating and sensing models in support B are used to derive the elastic transducer models with short circuited (sc) and open circuited (oc) electrodes.

Figure 3.6 shows the electromechanical model of a single piezolectric layer as well as the electromechanical model of the transducer $\mathrm{P}_{z,\mathrm{B}}$ from figure 3.3b, which are used to generally derive the actuating, the sensing and the elastic short circuited and open circuited transducer models in axial transducers 3-direction. Based on these models, the models for the transducers $\mathrm{P}_{y,\mathrm{A}}$, $\mathrm{P}_{z,\mathrm{A}}$, $\mathrm{P}_{y,\mathrm{B}}$ and $\mathrm{P}_{z,\mathrm{B}}$ in the beam-column x-, y- and z-coordinates are derived.

General derivation of transducer models

As introduced in section 3.2, the transducer $\mathrm{P}_{z,\mathrm{B}}$ of length l_p and square cross-section area A_p is formed by N_p layers of piezoelectric material. One of these layers with electrodes on the left and right side is shown in figure 3.6a. The direct and the

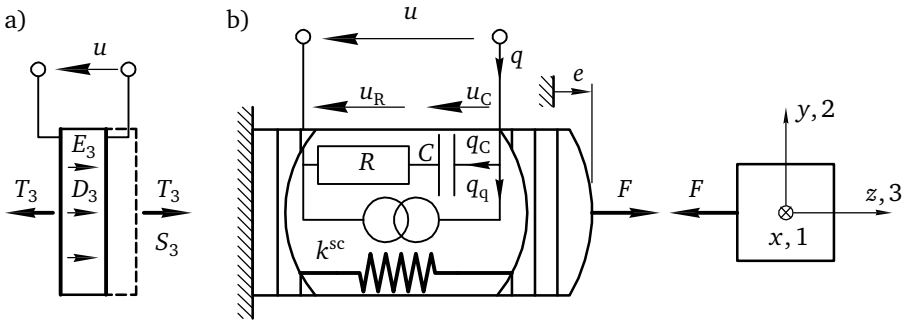

Figure 3.6: a) electroded piezoelectric layer, b) electromechanical model of transducer $\mathrm{P}_{z,\mathrm{B}}$ that acts on the FE beam-column via the axial extension

inverse piezoelectric effect of this single piezoelectric layer in axial transducer direction are described by the coupled one-dimensional linear piezoelectric material constitutive equations, [77],

$$\begin{bmatrix} D_3(t) \\ S_3(t) \end{bmatrix} = \begin{bmatrix} \varepsilon_3^{\mathrm{T}} & d_3 \\ d_3 & s_3^{\mathrm{sc}} \end{bmatrix} \begin{bmatrix} E_3(t) \\ T_3(t) \end{bmatrix} \tag{3.15}$$

with the permittivity $\varepsilon_3^{\mathrm{T}}$ under constant mechanical stress, mechanical material compliance s_3^{sc} and piezoelectric material constant d_3, representing small signal levels electromechanical material properties with both orientation of the electric field and mechanical deformation in axial transducer direction 3. In (3.15), $D_3(t)$ is the electric displacement, $E_3(t)$ is the electric field, $T_3(t)$ is the mechanical stress and $S_3(t)$ is the mechanical strain.

To connect shunts, it is common to derive the layer piezoelectric constitutive equation with $E_3(t)$ and $S_3(t)$ to be the independent variables instead of $E_3(t)$ and $T_3(t)$ as in (3.15), [77]. Then, (3.15) becomes

$$\begin{bmatrix} D_3(t) \\ T_3(t) \end{bmatrix} = \begin{bmatrix} \varepsilon_3^{\mathrm{S}} & d_3/s_3^{\mathrm{sc}} \\ -d_3/s^{\mathrm{sc}} & 1/s_3^{\mathrm{sc}} \end{bmatrix} \begin{bmatrix} E_3(t) \\ S_3(t) \end{bmatrix} \tag{3.16}$$

where $\varepsilon_3^{\mathrm{S}}$ is the permittivity under zero mechanical strain, i.e. the layer deformation in 3-direction is blocked.

With (3.16), the linear actuating and sensing model of transducer $\mathrm{P}_{z,\mathrm{B}}$ in figure 3.6b due to the direct and inverse piezoelectric effect with uniformly distributed electriomechanical quantities is derived with the charge $q(t)$ and the voltage $u(t)$ at the transducer electrodes as well as the axial elongation $e(t)$ and transducer force $F(t)$ in axial transducer 3-direction. Therefore, the electromechanical quantities in (3.16) are replaced by

$$\begin{aligned} D_3(t) &= \frac{q(t)}{N_{\mathrm{p}} A_{\mathrm{p}}}, \qquad S_3(t) = \frac{e(t)}{l_{\mathrm{p}}}, \qquad T_3(t) = \frac{F(t)}{A_{\mathrm{p}}}, \\ E_3(t) &= \frac{N_{\mathrm{p}}\, u(t)}{l_{\mathrm{p}}}, \qquad \varepsilon_3^{\mathrm{S}} = \frac{C\, l_{\mathrm{p}}}{N_{\mathrm{p}}^2 A_{\mathrm{p}}}, \qquad s_3^{\mathrm{sc}} = \frac{A_{\mathrm{p}}}{k^{\mathrm{sc}}\, l_{\mathrm{p}}} \end{aligned} \tag{3.17}$$

as derived in [77]. In (3.17), C is the electrical transducer capacitance under zero mechanical strain and k^{sc} is the transducer stiffness valid for short circuited electrodes. By substitution of (3.17) in (3.16), the coupled **actuating and sensing equations with voltage driven electrodes** of transducer $\mathrm{P}_{z,\mathrm{B}}$ become

$$q(t) = \Theta\, e(t) + C\, u(t) \tag{3.18}$$

$$F(t) = k^{\mathrm{sc}}\, e(t) - \Theta\, u(t) \tag{3.19}$$

with the transducer force constant $\Theta = N_{\mathrm{p}}\, d_3\, k^{\mathrm{sc}}$.

So far, the transducer incorporates the electrical behavior of an ideal capacitance. However, piezoelectric materials in general show dielectric losses. These additional losses need to be taken into account for the transducers in support B to not overestimate the shunt damping resistance value R^{D} in the shunt tuning process in section 3.5. One approach for linear systems to model dielectric losses is by taking into account an ohmic resistance R, [45]. As shown in figure 3.6b, the resistance R is connected in series to the transducer capacitance C. By applying the

law of charge conservation at the transducer electrodes, the charge $q_\mathrm{C}(t)$ at the capacitance becomes

$$q_\mathrm{C}(t) = q(t) - q_\mathrm{q}(t) = q(t) - \Theta\, e(t) \tag{3.20}$$

with the charge $q(t)$ at the transducer electrodes and the charge $q_\mathrm{q}(t)$ due to the piezoelectric effect. Consequently, the voltage at the transducer electrodes is calculated by

$$u(t) = u_\mathrm{C}(t) + u_\mathrm{R}(t) = q_\mathrm{C}(t)/C + R\,\dot{q}_\mathrm{C}(t) \tag{3.21}$$

with the voltage $u_\mathrm{C}(t)$ across the capacitance and the voltage $u_\mathrm{R}(t)$ across the resistance. Replacing $q_\mathrm{C}(t)$ and $\dot{q}_\mathrm{C}(t)$ in (3.21) with (3.20) and its time derivative, the **sensing model with charge $q(t)$ and current $\dot{q}(t)$ driven electrodes** becomes

$$u(t) = -\frac{\Theta}{C} e(t) - R\Theta\,\dot{e}(t) + \frac{1}{C} q(t) + R\Theta\,\dot{q}(t) \tag{3.22}$$

with the dielectric loss terms $R\Theta\,\dot{e}(t)$ and $R\Theta\,\dot{q}(t)$.

By plugging (3.22) in (3.19), the **actuating model with charge $q(t)$ and current $\dot{q}(t)$ driven electrodes** becomes

$$F(t) = \underbrace{\left(k^\mathrm{sc} + \frac{\Theta^2}{C}\right)}_{k^\mathrm{oc}} e(t) + R\Theta^2\,\dot{e}(t) - \frac{\Theta}{C} q(t) - R\Theta\,\dot{q}(t). \tag{3.23}$$

As introduced in section 2.2.1, the short circuited and the open circuited electrode state can be distinguished for transducers when no shunt is connected, which lead to two different transducer stiffness properties:

- **Short circuited**: When operating the transducer with short circuited (sc) electrodes, i.e. $u(t) = 0$, (3.19) simplifies to

  $$F(t) = k^\mathrm{sc}\, e(t) \tag{3.24}$$

  and the transducer force corresponds to an elastic force with short circuit stiffness k^sc.

- **Open circuited**: When operating the transducer with open circuited (oc) electrodes, i.e. $q(t) = 0$, (3.23) simplifies to

$$F(t) = \left(k^{\mathrm{sc}} + \frac{\Theta^2}{C} \right) e(t) = k^{\mathrm{oc}}\, e(t) \tag{3.25}$$

  and the transducer force corresponds to an elastic force with increased open circuit stiffness k^{oc}. When operating the transducers oc without attenuation by shunts, the damping due to dielectric losses can be neglected, [83]. Hence, (3.25) represents only an elastic force.

For the beam-column system in figure 3.2, vibration excitation with transducers in support A is modeled with the actuating transducer model and voltage driven electrodes, (3.19). In support B, transducers are represented by the actuating and sensing transducer models with charge and current driven electrodes, (3.22) and (3.23). Furthermore, the short and open circuited transducer models (3.24) and (3.25) are used to model the elastic behavior of transducers in support B with open and short circuited transducer electrodes when no shunt is connected.

Actuating transducer model in support A

In support A in figure 3.3, lateral transducer forces are

$$\boldsymbol{F}_{\mathrm{A}}(t) = \begin{bmatrix} F_{y,\mathrm{A}}(t) \\ F_{z,\mathrm{A}}(t) \end{bmatrix} = \boldsymbol{k}_{\mathrm{A}}^{\mathrm{sc}}\, \boldsymbol{e}_{\mathrm{A}}(t) - \boldsymbol{\Theta}_{\mathrm{A}}\, \boldsymbol{u}_{\mathrm{A}}(t) \tag{3.26}$$

according to the actuating model (3.19) with

$$\boldsymbol{k}_{\mathrm{A}}^{\mathrm{sc}} = \mathrm{diag}(k_{y,\mathrm{A}}^{\mathrm{sc}},\, k_{z,\mathrm{A}}^{\mathrm{sc}}) \quad \text{and} \quad \boldsymbol{\Theta}_{\mathrm{A}} = \mathrm{diag}(\Theta_{y,\mathrm{A}},\, \Theta_{z,\mathrm{A}}) \tag{3.27}$$

for the transducers $\mathrm{P}_{y,\mathrm{A}}$ and $\mathrm{P}_{z,\mathrm{A}}$. The forces are proportional to their axial elongation $\boldsymbol{e}_{\mathrm{A}}(t) = [e_{y,\mathrm{A}}(t),\, e_{z,\mathrm{A}}(t)]^{\mathrm{T}}$ in transducer y- and z-direction and to the voltages $\boldsymbol{u}_{\mathrm{A}}(t) = [u_{y,\mathrm{A}}(t),\, u_{z,\mathrm{A}}(t)]^{\mathrm{T}}$ applied to the transducers $\mathrm{P}_{y,\mathrm{A}}$ and $\mathrm{P}_{z,\mathrm{A}}$.

Actuating, sensing, short and open circuited transducer models in support B

In support B in figure 3.3, lateral transducer forces are

$$\boldsymbol{F}_{\mathrm{B}}(t) = \begin{bmatrix} F_{y,\mathrm{B}}(t) \\ F_{z,\mathrm{B}}(t) \end{bmatrix} = \boldsymbol{k}_{\mathrm{B}}^{\mathrm{oc}}\, \boldsymbol{e}_{\mathrm{B}}(t) + \boldsymbol{R}_{\mathrm{B}}\, \boldsymbol{\Theta}_{\mathrm{B}}^2\, \dot{\boldsymbol{e}}_{\mathrm{B}}(t) - \boldsymbol{\Theta}_{\mathrm{B}}\, \boldsymbol{C}_{\mathrm{B}}^{-1}\, \boldsymbol{q}_{\mathrm{B}}(t) - \boldsymbol{R}_{\mathrm{B}}\, \boldsymbol{\Theta}_{\mathrm{B}}\, \dot{\boldsymbol{q}}_{\mathrm{B}}(t) \tag{3.28}$$

according to the actuating model (3.23) with

$$\begin{aligned} \boldsymbol{k}_{\mathrm{B}}^{\mathrm{oc}} &= \mathrm{diag}(k_{y,\mathrm{B}}^{\mathrm{oc}}, k_{z,\mathrm{B}}^{\mathrm{oc}}), & \boldsymbol{R}_{\mathrm{B}} &= \mathrm{diag}(R_{y,\mathrm{B}}, R_{z,\mathrm{B}}), \\ \boldsymbol{\Theta}_{\mathrm{B}} &= \mathrm{diag}(\Theta_{y,\mathrm{B}}, \Theta_{z,\mathrm{B}}) \quad \text{and} & \boldsymbol{C}_{\mathrm{B}} &= \mathrm{diag}(C_{y,\mathrm{B}}, C_{z,\mathrm{B}}) \end{aligned} \tag{3.29}$$

for the transducers $\mathrm{P}_{y,\mathrm{B}}$ and $\mathrm{P}_{z,\mathrm{B}}$. The forces are proportional to their axial elongations $\boldsymbol{e}_{\mathrm{B}}(t) = [e_{y,\mathrm{B}}(t), e_{z,\mathrm{B}}(t)]^{\mathrm{T}}$ and velocities $\dot{\boldsymbol{e}}_{\mathrm{B}}(t) = [\dot{e}_{y,\mathrm{B}}(t), \dot{e}_{z,\mathrm{B}}(t)]^{\mathrm{T}}$ in y- and z-direction as wells as to the charges $\boldsymbol{q}_{\mathrm{B}}(t) = [q_{y,\mathrm{B}}(t), q_{z,\mathrm{B}}(t)]^{\mathrm{T}}$ and currents $\dot{\boldsymbol{q}}_{\mathrm{B}}(t) = [\dot{q}_{y,\mathrm{B}}(t), \dot{q}_{z,\mathrm{B}}(t)]^{\mathrm{T}}$ flowing into the transducers $\mathrm{P}_{y,\mathrm{B}}$ and $\mathrm{P}_{z,\mathrm{B}}$. Furthermore, according to the sensing model (3.22) the voltages

$$\boldsymbol{u}_{\mathrm{B}}(t) = \begin{bmatrix} u_{\mathrm{B},y}(t) \\ u_{\mathrm{B},z}(t) \end{bmatrix} = -\boldsymbol{\Theta}_{\mathrm{B}}\, \boldsymbol{C}_{\mathrm{B}}^{-1}\, \boldsymbol{e}_{\mathrm{B}}(t) - \boldsymbol{R}_{\mathrm{B}}\, \boldsymbol{\Theta}_{\mathrm{B}}\, \dot{\boldsymbol{e}}_{\mathrm{B}}(t) + \boldsymbol{C}_{\mathrm{B}}^{-1}\, \boldsymbol{q}_{\mathrm{B}}(t) + \boldsymbol{R}_{\mathrm{B}}\, \boldsymbol{\Theta}_{\mathrm{B}}\, \dot{\boldsymbol{q}}_{\mathrm{B}}(t) \tag{3.30}$$

are generated at the transducer electrodes.

In case the electrodes are short circuited, the lateral transducer forces according to (3.24) become

$$\boldsymbol{F}_{\mathrm{B}}^{\mathrm{sc}}(t) = \boldsymbol{k}_{\mathrm{B}}^{\mathrm{sc}}\, \boldsymbol{e}_{\mathrm{B}}(t). \tag{3.31}$$

In case the electrodes are open circuited, the lateral transducer forces according to (3.25) become

$$\boldsymbol{F}_{\mathrm{B}}^{\mathrm{oc}}(t) = \boldsymbol{k}_{\mathrm{B}}^{\mathrm{oc}}\, \boldsymbol{e}_{\mathrm{B}}(t). \tag{3.32}$$

3.3.4 Model vibration excitation and measurement signals

The vibration excitation and measurement signals are used to excite and to characterize the vibration of the FE beam-column in figure 3.3. Excitation and measurement signals are first given in x-, y- and z-coordinates and then transformed into tilted x-, y_α- and z_α-coordinates in order to describe vibration in and orthogonal to the direction of excitation as proposed section 3.2.

Excitation and measurement signals in x-, y- and z-coordinates

The forces $\boldsymbol{F}_{\mathrm{A}}(t)$ (3.26) of the transducers $\mathrm{P}_{y,\mathrm{A}}$ and $\mathrm{P}_{z,\mathrm{A}}$ in support A laterally excite the beam-column in y- and z-direction proportional to the applied voltage

excitation signals $\boldsymbol{u}_\mathrm{A}(t) = [u_{y,\mathrm{A}}(t), u_{z,\mathrm{A}}(t)]^\mathrm{T}$. To characterize the beam-column vibrations, the lateral beam-column displacements

$$\boldsymbol{y}(t) = \begin{bmatrix} r_{y,\mathrm{s}}(t) \\ r_{z,\mathrm{s}}(t) \end{bmatrix} \tag{3.33}$$

of the node n_s at the sensor position x_s in y- and z-direction according to figure 3.3 are used. They are extracted from the FE displacement vector $\boldsymbol{r}(t)$ (3.13) by the output equation

$$\boldsymbol{y}(t) = \begin{bmatrix} 0 & 0 & 0 & 0 & \dots & 1 & 0 & 0 & 0 & \dots & 0 \\ 0 & 0 & 0 & 0 & \dots & \underbrace{0}_{\mathrm{lat}\,n_\mathrm{s}} & \underbrace{1}_{} & \underbrace{0}_{\mathrm{rot}\,n_\mathrm{s}} & \underbrace{0}_{} & \dots & 0 \end{bmatrix}^\mathrm{T} \boldsymbol{r}(t) = \boldsymbol{b}_\mathrm{s} \boldsymbol{r}(t) \tag{3.34}$$

with the $[2 \times 4N]$ extraction matrix $\boldsymbol{b}_\mathrm{s}$. For comparison with experimental results in chapters 5 and 6, the beam-column accelerations $a_y(t)$ and $a_z(t)$ in figure 3.2 are obtained by time differentiation of (3.34),

$$\ddot{\boldsymbol{y}}(t) = \begin{bmatrix} \ddot{r}_{y,\mathrm{s}}(t) \\ \ddot{r}_{z,\mathrm{s}}(t) \end{bmatrix} = \begin{bmatrix} a_y(t) \\ a_z(t) \end{bmatrix}. \tag{3.35}$$

Excitation and measurement signals in x-, y_α- and z_α-coordinates

In order to apply beam-column excitation in y_α-direction at an oblique angle α as introduced in section 3.2 and shown in figure 3.4, the excitation voltage signal $u_\alpha(t)$ is split between the transducer voltages $\boldsymbol{u}_\mathrm{A}(t)$ of the transducers $\mathrm{P}_{y,\mathrm{A}}$ and $\mathrm{P}_{z,\mathrm{A}}$ according to

$$\begin{bmatrix} u_{y,\mathrm{A}}(t) \\ u_{z,\mathrm{A}}(t) \end{bmatrix} = \begin{bmatrix} \cos(\alpha) \\ \sin(\alpha) \end{bmatrix} u_\alpha(t) = \boldsymbol{t}_\mathrm{u}\, u_\alpha(t) \tag{3.36}$$

by using the PYTHAGOREAN theorem in the voltage transformation matrix $\boldsymbol{t}_\mathrm{u}$.

The beam-column displacements $\boldsymbol{y}_\alpha(t) = [r_{y_\alpha,\mathrm{s}}(t), r_{z_\alpha,\mathrm{s}}(t)]^\mathrm{T}$ in tilted x-, y_α- and z_α-coordinates at node n_s are obtained from the transformation of the output equation (3.33) according to

$$\boldsymbol{y}_\alpha(t) = \begin{bmatrix} \cos(\alpha) & \sin(\alpha) \\ -\sin(\alpha) & \cos(\alpha) \end{bmatrix} \begin{bmatrix} r_{y,\mathrm{s}}(t) \\ r_{z,\mathrm{s}}(t) \end{bmatrix} = \boldsymbol{t}_\mathrm{r}\, \boldsymbol{y}(t) \tag{3.37}$$

with the displacement transformation matrix $\boldsymbol{t}_{\mathrm{r}}$. This does also apply for accelerations

$$\ddot{\boldsymbol{y}}_{\alpha}(t) = \begin{bmatrix} a_{\alpha}(t) \\ a_{\alpha^{\perp}}(t) \end{bmatrix} = \boldsymbol{t}_{\mathrm{r}}\, \ddot{\boldsymbol{y}}(t). \tag{3.38}$$

In (3.38), $a_{\alpha}(t)$ represents the beam-column acceleration in the direction of excitation y_{α}, and $a_{\alpha^{\perp}}(t)$ represents the beam-column acceleration orthogonal to the direction of excitation in z_{α}-direction.

3.3.5 Equations of motion of beam-column system

To simulate the beam-column system's dynamic behavior without shunts connected, the open-loop, the short circuited and the open circuited equations of motion are derived and used as introduced at the beginning of section 3.3.

With the global mass and stiffness matrices $\boldsymbol{M}$ and $\boldsymbol{K}(F_x)$ obtained from the element mass matrix (3.8) and stiffness matrix (3.10) in section 3.3.2 and a global damping matrix $\boldsymbol{D}^{*}$ that is further specified in this section, the general FE equation of motion of the beam-column with transducer forces in figure 3.3 is

$$\boldsymbol{M}\,\ddot{\boldsymbol{r}}(t) + \boldsymbol{D}^{*}\,\dot{\boldsymbol{r}}(t) + \boldsymbol{K}(F_x)\,\boldsymbol{r}(t) = -\boldsymbol{b}_{\mathrm{A}}\boldsymbol{F}_{\mathrm{A}}(t) - \boldsymbol{b}_{\mathrm{B}}\boldsymbol{F}_{\mathrm{B}}(t). \tag{3.39}$$

Open-loop, short circuited and open circuited equations of motion are derived by using the actuating, sensing, short circuited and open circuited transducer models from section 3.3.3 for transducer forces in (3.39).

- The **open-loop equations of motion** result from (3.39) by using the actuating model with voltage driven electrodes (3.26) for $\boldsymbol{F}_{\mathrm{A}}(t)$, the actuating model with charge and current driven electrodes (3.28) for $\boldsymbol{F}_{\mathrm{B}}(t)$, and by taking into account the sensing model (3.30).

- The **short circuited equation of motion** results from (3.39) by using the actuating model (3.26) for $\boldsymbol{F}_{\mathrm{A}}(t)$ and the transducer model with short circuited electrodes (3.31) for $\boldsymbol{F}_{\mathrm{B}}(t)$.

- The **open circuited equation of motion** results from (3.39) by using the actuating model (3.26) for $\boldsymbol{F}_{\mathrm{A}}(t)$ and the transducer model with open circuited electrodes (3.32) for $\boldsymbol{F}_{\mathrm{B}}(t)$.

The positioning matrices

$$\boldsymbol{b}_{\mathrm{A}} = \underbrace{\begin{bmatrix} 1 & 0 & \overbrace{0 & 0}^{\text{lat}} & \overbrace{0 & 0}^{\text{rot}} & 0 \dots 0 \\ 0 & 1 & 0 & 0 & 0 \dots 0 \end{bmatrix}^{\mathrm{T}}}_{[4N\times 2]} \quad \text{and} \quad \boldsymbol{b}_{\mathrm{B}} = \underbrace{\begin{bmatrix} 0 \dots 0 & \overbrace{1 & 0}^{\text{lat}} & \overbrace{0 & 0}^{\text{rot}} \\ 0 \dots 0 & 0 & 1 & 0 & 0 \end{bmatrix}^{\mathrm{T}}}_{[4N\times 2]} \tag{3.40}$$

in (3.39) allocate the transducer forces $\boldsymbol{F}_{\mathrm{A}}(t)$ and $\boldsymbol{F}_{\mathrm{B}}(t)$ to the lateral degrees of freedom in y- and z-direction of node $n = 1$ and $n = N$, figure 3.3. The positioning matrices (3.40) are negative in (3.39) due to the fact that the forces acting on the beam-column are opposed to those acting on the transducers. For all equations of motions, the axial transducer elongations $\boldsymbol{e}_{\mathrm{A/B}}(t)$ and velocities $\dot{\boldsymbol{e}}_{\mathrm{B}}(t)$ are related to the lateral beam-column displacements $\boldsymbol{r}(t)$ (3.13) and velocities $\dot{\boldsymbol{r}}(t)$ by

$$\boldsymbol{e}_{\mathrm{A}}(t) = \boldsymbol{b}_{\mathrm{A}}^{\mathrm{T}}\,\boldsymbol{r}(t), \quad \boldsymbol{e}_{\mathrm{B}}(t) = \boldsymbol{b}_{\mathrm{B}}^{\mathrm{T}}\,\boldsymbol{r}(t) \quad \text{and} \quad \dot{\boldsymbol{e}}_{\mathrm{B}}(t) = \boldsymbol{b}_{\mathrm{B}}^{\mathrm{T}}\,\dot{\boldsymbol{r}}(t). \tag{3.41}$$

Open-loop equations of motion

To mathematically connect the beam-column to the transducers in support A, figure 3.3, for vibration excitation due to applied voltage signals $\boldsymbol{u}_{\mathrm{A}}(t)$, the actuating equation (3.26) is left-multiplied by $\boldsymbol{b}_{\mathrm{A}}$, and $\boldsymbol{e}_{\mathrm{A}}(t)$ in (3.26) is substituted by (3.41) leading to

$$\boldsymbol{b}_{\mathrm{A}}\,\boldsymbol{F}_{\mathrm{A}}(t) = \underbrace{\boldsymbol{b}_{\mathrm{A}}\,\boldsymbol{k}_{\mathrm{A}}^{\mathrm{sc}}\,\boldsymbol{b}_{\mathrm{A}}^{\mathrm{T}}}_{\boldsymbol{K}_{\mathrm{A}}^{\mathrm{sc}}}\,\boldsymbol{r}(t) - \boldsymbol{b}_{\mathrm{A}}\,\boldsymbol{\Theta}_{\mathrm{A}}\,\boldsymbol{u}_{\mathrm{A}}(t). \tag{3.42}$$

To mathematically connect the beam-column to the transducers in support B, figure 3.3, for vibration attenuation, the actuating equation (3.28) is left-multiplied by $\boldsymbol{b}_{\mathrm{B}}$, and $\boldsymbol{e}_{\mathrm{B}}(t)$ and $\dot{\boldsymbol{e}}_{\mathrm{B}}$ in (3.28) are substituted by (3.41) leading to

$$\begin{aligned} \boldsymbol{b}_{\mathrm{B}}\,\boldsymbol{F}_{\mathrm{B}}(t) = {} & \overbrace{\boldsymbol{b}_{\mathrm{B}}\boldsymbol{k}_{\mathrm{B}}^{\mathrm{oc}}\,\boldsymbol{b}_{\mathrm{B}}^{\mathrm{T}}}^{\boldsymbol{K}_{\mathrm{B}}^{\mathrm{oc}}}\,\boldsymbol{r}(t) + \overbrace{\boldsymbol{b}_{\mathrm{B}}\boldsymbol{R}_{\mathrm{B}}\,\boldsymbol{\Theta}_{\mathrm{B}}^{2}\,\boldsymbol{b}_{\mathrm{B}}^{\mathrm{T}}}^{\boldsymbol{D}_{\mathrm{B}}}\,\dot{\boldsymbol{r}}(t) \\ & - \boldsymbol{b}_{\mathrm{B}}\boldsymbol{\Theta}_{\mathrm{B}}\,\boldsymbol{C}_{\mathrm{B}}^{-1}\,\boldsymbol{q}_{\mathrm{B}}(t) - \boldsymbol{b}_{\mathrm{B}}\boldsymbol{R}_{\mathrm{B}}\,\boldsymbol{\Theta}_{\mathrm{B}}\,\dot{\boldsymbol{q}}_{\mathrm{B}}(t). \end{aligned} \tag{3.43}$$

By plugging (3.42) and (3.43) in (3.39), the **open-loop beam-column equation** of motion with actuating transducer models in support A and B becomes

$$\begin{aligned} \boldsymbol{M}\,\ddot{\boldsymbol{r}}(t) + \overbrace{\left[\boldsymbol{D}^{\mathrm{sc}} + \boldsymbol{D}_{\mathrm{B}}\right]}^{\boldsymbol{D}}\,\dot{\boldsymbol{r}}(t) + \overbrace{\left[\boldsymbol{K}(F_x) + \boldsymbol{K}_{\mathrm{A}}^{\mathrm{sc}} + \boldsymbol{K}_{\mathrm{B}}^{\mathrm{oc}}\right]}^{\boldsymbol{K}^{\mathrm{oc}}}\,\boldsymbol{r}(t) = \\ \boldsymbol{b}_{\mathrm{A}}\,\boldsymbol{\Theta}_{\mathrm{A}}\,\boldsymbol{u}_{\mathrm{A}}(t) + \boldsymbol{b}_{\mathrm{B}}\boldsymbol{\Theta}_{\mathrm{B}}\,\boldsymbol{C}_{\mathrm{B}}^{-1}\,\boldsymbol{q}_{\mathrm{B}}(t) + \boldsymbol{b}_{\mathrm{B}}\boldsymbol{R}_{\mathrm{B}}\,\boldsymbol{\Theta}_{\mathrm{B}}\,\dot{\boldsymbol{q}}_{\mathrm{B}}(t). \end{aligned} \tag{3.44}$$

In (3.44), the transducer short and open circuited stiffness matrices $\boldsymbol{K}_{\mathrm{A}}^{\mathrm{sc}}$ from (3.42) and $\boldsymbol{K}_{\mathrm{B}}^{\mathrm{oc}}$ from (3.43) together with the lateral beam-column stiffness matrix $\boldsymbol{K}(F_x)$ (3.14) are condensed in the new global stiffness matrix $\boldsymbol{K}^{\mathrm{oc}}(F_x)$ with open circuited transducer stiffness in support B. The damping matrix $\boldsymbol{D}_{\mathrm{B}}$ due to dielectric losses in (3.43) together with the short circuited damping matrix $\boldsymbol{D}^{\mathrm{sc}}$ (3.60) is condensed in the new global open-loop damping matrix $\boldsymbol{D}$.

With (3.30), the **open-loop transducer sensing equation** is derived by substituting $e_{\mathrm{B}}(t)$ and $\dot{e}_{\mathrm{B}}(t)$ according to (3.41) leading to

$$\boldsymbol{u}_{\mathrm{B}}(t) = -\boldsymbol{\Theta}_{\mathrm{B}}\,\boldsymbol{C}_{\mathrm{B}}^{-1}\,\boldsymbol{b}_{\mathrm{B}}^{\mathrm{T}}\,\boldsymbol{r}(t) - \boldsymbol{R}_{\mathrm{B}}\,\boldsymbol{\Theta}_{\mathrm{B}}\,\boldsymbol{b}_{\mathrm{B}}^{\mathrm{T}}\,\dot{\boldsymbol{r}}(t) + \boldsymbol{C}_{\mathrm{B}}^{-1}\,\boldsymbol{q}_{\mathrm{B}}(t) + \boldsymbol{R}_{\mathrm{B}}\,\boldsymbol{\Theta}_{\mathrm{B}}\,\dot{\boldsymbol{q}}_{\mathrm{B}}(t). \tag{3.45}$$

Short circuited equation of motion

In case the electrodes in support B are short circuited, the transducer forces according to (3.31) simplify to $\boldsymbol{F}_{\mathrm{B}} = \boldsymbol{k}_{\mathrm{B}}^{\mathrm{sc}}\,\boldsymbol{b}_{\mathrm{B}}^{\mathrm{T}}\,\boldsymbol{r}$. Then, the short circuited beam-column equation of motion becomes

$$\boldsymbol{M}\,\ddot{\boldsymbol{r}}(t) + \boldsymbol{D}^{\mathrm{sc}}\,\dot{\boldsymbol{r}}(t) + \underbrace{\left[\boldsymbol{K}(F_x) + \boldsymbol{K}_{\mathrm{A}}^{\mathrm{sc}} + \boldsymbol{K}_{\mathrm{B}}^{\mathrm{sc}}\right]}_{\boldsymbol{K}^{\mathrm{sc}}}\,\boldsymbol{r}(t) = \boldsymbol{b}_{\mathrm{A}}\,\boldsymbol{\Theta}_{\mathrm{A}}\,\boldsymbol{u}_{\mathrm{A}}(t), \tag{3.46}$$

with the global stiffness matrix $\boldsymbol{K}^{\mathrm{sc}}(F_x)$ (3.14) and damping matrix $\boldsymbol{D}^{\mathrm{sc}}$ (3.60), both valid for short circuited transducer stiffness in support B.

Open circuited equation of motion

In case the electrodes in support B are open circuited, the transducer forces according to (3.32) simplify to $\boldsymbol{F}_{\mathrm{B}} = \boldsymbol{k}_{\mathrm{B}}^{\mathrm{oc}}\,\boldsymbol{b}_{\mathrm{B}}^{\mathrm{T}}\,\boldsymbol{r}$. Then, the **open circuited beam-column equation** of motion becomes

$$\boldsymbol{M}\,\ddot{\boldsymbol{r}}(t) + \boldsymbol{D}^{\mathrm{sc}}\,\dot{\boldsymbol{r}}(t) + \underbrace{\left[\boldsymbol{K}(F_x) + \boldsymbol{K}_{\mathrm{A}}^{\mathrm{sc}} + \boldsymbol{K}_{\mathrm{B}}^{\mathrm{oc}}\right]}_{\boldsymbol{K}^{\mathrm{oc}}}\,\boldsymbol{r}(t) = \boldsymbol{b}_{\mathrm{A}}\,\boldsymbol{\Theta}_{\mathrm{A}}\,\boldsymbol{u}_{\mathrm{A}}(t), \tag{3.47}$$

with the global stiffness matrix $\boldsymbol{K}^{\mathrm{oc}}(F_x)$ valid for open circuited transducer stiffness and damping matrix $\boldsymbol{D}^{\mathrm{sc}}$ (3.60). Also already stated in section 3.3.3, when operating the transducers oc without shunts for vibration attenuation, the damping due to dielectric losses can be neglected, leading to $\boldsymbol{D}^{\mathrm{oc}} \approx \boldsymbol{D}^{\mathrm{sc}}$.

3.3.6 Eigenfrequencies, eigenvectors and GEMCCs

Static axial loading, manufacturing and system assembly variations, uncertainty sources introduced in section 1.2, affect the resonance behavior of the beam-column and the electromechanical coupling of the transducers as shown in chapter 6. The beam-column resonance frequencies with short circuited and with open circuited transducers in support B of the m-th lateral vibration mode are obtained from the eigenvalue problem of the short circuited and open circuited equation of motion. The short circuited and the open circuited resonance frequencies are used to calculate the GEMCC, section 2.2.1, of transducers in support B. Furthermore, the eigenvalue problems yield the beam-column eigenvectors used in the model order reduction in section 3.3.7.

Short circuited eigenvalue problem

For small modal damping coefficients ζ_m, section 3.3.8, as experimentally identified for the beam-column, table 5.3, the damping $\boldsymbol{D}^{\mathrm{sc}}$ has negligible influence on the eigenfrequencies. Hence, $\boldsymbol{D}^{\mathrm{sc}}$ in (3.46) can be neglected, which leads to the homogeneous form

$$\boldsymbol{M}\,\ddot{\boldsymbol{r}}(t) + \boldsymbol{K}^{\mathrm{sc}}(F_x)\,\boldsymbol{r}(t) = 0 \tag{3.48}$$

of the short circuited equation of motion (3.46). The steady state time response of the displacements $\boldsymbol{r}(t)$ is given by the exponential approach $\boldsymbol{r}(t) = \widehat{\boldsymbol{r}}_m^{\mathrm{sc}}\,\mathrm{e}^{-j\,\omega_m^{\mathrm{sc}}\,t}$ that, when inserted in (3.48), forms the short circuited eigenvalue problem

$$\left[\boldsymbol{K}^{\mathrm{sc}}(F_x) - (\omega_m^{\mathrm{sc}})^2\,\boldsymbol{M}\right]\widehat{\boldsymbol{r}}_m^{\mathrm{sc}} = 0. \tag{3.49}$$

The solution of the short circuited characteristic equation

$$\det\left[\boldsymbol{K}^{\mathrm{sc}}(F_x) - (\omega_m^{\mathrm{sc}})^2\,\boldsymbol{M}\right] = 0 \tag{3.50}$$

of the undamped beam-column yields $m = 1, 2, \ldots, 4N$ values of short circuited angular eigenfrequencies $\omega_m^{\mathrm{sc}}(F_x)$. For $m = 1$ and $m = 2$ the short circuited eigenfrequencies $\omega_1^{\mathrm{sc}} = \omega_y^{\mathrm{sc}}$ and $\omega_2^{\mathrm{sc}} = \omega_z^{\mathrm{sc}}$ of the first lateral vibration mode in y- and z-direction are obtained.

For each eigenfrequency $\omega_m^{\mathrm{sc}}(F_x)$, an axial force dependent eigenvector $\widehat{\boldsymbol{r}}_m^{\mathrm{sc}}(F_x)$ exists that describes the vibration amplitude ratios of all displacements $\boldsymbol{r}(t)$ in (3.13)

when oscillating in phase with $\omega_m^{\mathrm{sc}}(F_x)$. The real and linear independent eigenvectors $\widehat{\boldsymbol{r}}_m^{\mathrm{sc}}(F_x)$ of dimension $[4N \times 1]$ are calculated by solving (3.49) after substituting the associated value for $\omega_m^{\mathrm{sc}}(F_x)$.

Open circuited eigenvalue problem

Analog to the short circuited eigenvalue problem, the open circuited eigenvalue problem is derived from the open circuited equation of motion (3.47) for neglected damping. The open circuited eigenvalue problem

$$\left[\boldsymbol{K}^{\mathrm{oc}}(F_x) - (\omega_m^{\mathrm{oc}})^2\, \boldsymbol{M}\right] \widehat{\boldsymbol{r}}_m^{\mathrm{oc}} = 0 \tag{3.51}$$

and characteristic equation

$$\det\left[\boldsymbol{K}^{\mathrm{oc}}(F_x) - (\omega_m^{\mathrm{oc}})^2\, \boldsymbol{M}\right] = 0 \tag{3.52}$$

yield the axial force dependent open circuited angular eigenfrequencies $\omega_m^{\mathrm{oc}}(F_x)$ and eigenvectors $\widehat{\boldsymbol{r}}_m^{\mathrm{oc}}(F_x)$. For $m = 1$ and $m = 2$ the open circuited eigenfrequencies $\omega_1^{\mathrm{oc}} = \omega_y^{\mathrm{oc}}$ and $\omega_2^{\mathrm{oc}} = \omega_z^{\mathrm{oc}}$ of the first lateral vibration mode in y- and z-direction are obtained.

Usually, the difference between the short and open circuited stiffness $\boldsymbol{K}^{\mathrm{sc}}(F_x)$ and $\boldsymbol{K}^{\mathrm{oc}}(F_x)$ is small. For $\boldsymbol{K}^{\mathrm{oc}}(F_x) \approx \boldsymbol{K}^{\mathrm{sc}}(F_x)$, the short and open circuited eigenvectors $\widehat{\boldsymbol{r}}_m^{\mathrm{sc}}(F_x)$ and $\widehat{\boldsymbol{r}}_m^{\mathrm{oc}}(F_x)$ are similar, and for simplification they are assumed to be identical with $\widehat{\boldsymbol{r}}_m^{\mathrm{sc}}(F_x) = \widehat{\boldsymbol{r}}_m^{\mathrm{oc}}(F_x) = \widehat{\boldsymbol{r}}_m(F_x)$ in the following. Additionally, the dependency of $\omega_m^{\mathrm{sc}}(F_x)$, $\omega_m^{\mathrm{oc}}(F_x)$ and $\widehat{\boldsymbol{r}}_m(F_x)$ from F_x is not written in the following but still accounted for.

General electromechanical coupling coefficient

As introduced in chapter 2, the general electromechanical coupling coefficient (GEMCC) γ_m of the transducers $\mathrm{P}_{y,\mathrm{B}}$ and $\mathrm{P}_{z,\mathrm{B}}$ associated to the m-th vibration mode in y- and z-direction is an important quantity for the transducer vibration attenuation potential with shunts. γ_m can be obtained from the short circuited eigenfrequency ω_m^{oc} (3.50) and the open circuited eigenfrequency ω_m^{oc} (3.52) by

$$\gamma_m = \sqrt{\frac{(\omega_m^{\mathrm{oc}})^2 - (\omega_m^{\mathrm{sc}})^2}{(\omega_m^{\mathrm{oc}})^2}} \tag{3.53}$$

as proposed in [64, 77]. For $m = 1, 2$ in (3.53), the coupling coefficients $\gamma_{y/z}$ of the first lateral vibration mode in y- and z-direction are obtained with $\omega^{\mathrm{sc}}_{y/z}$ (3.50) and $\omega^{\mathrm{oc}}_{y/z}$ (3.52).

3.3.7 Model order reduction

The open-loop equations of motion (3.44) and (3.45) and the short circuited equation of motion (3.46) are used to describe the beam-column system's dynamic behavior without shunts in chapters 5 and 6. To reduce the model calculation time in the MONTE-CARLO-Simulations, motivated in section 1.2 and performed in chapter 6, the model order of the open-loop equations of motion and the short circuited equation of motion are reduced.

Model order reduction is performed by modal truncation, [77], to eliminate higher vibration modes in the model that are not contributing significantly to the vibration in the investigated frequency range of the first lateral beam-column vibration mode, section 1.2. To eliminate higher vibration modes, the equations of motion are transformed to modal displacements by using the beam-column eigenvectors $\widehat{\boldsymbol{r}}_m$ (3.49) in the modal superposition approach

$$\boldsymbol{r}(t) = \sum_{m=1}^{4N} \widehat{\boldsymbol{r}}_m \, p_m(t) \tag{3.54}$$

with the modal displacements $p_m(t)$ in modal coordinates. The modal superposition (3.54) is truncated by the approximation

$$\boldsymbol{r}(t) \approx \sum_{m=1}^{2M} \widehat{\boldsymbol{r}}_m \, p_m(t) = \boldsymbol{\Phi}\, \boldsymbol{p}(t) \tag{3.55}$$

with the number $M < N$ of lateral vibration modes for to only include the significantly contributing modes that are sufficient to properly describe the lateral beam-column displacements in y- and z-direction. In (3.55), the $2M$ eigenvectors $\widehat{\boldsymbol{r}}_m$ of lateral vibration modes in y- and z-direction form the modal matrix $\boldsymbol{\Phi} = [\widehat{\boldsymbol{r}}_1, \widehat{\boldsymbol{r}}_2, ..., \widehat{\boldsymbol{r}}_{2M}]$ of dimension $[4N \times 2M]$, and $\boldsymbol{p}(t)$ is the modal displacement vector. $M = 30$ lateral modes are taken into account in the following.

Open-loop reduced equations of motion

With the set of $2M$ eigenvectors in the modal matrix $\boldsymbol{\Phi}$ (3.55), the **open-loop reduced beam-column equation** of motion is obtained by plugging (3.55) in (3.44) and left-multiplying (3.44) by $\boldsymbol{\Phi}^{\mathrm{T}}$, which leads to

$$\begin{aligned}\boldsymbol{\Phi}^{\mathrm{T}}\,\boldsymbol{M}\,\boldsymbol{\Phi}\,\ddot{\boldsymbol{p}}(t)+\boldsymbol{\Phi}^{\mathrm{T}}\,\boldsymbol{D}\,\boldsymbol{\Phi}\,\dot{\boldsymbol{p}}(t)+\boldsymbol{\Phi}^{\mathrm{T}}\,\boldsymbol{K}^{\mathrm{oc}}\,\boldsymbol{\Phi}\,\boldsymbol{p}(t)=\\ \boldsymbol{\Phi}^{\mathrm{T}}\,\boldsymbol{b}_{\mathrm{A}}\,\boldsymbol{\Theta}_{\mathrm{A}}\,\boldsymbol{u}_{\mathrm{A}}(t)+\boldsymbol{\Phi}^{\mathrm{T}}\,\boldsymbol{b}_{\mathrm{B}}\,\boldsymbol{\Theta}_{\mathrm{B}}\,\boldsymbol{C}_{\mathrm{B}}^{-1}\,\boldsymbol{q}_{\mathrm{B}}(t)+\boldsymbol{\Phi}^{\mathrm{T}}\,\boldsymbol{b}_{\mathrm{B}}\,\boldsymbol{\Theta}_{\mathrm{B}}\,\boldsymbol{R}_{\mathrm{B}}\,\dot{\boldsymbol{q}}_{\mathrm{B}}(t).\end{aligned} \tag{3.56}$$

Consequently, the reduced diagonal $[2M\times 2M]$ modal mass matrix, modal damping matrix and modal stiffness matrix

$$\boldsymbol{M}_{\mathrm{m}}=\boldsymbol{\Phi}^{\mathrm{T}}\boldsymbol{M}\boldsymbol{\Phi},\quad \boldsymbol{D}_{\mathrm{m}}=\boldsymbol{\Phi}^{\mathrm{T}}\boldsymbol{D}\boldsymbol{\Phi}\quad\text{and}\quad \boldsymbol{K}_{\mathrm{m}}^{\mathrm{oc}}=\boldsymbol{\Phi}^{\mathrm{T}}\boldsymbol{K}^{\mathrm{oc}}\boldsymbol{\Phi} \tag{3.57}$$

are obtained. Performing the same modal reduction for the **open-loop reduced transducer sensing equation** (3.45) results in

$$\boldsymbol{u}_{\mathrm{B}}(t)=-\boldsymbol{\Theta}_{\mathrm{B}}\,\boldsymbol{C}_{\mathrm{B}}^{-1}\,\boldsymbol{b}_{\mathrm{B}}^{\mathrm{T}}\,\boldsymbol{\Phi}\,\boldsymbol{p}(t)-\boldsymbol{R}_{\mathrm{B}}\,\boldsymbol{\Theta}_{\mathrm{B}}\,\boldsymbol{b}_{\mathrm{B}}^{\mathrm{T}}\,\boldsymbol{\Phi}\,\dot{\boldsymbol{p}}(t)+\boldsymbol{C}_{\mathrm{B}}^{-1}\,\boldsymbol{q}_{\mathrm{B}}(t)+\boldsymbol{R}_{\mathrm{B}}\,\boldsymbol{\Theta}_{\mathrm{B}}\,\dot{\boldsymbol{q}}_{\mathrm{B}}(t). \tag{3.58}$$

Short circuited reduced equation of motion

In case the transducers in support B are operated with short circuited electrodes, (3.46) in modal displacements becomes

$$\boldsymbol{M}_{\mathrm{m}}\,\ddot{\boldsymbol{p}}(t)+\boldsymbol{D}_{\mathrm{m}}^{\mathrm{sc}}\,\dot{\boldsymbol{p}}(t)+\boldsymbol{K}_{\mathrm{m}}^{\mathrm{sc}}(F_x)\,\boldsymbol{p}(t)=\boldsymbol{\Phi}^{\mathrm{T}}\,\boldsymbol{b}_{\mathrm{A}}\,\boldsymbol{\Theta}_{\mathrm{A}}\,\boldsymbol{u}_{\mathrm{A}}(t), \tag{3.59}$$

where $\boldsymbol{K}_{\mathrm{m}}^{\mathrm{sc}}$ and $\boldsymbol{D}_{\mathrm{m}}^{\mathrm{sc}}$ are the modal stiffness and damping matrices valid for short circuited electrodes obtained analogously to (3.57).

3.3.8 Approximation of damping

The beam-column damping matrix $\boldsymbol{D}^{\mathrm{sc}}$ with short circuited transducers $\mathrm{P}_{y,\mathrm{B}}$ and $\mathrm{P}_{z,\mathrm{B}}$ in support B is derived by assuming CAUGHEY damping with $\boldsymbol{D}^{\mathrm{sc}}$ being proportional to the global mass and stiffness matrices $\boldsymbol{M}$ and $\boldsymbol{K}^{\mathrm{sc}}(F_x)$ obtained in section 3.3.2. This is valid if no discrete damping elements are attached to the structure and damping due to friction in joints and connections are neglected, [54], which is the case for the investigated system. For modal damping coefficients ζ_m of the $m=1,\ldots,2M$ lateral vibration modes in y- and z-direction,

the global damping matrix is obtained from the superposition of modal damping matrices, [11], according to

$$\boldsymbol{D}^{\mathrm{sc}} = \boldsymbol{M}\,\boldsymbol{\Phi}\,\boldsymbol{M}_{\mathrm{m}}^{-1}\,\mathrm{diag}\left(2\zeta_1\omega_1^{\mathrm{sc}},\,...,\,2\zeta_{2M}\omega_{2M}^{\mathrm{sc}}\right)\boldsymbol{\Phi}^{\mathrm{T}}\,\boldsymbol{M} \tag{3.60}$$

with global mass matrix $\boldsymbol{M}$, modal mass matrix $\boldsymbol{M}_m$ (3.57) and the undamped beam-column eigenvectors $\boldsymbol{\Phi}$ (3.55) and eigenfrequencies ω_m^{sc} (3.50).

3.3.9 State space representations of beam-column system

To simulate the beam-column system's dynamic behavior in the frequency domain without shunts connected, state space representations of the open-loop and the short circuited model are derived and used as introduced at the beginning of section 3.3. The open-loop reduced differential equations (3.56) and (3.58) as well as the short circuited reduced differential equation (3.59) are transformed into state space first order differential equations with inputs and outputs shown in figure 3.7 to later derive open-loop and short circuited frequency transfer functions in section 3.3.10.

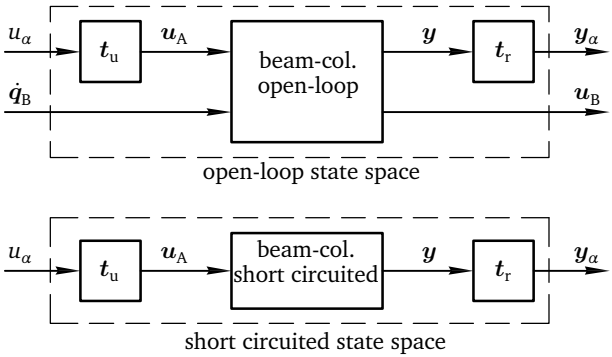

Figure 3.7: Open-loop and short circuited state space representations

As introduced in section 3.2, the transducers in support A in figure 3.2 are used to excite the beam-column in y- and z-direction as well as to apply excitation at an oblique angle α in y_α-direction. In order to describe the beam-column vibration in and orthogonal to the direction of excitation, the voltage transformation matrix $\boldsymbol{t}_{\mathrm{u}}$ (3.36) and the displacement transformation matrix $\boldsymbol{t}_{\mathrm{r}}$ (3.37) are used with the open-loop and short circuited equations of motion to realize the excitation signal

$u_\alpha(t)$ (3.36) as state space input and $\boldsymbol{y}_\alpha(t)$ (3.37) as state space output. For the transducers in support B, the currents $\dot{\boldsymbol{q}}_\mathrm{B}(t)$ and the voltages $\boldsymbol{u}_\mathrm{B}(t)$ are used as inputs and outputs in the state space.

Open-loop state space representation

The open-loop state space inputs and outputs as shown in figure 3.7 are summarized in the $[3\times1]$ open-loop state space input vector $\underline{\boldsymbol{u}}^\mathrm{ol}(t)$ and $[4\times1]$ open-loop output vector $\underline{\boldsymbol{y}}^\mathrm{ol}(t)$,

$$\underline{\boldsymbol{u}}^\mathrm{ol}(t)=\begin{bmatrix}u_\alpha(t)\\ \dot{\boldsymbol{q}}_\mathrm{B}(t)\end{bmatrix}\quad\text{and}\quad\underline{\boldsymbol{y}}^\mathrm{ol}(t)=\begin{bmatrix}\boldsymbol{y}_\alpha(t)\\ \boldsymbol{u}_\mathrm{B}(t)\end{bmatrix}. \tag{3.61}$$

With the open-loop state space input and output vectors (3.61), the reduced open-loop differential equations (3.56) and (3.58) with transformed transducer voltages (3.36) and displacements (3.37) are written in the first-order differential equations by using the $[(4M+2)\times1]$ open-loop state vector with modal displacements, modal velocities and transducer charges $\underline{\boldsymbol{x}}^\mathrm{ol}(t)=[\boldsymbol{p}^\mathrm{T}(t),\dot{\boldsymbol{p}}^\mathrm{T}(t),\boldsymbol{q}_\mathrm{B}^\mathrm{T}(t)]^\mathrm{T}$. The open-loop state space equations are

$$\begin{aligned}\dot{\underline{\boldsymbol{x}}}^\mathrm{ol}(t)=&\underbrace{\begin{bmatrix}\mathbf{0}&\mathbf{I}&\mathbf{0}\\ -\boldsymbol{M}_\mathrm{m}^{-1}\boldsymbol{K}_\mathrm{m}^\mathrm{oc}&-\boldsymbol{M}_\mathrm{m}^{-1}\boldsymbol{D}_\mathrm{m}&\boldsymbol{M}_\mathrm{m}^{-1}\boldsymbol{\Phi}^\mathrm{T}\boldsymbol{b}_\mathrm{B}\boldsymbol{\Theta}_\mathrm{B}\boldsymbol{C}_\mathrm{B}^{-1}\\ \mathbf{0}&\mathbf{0}&\mathbf{0}\end{bmatrix}}_{[(4M+2)\times(4M+2)]}\underline{\boldsymbol{x}}^\mathrm{ol}(t)\\ &+\underbrace{\begin{bmatrix}\mathbf{0}&\mathbf{0}\\ \boldsymbol{M}_\mathrm{m}^{-1}\boldsymbol{\Phi}^\mathrm{T}\boldsymbol{b}_\mathrm{A}\boldsymbol{\Theta}_\mathrm{A}\boldsymbol{t}_\mathrm{u}&\boldsymbol{M}_\mathrm{m}^{-1}\boldsymbol{\Phi}^\mathrm{T}\boldsymbol{b}_\mathrm{B}\boldsymbol{\Theta}_\mathrm{B}\boldsymbol{R}_\mathrm{B}\\ \mathbf{0}&\mathbf{I}\end{bmatrix}}_{[(4M+2)\times3]}\underline{\boldsymbol{u}}^\mathrm{ol}(t)\\ \underline{\boldsymbol{y}}^\mathrm{ol}(t)=&\underbrace{\begin{bmatrix}\boldsymbol{t}_\mathrm{r}\boldsymbol{b}_\mathrm{s}\boldsymbol{\Phi}&\mathbf{0}&\mathbf{0}\\ -\boldsymbol{\Theta}_\mathrm{B}\boldsymbol{C}_\mathrm{B}^{-1}\boldsymbol{b}_\mathrm{B}^\mathrm{T}\boldsymbol{\Phi}&-\boldsymbol{R}_\mathrm{B}\boldsymbol{\Theta}_\mathrm{B}\boldsymbol{b}_\mathrm{B}^\mathrm{T}\boldsymbol{\Phi}&\boldsymbol{C}_\mathrm{B}^{-1}\end{bmatrix}}_{[4\times(4M+2)]}\underline{\boldsymbol{x}}^\mathrm{ol}(t)+\underbrace{\begin{bmatrix}0&0\\ 0&\boldsymbol{R}_\mathrm{B}\boldsymbol{\Theta}_\mathrm{B}\end{bmatrix}}_{[4\times3]}\underline{\boldsymbol{u}}^\mathrm{ol}(t)\end{aligned} \tag{3.62}$$

with zero and identity matrices $\mathbf{0}$ and $\mathbf{I}$ of appropriate dimensions. Equation (3.62) in short form is written according to

$$\begin{aligned}\dot{\underline{\boldsymbol{x}}}^\mathrm{ol}(t)&=\underline{\boldsymbol{A}}^\mathrm{ol}\,\underline{\boldsymbol{x}}^\mathrm{ol}(t)+\underline{\boldsymbol{B}}^\mathrm{ol}\,\underline{\boldsymbol{u}}^\mathrm{ol}(t)\\ \underline{\boldsymbol{y}}^\mathrm{ol}(t)&=\underline{\boldsymbol{C}}^\mathrm{ol}\,\underline{\boldsymbol{x}}^\mathrm{ol}(t)+\underline{\boldsymbol{D}}^\mathrm{ol}\,\underline{\boldsymbol{u}}^\mathrm{ol}(t)\end{aligned} \tag{3.63}$$

with open-loop system matrix $\underline{\boldsymbol{A}}^{\mathrm{ol}}$, input matrix $\underline{\boldsymbol{B}}^{\mathrm{ol}}$, output matrix $\underline{\boldsymbol{C}}^{\mathrm{ol}}$ and feedthrough matrix $\underline{\boldsymbol{D}}^{\mathrm{ol}}$.

Short circuited state space representation

The short circuited state space inputs and outputs as shown in figure 3.7 are summarized in the short circuited state space input $\underline{u}^{\mathrm{sc}}(t)$ and $[2 \times 1]$ short circuited output vector $\underline{\boldsymbol{y}}^{\mathrm{sc}}(t)$,

$$\underline{u}^{\mathrm{sc}}(t) = u_{\alpha}(t) \quad \text{and} \quad \underline{\boldsymbol{y}}^{\mathrm{sc}}(t) = \boldsymbol{y}_{\alpha}(t). \tag{3.64}$$

With the short circuited state space inputs and output vectors (3.64), the reduced short circuited differential equations (3.59) with transformed transducer voltages (3.36) and displacements (3.37) are written in the first-order differential equations by using the $[4M \times 1]$ short circuited state vector with model displacements and modal velocities $\underline{\boldsymbol{x}}^{\mathrm{sc}}(t) = [\boldsymbol{p}^{\mathrm{T}}(t), \dot{\boldsymbol{p}}^{\mathrm{T}}(t)]^{\mathrm{T}}$. The sc state space equations are

$$\begin{aligned}
\dot{\underline{\boldsymbol{x}}}^{\mathrm{sc}}(t) &= \underbrace{\begin{bmatrix} \mathbf{0} & \mathbf{I} \\ -\boldsymbol{M}_{\mathrm{m}}^{-1}\boldsymbol{K}_{\mathrm{m}}^{\mathrm{sc}} & -\boldsymbol{M}_{\mathrm{m}}^{-1}\boldsymbol{D}_{\mathrm{m}}^{\mathrm{sc}} \end{bmatrix}}_{[4M \times 4M]} \underline{\boldsymbol{x}}^{\mathrm{sc}}(t) + \underbrace{\begin{bmatrix} \mathbf{0} \\ \boldsymbol{M}_{\mathrm{m}}^{-1}\boldsymbol{\Phi}^{\mathrm{T}}\boldsymbol{b}_{\mathrm{A}}\boldsymbol{\Theta}_{\mathrm{A}}\boldsymbol{t}_{\mathrm{u}} \end{bmatrix}}_{[4M \times 1]} \underline{\boldsymbol{u}}^{\mathrm{sc}}(t) \\
\underline{\boldsymbol{y}}^{\mathrm{sc}}(t) &= \underbrace{\begin{bmatrix} \boldsymbol{t}_{\mathrm{r}}\boldsymbol{b}_{\mathrm{s}}\boldsymbol{\Phi} & \mathbf{0} \end{bmatrix}}_{[2 \times 4M]} \underline{\boldsymbol{x}}^{\mathrm{sc}}(t) + \mathbf{0}\,\underline{\boldsymbol{u}}^{\mathrm{sc}}(t)
\end{aligned} . \tag{3.65}$$

Equation (3.65) in short form is written according to

$$\begin{aligned}
\dot{\underline{\boldsymbol{x}}}^{\mathrm{sc}}(t) &= \underline{\boldsymbol{A}}^{\mathrm{sc}}\,\underline{\boldsymbol{x}}^{\mathrm{sc}}(s) + \underline{B}^{\mathrm{sc}}\,\underline{u}^{\mathrm{sc}}(t) \\
\underline{\boldsymbol{y}}^{\mathrm{sc}}(t) &= \underline{\boldsymbol{C}}^{\mathrm{sc}}\,\underline{\boldsymbol{x}}^{\mathrm{sc}}(t)
\end{aligned} \tag{3.66}$$

with short circuited system matrix $\underline{\boldsymbol{A}}^{\mathrm{sc}}$, input matrix $\underline{\boldsymbol{B}}^{\mathrm{sc}}$, output matrix $\underline{\boldsymbol{C}}^{\mathrm{sc}}$ and zero feedthrough matrix $\underline{\boldsymbol{D}}^{\mathrm{sc}} = \mathbf{0}$.

3.3.10 Frequency transfer functions without shunts

The beam-column system's dynamic behavior without shunts is simulated in the frequency domain and analyzed via frequency transfer functions, as introduced at

the beginning of section 3.3. The beam-column system's frequency transfer functions are obtained by transforming the open-loop (3.63) and short circuited (3.66) state space representations from time to frequency domain.

The transformation from time domain into frequency domain is performed by using the LAPLACE transform, [8], with LAPLACE variable s. As an example, but valid for all time dependent variables used in this work, the LAPLACE transform of the states $\underline{\boldsymbol{x}}(t)$ is given by

$$\mathscr{L}\{\underline{\boldsymbol{x}}(t)\} = \underline{\boldsymbol{x}}(s) = \int_0^\infty \underline{\boldsymbol{x}}(t)\, e^{st}\, dt, \tag{3.67}$$

and the LAPLACE transforms of its time derivatives are $\mathscr{L}\{\dot{\underline{\boldsymbol{x}}}(t)\} = s\,\underline{\boldsymbol{x}}(s)$ and $\mathscr{L}\{\ddot{\underline{\boldsymbol{x}}}(t)\} = s^2\,\underline{\boldsymbol{x}}(s)$. After LAPLACE transform, the frequency domain behavior is obtained by using the conversion $s = j\Omega$ with excitation frequency Ω. This conversion is valid for signals that can be FOURIER transformed and systems with zero initial states $\underline{\boldsymbol{x}}(0) = 0$, as assumed for excitation and response signals of the beam-column system in this work.

Open loop frequency transfer functions

By use of the LAPLACE transform (3.67), the open-loop state space representation (3.63) in LAPLACE domain becomes

$$\begin{aligned} s\,\underline{\boldsymbol{x}}^{\mathrm{ol}}(s) &= \underline{\boldsymbol{A}}^{\mathrm{ol}}\,\underline{\boldsymbol{x}}^{\mathrm{ol}}(s) + \underline{\boldsymbol{B}}^{\mathrm{ol}}\,\underline{\boldsymbol{u}}^{\mathrm{ol}}(s) \\ \underline{\boldsymbol{y}}^{\mathrm{ol}}(s) &= \underline{\boldsymbol{C}}^{\mathrm{ol}}\,\underline{\boldsymbol{x}}^{\mathrm{ol}}(s) + \underline{\boldsymbol{D}}^{\mathrm{ol}}\,\underline{\boldsymbol{u}}^{\mathrm{ol}}(s). \end{aligned} \tag{3.68}$$

With (3.68), the $[4 \times 3]$ open-loop transfer function matrix

$$\boldsymbol{G}^{\mathrm{ol}}(s) = \frac{\underline{\boldsymbol{y}}^{\mathrm{ol}}(s)}{\underline{\boldsymbol{u}}^{\mathrm{ol}}(s)} = \left[\underline{\boldsymbol{C}}^{\mathrm{ol}}(s\,\mathbf{I} - \underline{\boldsymbol{A}}^{\mathrm{ol}})^{-1}\,\underline{\boldsymbol{B}}^{\mathrm{ol}} + \underline{\boldsymbol{D}}^{\mathrm{ol}}\right] = \begin{bmatrix} \boldsymbol{G}_{\mathrm{ru}}(s) & \boldsymbol{G}_{\mathrm{r\dot{q}}}(s) \\ \boldsymbol{G}_{\mathrm{uu}}(s) & \boldsymbol{G}_{\mathrm{u\dot{q}}}(s) \end{bmatrix} \tag{3.69}$$

relates the open-loop input vector $\underline{\boldsymbol{u}}^{\mathrm{ol}}(s)$ to the open-loop output vector $\underline{\boldsymbol{y}}^{\mathrm{ol}}(s)$, [20, 88]. By using the conversion $s = j\Omega$ as introduced at the beginning of this section, (3.69) is transformed into frequency domain and becomes a function of the excitation frequency Ω,

$$\boldsymbol{G}^{\mathrm{ol}}(\Omega) = \left[\underline{\boldsymbol{C}}^{\mathrm{ol}}(j\Omega\,\mathbf{I} - \underline{\boldsymbol{A}}^{\mathrm{ol}})^{-1}\,\underline{\boldsymbol{B}}^{\mathrm{ol}} + \underline{\boldsymbol{D}}^{\mathrm{ol}}\right] = \begin{bmatrix} \boldsymbol{G}_{\mathrm{ru}}(\Omega) & \boldsymbol{G}_{\mathrm{r\dot{q}}}(\Omega) \\ \boldsymbol{G}_{\mathrm{uu}}(\Omega) & \boldsymbol{G}_{\mathrm{u\dot{q}}}(\Omega) \end{bmatrix}. \tag{3.70}$$

In (3.70), $\boldsymbol{G}_{\mathrm{ru}}(\Omega)$ relates the input excitation voltage $u_\alpha(\Omega)$ to the output displacements $\boldsymbol{y}_\alpha(\Omega)$, $\boldsymbol{G}_{\mathrm{u\dot{q}}}(\Omega)$ relates the input transducer currents $\dot{\boldsymbol{q}}_{\mathrm{B}}(\Omega)$ to the output transducer voltages $\boldsymbol{u}_{\mathrm{B}}(s)$, $\boldsymbol{G}_{\mathrm{r\dot{q}}}(\Omega)$ relates the input transducer currents $\dot{\boldsymbol{q}}_{\mathrm{B}}(\Omega)$ to the output displacement $\boldsymbol{y}_\alpha(\Omega)$, and $\boldsymbol{G}_{\mathrm{uu}}(\Omega)$ relates the input excitation voltage $u_\alpha(\Omega)$ to the output transducer voltages $\boldsymbol{u}_{\mathrm{B}}(\Omega)$.

In particular, the two scalar beam-column displacement frequency transfer functions

$$\boldsymbol{G}_{\mathrm{ru}}(\Omega) = \begin{bmatrix} \frac{r_{y_\alpha,\mathrm{s}}(\Omega)}{u_\alpha(\Omega)} & \frac{r_{z_\alpha,\mathrm{s}}(\Omega)}{u_\alpha(\Omega)} \end{bmatrix}^{\mathrm{T}}, \tag{3.71}$$

characterize the forced beam-column vibration in and orthogonal to the direction of excitation by support A in figure 3.2. After multiplication with $-\Omega^2$, the scalar acceleration frequency transfer functions

$$\begin{bmatrix} G_\alpha(\Omega) & G_{\alpha\perp}(\Omega) \end{bmatrix}^{\mathrm{T}} = -\Omega^2 \boldsymbol{G}_{\mathrm{ru}}(\Omega) = \begin{bmatrix} \frac{a_\alpha(\Omega)}{u_\alpha(\Omega)} & \frac{a_{\alpha\perp}(\Omega)}{u_\alpha(\Omega)} \end{bmatrix}^{\mathrm{T}} \tag{3.72}$$

of accelerations $\ddot{\boldsymbol{y}}_\alpha(\Omega)$ (3.38) are obtained as needed for the comparison with experimental results in chapters 5 and 6. Furthermore in (3.70), the two scalar transducer impedance frequency transfer functions

$$\boldsymbol{G}_{\mathrm{u\dot{q}}}(\Omega) = \begin{bmatrix} Z_{y,\mathrm{B}}(\Omega) & 0 \\ 0 & Z_{z,\mathrm{B}}(\Omega) \end{bmatrix} = \begin{bmatrix} \frac{u_{y,\mathrm{B}}(\Omega)}{\dot{q}_{y,\mathrm{B}}(\Omega)} & 0 \\ 0 & \frac{u_{z,\mathrm{B}}(\Omega)}{\dot{q}_{z,\mathrm{B}}(\Omega)} \end{bmatrix} \tag{3.73}$$

characterize the dynamic transducer transfer behavior of transducers in support B in figure 3.2. In section 3.4, the open-loop transfer function matrix $\boldsymbol{G}^{\mathrm{ol}}(\Omega)$ (3.70) is additionally used to derive the beam-column vibration frequency transfer functions with shunts.

Short circuited frequency transfer function

The short circuited beam-column displacement vibration frequency transfer functions

$$\boldsymbol{G}^{\mathrm{sc}}_{\mathrm{ru}}(s) = \frac{\underline{\boldsymbol{y}}^{\mathrm{sc}}(\Omega)}{\underline{\boldsymbol{u}}^{\mathrm{sc}}(\Omega)} = \left[\underline{\boldsymbol{C}}^{\mathrm{sc}} (j\Omega \mathbf{I} - \underline{\boldsymbol{A}}^{\mathrm{sc}})^{-1} \underline{\boldsymbol{B}}^{\mathrm{sc}} \right] \tag{3.74}$$

are obtained from the LAPLACE transform of the short circuited state space representation (3.66) by using the conversion $s = j\Omega$ as shown for the open-loop case in the last paragraph.

After multiplication of (3.74) with $-\Omega^2$, the short circuited beam-column acceleration frequency transfer functions

$$\left[G_{\alpha}^{\mathrm{sc}}(\Omega) \quad G_{\alpha^{\perp}}^{\mathrm{sc}}(\Omega)\right]^{\mathrm{T}} = -\Omega^2 \boldsymbol{G}_{\mathrm{ru}}^{\mathrm{sc}}(\Omega) \tag{3.75}$$

with short circuited transducers in support B characterize the beam-column vibration without vibration attenuation through shunts.

3.4 Models of beam-column with piezo-elastic supports with shunts

In this work, the capability of piezo-elastic support B to attenuate lateral vibrations of the beam-column in figure 3.2 is investigated and compared for transducers in support B connected to RL-shunts and to RL-shunts extended by a negative capacitance, the RLC-shunt, in order to increase the vibration attenuation capability of the resonant shunt, section 2.2. To simulate vibration attenuation with shunts in chapters 5 and 6, frequency transfer functions are derived of the beam-column system's model with shunts in this section.

First, electrical shunt impedance models of the RL- and RLC-shunts used in this work are introduced. Secondly, the shunt models are mathematically connected to the open-loop frequency transfer functions from section 3.3.10 to derive shunted beam-column acceleration transfer functions with transducers in support B connected to RL- or RLC-shunts. To tune the used shunts for optimal vibration attenuation, a numerical tuning procedure is presented in section 3.5.

3.4.1 RL-shunt model

The linear electrical RL-shunt impedance model used in this work for the simulation of vibration attenuation with RL-shunts is derived from the series RL-shunt circuit in figure 3.8a. The RL-shunt model includes a damping resistor with electrical damping resistor impedance Z^{D} (3.77) and an inductor with electrical inductor impedance Z^{L} (3.78). The electrical RL-shunt circuit impedance Z^{RL} (3.76) is calculated in the frequency domain and describes the linear relation of the shunt current $\dot{q}(\Omega)$ to the shunt voltage $u(\Omega)$ according to

$$Z^{\mathrm{RL}}(\Omega) = \frac{u(\Omega)}{\dot{q}(\Omega)} = Z^{\mathrm{D}}(\Omega) + Z^{\mathrm{L}}(\Omega). \tag{3.76}$$

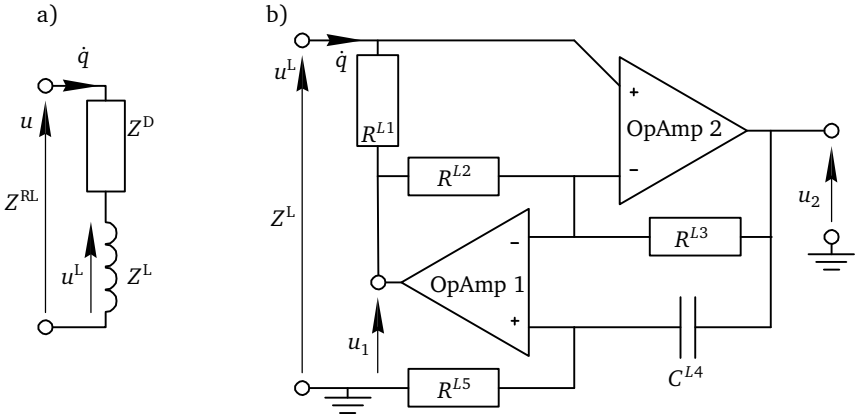

Figure 3.8: a) series RL-shunt circuit, b) inductor circuit layout

According to the OHM's law, the damping resistor impedance $Z^{\mathrm{D}}(\Omega)$ in (3.76) is constant and can be replaced by the damping resistance R^{D},

$$Z^{\mathrm{D}}(\Omega) = R^{\mathrm{D}}. \tag{3.77}$$

As introduced in section 2.2.1, for experimental implementations the gyrator circuit in figure 3.8b is a common approach to obtain a precisely tunable inductor with impedance $Z^{\mathrm{L}}(\Omega)$ in order to represent an inductance L as needed for the tuning of the RL-shunt, [41, 60, 89]. For shunt tuning, section 3.5, the resistance R^{D} and the impedance $Z^{\mathrm{L}}(\Omega)$ are adjusted.

Inductor circuit with adjustable and constant circuit parameters

The inductor circuit in figure 3.8b consists of two ideal operational amplifiers (OpAmp) with infinitive input resistance and zero output resistance, not explicitly shown in figure 3.8b, four resistors with resistances R^{L1}, R^{L2}, R^{L3} and R^{L5} and one capacitor with capacitance C^{L4}. For ideal operational amplifiers, the inductor circuit impedance $Z^{\mathrm{L}}(\Omega)$ in figure 3.8 in complex frequency domain becomes

$$Z^{\mathrm{L}}(\Omega) = \frac{u^{\mathrm{L}}(\Omega)}{\dot{q}(\Omega)} = j\Omega \frac{R^{\mathrm{L1}} R^{\mathrm{L3}} C^{\mathrm{L4}} R^{\mathrm{L5}}}{R^{\mathrm{L2}}} \tag{3.78}$$

with shunt current $\dot{q}(\Omega)$ and inductor voltage $u^{\mathrm{L}}(\Omega)$, [41].

With (3.78), the inductance L of the inductor circuit in figure 3.8b as needed for the tuning of the RL-shunt, see figure 2.1b, is obtained by

$$L = \frac{\Im\{Z^{\mathrm{L}}(j\Omega)\}}{\Omega} = R^{\mathrm{L1}} \frac{R^{\mathrm{L3}}}{R^{\mathrm{L2}}} C^{\mathrm{L4}} R^{\mathrm{L5}} \tag{3.79}$$

with the imaginary part $\Im\{Z^{\mathrm{L}}(j\Omega)\}$ of the inductor circuit impedance $Z^{\mathrm{L}}(j\Omega)$.

In the shunt optimization in section 3.5 and in the experimental RL-shunt realization in section 4.1.3, the resistance R^{L1} is varied to adjust the inductance L (3.79), and constant values are assigned to R^{L2}, R^{L3}, C^{L4} and R^{L5} in order to receive equal and limited complex operational amplifier output voltages $u_1(j\Omega)$ and $u_2(j\Omega)$ in consequence of the inductor voltage $u^{\mathrm{L}}(j\Omega)$ in figure 3.8. The operational amplifier output voltage transfer functions

$$\frac{u_1(\Omega)}{u(\Omega)} = \frac{1 + j\,\Omega/\omega_{\mathrm{c1}}}{j\,\Omega/\omega_{\mathrm{c1}}} \quad \text{and} \quad \frac{u_2(\Omega)}{u(\Omega)} = \frac{1 + j\,\Omega/\omega_{\mathrm{c2}}}{j\,\Omega/\omega_{\mathrm{c2}}}, \tag{3.80}$$

as derived in [41], show a proportional-integral transfer behavior with the corner frequencies

$$\omega_{\mathrm{c1}} = \frac{1}{R^{\mathrm{L5}}\, C^{\mathrm{L4}}} \quad \text{and} \quad \omega_{\mathrm{c2}} = \frac{R^{\mathrm{L2}}}{R^{\mathrm{L3}}} \omega_{\mathrm{c1}}. \tag{3.81}$$

For $R^{\mathrm{L2}} = R^{\mathrm{L3}}$, the corner frequencies ω_{c1} and ω_{c2} in (3.81) become equal. This leads to equal operational amplifier output voltage transfer functions in (3.80). As suggested by [57], the capacitance C^{L4} and the resistance R^{L5} in (3.81) should be chosen to make the corner frequency ω_{c1} small compared to the first short circuited beam-column resonance frequencies $\omega^{\mathrm{sc}}_{y/z}$ (3.50) in order to avoid operational amplifier output voltage saturation effects and to guarantee a linear inductor circuit behavior. For $R^{\mathrm{L2}} = R^{\mathrm{L3}}$, the inductance L of the inductor circuit from (3.79) simplifies to

$$L = R^{\mathrm{L1}}\, R^{\mathrm{L5}}\, C^{\mathrm{L4}}. \tag{3.82}$$

RL-shunt impedance model

For vibration attenuation in y- and z-direction with transducers $\mathrm{P}_{y,\mathrm{B}}$ and $\mathrm{P}_{z,\mathrm{B}}$ connected to RL-shunts, individual RL-shunt impedance models

$$Z^{\mathrm{RL}}_{y/z}(\Omega) = R^{\mathrm{D}}_{y/z} + \Omega \frac{R^{\mathrm{L1}}_{y/z} R^{\mathrm{L3}}_{y/z} C^{\mathrm{L4}}_{y/z} R^{\mathrm{L5}}_{y/z}}{R^{\mathrm{L2}}_{y/z}} \tag{3.83}$$

are received from (3.76) with $Z^{\mathrm{D}}(\Omega)$ (3.77) and $Z^{\mathrm{L}}(\Omega)$ (3.78) for individual damping resistances $R^{\mathrm{D}}_{y/z}$, inductor circuit resistances $R^{\mathrm{L1}}_{y/z}$, $R^{\mathrm{L2}}_{y/z}$, $R^{\mathrm{L3}}_{y/z}$, $R^{\mathrm{L5}}_{y/z}$ and inductor circuit capacitances $C^{\mathrm{L4}}_{y/z}$. The RL-shunt impedance models $Z^{\mathrm{RL}}_{y/z}(\Omega)$ are summarized in the RL-shunt transfer function matrix

$$\boldsymbol{G}^{\mathrm{RL}}(j\Omega) = \begin{bmatrix} Z^{\mathrm{RL}}_{y}(\Omega) & 0 \\ 0 & Z^{\mathrm{RL}}_{z}(\Omega) \end{bmatrix}^{-1}. \tag{3.84}$$

$\boldsymbol{G}^{\mathrm{RL}}(\Omega)$ is mathematically connected to the open-loop beam-column transfer functions in section 3.4.3.

3.4.2 RLC-shunt model

The linear electrical RLC-shunt impedance model used in this work for the simulation of vibration attenuation with RLC-shunts is derived from the series RLC-shunt circuit in figure 3.9a. The RLC-model includes a damping resistor with electrical damping resistor impedance Z^{D} (3.77), the inductor with electrical inductor impedance Z^{L} (3.78) from last section and a negative capacitor with negative capacitor impedance Z^{N} (3.86). Analogously to (3.76), the electrical RLC-shunt circuit impedance Z^{RLC} (3.85) is calculated in the frequency domain by

$$Z^{\mathrm{RLC}}(\Omega) = \frac{u(\Omega)}{\dot{q}(\Omega)} = Z^{\mathrm{D}}(\Omega) + Z^{\mathrm{L}}(\Omega) + Z^{\mathrm{N}}(\Omega). \tag{3.85}$$

As introduced in section 2.2.1, for experimental implementations the negative capacitor circuit in figure 3.9b is a common approach to obtain a precisely tunable negative capacitor with impedance $Z^{\mathrm{N}}(\Omega)$ in order to represent a negative capacitance C^{n} as needed for vibration attenuation, [6, 74, 76]. For shunt tuning, section 3.5, the resistance R^{D} and the impedances $Z^{\mathrm{L}}(\Omega)$ and $Z^{\mathrm{N}}(\Omega)$ are adjusted.

Negative capacitor circuit with adjustable and constant circuit parameters

The negative capacitor circuit in figure 3.9b consists of one ideal operational amplifier, three resistors with resistances R^{N1}, R^{N2} and R^{N3} and one capacitor with capacitance C^{N4}. For ideal operational amplifiers, the negative capacitor circuit input impedance $Z^{\mathrm{N}}(\Omega)$ in frequency domain becomes

$$Z^{\mathrm{N}}(\Omega) = \frac{u^{\mathrm{N}}(\Omega)}{\dot{q}(\Omega)} = -\frac{R^{\mathrm{N2}}}{R^{\mathrm{N1}}} \frac{1}{j\Omega\, C^{\mathrm{N4}} + 1/R^{\mathrm{N3}}} \tag{3.86}$$

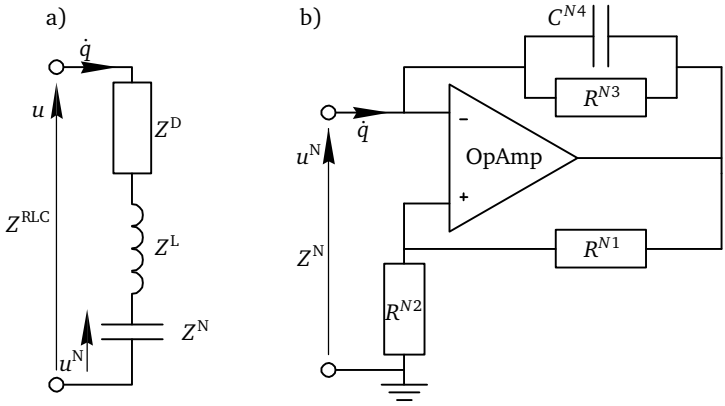

Figure 3.9: a) series RLC-shunt circuit, b) negative capacitor circuit layout

with shunt current $\dot{q}(\Omega)$ and negative capacitor voltage $u^{\mathrm{N}}(\Omega)$, [53]. With (3.86), the negative capacitance C^{n} of the circuit in figure 3.9b as needed for the RLC-shunt, see figure 2.1b, is obtained by

$$C^{\mathrm{n}}(\Omega) = \frac{-1}{\Omega\,\Im\{Z^{\mathrm{N}}(\Omega)\}} \tag{3.87}$$

with

$$\Im\{Z^{\mathrm{N}}(j\Omega)\} = \frac{R^{\mathrm{N2}}}{R^{\mathrm{N1}}}\frac{\Omega\,C^{\mathrm{N4}}(R^{\mathrm{N3}})^2}{1+(\Omega\,C^{\mathrm{N4}}R^{\mathrm{N3}})^2} \tag{3.88}$$

the imaginary part of the negative capacitor circuit impedance $Z^{\mathrm{N}}(j\Omega)$ (3.86). Equation (3.88) is substituted into (3.87) to obtain the negative capacitance

$$C^{\mathrm{n}}(\Omega) = -\frac{1}{\Omega}\frac{R^{\mathrm{N1}}}{R^{\mathrm{N2}}}\frac{1+(\Omega\,C^{\mathrm{N4}}R^{\mathrm{N3}})^2}{\Omega\,C^{\mathrm{N4}}(R^{\mathrm{N3}})^2}. \tag{3.89}$$

In the shunt optimization in section 3.5 and in the experimental RLC-shunt realization in section 4.1.3, the resistance R^{N1} is varied to adjust the negative capacitance value C^{n} in (3.89) and constant values are assigned to R^{N2}, R^{N3} and C^{N4}. Based on experimental observations, the authors in [53] suggest to chose the resistance of R^{N3} to be of several mega ohms to solve bias-current and offset-voltage issues. Furthermore, the authors in [53] and [83] suggest to chose the capacitance C^{N4}

close to the static transducer capacitance C^{s} (3.106). For big values of R^{N3} with $R^{\mathrm{N3}} \to \infty$, the negative capacitance from (3.89) simplifies to

$$C^{\mathrm{n}} = -\frac{R^{\mathrm{N1}}}{R^{\mathrm{N2}}} C^{\mathrm{N4}}. \tag{3.90}$$

RLC-shunt impedance model

For the vibration attenuation in y- and z-direction with transducers $\mathrm{P}_{y,\mathrm{B}}$ and $\mathrm{P}_{z,\mathrm{B}}$ connected to RLC-shunts, individual RLC-shunt impedance models

$$Z^{\mathrm{RLC}}_{y/z}(\Omega) = R^{\mathrm{D}}_{y/z} + j\Omega \frac{R^{\mathrm{L1}}_{y/z} R^{\mathrm{L3}}_{y/z} C^{\mathrm{L4}}_{y/z} R^{\mathrm{L5}}_{y/z}}{R^{\mathrm{L2}}_{y/z}} - \frac{R^{\mathrm{N2}}_{y/z}}{R^{\mathrm{N1}}_{y/z}} \frac{1}{j\Omega C^{\mathrm{N4}}_{y/z} + 1/R^{\mathrm{N3}}_{y/z}} \tag{3.91}$$

are received from (3.85) with $Z^{\mathrm{D}}(j\Omega)$ (3.77), $Z^{\mathrm{L}}(\Omega)$ (3.78) and $Z^{\mathrm{N}}(\Omega)$ (3.86) for individual damping resistances $R^{\mathrm{D}}_{y/z}$, inductor circuit resistances $R^{\mathrm{L1}}_{y/z}$, $R^{\mathrm{L2}}_{y/z}$, $R^{\mathrm{L3}}_{y/z}$, $R^{\mathrm{L5}}_{y/z}$ and capacitances $C^{\mathrm{L4}}_{y/z}$ and negative capacitor circuit resistances $R^{\mathrm{N1}}_{y/z}$, $R^{\mathrm{N2}}_{y/z}$ and $R^{\mathrm{N3}}_{y/z}$ and capacitances $C^{\mathrm{N4}}_{y/z}$. The RLC-shunt impedance models $Z^{\mathrm{RLC}}_{y/z}(\Omega)$ are summarized in the RLC-shunt transfer function matrix

$$\boldsymbol{G}^{\mathrm{RLC}}(\Omega) = \begin{bmatrix} Z^{\mathrm{RLC}}_{y}(\Omega) & 0 \\ 0 & Z^{\mathrm{RLC}}_{z}(\Omega) \end{bmatrix}^{-1}. \tag{3.92}$$

$\boldsymbol{G}^{\mathrm{RLC}}(\Omega)$ is mathematically connected to the open-loop beam-column transfer functions in section 3.4.3.

3.4.3 Frequency transfer functions with shunted transducers

For vibration attenuation simulation and numerical shunt tuning, shunted beam-column transfer functions with transducers $\mathrm{P}_{y,\mathrm{B}}$ and $\mathrm{P}_{z,\mathrm{B}}$ in support B connected to RL- or RLC-shunts are obtained by connecting the electrical inputs and outputs of the open-loop transfer functions $\boldsymbol{G}_{\mathrm{ru}}(\Omega)$, $\boldsymbol{G}_{\mathrm{r\dot{q}}}(\Omega)$, $\boldsymbol{G}_{\mathrm{uu}}(\Omega)$ and $\boldsymbol{G}_{\mathrm{u\dot{q}}}(\Omega)$ (3.70) to the general shunt (sh) transfer function $\boldsymbol{G}_{\mathrm{sh}}(\Omega)$ as shown in figure 3.10 with $\boldsymbol{G}_{\mathrm{sh}}(\Omega) = \boldsymbol{G}^{\mathrm{RL}}(\Omega)$ (3.84) for RL-shunts and $\boldsymbol{G}_{\mathrm{sh}}(\Omega) = \boldsymbol{G}^{\mathrm{RLC}}(\Omega)$ (3.92) for RLC-shunts.

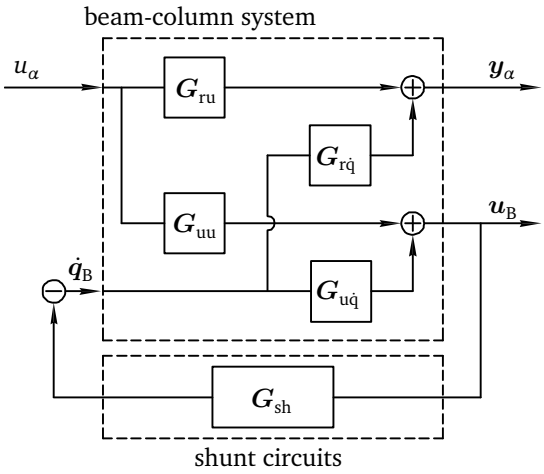

Figure 3.10: Block diagram of the beam-column system with transducers $\mathrm{P}_{y,\mathrm{B}}$ and $\mathrm{P}_{z,\mathrm{B}}$ in support B connected to shunt circuits

According to figure 3.10, the frequency transfer functions

$$\frac{\boldsymbol{y}_\alpha(\Omega)}{u_\alpha(\Omega)} = \boldsymbol{G}_{\mathrm{ru}}(\Omega) - \boldsymbol{G}_{\mathrm{r\dot{q}}}(\Omega)\,\boldsymbol{G}_{\mathrm{sh}}(\Omega)\left[\mathbf{I} + \boldsymbol{G}_{\mathrm{u\dot{q}}}(\Omega)\,\boldsymbol{G}_{\mathrm{sh}}(\Omega)\right]^{-1}\boldsymbol{G}_{\mathrm{uu}}(\Omega) \tag{3.93}$$

relate the excitation voltage $u_\alpha(\Omega)$ to the beam-column displacements $\boldsymbol{y}_\alpha(\Omega)$ when shunts $\boldsymbol{G}_{\mathrm{sh}}(\Omega)$ are connected. The shunted acceleration transfer functions with transducers connected to RL- and RLC-shunts as needed for comparison with experimental results in chapters 5 and 6 are obtained by multiplication of (3.93) with $-\Omega^2$ and substitution of $\boldsymbol{G}_{\mathrm{sh}}(\Omega)$ in (3.93) by $\boldsymbol{G}^{\mathrm{RL}}(\Omega)$ (3.84) or $\boldsymbol{G}^{\mathrm{RLC}}(\Omega)$ (3.92). The acceleration frequency transfer functions in and orthogonal to the direction of excitation of $\ddot{\boldsymbol{y}}_\alpha(\Omega)$ (3.38) with RL-shunts and RLC-shunts are

$$\left[G_\alpha^{\mathrm{RL}}(\Omega) \quad G_{\alpha^\perp}^{\mathrm{RL}}(\Omega)\right]^{\mathrm{T}} = -\Omega^2 \frac{\boldsymbol{y}_\alpha^{\mathrm{RL}}(\Omega)}{u_\alpha(\Omega)} \tag{3.94}$$

and

$$\left[G_\alpha^{\mathrm{RLC}}(\Omega) \quad G_{\alpha^\perp}^{\mathrm{RLC}}(\Omega)\right]^{\mathrm{T}} = -\Omega^2 \frac{\boldsymbol{y}_\alpha^{\mathrm{RLC}}(\Omega)}{u_\alpha(\Omega)}. \tag{3.95}$$

3.5 Numerical RL- and RLC-shunt tuning procedure

For optimal vibration attenuation with resonant shunts, the shunt parameter values must be optimally tuned to the resonance behavior of the host structure, section 2.2.1. In this work, the RL- and RLC-shunts in figures 3.8a and 3.9a have been connected to the transducers $\mathrm{P}_{y,\mathrm{B}}$ and $\mathrm{P}_{z,\mathrm{B}}$, figure 3.2, in section 3.4. In this section, the shunts are tuned numerically to achieve optimal vibration attenuation of the first lateral beam-column resonance of the axially unloaded beam-column with $F_x = 0\,\mathrm{N}$. Optimally tuned shunts are used in chapter 5 to quantify the vibration attenuation potential of the piezo-elastic support with shunted transducers when no uncertainty is taken into account, and serve as reference in chapter 6 to evaluate probabilistic and non-probabilistic uncertainty, defined in section 2.3.1, in the vibration attenuation due to static load, manufacturing and system assembly variations.

Shunt tuning approach

In this work, shunts connected to transducer $\mathrm{P}_{y,\mathrm{B}}$ are tuned to optimally attenuate beam-column vibrations in y-direction when excitation is applied at $\alpha = 0^\circ$ and shunts connected to transducer $\mathrm{P}_{z,\mathrm{B}}$ are tuned to optimally attenuate vibrations in z-direction when excitation is applied at $\alpha = 90^\circ$. This also leads to appropriate vibration attenuation in y_α- and z_α-direction of the tilted coordinate system, introduced in section 3.2, when the beam-column is excited at an oblique angle with $\alpha \neq 0^\circ$ and $\alpha \neq 90^\circ$, as shown in chapter 5. Optimal values of the adjustable RL- and RLC-shunt resistances, which tune the shunts for optimal vibration attenuation of the beam-column in y- and z-direction, are obtained by minimizing the peak gains $\widehat{G}_\alpha^{\mathrm{RL}}$ and $\widehat{G}_\alpha^{\mathrm{RLC}}$, introduced in figure 2.2, of the first mode of the acceleration transfer functions in the direction of excitation with RL-shunts $G_\alpha^{\mathrm{RL}}(\Omega)$ (3.94) and with RLC-shunts $G_\alpha^{\mathrm{RLC}}(\Omega)$ (3.95) in a numerical optimization routine.

3.5.1 RL-shunt tuning

For transducer $\mathrm{P}_{y,\mathrm{B}}$ connected to the RL-shunt with adjustable resistances R_y^{D} and R_y^{L1}, section 3.4.1, the peak gain of the first lateral beam-column mode is calculated by

$$\widehat{G}_\alpha^{\mathrm{RL}} = ||G_\alpha^{\mathrm{RL}}(\Omega)\, G_{\mathrm{LP}}(\Omega)||_\infty. \tag{3.96}$$

In (3.96), the peak gain $\widehat{G}_\alpha^{\mathrm{RL}}$ corresponds to the $\mathscr{H}_\infty$-norm, [88], of the acceleration frequency transfer function $G_\alpha^{\mathrm{RL}}(\Omega)$ (3.94) multiplied by the filter transfer function $G_{\mathrm{LP}}(\Omega)$ of an 8^{th} order BUTTERWORTH lowpass filter. The filter transfer function $G_{\mathrm{LP}}(\Omega)$ ensures that the peak gain $\widehat{G}_\alpha^{\mathrm{RL}}$ always corresponds to vibrations of the first mode by reducing the vibration of higher modes in the tuning procedure. The example of the filtered amplitude response $|G_\alpha^{\mathrm{RL}}(\Omega)G_{\mathrm{LP}}(\Omega)|$ in figure 3.11, red line, shows that, due to the filter $G_{\mathrm{LP}}(\Omega)$, vibrations of the second and the third mode are reduced compared to the unfiltered amplitude response of $G_\alpha^{\mathrm{sc}}(\Omega)$, black line.

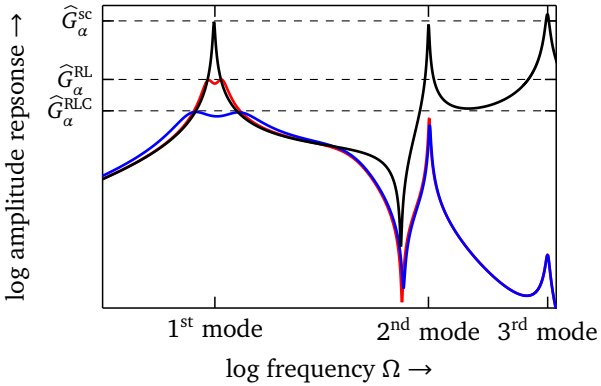

Figure 3.11: Amplitude responses for demonstration of shunt tuning procedure:
with RL-shunt and filtered $|G_\alpha^{\mathrm{RL}}(\Omega)G_{\mathrm{LP}}(\Omega)|$ (——),
with RLC-shunt and filtered $|G_\alpha^{\mathrm{RLC}}(\Omega)G_{\mathrm{LP}}(\Omega)|$ (——),
short circuited and not filtered $|G_\alpha^{\mathrm{sc}}(\Omega)|$ (——)

With (3.96), the optimal RL-shunt resistances R_y^{D} and R_y^{L1} that achieve maximum vibration attenuation of the first vibration mode, figure 3.11, are calculated by solving the optimization problem

$$\min_{R_y^{\mathrm{D}},R_y^{\mathrm{L1}}} \quad ||G_\alpha^{\mathrm{RL}}(\Omega)\, G_{\mathrm{LP}}(\Omega)||_\infty. \tag{3.97}$$

The solution of (3.97) is calculated by using the *fmincon* algorithm in MATLAB. The calculation of the optimal resistances R_z^{D} and R_z^{L1} of the RL-shunt connected to transducer $\mathrm{P}_{z,\mathrm{B}}$ is performed analog to transducer $\mathrm{P}_{y,\mathrm{B}}$.

3.5.2 RLC-shunt tuning

For transducer $\mathrm{P}_{y,\mathrm{B}}$ connected to the RLC-shunt with adjustable resistances R_y^{D}, R_y^{L1} and R_y^{N1}, section 3.4.2, the peak gain of the first lateral beam-column mode is calculated analog to the RL-shunt by

$$\widehat{G}_\alpha^{\mathrm{RLC}} = ||G_\alpha^{\mathrm{RLC}}(\Omega)\, G_{\mathrm{LP}}(\Omega)||_\infty. \tag{3.98}$$

Again, the filter transfer function $G_{\mathrm{LP}}(\Omega)$ ensures that the peak gain $\widehat{G}_\alpha^{\mathrm{RLC}}$ corresponds to the vibration of the first mode, blue line in figure 3.11. With (3.98), the optimal RLC-shunt resistances R_y^{D}, R_y^{L1} and R_y^{N1} that achieve maximum vibration attenuation of the first vibration mode, figure 3.11, are calculated by solving the optimization problem

$$\min_{R_y^{\mathrm{D}}, R_y^{\mathrm{L1}}, R_y^{\mathrm{N1}}} \quad ||G_\alpha^{\mathrm{RLC}}(j\Omega)\, G_{\mathrm{LP}}(j\Omega)||_\infty. \tag{3.99}$$

As introduced in section 2.2.1, when tuned incorrectly, the negative capacitance behavior of the circuit in figure 3.9 b may destabilize the lateral beam-column vibration attenuation with RLC-shunt. Therefore, a stability limit for the negative capacitance C^{n} (3.90) is considered in the optimization (3.99). To derive the stability of C^{n}, the authors in [53] analyze the stability of the equivalent proportional feedback controller of a transducer connected to a negative capacitance. By neglecting the damping resistance R^{D} and the inductor circuit impedance $Z^{\mathrm{L}}(\Omega)$, which are assumed to not influence the stability, in the RLC-shunt, the equivalent proportional feedback controller of transducer $\mathrm{P}_{y,\mathrm{B}}$ becomes

$$T(\Omega) = \frac{j\Omega\, C^{\mathrm{s}}\, Z^{\mathrm{N}}(\Omega)}{1 + j\Omega\, C^{\mathrm{s}}\, Z^{\mathrm{N}}(\Omega)} \tag{3.100}$$

with the static transducer capacitance C^{s} (3.106) shunted to the negative capacitor circuit impedance $Z^{\mathrm{N}}(\Omega)$ (3.86), [53]. For $T(\Omega)$, stability and limited feedback gain are guaranteed in case of a negative real part $\Re\{T(\Omega)\} < 0$. According to [53], this is given if the imaginary part $\Im\{Z^{\mathrm{N}}(j\Omega)\}$ (3.88) of the negative capacitor circuit impedance satisfies

$$0 < \Im\{Z^{\mathrm{N}}(j\Omega)\} < \frac{1}{\Omega\, C^{\mathrm{s}}}. \tag{3.101}$$

For high values of R^{N3} with $R^{\mathrm{N3}} \to \infty$, as already discussed for the negative capacitor circuit in section 3.4.2, (3.101) simplifies to

$$0 < \frac{R^{\mathrm{N2}}}{R^{\mathrm{N1}}} \frac{1}{C^{\mathrm{N4}}} < \frac{1}{C^{\mathrm{s}}} \quad \text{with} \quad -\frac{1}{C^{\mathrm{n}}} = \frac{R^{\mathrm{N2}}}{R^{\mathrm{N1}}} \frac{1}{C^{\mathrm{N4}}}. \tag{3.102}$$

Regarding the stability analysis of shunts with negative capacitance, the negative capacitance ratio

$$\delta = \frac{C^{\mathrm{s}}}{C^{\mathrm{n}}} \tag{3.103}$$

is often used, [55, 65], by which the stability analysis is reduced to the ratio of the static transducer capacitance C^{s} (3.106) and the negative capacitance C^{n} (3.90). With (3.103) and C^{n} from (3.90), (3.102) is rewritten to

$$-1 < \delta < 0. \tag{3.104}$$

According to [55], however, in real applications the stability limit is usually reached before the theoretical stability limit $\delta_{\mathrm{crit}} = -1$, e.g. due to model inaccuracies. Therefore, and for all further analysis of vibration attenuation with RLC-shunts in this work, the stability limit is given for $\delta_{\mathrm{crit}} = -0.95$.

The calculation of the optimal resistances R_z^{D}, R_z^{L1} and R_z^{N1} of the RLC-shunt connected to transducer $\mathrm{P}_{z,\mathrm{B}}$ is performed analog to transducer $\mathrm{P}_{y,\mathrm{B}}$.

3.6 Transfer functions and characteristic quantities of the beam-column system's dynamic behavior

For all simulations and measurements in this work, the beam-column system in figure 3.2 is generally distinguished in the states without and with RL- or RLC-shunts connected to transducers in support B. This section summarizes the respective transfer functions and characteristic quantities that are used for model validation and uncertainty discussion in chapters 5 and 6.

No shunts connected to transducers in support B

Short circuited acceleration transfer functions: The beam-column acceleration transfer functions in direction of excitation $G_{\alpha}^{\mathrm{sc}}(\Omega)$ and orthogonal to direction of

excitation $G^{sc}_{\alpha^\perp}(\Omega)$ (3.75) describe the beam-column vibration without vibration attenuation through shunts. The peak gains $\widehat{G}^{sc}_{\alpha}$ and $\widehat{G}^{sc}_{\alpha^\perp}$ of the acceleration transfer functions $G^{sc}_{\alpha}(\Omega)$ and $G^{sc}_{\alpha^\perp}(\Omega)$, see figure 3.11, and the short circuited resonance frequencies $\omega^{sc}_{y/z}$ (3.50) represent the characteristic quantities used to quantify the vibration of the first beam-column lateral vibration mode with short circuited transducers in support B.

Capacitance transfer functions: The transducer impedance transfer functions $\boldsymbol{G}_{u\dot{q}}(\Omega)$ (3.73) describe the electric dynamic transducer behavior. As introduced in section 3.3.3, piezoelectric stack transducers electrically behave like capacitances and its behavior must be known exactly to tune shunts. With the transducer impedance transfer functions $\boldsymbol{G}_{u\dot{q}}(\Omega)$ (3.73), the transducer capacitance transfer functions

$$Y_y(\Omega) = \frac{1}{j\Omega}\frac{\dot{q}_{y,B}(\Omega)}{u_{y,B}(\Omega)} \quad \text{and} \quad Y_z(\Omega) = \frac{1}{j\Omega}\frac{\dot{q}_{z,B}(\Omega)}{u_{z,B}(\Omega)} \tag{3.105}$$

of the transducer $P_{y,B}$ and $P_{z,B}$ are derived, which contain information about the inherent transducer capacitance and the GEMCC, [55].

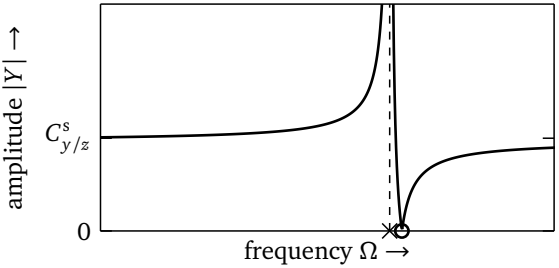

Figure 3.12: Qualitative amplitude response of dynamic transducer capacitance $|Y_{y/z}(\Omega)|$: short circuited resonance frequency $\omega^{sc}_{y/z}$ (×), open circuited resonance frequency $\omega^{sc}_{y/z}$ (∘), static transducer capacitance $C^s_{y/z}$

Figure 3.12 qualitatively shows the amplitude response $|Y_{y/z}(\Omega)|$ of the dynamic transducer capacitance that exhibits one pole and one zero, which correspond to the short circuited (3.50) and open circuited (3.52) resonance frequencies. Their difference affects the GEMCCs $\gamma_{y/z}$ (3.53). For $\Omega \to 0$, the amplitude response converges to the static transducer capacitance $|Y_{y/z}(0)| = C^s_{y/z}$. In the numerical calculation, the static capacitances of transducers $P_{y,B}$ and $P_{z,B}$

$$C^s_y = |Y_y(\Omega \to 0)| \quad \text{and} \quad C^s_z = |Y_z(\Omega \to 0)| \tag{3.106}$$

are obtained from the dynamic capacitance functions for quasi-static excitation $\Omega = 0.01\,\mathrm{rad/s}$. The GEMCC $\gamma_{y/z}$ and the static capacitance $C^{\mathrm{s}}_{y/z}$ of transducer $\mathrm{P}_{y,\mathrm{B}}$ and $\mathrm{P}_{z,\mathrm{B}}$ represent the characteristic quantities of the dynamic transducer behavior. Hence, by calibration of $Y_{y/z}(\Omega)$, section 4.3.5, all important transducer properties can be adjusted for the model.

RL- and RLC-shunts connected to transducers in support B

Acceleration transfer functions with RL-shunts: The beam-column acceleration transfer functions $G^{\mathrm{RL}}_{\alpha}(\Omega)$ and $G^{\mathrm{RL}}_{\alpha^{\perp}}(\Omega)$ (3.94) describe the attenuated beam-column vibration with transducers in support B connected to RL-shunts, figure 3.8. The peak gains $\widehat{G}^{\mathrm{RL}}_{\alpha}$ and $\widehat{G}^{\mathrm{RL}}_{\alpha^{\perp}}$ of the acceleration transfer functions $G^{\mathrm{RL}}_{\alpha}(\Omega)$ and $G^{\mathrm{RL}}_{\alpha^{\perp}}(\Omega)$ represent the characteristic quantities used to quantify the attenuated vibration of the first beam-column lateral vibration mode with RL-shunts.

Acceleration transfer functions with RLC-shunts: The beam-column acceleration transfer functions $G^{\mathrm{RLC}}_{\alpha}(\Omega)$ and $G^{\mathrm{RLC}}_{\alpha^{\perp}}(\Omega)$ (3.95) describe the attenuated beam-column vibration with transducers in support B connected to RLC-shunts, figure 3.9. The peak gains $\widehat{G}^{\mathrm{RLC}}_{\alpha}$ and $\widehat{G}^{\mathrm{RLC}}_{\alpha^{\perp}}$ of the acceleration transfer functions $G^{\mathrm{RLC}}_{\alpha}(\Omega)$ and $G^{\mathrm{RLC}}_{\alpha^{\perp}}(\Omega)$ represent the characteristic quantities used to quantify the attenuated vibration of the first beam-column lateral vibration mode with RLC-shunts.

All characteristic quantities of the beam-column system without and with shunts are summarized in table 3.1.

Table 3.1: Characteristic quantities of the dynamic beam-column system without and with shunts used for model validation and uncertainty discussion in chapters 5 and 6

case	description		
without shunt	short circuited resonance frequency	ω^{sc}_{y}	ω^{sc}_{z}
	GEMCC	γ_{y}	γ_{z}
	static transducer capacitance	C^{s}_{y}	C^{s}_{z}
	short circuited peak gain	$\widehat{G}^{\mathrm{sc}}_{\alpha}$	$\widehat{G}^{\mathrm{sc}}_{\alpha^{\perp}}$
with shunt	peak gain with RL-shunt	$\widehat{G}^{\mathrm{RL}}_{\alpha}$	$\widehat{G}^{\mathrm{RL}}_{\alpha^{\perp}}$
	peak gain with RLC-shunt	$\widehat{G}^{\mathrm{RLC}}_{\alpha}$	$\widehat{G}^{\mathrm{RLC}}_{\alpha^{\perp}}$

4 Experimental test setup

This chapter presents the experimental realization of the beam-column system introduced in section 3.2 and the experimental realizations of the RL-shunt and the RLC-shunt introduced in sections 3.4.1 and 3.4.2. The data acquisition and processing is shown and the determination of the experimental beam-column system's dynamic behavior with and without shunts is explained.

4.1 Experimental realization

In sections 4.1.1 and 4.1.2, the experimental beam-column test setup is shown and the realization of the piezo-elastic supports used for vibration excitation and vibration attenuation with all relevant components is explained. Section 4.1.3 presents the electrical shunt board of the electrical RL- and RLC-shunt circuits.

4.1.1 Beam-column with piezo-elastic supports

The experimental test setup in figure 4.1 implements experimentally the concept introduced in section 3.2 of the axially loaded beam-column with circular cross-section embedded in the two piezo-elastic supports A and B. Table 4.1 summarizes the numbering, quantity and properties of all relevant components and sensors used in the test setup. The experimental test setup is used to experimentally investigate the vibration attenuation potential of transducers in piezo-elastic support B connected to RL- or RLC-shunts, chapter 5. Furthermore, it is used to quantify the effects of a static tensile or compressive force, and the effects of manufacturing and system assembly variations on vibrations with and without shunts, chapter 6.

In figure 4.1, the beam-column (1) is embedded in the piezo-elastic supports A and B. Support A is attached to a parallel guidance boundary (2) while support B is connected to a fixed boundary (3). To apply a static axial compressive or tensile force F_x on the beam-column, a spindle-type lifting gear with electronic step drive (4) is connected to the parallel guidance boundary (2). Via controlled step drive, the applied axial force F_x is kept at a constant force value, which is measured by the

force sensor (5). Lateral beam-column accelerations $a_y(t)$ and $a_z(t)$ in y- and z-direction at the sensor position x_s in figure 3.2 are measured with two piezoelectric accelerometers (6).

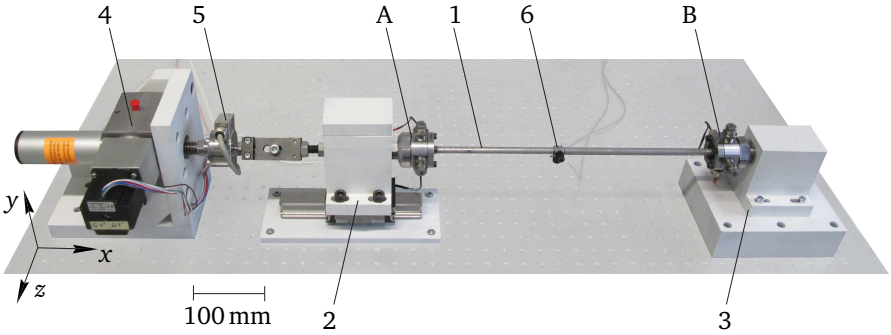

Figure 4.1: Experimental test setup of the beam-column system

Table 4.1: Numbering, quantity and properties of all relevant components and sensors of the test setup of the experimental beam-column system

no.	quant.	description, nominal value, material
1	1	beam-column, rod aluminum alloy 7075, DIN EN 754-3, nominal length $l_b = 400\,\text{mm}$, nominal radius $r_b = 5\,\text{mm}$
2	1	parallel guidance boundary, steel 1.0037
3	1	fixed bounary, steel 1.0037
4	1	spindle-type lifting gear STROSS *SJ5* with step drive NEMA *ST5918M2008*
5	1	strain gauge force sensor HBM *U2B-T*, measure. range ±2000 N, sensitivity 5 mV/N
6	2	piezoelectric accelerometers IDS *KS95B.100*, sensitivity 100 mV/g, measure. range ±60 g, resolution 0.0003 g ($1\,\text{g} = 9.81\,\text{m/s}^2$)
A	1	piezo-elastic support A
B	1	piezo-elastic support B
B1	1	support housing, steel 1.4305
B2	1	clamp, steel 1.4305
B3	1	retainer nut, steel 1.4305
B4	1	connector, steel 1.4305
B5	2	multilayer stack transducer, PI *P-885.51*; housing, steel 1.4305
B6	2	helical disc spring, $k_{pre} = 180\,\text{N/mm}$; housing, steel 1.4305
B7	1	axial extension, hardened steel 1.2312
B8	1	membrane-like spring element, spring steel 1.1248, sheet thickness 0.5 mm, nominal height $h = 2.3\,\text{mm}$, nominal diameter $d = 44\,\text{mm}$

4.1.2 Piezo-elastic support

The piezo-elastic support A is used for lateral beam-column vibration excitation and the support B is used for lateral vibration attenuation, as formerly introduced in section 3.2. However, both piezo-elastic supports A and B are designed according to the concept in [16] and have the same structural components.

Components

Figure 4.2 shows a cutaway view of the CAD model of the piezo-elastic support B and its experimental realization. The piezo-elastic support components are the support housing (B1), the clamp (B2), the retainer nut (B3), the connector part (B4), the piezoelectric transducers contained in relatively stiff housings (B5), the helical disc springs also contained in relatively stiff housings (B6), the axial extension (B7) and the membrane-like spring element (B8). The support housing (B1) with the clamp (B2) holds the membrane-like spring element with four M5 bolts. The retainer nut (B3) connects the support housing with the connector part (B4) that, in turn, is attached to the boundary. The transducers (B5) are prestressed by helical disc springs (B6) for dynamic load operation. The beam-column (1) and the axial extension (B7) are fixed to the center of the membrane-like spring element (B8) via an M5 bolt.

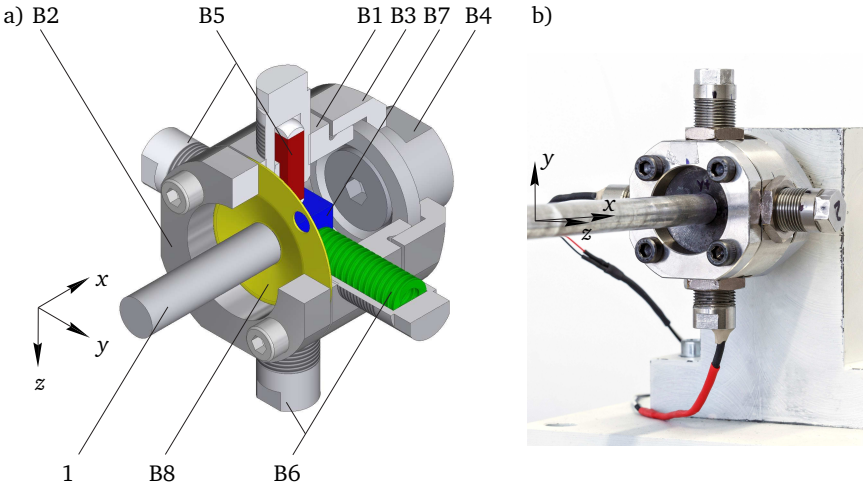

Figure 4.2: Piezo-elastic support B, a) CAD model cutaway view, b) realization

Design

In order to achieve a sufficiently high GEMCC (3.53) of the transducers in the piezo-elastic support as needed for vibration attenuation with shunts, figure 2.2, the stiffness properties of the membrane-like spring element and the length of the axial extension l_{ext}, see figure 3.2, should be adjusted, as thoroughly investigated in an earlier own study [24].

To positively affect the GEMCC of the transducers in the piezo-elastic supports, the rotational stiffness $k_{\varphi_{y/z}}$ and the lateral stiffness $k_{y/z}$, see figure 3.2, of the membrane-like spring element when clamped in the support housing must be relatively low for rotational deformation and relatively high for lateral deformation. Likewise, the axial stiffness of the membrane-like spring element must be relatively high in order to prevent changes in the GEMCC in consequence to changes of the axial extension length l_{ext} when a static axial load is applied in x-direction to the beam-column system, see figure 4.4.

Figure 4.3 shows a detailed view of the membrane-like spring element as used in the piezo-elastic supports A and B with truncated cone-shape design and truncated cone height h, which is the result of a numerical optimization of the GEMCC performed in [100].

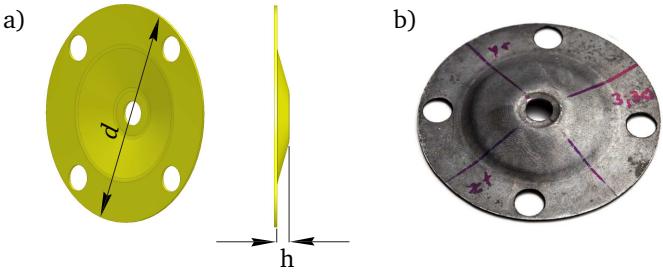

Figure 4.3: Membrane-like spring element, a) CAD model, b) realization

As shown in figure 4.4, the length of the axial extension l_{ext} is equal to the distance between the points T and P in x-direction, and depends on the membrane-like spring element height h. The point T represents the end of the beam-column, location $x = l_{\text{b}}$ in figure 3.2, and the point P represents the location where the transducers are connected to the axial extension, location $x = l_{\text{b}} + l_{\text{ext}}$ in figure 3.2. The axial extension length is calculated by

$$l_{\text{ext}} = 9\,\text{mm} - h \tag{4.1}$$

with the fixed distance between P and the spring element clamping in x-direction, which is equal to 9 mm.

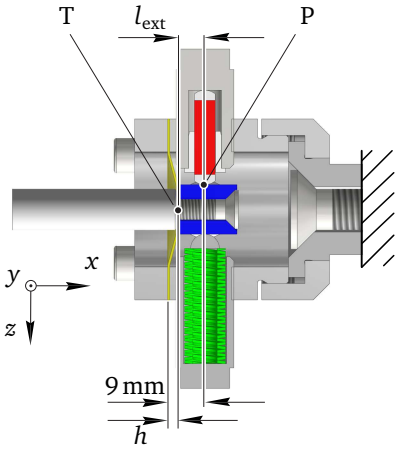

Figure 4.4: Piezo-elastic support B, CAD model cross-section

Membrane-like spring element manufacturing

The membrane-like spring element is manufactured by a single point incremental forming (SPIF) process performed with a multi-technology machine 3D Servo Press as part of the cooperation in the SFB 805, [29, 37]. During a SPIF process, an evenly clamped sheet metal is being formed along a tool path by a forming tool, which makes it suitable for the production of truncated cone components such as the membrane-like spring element. However, the forming process is subject to variations in the process forces and displacements that lead to variations in the membrane-like spring element geometry. Variations in the membrane-like spring element geometry affect the lateral and rotational support stiffness $k_{\varphi_{y/z}}$ and $k_{y/z}$ as well as the height h, as observed in own stiffness and geometry measurements shown in figure 4.5. The stiffness values in figure 4.5 are obtained from static measurements performed on a material testing machine as described in [26] and the values of h are obtained on a precision coordinate measurement machine.

System assembly sequence

The assembly sequence depicted in figure 4.6 is applied to assemble supports A and B. Therefore, the sequence is only explained for support B. In step (I), the spring element is mounted with the clamp to the support housing with the four

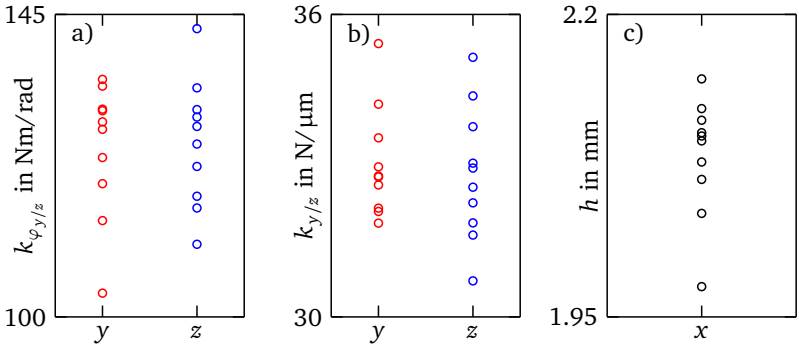

Figure 4.5: Experimental variations of 10 membrane-like spring elements a) rotational stiffness $k_{\varphi_{y/z}}$, b) lateral stiffness $k_{y/z}$, c) height h

bolts crosswise tightened with 6 Nm. In step (II), the beam-column is attached to the spring element and the axial extension by the bolt tightened with 5 Nm. In step (III), the retainer nut is fastened by hand to connect the support to the boundary. In step (IV), the transducers contained in separate housings are fastened by hand until they touch the axial extension. They are preloaded alternating by turning the housings of the helical disc springs up to two full turnings by hand. The effects of spring element manufacturing and system assembly variations on the beam-column vibration attenuation caused by the presented manufacturing process and assembly sequence are discussed in chapter 6.

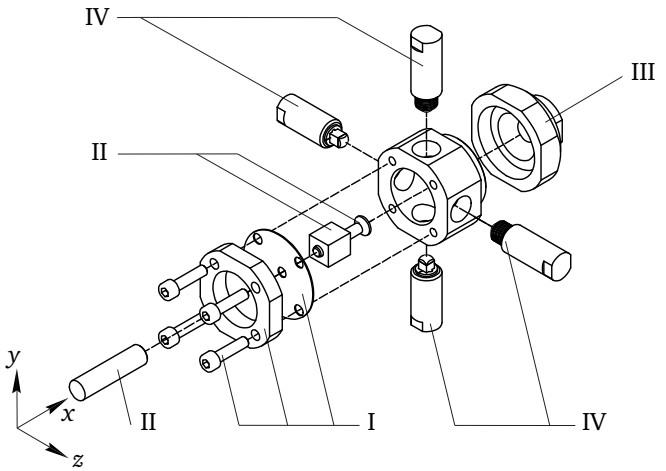

Figure 4.6: Assembly sequence of beam-column and piezo-elastic support

4.1.3 RL- and RLC-shunt circuits

For experimental vibration attenuation with RL- and RLC-shunts in chapters 5 and 6, each of the transducers $P_{y,B}$ and $P_{z,B}$ in support B in figure 4.2 is connected to an electrical shunt circuit board, which is shown in figure 4.7. On the shunt circuit board, the series RL-shunt circuit in figure 3.8a and the series RLC-shunt in figure 3.9a by using the inductor circtuit in figure 3.8b and the negative capacitor circuit in figure 3.9b are implemented.

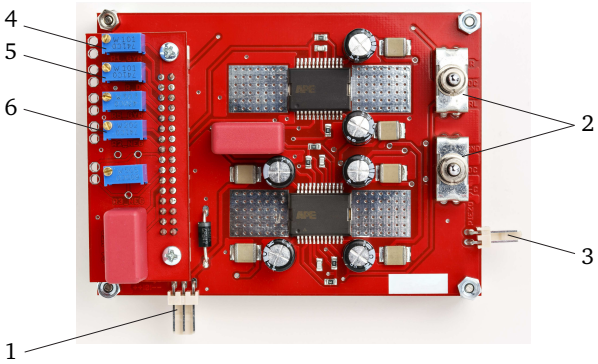

Figure 4.7: Electrical shunt circuit board of the RL- and RLC-shunt

The shunt circuit board is operated with a symmetric direct current voltage supply at ±30 V connected to (1) as needed for the supply of the operational amplifiers. The switches (2) are used to select between the RL- and the RLC-shunt, which is connected to the transducer via the connector (3). As formerly introduced in sections 3.4.1 and 3.4.2, the RL- and the RLC-shunt have adjustable and constant circuit components. On the shunt circuit board in figure 4.7, the damping resistance R^{D} (4), the inductor circuit resistance R^{L1} (5) and the negative capacitor circuit resistance R^{N1} (6) are realized by potentiometers and used to adjust the tuning of the RL- and RLC-shunt.

Table 4.2: Inductor circuit constant resistor and capacitor values used in experimental and numerical RL- and RLC-shunts with transducers $P_{y,B}$ and $P_{z,B}$.

Transducer	R^{L2} in Ohm	R^{L3} in Ohm	R^{L5} in Ohm	C^{L4} in µF
$P_{y,B}$	1000	1000	20064	1.04
$P_{z,B}$	1000	1000	20083	1.00

Table 4.3: Negative capacitor circuit constant resistor and capacitor values used in experimental and numerical RLC-shunts with transducers $\mathrm{P}_{y,\mathrm{B}}$ and $\mathrm{P}_{z,\mathrm{B}}$.

Transducer	R^{N2} in Ohm	R^{N3} in Ohm	C^{N4} in µF
$\mathrm{P}_{y,\mathrm{B}}$	1000	994000	1.54
$\mathrm{P}_{z,\mathrm{B}}$	1000	993200	1.54

The constant inductor circuit and negative capacitor circuit resistances and capacitances are summarized in tables 4.2 and 4.3. The values were chosen to receive equal and limited operational amplifier output voltages and to solve bias-current and offset-voltage issues as discussed in sections 3.4.1 and 3.4.2.

4.2 Measurement setup and data acquisition

Two different measurement setups are used to measure the experimental dynamic behavior of the beam-column system in figure 4.1 without and with shunts. The beam-column vibration measurement setup is used to measure the beam-column accelerations due to excitation via transducers in support A without and with shunts in order to calculate experimental beam-column acceleration transfer functions, section 4.3.1. The transducer impedance measurement setup is used to measure the electrical impedances of the transducers in support B in order to derive experimental transducer capacitance transfer functions, section 4.3.2.

4.2.1 Beam-column vibration measurement setup

The beam-column vibration measurement setup is shown in figure 4.8. The vibration excitation voltage signals $u_{y,\mathrm{A}}(t)$ and $u_{z,\mathrm{A}}(t)$ are applied to the transducers in support A in figure 4.1 in order to excite the beam-column to vibrate laterally in the y-z-plane, section 3.3.4. For vibration excitation, band-limited white noise signals are used. The lateral beam-column vibration response accelerations $a_y(t)$ and $a_z(t)$ at the sensor position in y- and z-direction are measured by two accelerometers, figure 4.1.

For signal generation and acquisition, a dSPACE *MicroLabBox* real-time platform connected to a PC is used. The platform output excitation signals are lowpass filtered for signal reconstruction and amplified by a factor of 10 via a PI *E-663.00*

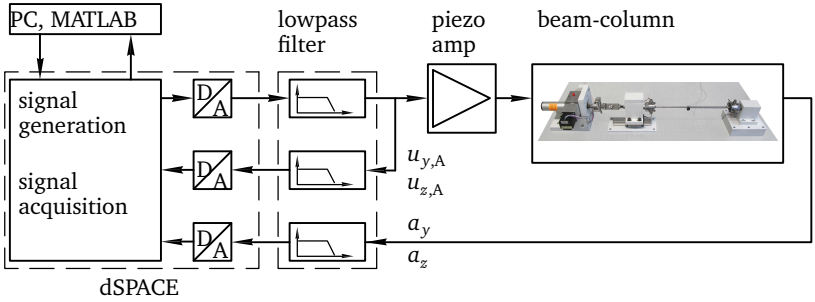

Figure 4.8: Beam-column vibration measurement setup to apply and to measure vibration excitation signals $u_{y,A}(t)$ and $u_{z,A}(t)$ and response acceleration signals $a_y(t)$ and $a_z(t)$

piezo amplifier before being applied to the transducers in support A. The platform input measurement excitation and response signals are lowpass filtered to avoid aliasing and amplified by filter integrated measurement amplifiers.

The dSPACE *MicroLabBox* features analog inputs and outputs with ±10 V in- and output voltage range and 16-bit A/D- and D/A-converters. A sampling rate of $f_s = 5000$ Hz is used. KEMO *BenchMaster 21M* 6-pole elliptic lowpass filters with cutoff frequency $f_c = 1500$ Hz are used. MATLAB has been used to control the dSPACE *MicroLabBox*, and to perform the measurement data acquisition and processing in.

The force sensor in figure 4.1 measures the applied static tensile or compressive beam-column force F_x. The force signal is filtered and processed by a PEEKELPICAS strain gauge amplifier and also recorded with the dSPACE but not shown in figure 4.8.

4.2.2 Transducer impedance measurement setup

The transducer impedance measurement is performed separately and analogously for the transducers $P_{y,B}$ and $P_{z,B}$ connected to the beam-column in support B in figure 4.1. Figure 4.9 shows the used measurement setup.

The electrical impedance of transducer $P_{y,B}$ is given by the relation $Z_{y,B}(t) = u_{y,B}(t)/\dot{q}(t)_{y,B}$ (3.73). Since voltage measurements are easier to perform than current measurements, the excitation voltage signal $u_{y,B}(t)$, a band-limited white noise signal, is applied to the transducer and the response voltage signal $u_Z(t)$

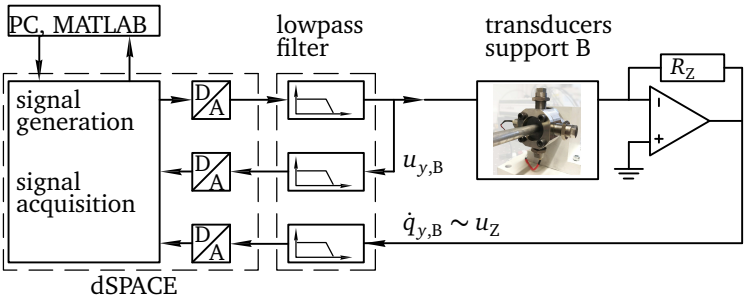

Figure 4.9: Transducer impedance measurement setup to apply and to measure the impedance measurement excitation signal $u_{y,B}(t)$ and the impedance response signal $\dot{q}_{y,B}(t)$

is measured by using the operational amplifier circuit in figure 4.9, as proposed in [47]. The response voltage signal $u_Z(t)$ is directly proportional to the current $\dot{q}_{y,B}(t)$ scaled by the feedback resistance R_Z with

$$u_Z(t) = R_Z \, \dot{q}_{y,B}(t) \tag{4.2}$$

with $R_Z = 695\,\Omega$hm used in the measurement setup. The measured voltage signals $u_{y,B}(t)$ and $u_Z(t)$ are used to derive the impedance according to

$$Z_{y,B}(t) = -\frac{u_{y,B}(t)}{u_Z(t)} R_Z. \tag{4.3}$$

Again, the dSPACE *MicroLabBox* real-time platform and the filters described in section 4.2.1 are used. For the transducer impedance measurement, all real-time platform output and input signals are lowpass filtered with cutoff frequency $f_c = 300\,$Hz. The same measurement is performed for the transducer $P_{z,B}$ to obtain its impedance $Z_{z,B}(t)$.

4.3 Experimental dynamic behavior of the beam-column system and model calibration

The experimental behavior of the beam-column system in figure 4.1 is also analyzed for the cases when no shunts are connected to transducers in support B and when RL- or RLC-shunts are connected to transducers in support B, in order to calibrate and validate the models from chapter 3.

The experimental short circuited acceleration and the capacitance frequency transfer functions of the beam-column system without shunts and the acceleration transfer functions with RL- and RLC-shunts of the beam-column with shunts as well as their respective characteristic quantities, table 3.1, are estimated from measurements with the vibration and impedance measurement setups in sections 4.2.2 and 4.2.1. Additionally to the experimental quantities in the frequency domain and only for the experimental beam-column system, orbit plots of the time acceleration signals are introduced to graphically analyze the orientation of the beam-column vibration in the y-z-plane. Finally, the beam-column model calibration with experimental frequency transfer functions is explained.

4.3.1 Acceleration frequency transfer functions

The experimental acceleration transfer functions in direction and orthogonal to the direction of excitation with short circuited transducers in support B, $G_{\alpha}^{\mathrm{sc}}(\Omega)$ and $G_{\alpha^{\perp}}^{\mathrm{sc}}(\Omega)$ analog to (3.75), with transducers in support B connected to RL-shunts, $G_{\alpha}^{\mathrm{RL}}(\Omega)$ and $G_{\alpha^{\perp}}^{\mathrm{RL}}(\Omega)$ analog to (3.94), and with transducers in support B connected to RLC-shunts, $G_{\alpha}^{\mathrm{RLC}}(\Omega)$ and $G_{\alpha^{\perp}}^{\mathrm{RLC}}(\Omega)$ analog to (3.95), are measured.

In general, the experimental acceleration transfer functions $G_{\alpha}(\Omega)$ and $G_{\alpha^{\perp}}(\Omega)$ are estimated from averaged cross power spectral and power spectral densities, [8]. The cross power spectral and power spectral densities are calculated with the discrete FOURIER transform of the experimental excitation voltage signal $u_{\alpha}(t)$ and the experimental acceleration signals $a_{\alpha}(t)$ and $a_{\alpha^{\perp}}(t)$ in tilted x-, y_{α}- and z_{α}-coordinates. The signals in tilted coordinates according to the tilt angle α introduced in section 3.2 result from the transformation of the measured voltages $u_{y/z,\mathrm{A}}(t)$ and accelerations $a_{y/z}(t)$, as introduced in section 3.3.4.

FOURIER transform

The voltage excitation signal $u_{\alpha}(t)$ is sampled N times over the time range $0 < t < \widehat{T}$ and transformed into the discrete time signal $u_{\alpha}(t_n)$. The FOURIER transform of the discrete excitation voltage signal $u_{\alpha}(t_n)$ reads

$$u_{\alpha}(\Omega_k) = \mathscr{F}\{u_{\alpha}(t_n)\} = \frac{1}{N}\sum_{n=0}^{N-1} u_{\alpha}(t_n)\, e^{-j\,\Omega_k\, t_n} \tag{4.4}$$

calculated at $k = 1, \ldots, N/2$ evenly-spaced frequencies $\Omega_k = k\,2\pi\,\Delta f$ with time samples $t_n = n/f_{\mathrm{s}}$ and sampling frequency f_{s}, [8]. The FOURIER transforms of the

accelerations $a_\alpha(\Omega)$ and $a_{\alpha^\perp}(\Omega)$ are calculated in the same way as $u_\mathrm{A}(\Omega)$ in (4.4) with their discrete signals $a_\alpha(t_n)$ and $a_{\alpha^\perp}(t_n)$.

Power spectral densities

The averaged cross power spectral densities

$$P_\mathrm{au}(\Omega) = \frac{1}{\widehat{N}} \sum_{n=1}^{\widehat{N}} a_\alpha^*(\Omega)\, u_\alpha(\Omega) \quad \text{and} \quad P_\mathrm{au}^\perp(\Omega) = \frac{1}{\widehat{N}} \sum_{n=1}^{\widehat{N}} a_{\alpha^\perp}^*(\Omega)\, u_\alpha(\Omega) \tag{4.5}$$

and the averaged power spectral density

$$P_\mathrm{uu}(\Omega) = \frac{1}{\widehat{N}} \sum_{n=1}^{\widehat{N}} u_\alpha^*(\Omega)\, u_\alpha(\Omega) \tag{4.6}$$

with average number $\widehat{N}$ are obtained from the FOURIER transforms of $u_\alpha(\Omega)$, $a_\alpha(t_n)$ and $a_{\alpha^\perp}(t_n)$ (4.4). In (4.5) and (4.6), $u_\alpha^*(\Omega)$, $a_\alpha^*(t_n)$ and $a_{\alpha^\perp}^*(t_n)$ are the conjugate complex FOURIER transforms.

Frequency transfer functions

The acceleration frequency transfer functions

$$G_\alpha(\Omega) = \frac{P_\mathrm{au}(\Omega)}{P_\mathrm{uu}(\Omega)} \quad \text{and} \quad G_{\alpha^\perp}(\Omega) = \frac{P_\mathrm{au}^\perp(\Omega)}{P_\mathrm{uu}(\Omega)} \tag{4.7}$$

are estimated from the averaged cross power spectral densities $P_\mathrm{au}(\Omega)$ and $P_\mathrm{au}^\perp(\Omega)$ (4.5) and the power spectral density $P_\mathrm{uu}(\Omega)$ (4.7), [8].

The estimation of (4.7) is performed with the *tfestimate* algorithm in MATLAB by using a HANNING time window and a window overlap of 50%. The frequency resolution is $\Delta f = 0.15\,\mathrm{Hz}$ and averaging with $\widehat{N} = 30$ is performed to obtain a good signal-to-noise ratio.

4.3.2 Capacitance frequency transfer functions

The experimental capacitance transfer functions $Y_{y/z}(\Omega)$ of transducers in support B are calculated with the experimental transducer impedances $Z_{y/z,\mathrm{B}}(\Omega)$ as

already shown for the mathematical model in section 3.6. The experimental transducer impedances $Z_{y/z,\mathrm{B}}(\Omega)$ are estimated from averaged cross power spectral and power spectral densities with the discrete FOURIER transforms of the voltage signals $u_{y/z,\mathrm{B}}(t)$ and $u_{\mathrm{Z}}(t)$ measured with the transducer impedance measurement setup in section 4.2.2.

For transducer $\mathrm{P}_{y,\mathrm{B}}$, the transducer impedance transfer function of $Z_{y,\mathrm{B}}(t)$ (4.3) reads

$$Z_{y,\mathrm{B}}(\Omega) = -\frac{P_{\dot{\mathrm{q}}\mathrm{u}}(\Omega)}{P_{\mathrm{uu}}(\Omega)} R_{\mathrm{Z}} \tag{4.8}$$

with the averaged cross power spectral and averaged power spectral density

$$P_{\dot{\mathrm{q}}\mathrm{u}}(\Omega) = \frac{1}{\widehat{N}} \sum_{n=1}^{\widehat{N}} u_{y,\mathrm{B}}^{*}(\Omega)\, u_{\mathrm{Z}}(\Omega) \quad \text{and} \quad P_{\mathrm{uu}}(\Omega) = \frac{1}{\widehat{N}} \sum_{n=1}^{\widehat{N}} u_{\mathrm{Z}}^{*}(\Omega)\, u_{\mathrm{Z}}(\Omega) \tag{4.9}$$

of $u_{y,\mathrm{B}}(\Omega)$ and $u_{\mathrm{Z}}(\Omega)$ calculated analogously to (4.5) and (4.6).

The experimental capacitance transfer function $Y_y(\Omega)$ calculates to

$$Y_y(\Omega) = \frac{1}{j\Omega} \left(-\frac{P_{\dot{\mathrm{q}}\mathrm{u}}(\Omega)}{P_{\mathrm{uu}}(\Omega)} R_{\mathrm{Z}} \right)^{-1} \tag{4.10}$$

by using (4.9) in (3.105). For transducer $\mathrm{P}_{z,\mathrm{B}}$, $Y_z(\Omega)$ is obtained from (4.10) by applying $u_{z,\mathrm{B}}(t)$ to the transducer and measuring $u_{\mathrm{Z}}(t)$.

4.3.3 Experimental characteristic quantities

The characteristic quantities of the beam-column system's dynamic behavior without and with shunts, as already presented for the mathematical model in section 3.6, are derived from the measured beam-column and transducer transfer functions (4.7) and (4.10) in sections 4.3.1 and 4.3.2.

Peak gains

The experimental peak gains of the acceleration transfer functions with short circuited electrodes $\widehat{G}_{\alpha}^{\mathrm{sc}}$ and $\widehat{G}_{\alpha^{\perp}}^{\mathrm{sc}}$, with RL-shunts $\widehat{G}_{\alpha}^{\mathrm{RL}}$ and $\widehat{G}_{\alpha^{\perp}}^{\mathrm{RL}}$, and with RLC-shunts

$\widehat{G}_{\alpha}^{\mathrm{RLC}}$ and $\widehat{G}_{\alpha^{\perp}}^{\mathrm{RLC}}$ are obtained by picking the maximum levels of the amplitude responses in the frequency range of the first lateral vibration mode of $G_{\alpha}(\Omega)$ and $G_{\alpha^{\perp}}(\Omega)$ (4.7) with short circuited or shunted transducers. This is assumed to give results equivalent to those of the mathematical model in figure 3.11.

Short circuited frequencies, GEMCCs and static capacitances

The experimental values of the short circuited resonance frequencies $\omega_{y/z}^{\mathrm{sc}}$, the GEMCCs $\gamma_{y/z}$ and the static capacitances $C_{y/z}^{\mathrm{s}}$ are obtained by fitting a modal capacitance model $\widetilde{Y}(\Omega)$ of transducers $\mathrm{P}_{y,\mathrm{B}}$ and $\mathrm{P}_{z,\mathrm{B}}$ to the experimental capacitance transfer functions $Y_{y/z}(\Omega)$. With this approach, the values of the named quantities are obtained at the same time from a single measurement, as already explained in figure 3.12. Furthermore, it leads to accurate experimental values since the estimation of the resonance frequency as well as the GEMCC is less influenced by the used frequency resolution in the frequency response function, [47].

The general equation of the modal transducer capacitance model of transducers $\mathrm{P}_{y,\mathrm{B}}$ and $\mathrm{P}_{z,\mathrm{B}}$ is given by

$$\widetilde{Y}(\Omega) = \frac{C}{1 + j\,\Omega\,C\,R} + \gamma^2\,C\,\frac{(\omega^{\mathrm{sc}})^2}{(\omega^{\mathrm{sc}})^2 - \Omega^2 + j\,2\zeta\,(\omega^{\mathrm{sc}})^2}. \tag{4.11}$$

$\widetilde{Y}(\Omega)$ directly depends on the short circuited resonance frequency ω^{sc}, the GEMCC γ, transducer capacitance C under zero mechanical strain, resistance R of dielectric losses, as introduced in section 3.3.3, and the modal damping ζ. Equation (4.11) has been derived in detail in a own earlier work, [22].

In the model fit process, the parameters C, R, γ, ω^{sc} and ζ in (4.11) are varied to solve the least squares curve fitting problem

$$\min_{C,R,\gamma,\omega^{\mathrm{sc}},\eta} ||\widetilde{Y}(C, R, \gamma, \omega^{\mathrm{sc}}, \zeta, \Omega) - Y_{\mathrm{exp}}(\Omega)||_2^2 \tag{4.12}$$

with the experimental dynamic transducer capacitance $Y_{\mathrm{exp}}(\Omega)$ (4.10). The least squares curve fitting problem is solved by the *lsqnonlin* algorithm readily implemented in MATLAB. With (4.12), ω^{sc} and γ are directly obtained from the fit and the static transducer capacitance C^{s} is calculated with

$$C^{\mathrm{s}} = |\widetilde{Y}(\Omega = 0)|. \tag{4.13}$$

4.3.4 Acceleration orbits

The beam-column is excited by transducers in support A to apply excitation in y_α-direction at angle α to investigate the vibration attenuation capability of transducers in support B, section 5.2. To experimentally show that the superposed excitation of transducers in support A in figure 4.1 excites the beam-column in the assumed direction of excitation y_α at angle α as introduced in section 3.2, the acceleration time signals $a_y(t)$ and $a_z(t)$ are plotted on the y-z-coordinate system and approximated by acceleration orbits to graphically analyze the plane vibration. Furthermore, the portions of vibration in direction of excitation y_α and orthogonal to the direction of excitation z_α are used to quantify the vibration.

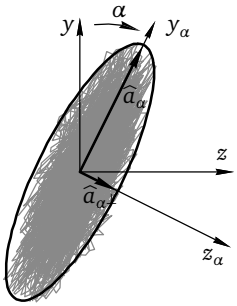

Figure 4.10: Qualitative presentation of an acceleration orbit

Figure 4.10 shows a qualitative acceleration orbit of white noise acceleration time signals, introduced in section 4.2.1, for excitation applied at an oblique angle α. The acceleration orbit is characterized by its acceleration peaks in direction of excitation $\widehat{a}_\alpha$ and orthogonal to direction of excitation $\widehat{a}_{\alpha\perp}$, by which the orbit is approximated via an elliptical shape. $\widehat{a}_\alpha$ and $\widehat{a}_{\alpha\perp}$ are the maximum accelerations in y_α- and z_α-direction of the transformed accelerations $a_y(t)$ and $a_z(t)$, (3.38).

4.3.5 Calibration procedure of beam-column system's model

In this work, the beam-column system's model without shunts is adapted to the real beam-column system without shunts to precisely represent the experimental beam-column vibration and the dynamic transducer behavior of transducers in support B. This is needed to optimally tune shunts for experimental beam-column vibration attenuation in chapter 5 with the model-based numerical procedure explained in

section 3.5, and to correctly represent the effects of static beam-column loading and spring element manufacturing variations by the model, chapter 6.

The model update is performed by minimization of the sum of the error squares

$$\min_{\boldsymbol{P}} ||G^{\mathrm{sc}}_{\alpha,\mathrm{exp}}(\Omega) - G^{\mathrm{sc}}_{\alpha,\mathrm{num}}(\Omega,\boldsymbol{P})||_2^2 + ||Y_{y/z,\mathrm{exp}}(\Omega) - Y_{y/z,\mathrm{num}}(\Omega,\boldsymbol{P})||_2^2 \tag{4.14}$$

between the experimental acceleration and capacitance transfer functions, $G^{\mathrm{sc}}_{\alpha,\mathrm{exp}}(\Omega)$ (4.7) and $Y_{y/z,\mathrm{exp}}(\Omega)$ (4.10), and the numerical acceleration and capacitance transfer functions, $G^{\mathrm{sc}}_{\alpha,\mathrm{num}}(\Omega,\boldsymbol{P})$ (3.75) and $Y_{y/z,\mathrm{num}}(\Omega,\boldsymbol{P})$ (3.105), for $\alpha = 0^\circ$ and $\alpha = 90^\circ$, in y- and z-direction respectively. In (4.14), $\boldsymbol{P}$ summarizes the model parameters to be calibrated. Different parameters $\boldsymbol{P}$ are calibrated in chapters 5 and 6.

4.3.6 Evaluating the match of model and experiment

The goodness of match of models and experiments in this work is evaluated with normalized root mean square error (NRMSE) and relative deviation. For frequency transfer functions, the NRMSE between numerical and experimental results is calculated over a certain frequency range. For single quantities, the relative deviation of the numerically calculated value from the experimental value is used.

As an example, the NRMSE of the numerical and experimental short circuited transfer function is calculated by

$$\mathrm{NRMSE} = 1 - \frac{||G^{\mathrm{sc}}_{\alpha,\mathrm{exp}}(\Omega) - G^{\mathrm{sc}}_{\alpha,\mathrm{num}}||}{||G^{\mathrm{sc}}_{\alpha,\mathrm{exp}}(\Omega) - \overline{G^{\mathrm{sc}}_{\alpha,\mathrm{exp}}(\Omega)}||} \tag{4.15}$$

with the arithmetic mean $\overline{G^{\mathrm{sc}}_{\alpha,\mathrm{exp}}(\Omega)}$ of the experimental transfer function in the considered frequency domain. The NRMSE value varies between $-\infty$, representing a bad fit, to 1, representing a perfect fit. If the cost function is equal to zero, then the model is no better than a straight line fitting the experimental data.

As an example, the relative deviation of the numerical from the experimental short circuited resonance frequency in percentage is calculated by

$$\mathrm{err}(\omega^{\mathrm{sc}}) = \frac{\omega^{\mathrm{sc}}_{\mathrm{exp}} - \omega^{\mathrm{sc}}_{\mathrm{num}}}{\omega^{\mathrm{sc}}_{\mathrm{num}}} \cdot 100\,\%. \tag{4.16}$$

5 Deterministic vibration attenuation with shunts

In this chapter, deterministic experimental and numerical results of vibration attenuation of the first lateral beam-column vibration mode are presented to quantify the capability of vibration attenuation of piezo-elastic support B with shunted transducers when uncertainty is disregarded. Therefore, the acceleration transfer functions of the beam-column with tuned RL- and RLC-shunts connected to the transducers in support B are compared to the acceleration transfer functions with short circuited transducers in support B. For all investigation in this chapter, the beam-column is unloaded with $F_x = 0\,\mathrm{N}$ and uncertainty due to manufacturing or system assembly variations is disregarded.

In section 5.1, experimental and numerical results are shown to quantify the optimal experimental and numerical vibration attenuation with numerically tuned RL- and RLC-shunts when the beam-column is excited at $\alpha = 0\,^\circ$ and $\alpha = 90\,^\circ$ according to figure 3.2, in y- and z-direction respectively. In section 5.2, vibration attenuation with RL- and RLC-shunts as tuned in section 5.1 is studied for excitation at an oblique angle α.

5.1 Experimental and numerical vibration attenuation with optimally tuned RL- and RLC-shunts

Optimally tuned RL- and RLC-shunts for vibration attenuation of the first beam-column mode in simulation and experiment are calculated for excitation in y- and z-direction by use of the the numerical tuning procedure in section 3.5.

First in section 5.1.1, the experimental short circuited acceleration transfer functions and the capacitance transfer functions of the beam-column system are shown. Afterwards in section 5.1.2, the parameters of the beam-column system's model without shunts are calibrated with the experimental results presented in section 5.1.1. Finally in section 5.1.3, RL- and RLC-shunts are tuned numerically for optimal vibration attenuation by using the calibrated parameters from section 5.1.2

in the beam-column system's model with shunts. To validate the shunt tuning procedure, numerical and experimental acceleration transfer functions with RL- and RLC-shunts are compared. To evaluate vibration attenuation, section 5.1.4 summarizes the experimental and numerical short circuited and shunted acceleration transfer functions.

5.1.1 Experimental beam-column system's dynamic behavior without shunts

Figure 5.1 shows the experimental short circuited acceleration transfer functions in excitation direction with short circuited transducers in support B $G^{\mathrm{sc}}_{y/z,\mathrm{exp}}(\Omega)$ (4.7) in the frequency range $10\,\mathrm{Hz} \leq \Omega/2\pi \leq 1250\,\mathrm{Hz}$. Three distinct beam-column vibration modes in y- and z-direction are observable and characterized by their sharp peaks in the amplitude responses. In this work, the first lateral beam-column mode in the frequency range $100\,\mathrm{Hz} \leq \Omega/2\pi \leq 300\,\mathrm{Hz}$ (gray areas) is investigated for vibration attenuation with RL- or RLC-shunts. The first mode is chosen for investigations of vibration attenuation with resonant shunts as it is separated from higher modes in frequency, it shows high vibration levels due to small damping, and the associated GEMCCs are relatively high, table 5.1 .

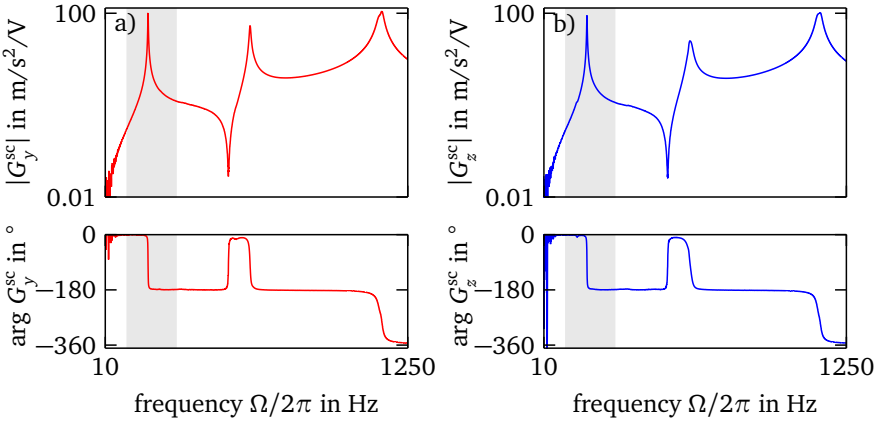

Figure 5.1: Experimental short circuited acceleration transfer functions,
a) in y-direction $G^{\mathrm{sc}}_{y,\mathrm{exp}}(\Omega)$ (——),
b) in z-direction $G^{\mathrm{sc}}_{z,\mathrm{exp}}(\Omega)$(——)

Figure 5.2 shows the experimental capacitance transfer functions $Y_{y/z,\mathrm{exp}}(\Omega)$ of the transducers in support B in the frequency range of the first lateral beam-column vibration mode. Additionally, and only in y-direction, figure 5.2a shows the fitted

transfer function of the modal dynamic transducer capacitance $\widetilde{Y}_{\mathrm{num}}(\Omega)$ (4.11). The numerical and the experimental curve show a good agreement with a NRMSE of 0.94, (4.15).

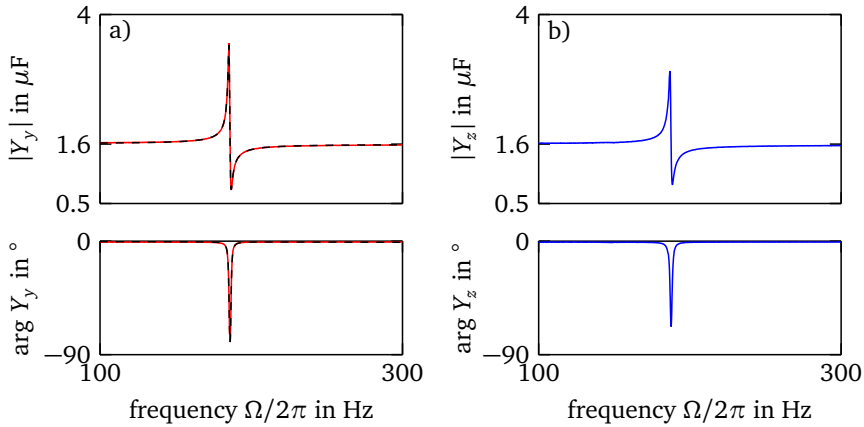

Figure 5.2: Exp. and num. transducer capacitance transfer functions,
a) in y-direction $Y_{y,\mathrm{exp}}(\Omega)$ (——), $\widetilde{Y}_{\mathrm{num}}(\Omega)$ (——),
b) in z-direction $Y_{z,\mathrm{exp}}(\Omega)$ (——)

Table 5.1 summarizes the characteristic quantities, introduced in table 3.1, of the experimental behavior of the beam-column system without shunts in figures 5.1 and 5.2. The values are obtained from the fitted modal transducer model $\widetilde{Y}_{\mathrm{num}}(\Omega)$, as explained in section 4.3.3. Additionally, table 5.1 shows the modal damping coefficients $\zeta_{y/z,\mathrm{exp}}$ of the first mode calculated with the half-power method, [72].

Table 5.1: Experimental characteristic quantities of the beam-column system's dynamic behavior without shunts

dir.	$\widehat{G}^{\mathrm{sc}}$ in m/s^2/V	$\omega^{\mathrm{sc}}/2\pi$ in Hz	γ in %	C^{s} in µF	ζ in %
y	100.8	185.5	10.0	1.613	0.47
z	89.6	186.5	9.8	1.600	0.49

In general, the experimental acceleration and capacitance transfer functions in figures 5.1 and 5.2 are similar in y- and z-directions. However, small differences in all characteristic quantities in table 5.1 are observed. The differences in the experimental resonance frequencies $\omega^{\mathrm{sc}}_{y/z,\mathrm{exp}}$, GEMCCs $\gamma_{y/z,\mathrm{exp}}$ and static capacitances

$C^{s}_{y/z,\mathrm{exp}}$ in y- and z-direction could be attributed to non-symmetric support stiffness conditions due to spring element manufacturing and system assembly variations as later discussed in section 6.3, and due to non-symmetric stiffness conditions realized by the parallel guidance and fixed boundary in the test setup in figure 4.1.

5.1.2 Calibration of beam-column system's model without shunts

Figures 5.3 and 5.4 show the numerical short circuited acceleration transfer functions $G^{\mathrm{sc}}_{y/z,\mathrm{num}}(\Omega)$ (3.75) and the numerical capacitance transfer functions $Y_{y/z,\mathrm{num}}(\Omega)$ (3.105) after the calibration. The spring element stiffness and transducer parameters in the vector

$$\boldsymbol{P} = [k_{y/z,\mathrm{A}},\, k_{y/z,\mathrm{B}},\, k_{\varphi_{y/z},\mathrm{A}},\, k_{\varphi_{y/z},\mathrm{B}},\, \Theta_{y/z,\mathrm{A}},\, \Theta_{y/z,\mathrm{B}},\, k^{\mathrm{sc}}_{y/z,\mathrm{A}},\, k^{\mathrm{sc}}_{y/z,\mathrm{B}},\, C_{y/z,\mathrm{B}},\, R_{y/z,\mathrm{B}}] \tag{5.1}$$

were calibrated to accurately represent the lateral mechanical dynamic behavior of the elastically supported beam-column and the electromechanical dynamic transducer behavior of experimental results from figures 5.1 and 5.2 in the frequency range $100\,\mathrm{Hz} \leq \Omega/2\pi \leq 300\,\mathrm{Hz}$. All beam-column and transducer parameters are summarized in table 5.3.

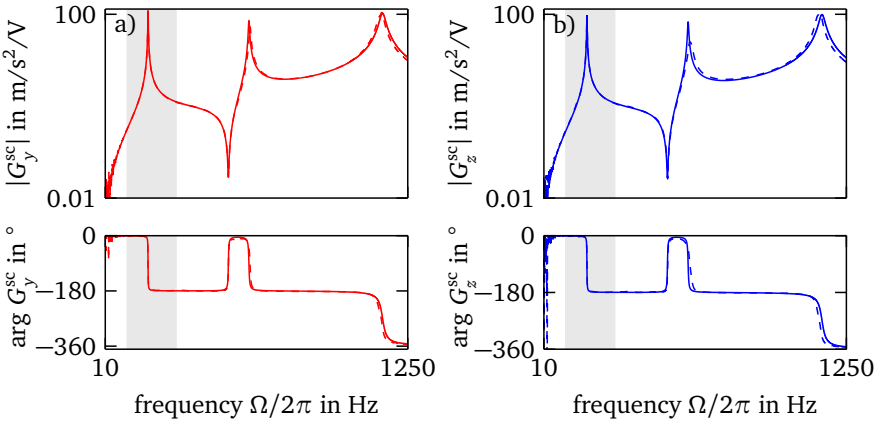

Figure 5.3: Exp. and num. short circuited acceleration transfer functions,
a) y-direction $G^{\mathrm{sc}}_{y,\mathrm{exp}}(\Omega)$ (– –) and $G^{\mathrm{sc}}_{y,\mathrm{num}}(\Omega)$ (——),
b) z-direction $G^{\mathrm{sc}}_{z,\mathrm{exp}}(\Omega)$ (– –) and $G^{\mathrm{sc}}_{z,\mathrm{num}}(\Omega)$ (——)

In figure 5.3, the numerical short circuited acceleration transfer functions $G^{sc}_{y/z,num}(\Omega)$ show a good agreement in the presented frequency range $10\,\text{Hz} \leq \Omega/2\pi \leq 1250\,\text{Hz}$, which demonstrates that the model also adequately represents higher vibration modes. In the calibration frequency range of the first mode, the NRMSE (4.15) is 0.9 for $G^{sc}_{y}(\Omega)$ and 0.91 for $G^{sc}_{z}(\Omega)$. The capacitance transfer functions in figure 5.4, also show a good agreement with a NRMSE of 0.95 for $Y_{y,num}(\Omega)$ and 0.94 for $Y_{z,num}(\Omega)$. As shown in table 5.2, the numerical and the experimental characteristic quantities $\omega^{sc}_{y/z}$, $\gamma_{y/z}$ and $C^{s}_{y/z}$ only show small relative errors. The calibrated model is used in the next section in the model-based shunt tuning.

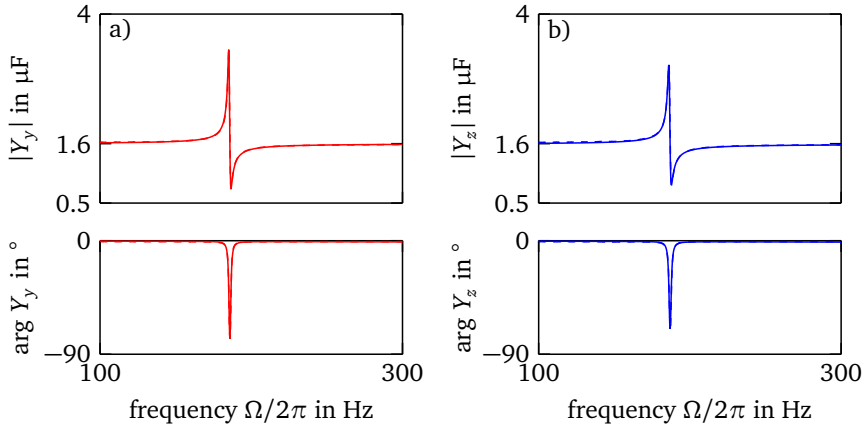

Figure 5.4: Exp. and num. transducer capacitance transfer functions,
a) in y-direction $Y_{y,exp}(\Omega)$ (– –), $Y_{y,num}(\Omega)$ (——),
b) in z-direction $Y_{y,exp}(\Omega)$ (– –), $Y_{y,num}(\Omega)$ (——)

Table 5.2: Experimental and numerical characteristic quantities of the beam-column system's dynamic behavior without shunts, experimental values from table 5.1, $\omega^{sc}/2\pi$ in Hz, γ in %, C^{s} in µF, rel. deviation in %

	experimental			numerical			relative deviation		
dir.	$\omega^{sc}/2\pi$	γ	C^{s}	$\omega^{sc}/2\pi$	γ	C^{s}	err(ω^{sc})	err(γ)	err(C^{s})
y	185.5	10.0	1.613	185.4	10.0	1.610	0.1	0.0	0.2
z	186.5	9.8	1.600	186.4	10.0	1.599	0.1	-2.0	0.1

Table 5.3: Deterministic model parameter values of the beam-column system for the components beam-column, axial extensions, support A and support B, *) calibrated

property	variable	value	unit
beam-colum			
length	l_b	$4.0 \cdot 10^{-1}$	m
radius	r_b	$5.0 \cdot 10^{-3}$	m
density	ϱ_b	$2.8 \cdot 10^{3}$	kg/m^3
Young's modulus	E_b	$7.4 \cdot 10^{10}$	N/m^2
modal damping coeff.	$[\zeta_y, \zeta_z]$	$[4.7, 4.9] \cdot 10^{-3}$	–
position of sensor	x_s	$0.475\, l_\mathrm{b}$	m
axial extension			
length	$[l_\mathrm{ext,A}, l_\mathrm{ext,B}]$	$[6.7, 6.7] \cdot 10^{-3}$	m
edge length	$t_\mathrm{ext,A/B}$	$6.0 \cdot 10^{-3}$	m
density	$\varrho_\mathrm{ext,A/B}$	$7.8 \cdot 10^{-3}$	kg/m^3
Young's modulus	$E_\mathrm{ext,A/B}$	$2.1 \cdot 10^{12}$	N/m^2
support A			
lateral stiffness*	$[k_{y,\mathrm{A}}, k_{z,\mathrm{A}}]$	$[31.1, 32.4] \cdot 10^{6}$	N/m
rotational stiffness*	$[k_{\varphi_y,\mathrm{A}}, k_{\varphi_z,\mathrm{A}}]$	$[123.5, 125.5]$	Nm/rad
transducer stiffness*	$[k^\mathrm{sc}_{y,\mathrm{A}}, k^\mathrm{sc}_{z,\mathrm{A}}]$	$[32.4, 32.7] \cdot 10^{6}$	N/m
transducer force const.*	$[\Theta_{y,\mathrm{A}}, \Theta_{z,\mathrm{A}}]$	$[3.34, 3.15]$	N/V
support B			
lateral stiffness*	$[k_{y,\mathrm{B}}, k_{z,\mathrm{B}}]$	$[31.1, 32.4] \cdot 10^{6}$	N/m
rotational stiffness*	$[k_{\varphi_y,\mathrm{B}}, k_{\varphi_z,\mathrm{B}}]$	$[123.5, 125.5]$	Nm/rad
transducer stiffness*	$[k^\mathrm{sc}_{y,\mathrm{B}}, k^\mathrm{sc}_{z,\mathrm{B}}]$	$[32.4, 32.7] \cdot 10^{6}$	N/m
transducer force const.*	$[\Theta_{y,\mathrm{B}}, \Theta_{z,\mathrm{B}}]$	$[2.99, 3.17]$	N/V
transducer capacitance*	$[C_{y,\mathrm{B}}, C_{z,\mathrm{B}}]$	$[1.43, 1.38]$	µF
transducer resistance*	$[R_{y,\mathrm{B}}, R_{z,\mathrm{B}}]$	$[11.9, 12.1]$	Ohm

5.1.3 Experimental and numerical beam-column system's dynamic behavior with optimally tuned RL- and RLC-shunts

The adjustable shunt resistances $R^\mathrm{D}_{y/z}$, $R^\mathrm{L1}_{y/z}$ and $R^\mathrm{N1}_{y/z}$ of the RL-shunts (3.83) and RLC-shunts (3.91) are calculated for optimal attenuation of the experimental and numerical vibrations of the first beam-column mode in figure 5.3 (gray areas) for excitation in y- and z-direction. The parameters in table 5.3 of the beam-column system's model, the constant shunt resistances and capacitances in tables 4.3 and 4.2 and the numerical acceleration transfer functions with RL-shunt $G^\mathrm{RL}_{y/z,\mathrm{num}}(\Omega)$

(3.94) and RLC-shunts $G^{\mathrm{RLC}}_{y/z,\mathrm{num}}(\Omega)$ (3.95) are used to solve the optimization problems (3.97) and (3.99). The RL- and RLC-shunt resistances that optimally tune the shunts are summarized in table 5.4. For the RLC-shunt, a negative capacitance ratio $\delta = -0.9$ (3.103) is used to ensure stability in the experiment.

Table 5.4: RL- and RLC-shunt resistances for optimal vibration attenuation in y- and z-direction of shunts connected to transducers $\mathrm{P}_{y,\mathrm{B}}$ and $\mathrm{P}_{z,\mathrm{B}}$

		RL-shunt		RLC-shunt		
property	symbol	$\mathrm{P}_{y,\mathrm{B}}$	$\mathrm{P}_{z,\mathrm{B}}$	$\mathrm{P}_{y,\mathrm{B}}$	$\mathrm{P}_{z,\mathrm{B}}$	unit
resistance	R^{D}	61.01	60.65	15.84	16.37	Ohm
	R^{L1}	22.70	22.30	2.36	2.34	Ohm
	R^{N1}	–	–	1168.34	1169.61	Ohm
neg. cap. ratio	δ	–	–	−0.90	−0.90	Ohm
inductance	L	0.455	0.458	0.0462	0.0491	Henry
neg. capacitance	C^{n}	–	–	-1.799	-1.801	µF

The numerical and experimental acceleration transfer functions are analyzed and compared for the tuned RL- and RLC-shunt resistances in table 5.4. Figure 5.5 shows the numerical and experimental transfer functions $G^{\mathrm{RL}}_{y/z,\mathrm{num}}(\Omega)$ (4.7) and $G^{\mathrm{RL}}_{y/z,\mathrm{exp}}(\Omega)$ (3.94), and figure 5.6 shows the numerical and experimental acceleration transfer functions $G^{\mathrm{RLC}}_{y/z,\mathrm{num}}(\Omega)$ (4.7) and $G^{\mathrm{RLC}}_{y/z,\mathrm{exp}}(\Omega)$ (3.95). Their respective peak gains $\widehat{G}^{\mathrm{RL}}$ and $\widehat{G}^{\mathrm{RLC}}$ are summarized in table 5.5.

For vibration attenuation with RL-shunts in figure 5.5, the numerical acceleration amplitude responses $|G^{\mathrm{RL}}_{y/z,\mathrm{num}}(\Omega)|$ show the typical curve of the balanced calibration approach, section 2.2.1, with similar vibration attenuation in y- and z-direction as observed by similar peak gains $\widehat{G}^{\mathrm{RL}}_{y/z}$, refer to table 5.5. The experimental acceleration amplitude responses $|G^{\mathrm{RL}}_{y/z,\mathrm{exp}}(\Omega)|$ also show the typical curve of balanced calibration. The numerical and the experimental acceleration amplitude responses are in good agreement: The NRMSEs (4.15) of the respective transfer function are greater than 0.91, and the relative deviations between the numerical and experimental peak gains are less than 2.4 %, refer to table 5.5.

For vibration attenuation with RLC-shunts in figure 5.6, the numerical acceleration amplitude responses $|G^{\mathrm{RLC}}_{y/z,\mathrm{num}}(\Omega)|$ show the typical curve of the balanced calibration approach, section 2.2.1, with similar vibration attenuation in y- and z-direction as observed by similar peak gains $\widehat{G}^{\mathrm{RLC}}_{y/z}$, refer to table 5.5. The experimental amplitude responses $|G^{\mathrm{RLC}}_{y/z,\mathrm{exp}}(\Omega)|$ also show the typical curve of balanced

calibration. The numerical and the experimental acceleration amplitude responses are in good agreement: The NRMSEs (4.15) of the respective transfer function are greater than 0.92, and the relative deviations between the numerical and experimental peak gains are less than 2.7 %, refer to table 5.5.

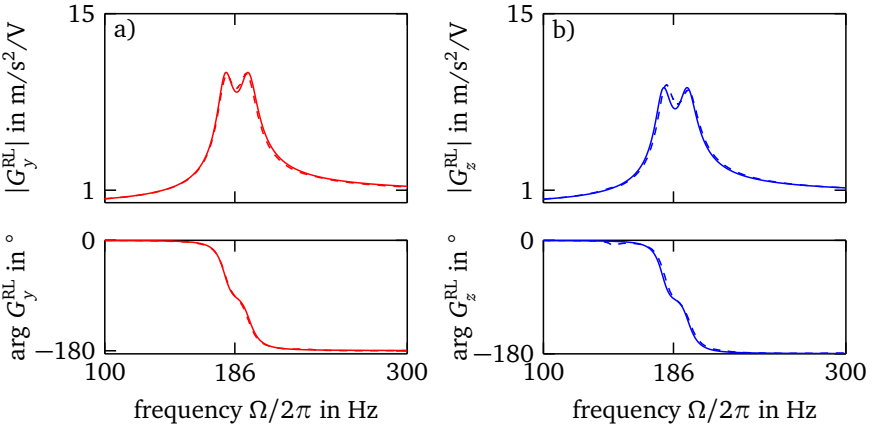

Figure 5.5: Exp. and num. acceleration transfer functions with RL-shunts,
a) y-direction $G_{y,\mathrm{exp}}^{\mathrm{RL}}(\Omega)$ (– –), $G_{y,\mathrm{num}}^{\mathrm{RL}}(\Omega)$ (——),
b) z-direction $G_{z,\mathrm{exp}}^{\mathrm{RL}}(\Omega)$ (– –), $G_{z,\mathrm{num}}^{\mathrm{RL}}(\Omega)$ (——)

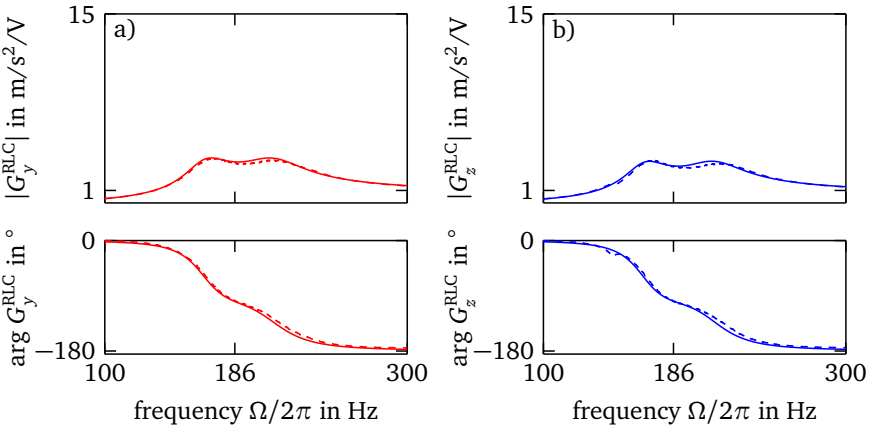

Figure 5.6: Exp. and num. acceleration transfer functions with RLC-shunts,
a) y-direction $G_{y,\mathrm{exp}}^{\mathrm{RLC}}(\Omega)$ (– –), $G_{y,\mathrm{num}}^{\mathrm{RLC}}(\Omega)$ (——),
b) z-direction $G_{z,\mathrm{exp}}^{\mathrm{RLC}}(\Omega)$ (– –), $G_{z,\mathrm{num}}^{\mathrm{RLC}}(\Omega)$ (——)

The numerical and the experimental acceleration transfer functions with RL- and RLC-shunt show that the model-based tuning approach achieves good and similar vibration attenuation for the numerical and the experimental beam-column system for RL- and RLC-shunts in y- and z-direction. The comparison of beam-column accelerations with and without shunts to evaluate vibration attenuation is shown in the next section.

Table 5.5: Optimal experimental and numerical peak gains $\widehat{G}^{\mathrm{RL}}$ and $\widehat{G}^{\mathrm{RLC}}$ with optimal shunts from table 5.4, all in $\mathrm{m/s^2/V}$, rel. deviation in %

	experimental		numerical		relative deviation	
dir.	$\widehat{G}^{\mathrm{RL}}$	$\widehat{G}^{\mathrm{RLC}}$	$\widehat{G}^{\mathrm{RL}}$	$\widehat{G}^{\mathrm{RLC}}$	$\mathrm{err}(\widehat{G}^{\mathrm{RL}})$	$\mathrm{err}(\widehat{G}^{\mathrm{RLC}})$
y	10.27	3.58	10.34	3.57	-0.7	0.3
z	9.36	3.40	9.14	3.31	2.4	2.7

5.1.4 Evaluation of experimental and numerical optimal vibration attenuation

Figure 5.7 compares the numerical and experimental amplitude responses of the acceleration transfer functions with short circuited transducers from figure 5.3 to amplitude responses with RL-shunts from figure 5.5 and RLC-shunts from figure 5.6. With RL-shunts, the numerical and experimental peak gains $\widehat{G}^{\mathrm{RL}}_{y/z}$ are similar in y-

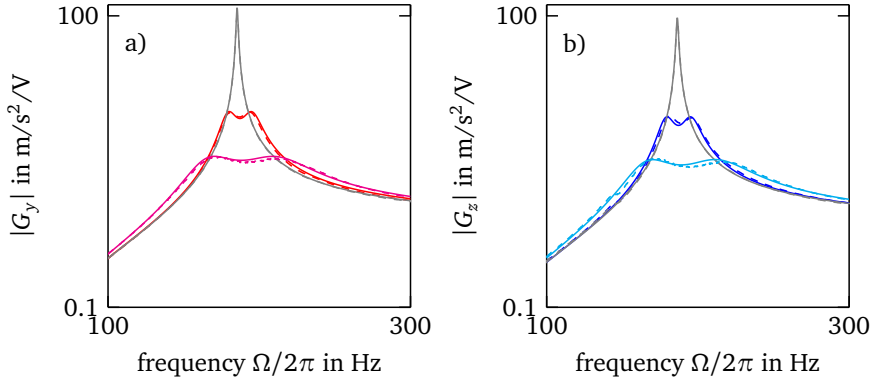

Figure 5.7: Exp. and num. short circuited and shunted amplitude responses,
a) $G^{\mathrm{sc}}_{y,\mathrm{exp}}(\Omega)$ (– –), $G^{\mathrm{sc}}_{y,\mathrm{num}}(\Omega)$ (——), $G^{\mathrm{RL}}_{y,\mathrm{exp}}(\Omega)$ (– –), $G^{\mathrm{RL}}_{y,\mathrm{num}}(\Omega)$ (——), $G^{\mathrm{RLC}}_{y,\mathrm{exp}}(\Omega)$ (– –), $G^{\mathrm{RLC}}_{y,\mathrm{num}}(\Omega)$ (——)
b) $G^{\mathrm{sc}}_{z,\mathrm{exp}}(\Omega)$ (– –), $G^{\mathrm{sc}}_{z,\mathrm{num}}(\Omega)$ (——), $G^{\mathrm{RL}}_{z,\mathrm{exp}}(\Omega)$ (– –), $G^{\mathrm{RL}}_{z,\mathrm{num}}(\Omega)$ (——), $G^{\mathrm{RLC}}_{z,\mathrm{exp}}(\Omega)$ (– –), $G^{\mathrm{RLC}}_{z,\mathrm{num}}(\Omega)$ (——)

and z-direction and 90 % smaller than the short circuited peak gains $\widehat{G}^{\mathrm{sc}}_{y/z}$. With RLC-shunts, the numerical and experimental peak gains $\widehat{G}^{\mathrm{RL}}_{y/z}$ are similar in y- and z-direction and 96 % smaller than the short circuited peak gains $\widehat{G}^{\mathrm{sc}}_{y/z}$. This represents an appropriate and equal vibration attenuation in simulation and experiment with RL- and RLC-shunts in y- and z-direction, whereby the RLC-shunt performs better than the RL-shunt, as expected and discussed in section 2.2.1.

5.2 Effect of direction of excitation on the experimental vibration attenuation with RL- and RLC-shunts

The effect of excitation applied at an oblique angle α on the beam-column vibrations in direction of excitation y_α and orthogonal to direction of excitation z_α is studied for short circuited transducers in support B and for transducers in support B connected to RL- or RLC-shunts, coordinate system shown in figure 4.10.

In section 5.2.1 acceleration orbit plots as introduced in section 4.3.4 are used to graphically investigate how good the vibration direction of the beam-column agrees with the assumed direction of excitation. Furthermore, the comparison of acceleration orbits with short circuited transducers and shunted transducers in support B evaluates vibration attenuation. In section 5.2.2, acceleration transfer functions are used to investigate the beam-column vibrations with and without shunts due to excitation in different directions. Excitations at $0\,^\circ \leq \alpha \leq 90\,^\circ$ show comparable results to excitations at $90\,^\circ \leq \alpha \leq 180\,^\circ$. Therefore, results are only discussed at $\alpha = [0^\circ, 22.5^\circ, 45^\circ, 67.5^\circ, 90^\circ]$.

5.2.1 Analysis via acceleration orbits

The acceleration orbit plots for excitation at $\alpha = [0^\circ, 22.5^\circ, 45^\circ, 67.5^\circ, 90^\circ]$ of accelerations with short circuited transducers in support B are shown in figure 5.8. The acceleration orbit plots of accelerations with transducers in support B connected to RL- and RLC-shunts are shown in figure 5.9. The associated acceleration peaks in excitation direction $\widehat{a}_\alpha$ and orthogonal to the excitation direction $\widehat{a}_{\alpha^\perp}$ are summarized in table 5.6. Figure 5.8a, as an example for all orbits, shows the acceleration signals of $a^{\mathrm{sc}}_y(t)$ and $a^{\mathrm{sc}}_z(t)$ with a gray line, which have been used to approximate the orbit.

Transducers short circuited

In figures 5.8a and 5.8b, the orbits show that the beam-column vibrates in excitation direction and orthogonal to the exciation direction. The orientation of the orbits adequately follows the direction of excitation, which shows that the lateral beam-column can be forced to vibrate in the y_α-direction through the superposition of the excitation of the two transducers in support A, figure 4.2. On average, the acceleration peaks in excitation direction $\widehat{a}_\alpha^{\mathrm{sc}}$ are 3.6 times higher than the acceleration peaks orthogonal to the excitation direction $\widehat{a}_{\alpha\perp}^{\mathrm{sc}}$, table 5.6, which shows that the beam-column mainly vibrates in excitation direction. Comparable to experimental results in table 5.1, differences in the vibration peaks are observable and attributed to the non-ideal and non-symmetric stiffness and damping support conditions of the experimental beam-column system.

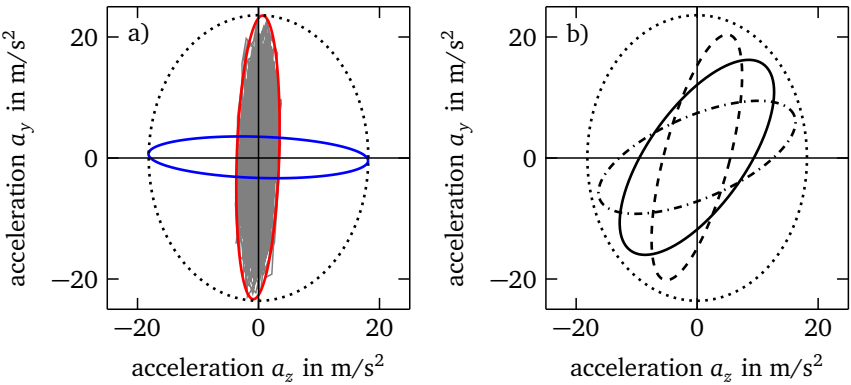

Figure 5.8: Experimental acceleration orbits short circuited for excitation at α,
a) 0° (——), 90° (——), acceleration time signal (——)
b) 22.5° (– –), 45° (——), 67.5° (–·–),
in a) and b) enveloping orbit (·····)

Transducers connected to RL- and RLC-shunts

In figure 5.9a, the orbits show that the beam-column with RL-shunts vibrates in excitation direction and orthogonal to the exciation direction. Again, the orientation of the orbits follows the direction of excitation. On average, the acceleration peaks in excitation direction $\widehat{a}_\alpha^{\mathrm{RL}}$ are 25.8 times higher than the acceleration peaks orthogonal to the excitation direction $\widehat{a}_{\alpha\perp}^{\mathrm{RL}}$, table 5.6. This shows that the vibration orthogonal to the excitation direction is negligible small due to the vibration

attenuation with RL-shunt. Compared to short circuited acceleration peaks in excitation direction $\widehat{a}_{\alpha}^{\mathrm{sc}}$ in figure 5.8, the acceleration peaks with RL-shunts $\widehat{a}_{\alpha}^{\mathrm{RL}}$ are 39 % smaller on average.

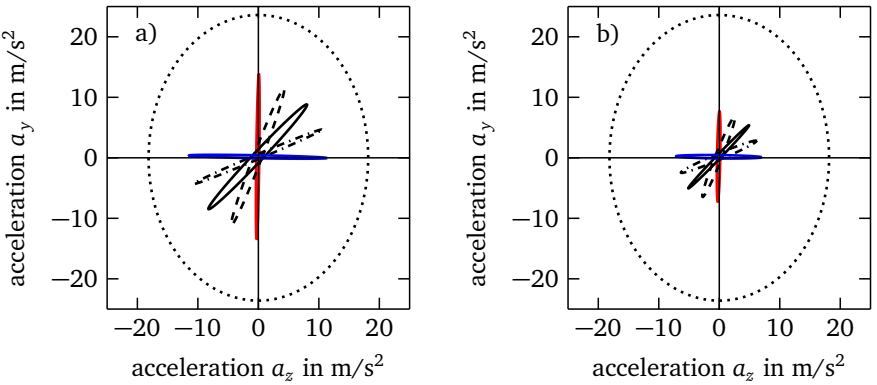

Figure 5.9: Experimental acceleration orbits with a) RL-shunts, b) RLC-shunts, excitation at α: 0° (——), 22.5° (− −), 45° (——), 67.5° (−·−), 90° (——), short circuited enveloping orbit (·····) from figure 5.8

In figure 5.9b, the beam-column with RLC-shunts vibrates in excitation direction and orthogonal to the exciation direction, and the orientation of the orbits follows the direction of excitation. On average, the acceleration peaks in excitation direction $\widehat{a}_{\alpha}^{\mathrm{RLC}}$ are 18 times higher than the acceleration peaks orthogonal to the excitation direction $\widehat{a}_{\alpha^{\perp}}^{\mathrm{RLC}}$, table 5.6, which is why the vibration orthogonal to the direction of excitation can likewise be neglected. Compared to short circuited acceleration peaks in excitation direction $\widehat{a}_{\alpha}^{\mathrm{sc}}$ in figure 5.8, the acceleration peaks with RLC-shunts $\widehat{a}_{\alpha}^{\mathrm{RLC}}$ are 64 % smaller on average.

The comparison of acceleration orbits with short circuited transducers in figure 5.8 to acceleration orbits with transducers connected to RL- and RLC-shunts in figure 5.9 shows that the RL- and RLC-shunts significantly reduced beam-column vibration for all investigated directions of excitation. Furthermore with shunts, the acceleration peaks orthogonal to the excitation direction are small according to table 5.6, which is why the vibration in this direction can be neglected and, thus, is not used in the numerical simulation in the following. The effect of shunts on the vibration orthogonal to the excitation direction is further investigated for acceleration transfer functions in the next section.

Table 5.6: Acceleration peaks of orbits in direction of excitation $\widehat{a}_\alpha$, orthogonal to direction of excitation $\widehat{a}_{\alpha^\perp}$ and mean values $\mu(\widehat{a})$ from figures 5.8 and 5.9, all in $\mathrm{m/s^2}$, angle α in degrees

	sc		RL-shunt		RLC-shunt	
α	$\widehat{a}_\alpha$	$\widehat{a}_{\alpha^\perp}$	$\widehat{a}_\alpha$	$\widehat{a}_{\alpha^\perp}$	$\widehat{a}_\alpha$	$\widehat{a}_{\alpha^\perp}$
0	23.45	3.50	13.68	0.25	7.51	0.27
22.5	20.95	5.39	12.07	0.70	7.14	0.56
45	18.91	8.07	11.88	0.78	7.25	0.33
67.5	17.51	6.79	11.51	0.39	6.78	0.51
90	18.17	3.41	11.43	0.25	7.06	0.28
$\mu(\widehat{a})$	19.80	5.43	12.11	0.47	7.15	0.39

5.2.2 Analysis via acceleration transfer functions

The amplitude responses for excitation at $\alpha = [0°, 22.5°, 45°, 67.5°, 90°]$ of the experimental short circuited acceleration transfer functions in excitation direction $G^{sc}_\alpha(\Omega)$ and orthogonal to the excitation direction $G^{sc}_{\alpha^\perp}(\Omega)$ (4.7) are shown in figure 5.10. The amplitude responses with transducers in support B connected to RL- and RLC-shunts are shown in figure 5.11. The respective peak gains in excitation direction $\widehat{G}_\alpha$ and orthogonal to the excitation direction $\widehat{G}_{\alpha^\perp}$ are summarized in table 5.7.

Transducers short circuited

In figure 5.10a, the amplitude responses in the direction of excitation $|G^{sc}_\alpha(\Omega)|$ lie on top of each other for all shown directions of excitation with sharp resonance peak gains close to the excitation frequency $\Omega/2\pi = 186\,\mathrm{Hz}$. However, the peak gains $\widehat{G}^{sc}_\alpha$ in table 5.7 reveal differences due to the different stiffness and damping support conditions of the experimental beam-column system in y- and z-direction as already observed in section 5.1.1.

In figure 5.10b, the amplitude responses orthogonal to the direction of excitation $|G^{sc}_{\alpha^\perp}(\Omega)|$ also lie on top of each other for all shown directions of excitation with sharp resonance peak gains close to the excitation frequency $\Omega/2\pi = 186\,\mathrm{Hz}$. In contrast to figure 5.10a, all shown amplitude responses $|G^{sc}_{\alpha^\perp}(\Omega)|$ decrease rapidly apart from 186 Hz. The peak gains $\widehat{G}^{sc}_{\alpha^\perp}$ according to table 5.7 also reveal differ-

ences due to the different stiffness and damping support conditions of the experimental beam-column system in y- and z-direction. On average, the peak gains in the direction of excitation $\widehat{G}_{\alpha}^{\mathrm{sc}}$ according to table 5.7 are 2.8 times higher than the peak gains orthogonal to the direction of excitation $\widehat{G}_{\alpha^{\perp}}^{\mathrm{sc}}$.

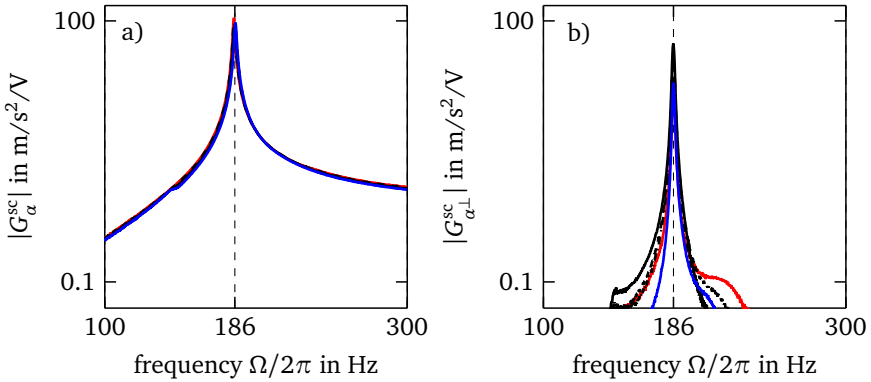

Figure 5.10: Experimental acceleration amplitude responses short circuited,
a) in direction of excitation $|G_{\alpha}^{\mathrm{sc}}(\Omega)|$,
b) orthogonal to direction of excitation $|G_{\alpha^{\perp}}^{\mathrm{sc}}(\Omega)|$,
exc. at α: 0° (——), 22.5° (– –), 45° (——), 67.5° (–·–), 90° (——)

Transducers connected to RL- and RLC-shunts

In figure 5.11a, the amplitude responses with RL-shunts in the direction of excitation $|G_{\alpha}^{\mathrm{RL}}(\Omega)|$ lie on top of each other for all shown directions of excitation with similiar vibration attenuation as observed by similar peak gains $\widehat{G}_{\alpha}^{\mathrm{RL}}$, table 5.7. On average, the peak gains in direction of excitation $\widehat{G}_{\alpha}^{\mathrm{RL}}$ are 25.8 times higher than the peak gains orthogonal to the direction of excitation $\widehat{G}_{\alpha^{\perp}}^{\mathrm{RL}}$. As previously shown by the narrow acceleration orbits due to RL-shunts in figure 5.9a, the acceleration transfer behavior orthogonal to the excitation direction G_{α}^{RL} can be neglected due to the vibration attenuation with RL-shunts. Compared to short circuited peak gains in excitation direction $\widehat{G}_{\alpha}^{\mathrm{sc}}$ in figure 5.10, the peaks with RL-shunts $\widehat{G}_{\alpha}^{\mathrm{RL}}$ are reduced by 89 % on average.

In figure 5.11b, the amplitude responses with RLC-shunts in the direction of excitation $|G_{\alpha}^{\mathrm{RLC}}(\Omega)|$ lie on top of each other for all shown directions of excitation with similiar vibration attenuation as observed by similar peak gains $\widehat{G}_{\alpha}^{\mathrm{RLC}}$, table 5.7. On average, the peak gains in direction of excitation $\widehat{G}_{\alpha}^{\mathrm{RLC}}$ are 18.9 times higher than the peak gains orthogonal to the direction of excitation $\widehat{G}_{\alpha^{\perp}}^{\mathrm{RLC}}$. Analogously to the

vibration attenuation with RL-shunts, the acceleration transfer behavior orthogonal to the excitation direction G_α^{RLC} can be neglected due to the vibration attenuation with RLC-shunts. Compared to short circuited peak gains in excitation direction $\widehat{G}_\alpha^{\mathrm{sc}}$ in figure 5.10, the peaks with RLC-shunts $\widehat{G}_\alpha^{\mathrm{RL}}$ are reduced by 96 % on average.

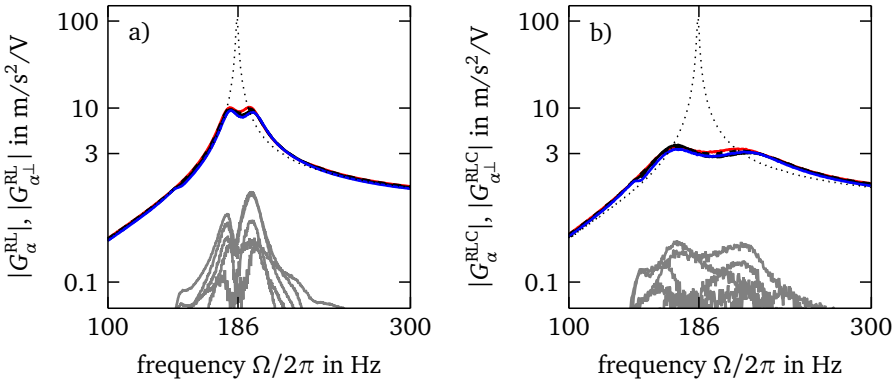

Figure 5.11: Exp. acceleration amplitude resp. with a) RL-shunts, b) RLC-shunts, in direction of excitation $|G_\alpha(\Omega)|$ at α: 0° (——), 22.5° (– –) 45° (——), 67.5° (–·–), 90° (——), orthogonal to direction of excitation $|G_{\alpha^\perp}(\Omega)|$ for all α (——), short circuited $|G_\alpha^{\mathrm{sc}}(\Omega)|$ for $\alpha = 0°$ (·····)

Table 5.7: Experimental peak gains in direction of excitation $\widehat{G}_\alpha$, orthogonal to the direction of excitation $\widehat{G}_{\alpha^\perp}$ and mean values $\mu(\widehat{G})$ from figures 5.10 and 5.11, all in m/s²/V, excitation direction α in degrees

	sc		RL-shunt		RLC-shunt	
α	$\widehat{G}_\alpha$	$\widehat{G}_{\alpha^\perp}$	$\widehat{G}_\alpha$	$\widehat{G}_{\alpha^\perp}$	$\widehat{G}_\alpha$	$\widehat{G}_{\alpha^\perp}$
0	100.75	12.77	10.27	0.29	3.55	0.10
22.5	94.45	34.63	9.94	1.01	3.65	0.28
45	68.80	50.43	9.67	1.10	3.79	0.17
67.5	75.07	37.48	9.42	0.51	3.57	0.30
90	89.63	17.83	9.36	0.32	3.39	0.10
$\mu(\widehat{G})$	85.74	30.63	9.73	0.65	3.59	0.19

Comparing the average vibration attenuation of the beam-column using transducers in support B with RL- and RLC-shunts for different directions of excitation in figure 5.11 with optimal vibration attenuation for excitation in y- and z-direction from figure 5.7, it can be inferred that the lateral beam-column vibrations in the y-z-plane are equally attenuated.

5.3 Summary of results and conclusion

The piezo-elastic support B is capable of attenuating beam-column vibrations in all lateral directions in the y-z-plane with transducers connected to RL- or RLC-shunts, which have been optimally tuned for vibration attenuation in y- and z-direction in the model-based numerical tuning procedure. Experimental lateral beam-column vibrations in the y-z-plane are reduced by 89 % with RL-shunts and by 96 % with RLC-shunts connected to transducers in support B compared to vibrations with short circuited transducers.

After calibrating the support stiffness and transducer properties of the beam-column system's model, the numerical and the experimental beam-column system's dynamic behavior without and with shunts show a good agreement in y- and z-direction. Experimental lateral beam-column vibrations orthogonal to the direction of excitation are small compared to vibrations in direction of excitation when shunts are connected. In the following, beam-column vibrations with shunts connected are the focus of investigation. Therefore, only vibrations in the direction of excitation y_α with $\alpha = 0\,^\circ$ and $\alpha = 90\,^\circ$, which corresponds to y- and z-direction, are considered in simulation and experiment. This chapter investigated the vibration attenuation capability of the piezo-elastic support with shunted transducers when uncertainty is disregarded. In the next chapter, vibration attenuation is investigated when uncertainty due to manufacturing, system assembly and load variations occurs.

6 Uncertainty in vibration attenuation with shunts due to static load, manufacturing and system assembly variations

The capability of the piezo-elastic support B to attenuate lateral beam-column vibrations with transducers connected to RL- and RLC-shunts, when uncertainty is disregarded, has been demonstrated in chapter 5 for the numerical and the experimental beam-column systems from figures 3.3 and 4.1. In general, uncertainty in the dynamic behavior of a host structure with resonant shunted transducers may significantly reduce the capability of vibration attenuation, as discussed in the state of research in section 2.3.2. In order to quantify and evaluate uncertainty in the vibration attenuation with the piezo-elastic support B connected to RL- and RLC-shunts, parameter uncertainty as defined in section 2.3.1 due to static axial tensile and compressive beam-column load variations, manufacturing variations and system assembly variations is considered in this chapter.

6.1 General approach and uncertainty sources

The goal of the uncertainty analysis in this chapter is to quantify changes and variations in the peak gain values $\widehat{G}^{\mathrm{RL}}$ and $\widehat{G}^{\mathrm{RLC}}$ of the acceleration transfer functions with shunts, comparable to figure 2.4b, in order to quantify and compare uncertainty in the vibration attenuation with the two shunt concepts. Uncertainty is evaluated by the discrepancy of the uncertain peak gains and the optimal peak gains, where optimal means that the shunt is optimally tuned and uncertainty is disregarded, chapter 5.

In the uncertainty analysis, the models of the beam-column system with RL- and RLC-shunts derived in chapter 3 are used to propagate uncertain model input parameters through the model to predict uncertainty in the model outputs, [81].

The parameter uncertainty is assumed in such a way that the variations are legitimated by own experiments and literature, [68]. Own experiments are performed to assume parameter uncertainty due to

- static axial tensile and compressive beam-column load variations,
- spring element manufacturing and system assembly variations.

Literature is used to assume parameter uncertainty due to

- shunt circuit components and transducer manufacturing variations.

Static load variations are investigated in own experiments because they affect vibration attenuation with RL- and RLC-shunts, as shown later, and they have not been subject to research so far. Furthermore, spring element manufacturing and system assembly variations affect vibration attenuation, and they have also not been subject to research because of the novelty of the piezo-elastic support. Variations in the shunt circuit components and transducer properties are known to have one of the most significant effect on the vibration attenuation with RL- and RLC-shunts, [21, 56, 73], and, therefore, are additionally considered in the analysis and used to rate uncertainty from own experiments.

Uncertainty due to static axial load, manufacturing and system assembly variations is investigated with the six cases in table 6.1 with their as uncertain assumed parameters. Uncertainty from own experiments and literature is first analyzed individually, cases I to IV, and then combined in cases V and VI. It is shown that uncertainty in cases I and II is similar for the beam-column system in y- and z-direction, hence, uncertainty in cases III to VI is only investigated in y-direction. The cases are described in the next section.

Table 6.1: Cases to investigate uncertainty in the vibration attenuation

Case	uncertainty source(s)	uncertain parameter(s)	investigated in section
I	static load	F_x	6.2
II	spring element manufacturing and system assembly	$k_{y,\mathrm{A/}B}$, $k_{\varphi_y,\mathrm{A/B}}$, $l_{\mathrm{ext,A/B}}$, $k_{z,\mathrm{A/}B}$, $k_{\varphi_z,\mathrm{A/B}}$	6.3
III	shunt component manufacturing	$R_y^{\square}$, $C_y^{\square}$	6.4
IV	transducer manufacturing	$k_{y,\mathrm{B}}^{\mathrm{sc}}$, $d_{3,y,\mathrm{B}}$, $C_{y,\mathrm{B}}$	6.4
V	combination of cases II, III and IV	see cases II, III and IV	6.5
VI	combination of cases I to IV	see cases I to IV	6.5

6.1.1 Description of investigated cases

The variation of parameters in table 6.1 is assumed to be probabilistic due to manufacturing and system assembly and non-probabilistic due to static load, section 2.3.1. The probabilistic variation of parameters due to manufacturing and system assembly in cases II, III and IV is assumed to be normally distributed.

Case I: Static axial tensile and compressive beam-column load variations result from static load variations about a nominal load as they may occur in truss-like structures comprising beam-columns, such as the upper truss of the SFB-Demonstrator in figure 2.3. To investigate this effect on the vibration attenuation, non-probabilistic uncertainty is assumed with static axial force F_x in figure 3.2 varying around the unloaded case $F_x = 0\,\mathrm{N}$ within lower tensile and upper compressive force limit $F_x = [F_x^-, F_x^+]$. Non-probabilistic uncertainty is compared for the tensile (t) load case $F_x^{\mathrm{t}} = [F_x^-; F_x^0]$ and the compressive (c) load case $F_x^{\mathrm{c}} = [F_x^0, F_x^+]$.

Case II: The spring element manufacturing process underlies variations in the process quantities that are assumed to cause variations in the elastic support stiffness properties and axial extension length as explained in section 4.1.2 and shown in figure 4.5. To investigate this effect on the vibration attenuation, different spring elements produced with the same nominal requirements are used in support B. Support A is not investigated for manufacturing variations, and the spring element is not changed. However, in order to change the spring element in support B, the beam-column system has to be disassembled and reassembled according to the assembly sequence described in section 4.1.2. For simplification, manufacturing and assembly variations in case II are treated superposed. To represent superposed manufacturing and system assembly variations, solely the lateral support stiffness $k_{y,\mathrm{A/}B}$ and $k_{z,\mathrm{A/}B}$, the rotational support stiffness $k_{\varphi_z,\mathrm{A/B}}$ and $k_{\varphi_y,\mathrm{A/B}}$ as well as the axial extension length $l_{\mathrm{ext,A/B}}$ of the beam-column system's model in figure 3.4 are assumed to vary. Mean values μ_X and standard deviations σ_X of assumed normal distributions are obtained from own experiments.

Case III: The adjustable and constant circuit parameters of the RL-shunt in figure 3.8 and the RLC-shunt in figure 3.9 underlie manufacturing variations. To investigate this effect on the vibration attenuation, the resistance $R_y^{\boxdot}$ of the resistors and capacitance $C_y^{\boxdot}$ of the capacitors in the shunt circuits are assumed to vary normally distributed with standard deviations σ_X assumed from manufacturer tolerances.

Case IV: The piezoelectric transducers in support B underlie manufacturing variations. To investigate this effect on the vibration attenuation, the transducer prop-

erties $k_{y,\mathrm{B}}^{\mathrm{sc}}$, $d_{3,y,\mathrm{B}}$ and $C_{y,\mathrm{B}}$, refer to section 3.3.3, are assumed to vary normally distributed with standard deviations σ_X assumed from manufacturer tolerances.

Case V: To investigate the combined effect of manufacturing and system assembly variations on the vibration attenuation, the probabilistic parameter uncertainty from cases II, III and IV is combined.

Case VI: The combination of non-probabilistic uncertainty due to static load variations from case I and probabilistic uncertainty due to manufacturing and system assembly variations from case V is analyzed. Therefore, the effects of the tensile force $F_x = F_x^-$ and the compressive force $F_x = F_x^+$ are investigated.

6.1.2 Concept to assume and quantify uncertainty from own experiments and literature

Own experiments

To assume and quantify uncertainty in the vibration attenuation from own experiments, the experimental and the numerical beam-column system without shunts and with shunts are used according to the following four steps:

1. Quantification of uncertainty by experiments without shunts: In order to explain the effect of the assumed uncertain parameters with respect to vibration attenuation with resonant shunted transducers, uncertainty in the experimental short circuited resonance frequencies $\omega_{y/z,\mathrm{exp}}^{\mathrm{sc}}$, GEMCCs $\gamma_{y/z,\mathrm{exp}}$ and static capacitances $C_{y/z,\mathrm{exp}}^{\mathrm{s}}$, the characteristic quantities of the experimental beam-column system's dynamic behavior without shunts in table 3.1 is quantified.

2. Calibration of model without shunts considering uncertainty: The beam-column system's model without shunts is calibrated to adequately represent the observed uncertainty in the characteristic quantities from (1.).

- For case I, the geometric portions of the lateral and the rational support stiffness $k_{y,\mathrm{A/B,g}}$, $k_{z,\mathrm{A/B,g}}$, $k_{\varphi_y,\mathrm{A/B,g}}$, $k_{\varphi_z,\mathrm{A/B,g}}$, in (3.12) are calibrated.
- For case II, μ_X and σ_X of the lateral support stiffness $k_{y,\mathrm{A/}B}$ and $k_{z,\mathrm{A/}B}$, the rotational support stiffness $k_{\varphi_z,\mathrm{A/B}}$ and $k_{\varphi_y,\mathrm{A/B}}$ as well as the axial extension length $l_{\mathrm{ext,A/B}}$ are estimated from a set of model calibrations.

3. Prediction of uncertainty by model with shunts: Uncertainty in the numerical peak gains with RL-shunts $\widehat{G}_{y/z,\mathrm{num}}^{\mathrm{RL}}$ and with RLC-shunts $\widehat{G}_{y/z,\mathrm{num}}^{\mathrm{RLC}}$ is predicted with

the beam-column system's model with shunts by use of the calibrated parameters from (2.).

4. Validation of predicted uncertainty: Uncertainty in the experimental peak gains with shunts $\widehat{G}^{\mathrm{RL}}_{y/z,\mathrm{exp}}$ and $\widehat{G}^{\mathrm{RLC}}_{y/z,\mathrm{exp}}$ is quantified and compared to numerically predicted results from (3.) to validate the predicted uncertainty.

Literature

Probabilistic parameter uncertainty due to manufacturing variations is assumed from manufacturer tolerances. The lower and upper ranges of the tolerance are expected to represent $\pm 3\sigma$ with 99.7% probability, which is an accepted approach to derive a standard deviation for assuming normal distribution, [86]. The parameter uncertainty is used in the beam-column system's model with shunts to predict uncertainty in the numerical peak gains $\widehat{G}^{\mathrm{RL}}_{y,\mathrm{num}}$ and $\widehat{G}^{\mathrm{RLC}}_{y,\mathrm{num}}$.

Disregarded uncertainty and assumptions

Variations in mechanical material properties, such as the Young's modulus E_{b} and the density ϱ_{b} of the beam-column, are generally neglected. Furthermore, cross-sections parameters, e.g. radius r_{b} of the beam-column, and the length of the beam-column are assumed to be constant. Variations in the structural modal damping coefficient ζ and in the dielectric loss resistances $R_{y,\mathrm{B}}$ and $R_{z,\mathrm{B}}$ of transducers in support B are assumed to be small and are not taken into account.

Moreover, the beam-column system's model without and with shunts is considered not uncertain and, therefore, model uncertainty is not taken into account in this work. Like for the deterministic beam-column system's dynamic behavior in section 5, the system's dynamic behavior is still considered independent in y- and z-direction and, therefore, also treated stochastically independent and separately in the lateral directions in this chapter.

6.2 Case I: Effect of static axial tensile and compressive load variations

This section presents experimental and numerical results to quantify non-probabilistic uncertainty in the vibration attenuation in y- and z-direction due to static axial tensile and compressive load variations as introduced by case I in table 6.1. The beam-column is loaded by the axial force F_x in the symmetric force range $F_x^- = -1200\,\mathrm{N} \leq F_x \leq 1200\,\mathrm{N} = F_x^+$. This force range was chosen by the author to ensure that elastic deformations of the beam-column and the spring elements remain small and, therefore, can be neglected as introduced in section 3.3.1. The following sections 6.2.1 to 6.2.4 present the results of the four steps used to assume and quantify uncertainty from own experiments as shown in section 6.1.2.

6.2.1 Quantification of uncertainty by experiments without shunts

The experimental short circuited acceleration transfer functions $G^{\mathrm{sc}}_{y/z,\mathrm{exp}}(\Omega, F_x)$ (4.7) with short circuited electrodes of transducers in support B and the experimental capacitance transfer functions $Y_{y/z,\mathrm{exp}}(\Omega, F_x)$ (4.10) of transducers in support B of the beam-column in figure 4.1 are measured for experimental static axial forces

$$\boldsymbol{F}_{x,\mathrm{exp}} = [-1200, -800, -400, -200, 0, 200, 400, 800, 1200]\mathrm{N} \tag{6.1}$$

applied with the spindle-type lifting gear.

Figure 6.1 shows the transfer functions $G^{\mathrm{sc}}_{y/z,\mathrm{exp}}(\Omega, F_x)$ and $Y_{y/z,\mathrm{exp}}(\Omega, F_x)$ of the unloaded beam-column with F_x^0 and for tensile and compressive forces F_x^- and F_x^+. To quantify the effect of static loading on the beam-column system's dynamic behavior without shunts, figure 6.2 shows the experimental characteristic quantities from table 3.1, the short circuited frequencies $\omega^{\mathrm{sc}}_{y/z,\mathrm{exp}}$, GEMCCs $\gamma_{y/z,\mathrm{exp}}$ and static capacitances $C^{\mathrm{s}}_{y/z,\mathrm{exp}}$ for all forces $\boldsymbol{F}_{x,\mathrm{exp}}$ (6.1), obtained with modal dynamic capacitance fits section 4.3.3. The experimental values of the characteristic quantities for the tensile F_x^{t} and the compressive F_x^{c} load case are summarized in table 6.2.

Experimental transfer functions

In figures 6.1a and b, the tensile force F_x^- detunes the beam-column resonance vibration in y- and z-direction towards higher frequencies due to increased lateral beam-column stiffness, which is observed by the resonance peak in the amplitude

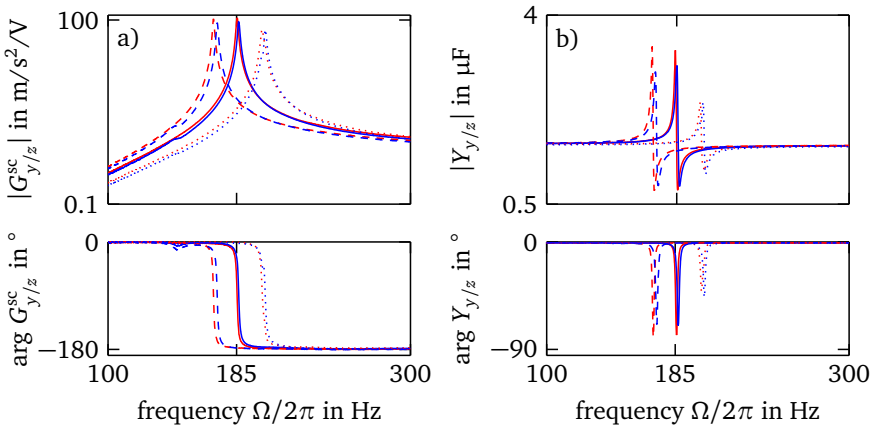

Figure 6.1: Case I: experimental beam-column system transfer functions without shunts subject to axial force F_x, a) $G^{sc}_{y/z,exp}(\Omega, F_x)$, b) $Y_{y/z,exp}(\Omega, F_x)$, y-direction: tensile F_x^- (⋯⋯), compressive F_x^+ (– –), unloaded F_x^0 (——), z-direction: tensile F_x^- (⋯⋯), compressive F_x^+ (– –), unloaded F_x^0 (——)

responses and the phase shifts in the phase responses, which are both on the right of the unloaded beam-column. Contrary, the compressive force F_x^+ reduces the lateral beam-column stiffness and, therefore, detunes the beam-column resonance vibration towards lower frequencies.

Experimental characteristic quantities

In figure 6.2, starting from the unloaded beam-column at F_x^0, all characteristic quantities increase or decrease monotonically for the investigated tensile and compressive forces. Furthermore, the slopes for tensile and compressive force are different. Based on the observed monotonic trends, non-probabilistic uncertainty due to the tensile and compressive load case is quantified by the following intervals:

Tensile load case $F_x = [F_x^-; F_x^0] = [-1200\,\mathrm{N}; 0\,\mathrm{N}]$: The short circuited resonance frequencies $\omega^{sc}_{y/z}$ increase and fall into the intervals $\omega^{sc}_{y/z} = [\omega^{sc}_{y/z}(F_x^0), \omega^{sc}_{y/z}(F_x^-)]$. Contrary, the transducer GEMCCs $\gamma_{y/z}$ reduce and fall into the intervals $\gamma_{y/z} = [\gamma_{y/z}(F_x^-), \gamma_{y/z}(F_x^0)]$. Likewise, the transducer static capacitances $C^s_{y/z}$ reduce and fall into the intervals $C^s_{y/z} = [C^s_{y/z}(F_x^0), C^s_{y/z}(F_x^-)]$. All three parameters are affected comparably in y- and z-direction by the force F_x^-. The GEMCCs $\gamma_{y/z}$ show the most relative change for F_x^- compared to F_x^0, whereas the static capacitances $C^s_{y/z}$ hardly change, table 6.2.

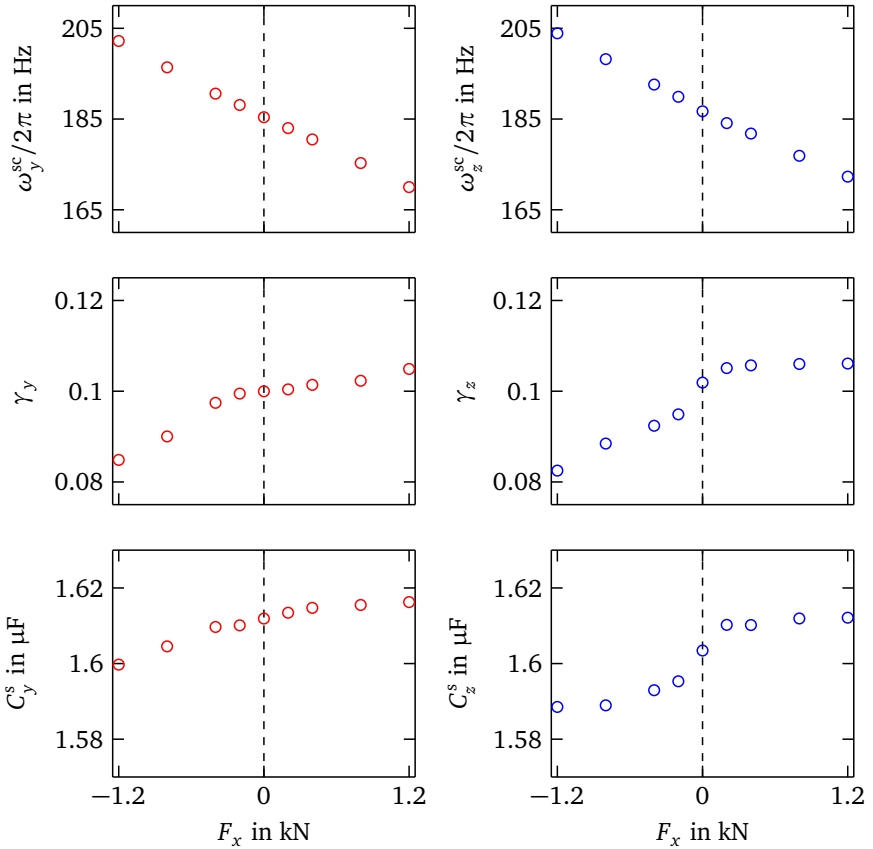

Figure 6.2: Case I: experimental short circuited frequencies $\omega^{sc}_{y/z,exp}(F_X)$, GEMCCs $\gamma_{y/z,exp}(F_X)$ and static capacitances $C^s_{y/z,exp}(F_X)$ subject to axial forces $\boldsymbol{F}_{x,exp}$, left: y-direction (o), right: z-direction (o)

Compressive load case $F_x = [F_x^0; F_x^+] = [0\,\text{N}; +1200\,\text{N}]$**:** The short circuited resonance frequencies $\omega^{sc}_{y/z}$ decrease and fall into the intervals $\omega^{sc}_{y/z} = [\omega^{sc}_{y/z}(F_x^+), \omega^{sc}_{y/z}(F_x^0)]$. Contrary, the transducer GEMCCs $\gamma_{y/z}$ increase and fall into the intervals $\gamma_{y/z} = [\gamma_{y/z}(F_x^0), \gamma_{y/z}(F_x^+)]$. Likewise, the transducer static capacitances $C^s_{y/z}$ increase and fall into the intervals $C^s_{y/z} = [C^s_{y/z}(F_x^0), C^s_{y/z}(F_x^+)]$. Again, all three parameters are affected comparably in y- and z-direction by the force F_x^+. Contrary to the tensile load case, the short circuited resonance frequencies $\omega^{sc}_{y/z}$ show the most relative change for F_x^+ compared to F_x^0, table 6.2. Comparable to the tensile load case, the static capacitances $C^s_{y/z}$ hardly change.

Table 6.2: Case I: exp. short circuited frequencies $\omega^{sc}_{y/z,exp}/2\pi$ in Hz, GEMCCs $\gamma_{y/z,exp}$ and static capacitances $C^{s}_{y/z,exp}$ in µF for tensile force F^{-}_{x}, compressive force F^{+}_{x} and unloaded F^{0}_{x} from figure 6.2, relative changes in %

	absolute change			relative change	
X	$X(F^{-}_{x})$	$X(F^{0}_{x})$	$X(F^{+}_{x})$	$X(F^{-}_{x})/X(F^{0}_{x})$	$X(F^{+}_{x})/X(F^{0}_{x})$
$\omega^{sc}_{y}/2\pi$	201.8	185.4	170.1	+8.8	−8.2
$\omega^{sc}_{z}/2\pi$	203.9	186.7	172.3	+9.2	−7.7
γ_{y}	0.085	0.099	0.105	−14.1	+6.0
γ_{z}	0.083	0.102	0.106	−18.6	+4.0
C^{s}_{y}	1.599	1.612	1.616	−0.8	+0.2
C^{s}_{z}	1.589	1.603	1.612	−0.9	+0.6

In general, a tensile force increases and a compressive force decreases the lateral stiffness of a beam-column, as also modeled in the beam-column stiffness matrix in (3.14). Consequently, the short circuited resonance frequencies increase and decrease (3.50), as observed in 6.2. The GEMCCs are affected conversely. This explains as follows: The transducer open circuited stiffness (3.24) and short circuited stiffness (3.25) are not affected by the axial force and, consequently, the difference between the global beam-column open circuited stiffness (3.44) and short circuited stiffness (3.46) decreases for a tensile and increase for a compressive force, compare to (3.53) and [51]. The static capacitances behave comparable to the GEMCCs, as explained in [55]. The different non-linear slopes for tensile and compressive forces observed in the characteristic quantities in figure 6.2 are attributed to the spring element in the supports A and B, figure 4.2. Comparable to the beam-column, the elements show stiffening and softening effects. Therefore, the geometric portions of the lateral and the rational support stiffness properties in the model are calibrated in the next section to represent the experimental force dependent elastic behavior.

6.2.2 Calibration of model without shunts considering uncertainty

The non-linear and non-symmetric spring element stiffness behavior observed for the tensile and compressive forces in figure 6.2 is approximated in the beam-column system's model with the linear elastic stiffness behavior of the lateral and rotational support stiffness properties in (3.12). In the model calibration, the geometric portions of the support stiffness properties

$$\boldsymbol{P} = [k_{y,\mathrm{A/B,g}},\, k_{z,\mathrm{A/B,g}},\, k_{\varphi_y,\mathrm{A/B,g}},\, k_{\varphi_z,\mathrm{A/B,g}}] \tag{6.2}$$

are varied to solve the sum of error squares optimization problem (4.14) by using the experimental short circuited and the capacitance transfer functions in figure 6.2. All other parameters are kept constant. The calibrated values of the geometric lateral and rotational support stiffness in support A and B are summarized in table 6.3.

Table 6.3: Case I: calibrated geometric lateral and rotational support stiffness

$k_{y,\mathrm{A/B,g}}$ in N/m/N	$k_{z,\mathrm{A/B,g}}$ in N/m/N	$k_{\varphi_y,\mathrm{A/B,g}}$ in Nm/rad/N	$k_{\varphi_z,\mathrm{A/B,g}}$ Nm/rad/N
2.0871	2.5788	0.0465	0.0447

Figure 6.3 compares the experimental characteristic quantities from figure 6.2 to numerical results after the calibration. The beam-column system's model with beam-column and elastic support stiffness properties, which linearly depend on the axial force F_x, represents the experimental beam-column behavior adequately with acceptable deviations of simulation and experiment, see table 6.4.

Table 6.4: Case I: exp. and num. short circuited frequencies $\omega^{\mathrm{sc}}_{y/z,}(F_x)/2\pi$ in Hz, GEMCCs $\gamma_{y/z,}(F_x)$ and static capacitances $C^{\mathrm{s}}_{y/z,}(F_x)$ in µF for tensile force F_x^-, compressive force F_x^+, unloaded F_x^0 from figure 6.3, rel. dev. in %

	experimental		numerical		relative deviation	
X	$X(F_x^-)$	$X(F_x^+)$	$X(F_x^-)$	$X(F_x^+)$	$\mathrm{err}(X(F_x^-))$	$\mathrm{err}(X(F_x^+))$
$\omega^{\mathrm{sc}}_y/2\pi$	202.20	170.04	201.75	170.00	0.2	0.0
$\omega^{\mathrm{sc}}_z/2\pi$	203.89	172.34	203.82	172.07	0.0	0.2
γ_y	0.085	0.105	0.090	0.104	-5.3	1.3
γ_z	0.082	0.106	0.093	0.107	-11.3	-0.7
C^{s}_y	1.600	1.616	1.596	1.620	0.3	-0.3
C^{s}_z	1.588	1.612	1.589	1.614	-0.1	-0.1

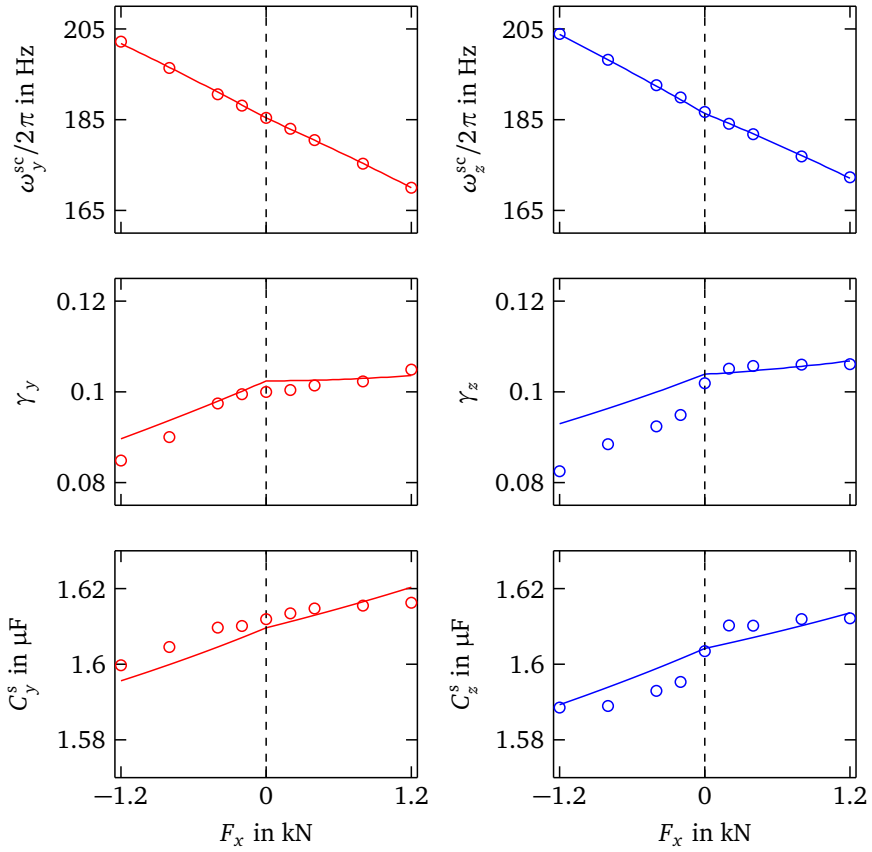

Figure 6.3: Case I : experimental and numerical short circuited frequencies $\omega_{y/z}^{sc}(F_X)$, GEMCCs $\gamma_{y/z}(F_X)$ and static capacitances $C_{y/z}^{s}(F_X)$ subject to axial forces $\boldsymbol{F_x}$, experimental results from figure 6.2,
left: y-direction experimental (o) and numerical (——),
right: z-direction experimental (o) and numerical (——)

6.2.3 Prediction of uncertainty by model with shunts

Non-probabilistic uncertainty in the vibration attenuation with RL- and RLC-shunts due to static axial tensile and compressive beam-column load variations is predicted by using the beam-column system's model with shunts, section 3.4. The optimal shunt resistances from table 5.4 and the calibrated geometric lateral and rotational support stiffness properties from table 6.3 are used in the simulation.

Figure 6.4 shows the numerical acceleration transfer functions with RL-shunts $G^{\mathrm{RL}}_{y/z,\mathrm{num}}(\Omega, F_x)$ (3.94) and with RLC-shunts $G^{\mathrm{RLC}}_{y/z,\mathrm{num}}(\Omega, F_x)$ (3.95) for the unloaded beam-column with F_x^0 and for tensile and compressive forces F_x^- and F_x^+. Figure 6.5 shows the numerical peak gains with RL-shunts $\widehat{G}^{\mathrm{RL}}_{y/z,\mathrm{num}}(F_x)$ (3.96) and with RLC-shunts $\widehat{G}^{\mathrm{RLC}}_{y/z,\mathrm{num}}(F_x)$ (3.98) of the acceleration transfer functions in for the whole investigated force range $-1200\,\mathrm{N} \leq F_x \leq 1200\,\mathrm{N}$. The numerical values of the peak gains for the tensile and the compressive load case are summarized in table 6.5.

Numerical transfer functions

For vibration attenuation with RL- and RLC-shunts in figure 6.4, the tensile force F_x^- and the compressive force F_x^+ detune the beam-column vibration in y- and

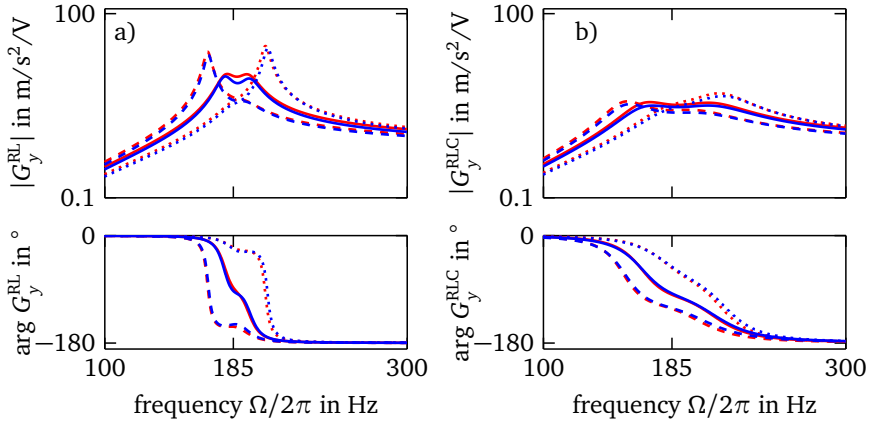

Figure 6.4: Case I: numerical accelerations transfer functions with shunts subject to force F_x, a) $G^{\mathrm{RL}}_{y/z,\mathrm{num}}(\Omega, F_x)$, b) $G^{\mathrm{RLC}}_{y/z,\mathrm{num}}(\Omega, F_x)$, y-direction: tensile F_x^- (····), compressive F_x^+ (– –), unloaded F_x^0 (——), z-direction: tensile F_x^- (····), compressive F_x^+ (– –), unloaded F_x^0 (——)

z-direction towards higher and lower frequencies, as explained before in section 6.2.1. Consequently, the RL- and RLC-shunts are not optimally tuned anymore to the beam-column resonance vibration behavior. This reduces the capability of vibration attenuation similarly in y- and z-direction, as observed by the increasing peak gains.

Numerical peak gains

In figure 6.5a, starting from the unloaded beam-column, the peak gains with RL-shunts in y- and z-direction increase monotonically for the investigated tensile and compressive forces. A comparable behavior is observed for the peak gains with RLC-shunts in y- and z-direction in figure 6.5b. However, the effect is much smaller. Based on the observed monotonic trends, non-probabilistic uncertainty due to the tensile and compressive load case is quantified by the following intervals.

Tensile load case $F_x = [F_x^-; F_x^0] = [-1200\,\mathrm{N}; 0\,\mathrm{N}]$**:** With RL-shunts, the peak gains $\widehat{G}^{\mathrm{RL}}_{y/z}$ increase by factor 2.87 in y-direction and 3.07 in z-direction for F_x^- compared to F_x^0 and fall into the intervals $\widehat{G}^{\mathrm{RL}}_{y/z} = [\widehat{G}^{\mathrm{RL}}_{y/z}(F_x^0), \widehat{G}^{\mathrm{RL}}_{y/z}(F_x^-)]$, table 6.5. With RLC-shunts, the peak gains $\widehat{G}^{\mathrm{RLC}}_{y/z}$ increase by factor 1.41 in y-direction and 1.42 in z-direction for F_x^- compared to F_x^0 and fall into the intervals $\widehat{G}^{\mathrm{RLC}}_{y/z} = [\widehat{G}^{\mathrm{RLC}}_{y/z}(F_x^0), \widehat{G}^{\mathrm{RLC}}_{y/z}(F_x^-)]$.

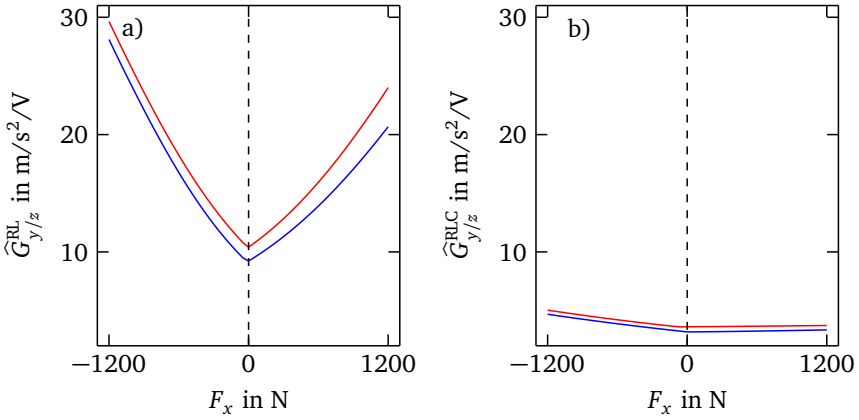

Figure 6.5: Case I: numerical peak gains with shunts subject to axial force F_x,
a) $\widehat{G}^{\mathrm{RL}}_{y,\mathrm{num}}(F_x)$ (——), $\widehat{G}^{\mathrm{RL}}_{z,\mathrm{num}}(F_x)$ (——),
b) $\widehat{G}^{\mathrm{RLC}}_{y,\mathrm{num}}(F_x)$ (——), $\widehat{G}^{\mathrm{RLC}}_{z,\mathrm{num}}(F_x)$ (——)

Compressive load case $F_x = [F_x^0; F_x^+] = [0\,\mathrm{N}; +1200\,\mathrm{N}]$**:** With RL-shunts, the peak gains $\widehat{G}_{y/z}^{\mathrm{RL}}$ increase by factor 2.32 in y-direction and 2.26 in z-direction for F_x^- compared to F_x^0 and fall into the intervals $\widehat{G}_{y/z}^{\mathrm{RL}} = [\widehat{G}_{y/z}^{\mathrm{RL}}(F_x^0), \widehat{G}_{y/z}^{\mathrm{RL}}(F_x^+)]$, table 6.5. With RLC-shunts, the peak gains $\widehat{G}_{y/z}^{\mathrm{RLC}}$ increase by factor 1.04 in y-direction and decrease by factor 1.01 in z-direction for F_x^+ compared to F_x^0 and fall into the intervals $\widehat{G}_{y/z}^{\mathrm{RLC}} = [\widehat{G}_{y/z}^{\mathrm{RLC}}(F_x^0), \widehat{G}_{y/z}^{\mathrm{RLC}}(F_x^+)]$.

Table 6.5: Case I: num. peak gains with shunts $\widehat{G}_{\mathrm{num}}^{\mathrm{RL}}(F_x)$ and $\widehat{G}_{\mathrm{num}}^{\mathrm{RLC}}(F_x)$ for tensile force F_x^-, compressive force F_x^+, unloaded F_x^0 from figure 6.5 in m/s^2/V

	absolute change			relative change	
X	$X(F_x^-)$	$X(F_x^0)$	$X(F_x^+)$	$X(F_x^-)/X(F_x^0)$	$X(F_x^+)/X(F_x^0)$
$\widehat{G}_y^{\mathrm{RL}}$	29.64	10.34	24.01	2.87	2.32
$\widehat{G}_z^{\mathrm{RL}}$	28.10	9.14	20.67	3.07	2.26
$\widehat{G}_y^{\mathrm{RLC}}$	5.04	3.57	3.73	1.41	1.04
$\widehat{G}_z^{\mathrm{RLC}}$	4.69	3.31	3.36	1.42	1.01

Comparing the numerical peak gains with RL- and RLC-shunts for the tensile and compressive load case, it can be concluded that vibration attenuation with RLC-shunts is less sensitive to detuning of the beam-column's resonance caused by a static tensile or compressive force F_x, than it is for vibration attenuation with RL-shunts. Furthermore, vibration attenuation with RL- and RLC-shunts is more sensitive to a tensile force than to a compressive force of the same value, figure 6.5. This can be explained with the experimental behavior in table 6.2, where a tensile force detunes the short circuit frequencies more and, aditionally, reduces the GEMCC. However, the main reason for the asymmetric behavior could be related to the elastic behavior of the piezo-elasic support, figure 4.2.

6.2.4 Validation of predicted uncertainty

Non-probabilistic uncertainty in the experimental beam-column vibration attenuation with RL- and RLC-shunts is quantified and compared to numerical results from last section in order to evaluate the numerically predicted uncertainty. The experimental acceleration transfer functions with RL-shunts $G_{y/z,\mathrm{exp}}^{\mathrm{RL}}(\Omega, F_x)$ and with RLC-shunts $G_{y/z,\mathrm{exp}}^{\mathrm{RLC}}(\Omega, F_x)$ (4.7) of the beam-column system in figure 4.1 are measured for experimental static axial forces $\boldsymbol{F}_{x,\mathrm{exp}}$ (6.1) applied with the spindle-type lifting gear.

Experimental transfer functions

Figure 6.6 shows the experimental acceleration transfer functions with RL-shunts $G^{\mathrm{RL}}_{y/z,\mathrm{exp}}(\Omega, F_x)$ and with RLC-shunts $G^{\mathrm{RLC}}_{y/z,\mathrm{exp}}(\Omega, F_x)$ (4.7) for the unloaded beam-column with F_x^0 and for tensile and compressive forces F_x^- and F_x^+. Similarly to the numerical simulation in figure 6.4, the tensile force F_x^- and the compressive force F_x^+ detune the beam-column vibration in y- and z-direction towards higher and lower frequencies and, thus, reduce the capability of vibration attenuation, similarly in y- and z-direction.

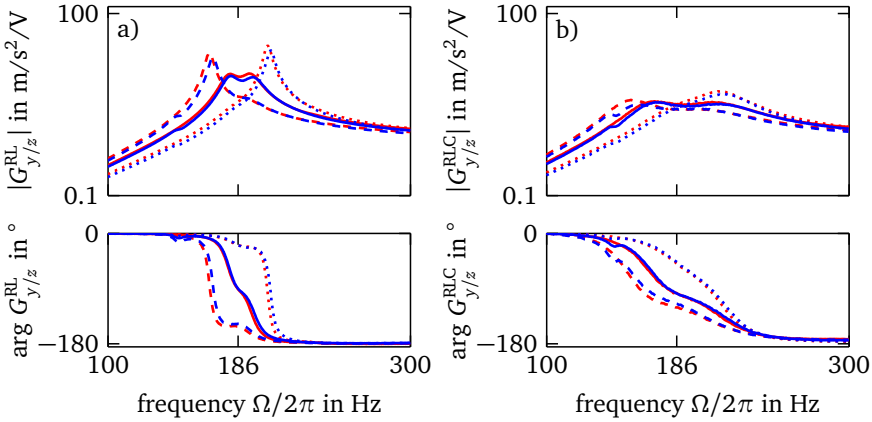

Figure 6.6: Case I: exp. accelerations transfer functions with shunts subject to axial force F_x, a) $G^{\mathrm{RL}}_{y/z,\mathrm{exp}}(\Omega, F_x)$, b) $G^{\mathrm{RLC}}_{y/z,\mathrm{exp}}(\Omega, F_x)$,
y-direction: tensile F_x^- (····), compressive F_x^+ (– –), unloaded F_x^0 (——),
z-direction: tensile F_x^- (····), compressive F_x^+ (– –), unloaded F_x^0 (——)

Comparison of experimental and numerical peak gains

Figure 6.7 shows experimental peak gains with RL-shunts $\widehat{G}^{\mathrm{RL}}_{z,\mathrm{exp}}(F_x)$ and with RLC-shunts $\widehat{G}^{\mathrm{RLC}}_{z,\mathrm{exp}}(F_x)$ of the acceleration transfer functions with shunts for $\boldsymbol{F}_{x,\mathrm{exp}}$ (6.1) together with the numerical results form figure 6.5. The experimental values and numerical curves of the peak gains with RL- and RLC-shunts in figure 6.7 show the same trends for tensile and compressive forces. The relative deviations in the peak gains for the tensile and compressive load case in table 6.6 are within acceptable limits.

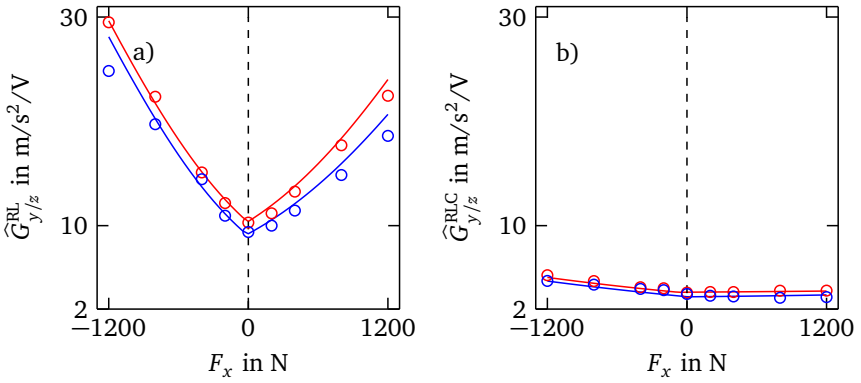

Figure 6.7: Case I: exp. and num. peak gains with shunts subject to force F_x
a) $\widehat{G}^{\mathrm{RL}}_{y,\mathrm{exp}}(F_x)$ (o), $\widehat{G}^{\mathrm{RL}}_{y,\mathrm{num}}(F_x)$ (——), $\widehat{G}^{\mathrm{RL}}_{z,\mathrm{exp}}(F_x)$ (o), $\widehat{G}^{\mathrm{RL}}_{z,\mathrm{num}}(F_x)$ (——),
b) $\widehat{G}^{\mathrm{RLC}}_{y,\mathrm{exp}}(F_x)$ (o), $\widehat{G}^{\mathrm{RLC}}_{y,\mathrm{num}}(F_x)$ (——), $\widehat{G}^{\mathrm{RLC}}_{z,\mathrm{exp}}(F_x)$ (o), $\widehat{G}^{\mathrm{RLC}}_{z,\mathrm{num}}(F_x)$ (——)

Table 6.6: Case I: exp. and num. peak gains with shunts $\widehat{G}^{\mathrm{RL}}_{y/z,}(F_x)$ and $\widehat{G}^{\mathrm{RLC}}_{y/z,}(F_x)$ for tensile force F_x^-, compressive force F_x^+, peak gains in m/s^2/V, relative deviation in %

	experimental		numerical		relative deviation	
X	$X(F_x^-)$	$X(F_x^+)$	$X(F_x^-)$	$X(F_x^+)$	$\mathrm{err}(X(F_x^-))$	$\mathrm{err}(X(F_x^+))$
$\widehat{G}^{\mathrm{RL}}_{y}$	29.50	22.45	29.64	24.01	−0.5	−6.5
$\widehat{G}^{\mathrm{RL}}_{z}$	24.83	18.61	28.10	20.67	−11.7	−10.0
$\widehat{G}^{\mathrm{RLC}}_{y}$	5.25	3.77	5.04	3.73	4.2	1.1
$\widehat{G}^{\mathrm{RLC}}_{z}$	4.70	3.15	4.69	3.36	0.3	−6.2

6.2.5 Summary of results and conclusion for case I

A static axial tensile or compressive load affects the dynamic behavior of the beam-column system and, hence, represents an important source of uncertainty that can significantly reduce the vibration attenuation with RL- and RLC-shunts as it has been shown in section 6.2 by experiments and simulation.

For the experimental beam-column system without shunts, the short circuited resonance frequencies $\omega^{\mathrm{sc}}_{y/z}$ increase for an increasing tensile force and decrease for an increasing compressive force F_x, compared to the unloaded beam-column. In

contrast, the GEMCCs $\gamma_{y/z}$ and the static capacitances $C^{s}_{y/z}$ decrease for a tensile and increase for a compressive force. The effect of tensile and compressive loading is monotonic and similar in y- and z-direction. The effect of a tensile force exceeds the effect of a compressive force due to the non-symmetric lateral beam-column system's elastic stiffness behavior caused by the piezo-elastic supports. After calibration of the geometric portions of the lateral and rotational support stiffness properties in (3.12), the influence of F_x is well represented in the beam-column's model without shunts.

For the numerical beam-column system with shunts, the peak gains with RL-shunt $\widehat{G}^{\mathrm{RL}}_{y/z}$ and with RLC-shunts $\widehat{G}^{\mathrm{RLC}}_{y/z}$ increase monotonically and non-linearly for an increasing tensile or compressive force F_x. The peak gains with RL-shunts are always greater than with RLC-shunts. For the tensile force $F_x^- = -1200\,\mathrm{N}$, the peak gains with RL-shunts are greater by a factor of 2.16. For the compressive force $F_x^+ = 1200\,\mathrm{N}$, the peak gains with RL-shunts are greater by a factor of 2.29. This suggests that vibration attenuation with RLC-shunts is less sensitive to variations in static tensile or compressive axial loading and, hence, less uncertain.

The experimentally observed and the numerically predicted peak gains with RL- and RLC-shunts show an adequate agreement for the investigated force range with a maximal relative deviation of 13.2 %. The experimental and numerical beam-column system's dynamic behavior without and with shunts is similar in y- and z-direction.

6.3 Case II: Effect of spring element manufacturing and system assembly variations

This section presents experimental and numerical results to quantify probabilistic uncertainty in the vibration attenuation in y- and z-direction due to spring element manufacturing and system assembly variations as introduced by case II in table 6.1. Probabilistic uncertainty is quantified based on a set of frequency transfer functions obtained for S different spring elements in support B in figure 4.2 and A iterations of system assembly for each spring element, table 6.7.

Table 6.7: Case II: samples of experimental frequency transfer functions in y- and z-direction for S spring elements and A iterations of system assembly

	S	A	$S \times A$
$G^{\mathrm{sc}}_{y/z}(\Omega)$	10	5	50
$Y_{y/z}(\Omega)$	10	5	50
$G^{\mathrm{RL}}_{y/z}(\Omega)$	10	1	10
$G^{\mathrm{RLC}}_{y/z}(\Omega)$	10	1	10

The following sections 6.3.1 to 6.3.4 present the results of the four steps used to assume and quantify uncertainty from own experiments as shown in section 6.1.2.

6.3.1 Quantification of uncertainty by experiments without shunts

The experimental short circuited acceleration transfer functions $G^{\mathrm{sc}}_{y/z,\mathrm{exp}}(\Omega)$ (4.7) and the experimental capacitance transfer functions $Y_{y/z,\mathrm{exp}}(\Omega)$ (4.10) of the experimental beam-column system without shunts in figure 4.1 are measured for $S \times A = 50$ samples, table 6.7. Variations in the beam-column system's dynamic behavior without shunts are quantified by variations in the characteristic quantities, table 3.1. Therefore, short circuited frequencies $\omega^{\mathrm{sc}}_{y/z,\mathrm{exp}}$, GEMCCs $\gamma_{y/z,\mathrm{exp}}$ and static capacitances $C^{\mathrm{s}}_{y/z,\mathrm{exp}}$ for all $S \times A = 50$ samples are obtained with modal dynamic capacitance fits, refer to section 4.3.3.

Experimental transfer functions

Figures 6.8 and 6.9 show the variations of $S \times A = 50$ experimental short circuited acceleration transfer functions $G^{\mathrm{sc}}_{y/z,\mathrm{exp}}(\Omega)$ and capacitance transfer functions

$Y_{y/z,\mathrm{exp}}(\Omega)$ (4.10) via envelopes of the amplitude and phase reponses in y- and z-direction. Figures 6.8 and 6.9 show that the used spring elements and assembly repetitions affect the short circuit resonance behavior in figure 6.8 and the dynamic transducer behavior in figure 6.9 in y- and z- direction.

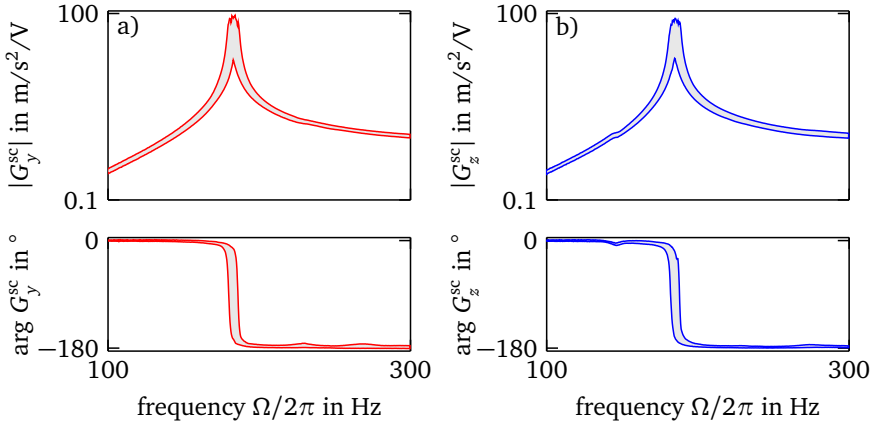

Figure 6.8: Case II: envelopes of $S \times A = 50$ exp. short circuited acceleration transfer functions, a) y-direction $G_y^{sc}(\Omega)$ (——), b) z-direction $G_z^{sc}(\Omega)$ (——)

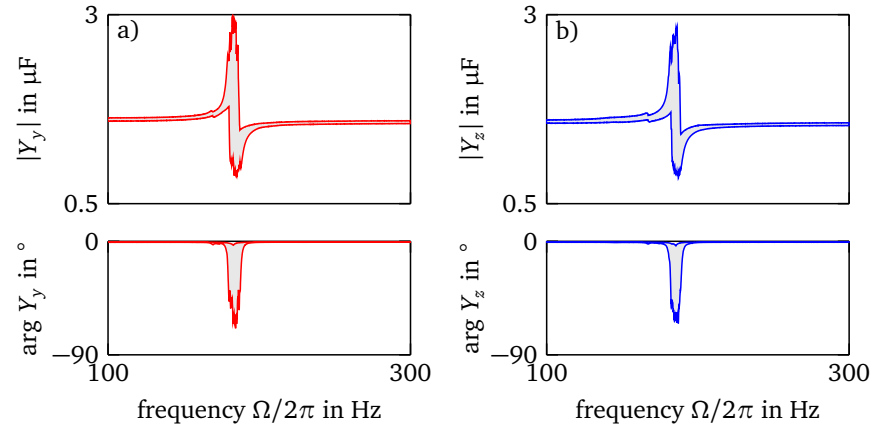

Figure 6.9: Case II: envelopes of $S \times A = 50$ experimental capacitance transfer functions, a) y-direction $Y_y(\Omega)$ (——), b) z-direction $Y_z(\Omega)$ (——)

Experimental characteristic quantities

Figure 6.10 shows the $A = 5$ experimental values of the short circuited resonance frequencies $\omega^{\mathrm{sc}}_{y/z,\mathrm{exp}}$, the GEMCCs $\gamma_{y/z,\mathrm{exp}}$ and static capacitances $C^{\mathrm{s}}_{y/z,\mathrm{exp}}$ for each of the $S = 10$ spring elements (a to c) and their respective mean values and standard deviations (d to f) calculated according to (2.5). In figure 6.10, the experimental values in y- and z-direction are shown in red and blue and slightly shifted for better visibility.

In figure 6.10a, the mean values of $\omega^{\mathrm{sc}}_{y/z,\mathrm{exp}}$ are generally decreasing. Together with the standard deviations of the assembly iterations, which are similar for all 10 spring elements, it is assumed that the investigated spring elements show manufacturing variations. The presented order of spring elements does not represent the chronological order of conducted experiments and, therefore, a drift due to systematic errors is excluded. The offset could be attributed to a higher experimental beam-column setup stiffness in z-direction, as already observed in section 5.1.1. For $\gamma_{y/z,\mathrm{exp}}$ and $C^{\mathrm{s}}_{y/z,\mathrm{exp}}$ in figures 6.10b and c, no general upward or downward trend is observed. The variation of the GEMCCs $\gamma_{y/z,\mathrm{exp}}$ in figure 6.10b are dominated by system assembly variations. The offset in figure 6.10c is also attributed to a higher experimental test setup stiffness in z-direction as well as to manufacturing differences in the used transducers.

As introduced in section 6.1.1, variations due to spring element manufacturing and system assembly in y- and z-direction in figures 6.10a to c are superposed to quantify probabilistic uncertainty in the beam-column dynamic behavior without shunts, as both, manufacturing and system assembly, affect the characteristic parameters.

In figure 6.11, the experimental values of $\omega^{\mathrm{sc}}_{y/z,\mathrm{exp}}$, $\gamma_{y/z,\mathrm{exp}}$ and $C^{\mathrm{s}}_{y/z,\mathrm{exp}}$ from scatter plots in figures 6.10a to c are shown as histogram plots. The histograms are normalized to obtain probability densities with the sum of the bar areas equal to 1. Furthermore, the fitted normal distribution probability density functions $p_{\mathcal{N}}(X)$ (2.4) are shown with normal distribution mean values μ_X and standard deviations σ_X summarized in table 6.8. According to probability plots shown in figure A.2 in the appendix, normal distributions can be assumed as the underlying distributions.

Figure 6.11 shows that the superposed spring element manufacturing and system assembly variations lead to significant variations in the characteristic quantities of the beam-column dynamic behavior without shunts. Furthermore, the relative variations of each quantity are similar in y- and z-direction, see table 6.8, with

$\gamma_{y/z,\mathrm{exp}}$ varying the most. Uncertainty in the vibration attenuation arising from the observed variations is discussed in section 6.3.3.

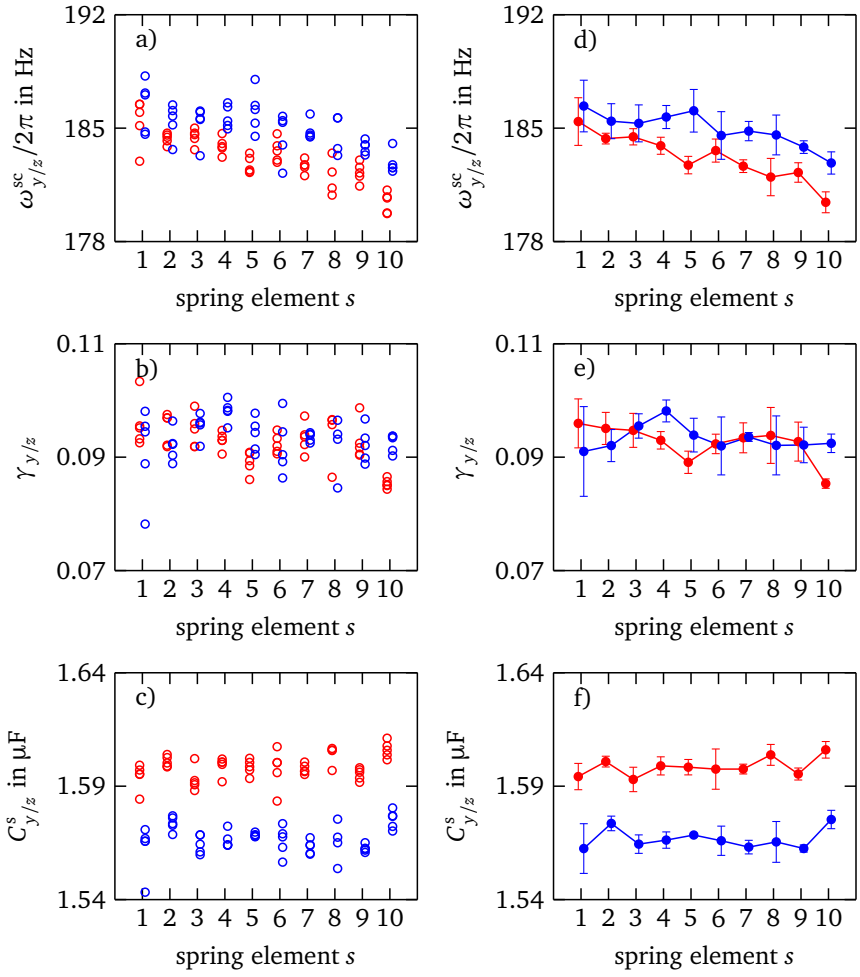

Figure 6.10: Case II: exp. variations of short circuited frequencies $\omega^{\mathrm{sc}}_{y/z,\mathrm{exp}}$, GEMCCs $\gamma_{y/z,\mathrm{exp}}$ and static capacitances $C^{\mathrm{s}}_{y/z,\mathrm{exp}}$ for $S = 10$ membrane-like spring elements and $A = 5$ repetitions of assembly, a) to c) variations in y-direction (o) and z-direction (o), d) to f) mean values μ_X (•) and (•) and standard deviations σ_X for assembly iterations

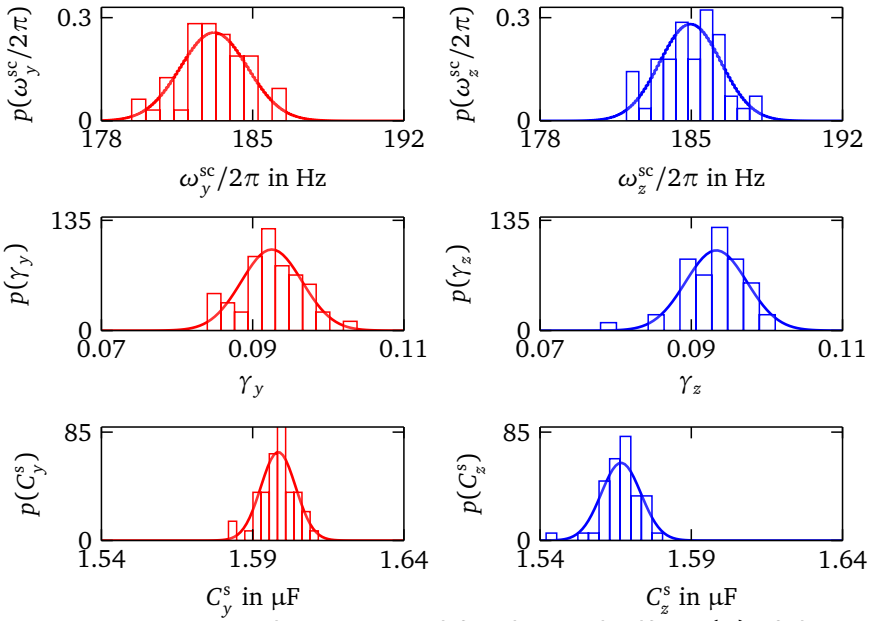

Figure 6.11: Case II: exp. histograms and fitted normal pdfs $p_{\mathcal{N}}(X)$ of short circuited frequencies $\omega^{sc}_{y/z,exp}$, GEMCC $\gamma_{y/z,exp}$ and static capacitances $C^s_{y/z,exp}$, left: y-direction (—), right: z-direction (—), values from figure 6.10

Table 6.8: Case II: exp. means values μ_X and standard deviations σ_X of short circuited frequencies $\omega^{sc}_{y/z,exp}/2\pi$, GEMCCs $\gamma_{y/z,exp}$ and static capacitances $C^s_{y/z,exp}$ from normal pdfs $p_{\mathcal{N}}(X)$ in figure 6.11

	absolute variation			relative variation
X	μ_X	σ_X	unit	σ_X/μ_X in %
$\omega_y^{sc}/2\pi$	183.2	1.6	Hz	0.9
$\omega_z^{sc}/2\pi$	185.0	1.4	Hz	0.8
γ_y	0.093	0.004	–	4.3
γ_z	0.093	0.004	–	4.3
C_y^s	1.598	0.006	µF	0.4
C_z^s	1.567	0.007	µF	0.4

6.3.2 Calibration of model without shunts considering uncertainty

The variations in the experimental beam-column system's dynamic behavior without shunts as presented in section 6.3.1 are used to estimate normally distributed input parameter uncertainty for the lateral and rotational support stiffness $k_{y,\mathrm{A/}B}$, $k_{z,\mathrm{A/}B}$, $k_{\varphi_y,\mathrm{A/B}}$, $k_{\varphi_z,\mathrm{A/B}}$ and axial extension lengths $l_{\mathrm{ext,A/B}}$ of support A and B, section 6.1.1. The stiffness properties are assumed to vary independently in y- and z-direction but equally for support A and B. The axial extension lengths vary equally for support A and B in y- and z-direction.

Calibration

In total, $N = S \times A = 50$ values of each parameter $k_{y,\mathrm{A/}B}$, $k_{z,\mathrm{A/}B}$, $k_{\varphi_y,\mathrm{A/B}}$, $k_{\varphi_z,\mathrm{A/B}}$ and $l_{\mathrm{ext,A/B}}$ are calibrated by solving the optimization problem (4.14) $n = 1, \ldots N$ times with

$$\boldsymbol{P}_n = [k_{y,\mathrm{A/}B},\, k_{z,\mathrm{A/}B},\, k_{\varphi_y,\mathrm{A/B}},\, k_{\varphi_z,\mathrm{A/B}},\, l_{\mathrm{ext,A/B}}]_n \tag{6.3}$$

for the 50 experimental short circuited and the 50 capacitance transfer functions in figures 6.8 and 6.9. All other parameters are kept constant with the parameter values in table 5.3.

Figure 6.12 shows the 50 values of $k_{y,\mathrm{A/}B}$, $k_{z,\mathrm{A/}B}$, $k_{\varphi_y,\mathrm{A/B}}$, $k_{\varphi_z,\mathrm{A/B}}$ and $l_{\mathrm{ext,A/B}}$ from the calibration in normalized histograms. Additionally, the fitted probability density functions $p_{\mathcal{N}}(X)$ (2.4) are shown and their respective normal distribution mean values μ_X and standard deviations σ_X summarized in table 6.9 represent probabilistic parameter uncertainty. The mean values μ_X of $k_{y,\mathrm{A/}B}$, $k_{z,\mathrm{A/}B}$, $k_{\varphi_y,\mathrm{A/B}}$, $k_{\varphi_z,\mathrm{A/B}}$ and $l_{\mathrm{ext,A/B}}$ in table 6.9 are the new mean support stiffness and geometry properties of beam-column system's model in figure 3.3.

Table 6.9: Case II: parameter uncertainty of support A and B assumed from own experiments, num. means $\mu_{X,\mathrm{num}}$ and standard deviations $\sigma_{X,\mathrm{num}}$ for normal pdfs from values in figure 6.12

property	X	μ_X	σ_X	unit
lateral support stiffness	$k_{y,\mathrm{A/}B}$	$30.10 \cdot 10^6$	$3.75 \cdot 10^6$	N/m
	$k_{z,\mathrm{A/}B}$	$33.35 \cdot 10^6$	$3.56 \cdot 10^6$	N/m
rotational stiffness	$k_{\varphi_y,\mathrm{A/B}}$	126.45	15.96	Nm/rad
	$k_{\varphi_z,\mathrm{A/B}}$	122.98	16.35	Nm/rad
axial extension	$l_{\mathrm{ext,A/B}}$	$6.70 \cdot 10^{-3}$	$0.08 \cdot 10^{-3}$	m

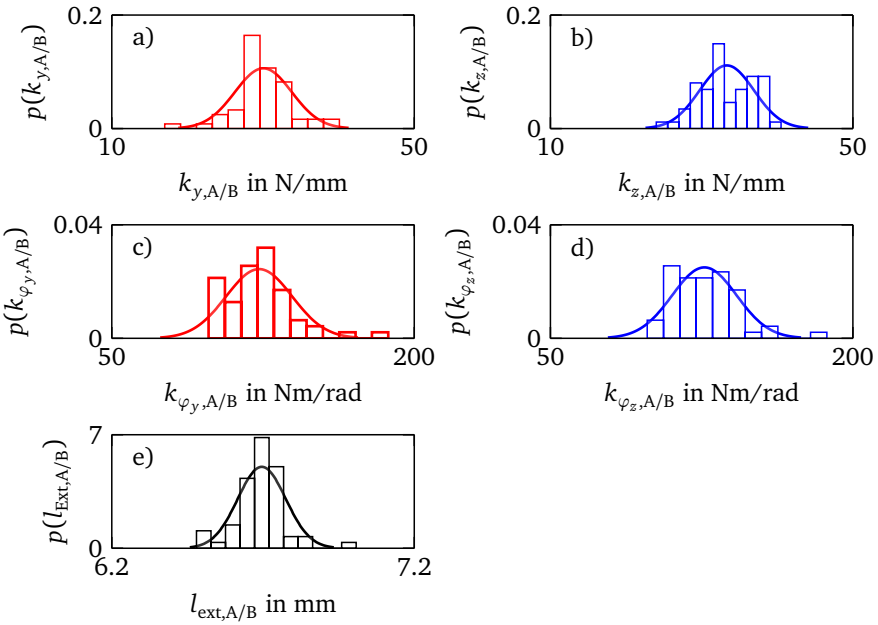

Figure 6.12: Case II: histograms of $S \times A = 50$ calibrated values and fitted normal pdfs $p_{\mathcal{N}}(X)$
a) and b) lateral support stiffness $k_{y,\mathrm{A/B}}$ (——), $k_{z,\mathrm{A/B}}$ (——)
c) and d) rotational support stiffness $k_{\varphi_y,\mathrm{A/B}}$ (——), $k_{\varphi_z,\mathrm{A/B}}$ (——)
e) axial extension lengths $l_{\mathrm{ext,A/B}}$ (——)

Evaluation of calibration

To evaluate the assumed parameter uncertainty in table 6.9, the normally distributed parameters are input for MONTE-CARLO-Simulation (MCS) to calculate numerical values of the short circuited frequencies $\omega^{\mathrm{sc}}_{y/z,\mathrm{num}}$ (3.50), GEMCCs $\gamma_{y/z,\mathrm{num}}$ (3.53) and static capacitances $C^{\mathrm{s}}_{y/z,\mathrm{num}}$ (3.106), whose mean values μ_X and standard deviation σ_X are then compared to experiments from table 6.8. In the MCS, $\omega^{\mathrm{sc}}_{y/z,\mathrm{num}}$, $\gamma_{y/z,\mathrm{num}}$ and $C^{\mathrm{s}}_{y/z,\mathrm{num}}$ are calculated $i = 1, ..., I$ times with $I = 20000$ samples of independently and quasi-randomly varying parameter values in the set

$$\boldsymbol{P}_i = [k_{y,\mathrm{A/B}}, k_{z,\mathrm{A/B}}, k_{\varphi_y,\mathrm{A/B}}, k_{\varphi_z,\mathrm{A/B}}, l_{\mathrm{ext,A/B}}]_i. \tag{6.4}$$

Figure 6.13 shows the results of the MCS via normalized histograms and fitted probability density functions $p_{\mathcal{N}}(X)$ (2.4). The numerical normal distribution mean values $\mu_{X,\mathrm{num}}$ and standard deviations $\sigma_{X,\mathrm{num}}$ of the numerically calculated samples are summarized in table 6.10 and compared to the experimental mean values $\mu_{X,\mathrm{exp}}$ and standard deviations $\sigma_{X,\mathrm{exp}}$ from table 6.10 by their relative deviation (4.16).

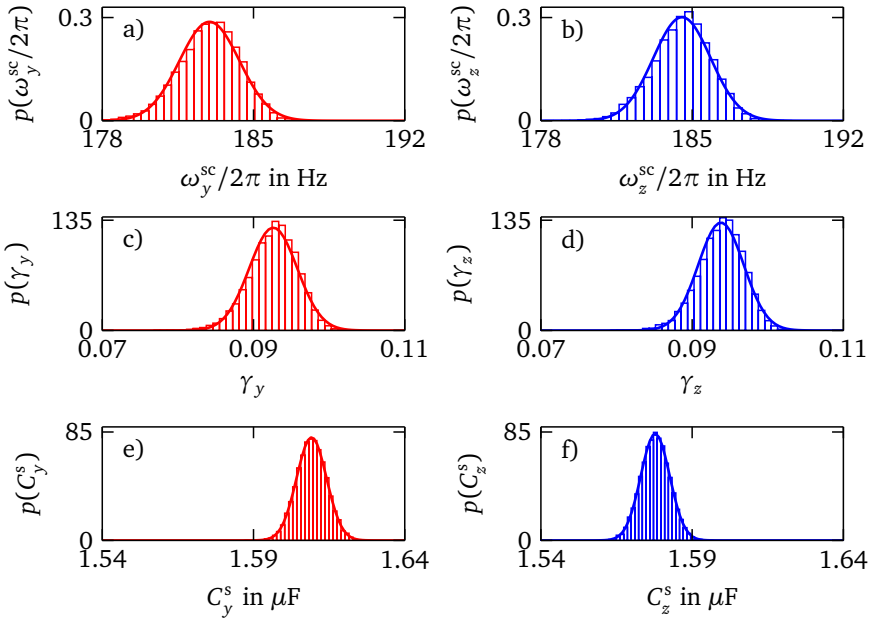

Figure 6.13: Case II: num. histograms with $I = 20000$ MCS and fitted normal pdfs $p_{\mathcal{N}}(X)$ of short circuited frequencies $\omega^{sc}_{y/z,\mathrm{num}}$, GEMCC $\gamma_{y/z,\mathrm{num}}$ and static capacitances $C^s_{y/z,\mathrm{num}}$, left: y-direction (——), right: z-direction (——)

The experimental and numerical mean values μ_X show a good agreement for all six parameters with a maximum relative deviation of 1.1 %. In contrast to that, the numerical standard deviations $\sigma_{X,\mathrm{num}}$ underestimate the experimental standard deviations $\sigma_{X,\mathrm{exp}}$ with a maximum relative deviation of 33.3 %. However, the deviations are acceptable as the assumed parameter uncertainty in table 6.9 adequately predicts uncertainty in the vibration attenuation as shown by the comparison with experiments in section 6.3.4.

Table 6.10: Case II: normal pdf mean μ_X and standard deviation σ_X from experiments in table 6.10 and MONTE-CARLO-Simulation in figure 6.13, short circuited frequencies $\omega^{\mathrm{sc}}_{y/z}/2\pi$ in Hz, GEMCCs $\gamma_{y/z}$ and static capacitances $C^{\mathrm{s}}_{y/z}$ in µF, rel. dev. in %

	experimental		numerical		relative deviation	
X	μ_X	σ_X	μ_X	σ_X	err(μ_X)	err(σ_X)
$\omega^{\mathrm{sc}}_y/2\pi$	183.2	1.6	183.0	1.4	0.1	14.3
$\omega^{\mathrm{sc}}_z/2\pi$	185.0	1.4	184.5	1.3	0.3	7.7
γ_y	0.093	0.004	0.093	0.003	−0.0	33.3
γ_z	0.093	0.004	0.094	0.003	−1.1	33.3
C^{s}_y	1.598	0.006	1.609	0.005	−0.7	20.0
C^{s}_z	1.567	0.007	1.578	0.005	−0.7	20.0

6.3.3 Prediction of uncertainty by model with shunts

Probabilistic uncertainty in the vibration attenuation with RL- and RLC-shunts due to spring element manufacturing and system assembly variations is predicted via MCS by using the assumed parameter uncertainty from table 6.9. To correctly predict uncertainty, the RL- and RLC-shunts are tuned with the new optimal shunt resistances in table 6.11, which optimally tune the shunts to the beam-column system with the new deterministic support stiffness and lateral extension length values represented by the mean values μ_X in table 6.9.

Table 6.11: Case II: reference RL- and RLC-shunt resistances for optimal vibration attenuation in y- and z-direction connected to transducers $\mathrm{P}_{y,\mathrm{B}}$ and $\mathrm{P}_{z,\mathrm{B}}$

		RL-shunt		RLC-shunt		
property	symbol	$\mathrm{P}_{y,\mathrm{B}}$	$\mathrm{P}_{z,\mathrm{B}}$	$\mathrm{P}_{y,\mathrm{B}}$	$\mathrm{P}_{z,\mathrm{B}}$	unit
resistance	R^{D}	55.51	56.38	13.51	13.66	Ohm
	R^{L1}	23.13	22.76	2.32	2.16	Ohm
	R^{N1}	–	–	1160.97	1138.31	Ohm
neg. cap. ratio	δ	–	–	−0.90	−0.90	–
inductance	L	0.473	0.457	0.048	0.043	Henry
neg. capacitance	C^{n}	–	–	−1.787	−1.753	µF

In the MCS, the numerical acceleration transfer functions with shunts $G^{\mathrm{RL}}_{y/z,\mathrm{num}}(\Omega)$ (3.94) and $G^{\mathrm{RLC}}_{y/z,\mathrm{num}}(\Omega)$ (3.95) and their respective peak gains $\widehat{G}^{\mathrm{RL}}_{y/z,\mathrm{num}}$ (3.96) and $\widehat{G}^{\mathrm{RLC}}_{y/z,\mathrm{num}}$ (3.98) are calculated $I = 20000$ times with I samples of independently varying parameter values in the set $\boldsymbol{P}_i$ (6.4), while all other beam-column system and shunt parameters remain constant.

The variations of the acceleration transfer functions with RL-shunts $G^{\mathrm{RL}}_{y/z,\mathrm{num}}(\Omega)$ and with RLC-shunts $G^{\mathrm{RLC}}_{y/z,\mathrm{num}}(\Omega)$ obtained from MCS are shown in figures 6.14 and 6.15. The variations of the acceleration transfer function peak gains with RL-shunts $\widehat{G}^{\mathrm{RL}}_{y/z,\mathrm{num}}$ and with RLC-shunts $\widehat{G}^{\mathrm{RL}}_{y/z,\mathrm{num}}$ are shown in figure 6.16. The most likely peak gain values Σ_X and the maximum peak gain values Q^{95}_X, in this case obtained from GUMBEL pdf fits, are used to quantify the peak gain variation, section 2.3.1.

Variation of numerical transfer functions

Figures 6.14 and 6.15 show the variations of $I = 20000$ samples of $G^{\mathrm{RL}}_{y/z,\mathrm{num}}(\Omega)$ and $G^{\mathrm{RLC}}_{y/z,\mathrm{num}}(\Omega)$ via envelopes of the amplitude and phase responses in y- and z-direction. Additionally, the respective optimally attenuated acceleration transfer functions, when uncertainty is disregarded, are shown with black lines.

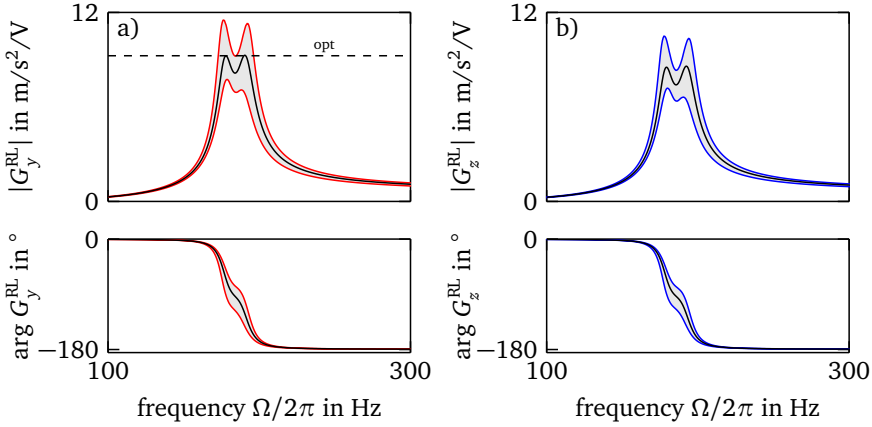

Figure 6.14: Case II: num. acceleration transfer funct. with RL-shunts,
a) $G^{\mathrm{RL}}_{y,\mathrm{num}}(\Omega)$: envelopes (——) of $I = 20000$ MCS, optimal (——)
b) $G^{\mathrm{RL}}_{z,\mathrm{num}}(\Omega)$: envelopes (——) of $I = 20000$ MCS, optimal (——)

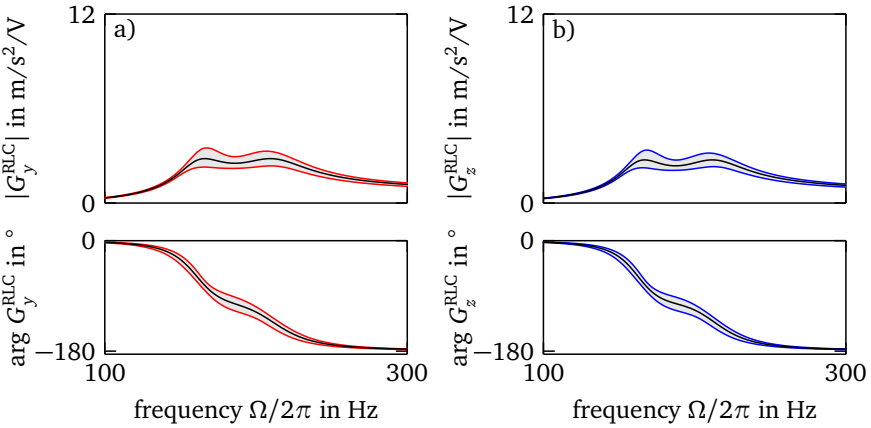

Figure 6.15: Case II: num. acceleration transfer funct. with RLC-shunts,
a) $G_{y,\mathrm{num}}^{\mathrm{RLC}}(\Omega)$: envelopes (——) of $I = 20000$ MCS, optimal (——)
b) $G_{z,\mathrm{num}}^{\mathrm{RLC}}(\Omega)$: envelopes (——) of $I = 20000$ MCS, optimal (——)

Comparing the uncertain vibration attenuation, represented by envelopes, and optimal vibration attenuation, represented by black lines, significant inclines in the vibration amplitudes are observed in the amplitude responses for vibration attenuation with RL- and RLC-shunts in y- and z-direction. To quantify uncertainty in the vibration attenuation, the variations of the peak gains of the varying acceleration transfer functions are analyzed in the next paragraph .

Variation of numerical peak gains

Figure 6.16 shows normalized histograms of the $I = 20000$ numerical values of the peak gains $\widehat{G}_{y/z,\mathrm{num}}^{\mathrm{RL}}$ and $\widehat{G}_{y/z,\mathrm{num}}^{\mathrm{RLC}}$ obtained from the MCS together with optimal peak gain values opt_X from figures 6.14 and 6.15 . All histograms are right-skewed with the mass of the pdfs concentrated on the left of the figure and can be approximated with GUMBEL pdfs $p_{\mathscr{G}}(X)$ (2.6), as justified by the probability plots shown in figure A.1 in the appendix. The GUMBEL parameters Σ_X and Δ_X as well as the percentile Q_X^{95} are summarized in table 6.12.

The most likely peak gains for RL-shunts $\Sigma_{\widehat{G}_{y/z}^{\mathrm{RL}}}$ and RLC-shunts $\Sigma_{\widehat{G}_{y/z}^{\mathrm{RLC}}}$ in y- and z-direction from figure 6.16 are greater than their respective optimal peak gain values opt_X, see table 6.12. This is plausible as the optimal peak gain values represent an optimum and deviations from the optimum normally result in reduced

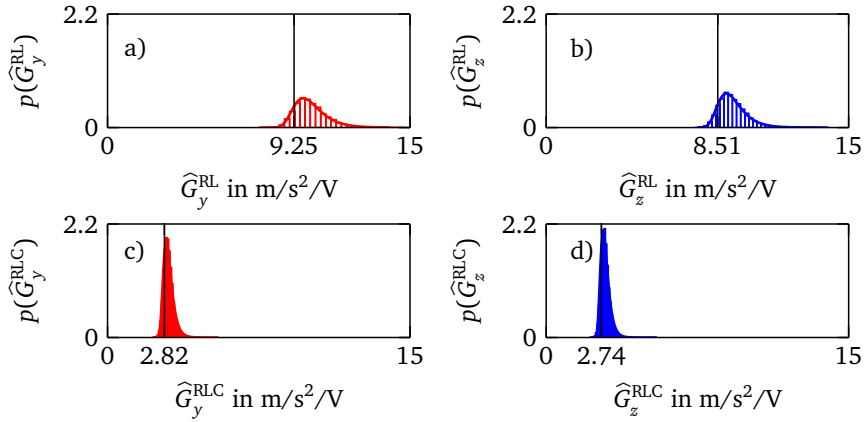

Figure 6.16: Case II: num. histograms with $I = 20000$ MCS and fitted GUMBEL pdfs $p_{\mathscr{G}}(X)$ of peak gains with RL-shunts and RLC-shunts
a) $\widehat{G}_{y,\mathrm{num}}^{\mathrm{RL}}$ (——), opt (——) b) $\widehat{G}_{z,\mathrm{num}}^{\mathrm{RL}}$ (——), opt (——)
c) $\widehat{G}_{y,\mathrm{num}}^{\mathrm{RLC}}$ (——), opt (——) d) $\widehat{G}_{z,\mathrm{num}}^{\mathrm{RLC}}$ (——), opt (——)

performance. Furthermore, some combinations of the used parameter uncertainty result in peak gain values smaller than the optimal peak gain values. This case is not further discussed as it does not lead to reduced vibration attenuation performance.

Uncertainty due to spring element manufacturing and system assembly, as represented with the parameter uncertainty in table 6.9, has the same relative effect on vibration attenuation with RL- and RLC-shunts. This is seen by similar values of Q_X^{95}/opt_X for all shunts in all directions. However, vibration attenuation with RLC-shunts still achieves higher vibration attenuation, as seen by most likely peak gains $\Sigma_{\widehat{G}_{y/z}^{\mathrm{RLC}}}$ and maximum peak gains $Q_{\widehat{G}_{y/z}^{\mathrm{RLC}}}^{95}$ with RLC-shunts that are smaller than those with RL-shunts. All relative changes in table 6.12 show that uncertainty due to spring element manufacturing and system assembly variations effect the vibration attenuation with RL- and RLC-shunts similarly in y- and z-direction.

6.3.4 Validation of predicted uncertainty

Probabilistic uncertainty in the experimental beam-column vibration attenuation with RL- and RLC-shunts is quantified and compared to numerical results from the last section in order to evaluate the numerically predicted uncertainty. The

Table 6.12: Case II: num. GUMBEL pdf parameters Σ_X and Δ_X and Q_X^{95} of the peak gains $\widehat{G}^{\mathrm{RL}}_{y/z,\mathrm{num}}$ and $\widehat{G}^{\mathrm{RLC}}_{y/z,\mathrm{num}}$ with RL- and RLC-shunts, all in $\mathrm{m/s^2/V}$

	absolute values				relative change	
X	opt_X	Σ_X	Δ_X	Q_X^{95}	Σ_X/opt_X	Q_X^{95}/opt_X
$\widehat{G}^{\mathrm{RL}}_{y}$	9.25	9.71	0.64	11.64	1.05	1.26
$\widehat{G}^{\mathrm{RL}}_{z}$	8.51	8.94	0.56	10.60	1.05	1.25
$\widehat{G}^{\mathrm{RLC}}_{y}$	2.82	2.92	0.20	3.51	1.03	1.25
$\widehat{G}^{\mathrm{RLC}}_{z}$	2.74	2.83	0.22	3.48	1.03	1.27

experimental acceleration transfer functions with RL-shunt $G^{\mathrm{RL}}_{y/z,\mathrm{exp}}(\Omega)$ and with RLC-shunts $G^{\mathrm{RLC}}_{y/z,\mathrm{exp}}(\Omega)$ (4.7) of the beam-column system in figure 4.1 with shunts are measured for $S \times A = 10$ samples, table 6.7, where each spring element in support B is only mounted once and no system assembly iterations are performed. The experimental shunts are tuned with the optimal shunt resistances in table 6.11 from section 6.3.3.

Variation of experimental transfer functions

Figures 6.17 and 6.18 show the variations of $S \times A = 10$ samples of $G^{\mathrm{RL}}_{y/z,\mathrm{exp}}(\Omega)$ and $G^{\mathrm{RLC}}_{y/z,\mathrm{exp}}(\Omega)$ via envelopes of the amplitude and phase reponses in y- and z-direction. The experimental envelopes show that the used spring elements affect the attenuated frequency transfer functions with RL- and RLC-shunts in y- and z-direction. To quantify uncertainty in the vibration attenuation, the variations of the peak gains of the varying acceleration transfer functions in figures 6.17 and 6.18 are analyzed in the next paragraph and compared to numerical results.

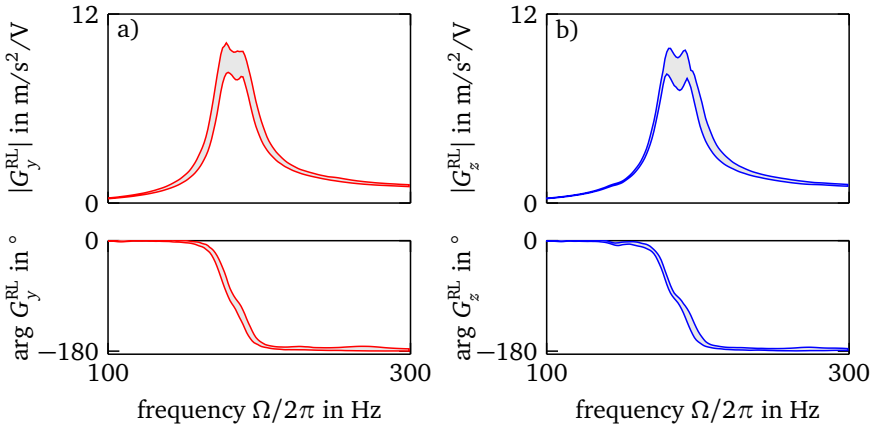

Figure 6.17: Case II: envelopes of $S \times A = 10$ experimental acceleration transfer functions with RL-shunts, a) $G^{\mathrm{RL}}_{y,\mathrm{exp}}(\Omega)$ (——), b) $G^{\mathrm{RL}}_{z,\mathrm{exp}}(\Omega)$ (——)

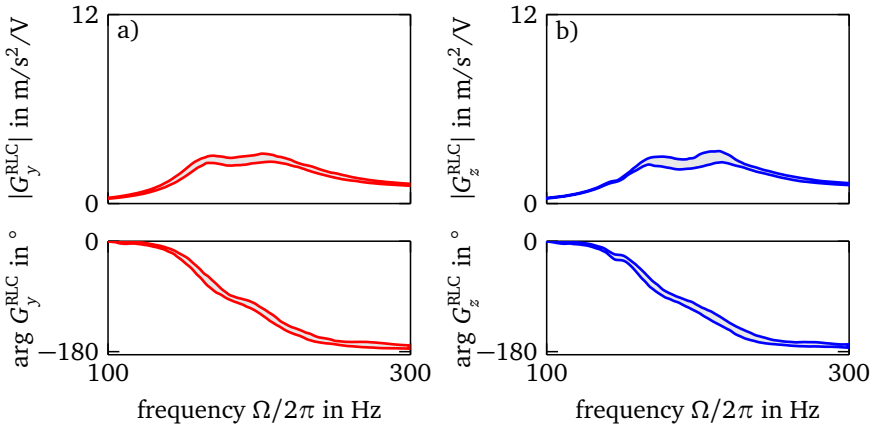

Figure 6.18: Case II: envelopes of $S \times A = 10$ experimental acceleration transfer functions with RLC-shunts, a) $G^{\mathrm{RLC}}_{y,\mathrm{exp}}(\Omega)$ (——), b) $G^{\mathrm{RLC}}_{z,\mathrm{exp}}(\Omega)$ (——)

Comparison of experimental and numerical peak gain variations

Figure 6.19 shows normalized histograms of the $S \times A = 10$ experimental values of the peak gains $\widehat{G}^{\mathrm{RL}}_{y/z,exp}$ and $\widehat{G}^{\mathrm{RLC}}_{y/z,\mathrm{exp}}$, obtained from shunted acceleration transfer functions in figures 6.17 and 6.18. To quantify uncertainty in the ex-

perimental peak gains and to compensate for the small number of samples, it is assumed that the experimental peak gains in figure 6.19 are distributed according the GUMBEL distribution. Based on the numerical results in section 6.3.3, this assumption is reasonable for analyzing peak gain variations due to spring element and system assembly variations. The fitted GUMBEL pdfs $p_{\mathscr{G}}(X)$ (2.6) are also shown in figure 6.19, and the respective experimental values of the most likely peak gain $\Sigma_{X,\mathrm{exp}}$, shape parameter $\Delta_{X,\mathrm{exp}}$ as well as the maximum peak gain $Q^{95}_{X,\mathrm{exp}}$ are summarized in table 6.13 and compared to the numerical results from table 6.12 by their relative deviation (4.16).

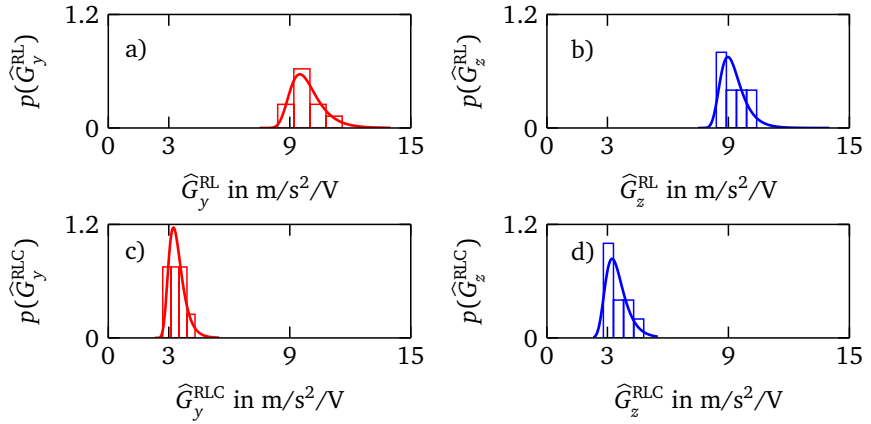

Figure 6.19: Case II: exp. histograms with $S \times A = 10$ values and fitted GUMBEL pdfs $p_{\mathscr{G}}(X)$ of peak gains with RL-shunts and RLC-shunts
a) $\widehat{G}^{\mathrm{RL}}_{y,\mathrm{exp}}$ (——), b) $\widehat{G}^{\mathrm{RL}}_{z,\mathrm{exp}}$ (——), c) $\widehat{G}^{\mathrm{RLC}}_{y,\mathrm{exp}}$ (——), d) $\widehat{G}^{\mathrm{RLC}}_{z,\mathrm{exp}}$ (——)

Uncertainty in the vibration attenuation with RL-shunts as predicted by the beam-column system's model via MCS shows a good agreement with experimentally observed uncertainty, based on the comparison in table 6.19. Especially the most likely peak gain value $\Sigma_{G^{\mathrm{RL}}}$ and maximum peak gain value $Q^{95}_{G^{\mathrm{RL}}}$, which are of interest in this work, match well. Uncertainty in the vibration attenuation with RLC-shunts, as predicted by the model via MCS, underestimates the experimentally observed uncertainty. This could be attributed to the small experimental sample size. In a future work, it should be validated by a bigger sample size if the GUMBEL distribution really does represent the experimental variation of peak gains with RLC-shunts due to spring element manufacturing and system assembly. However, the relative deviations of the experimental and the numerical most likely peak gain values Σ_X and maximum peak gain values Q^{95}_X for RL- and RLC-shunt

are considered to be in acceptable limits. Thus, the parameter uncertainty in table 6.9 is used in the investigations in case V and VI to represent the effect of spring element manufacturing and system assembly variations.

Table 6.13: Case II: GUMBEL pdf parameters Σ_X, Δ_X and percentile Q_X^{95} of experimental and numerical peak gains $\widehat{G}_{y/z}^{\mathrm{RL}}$, $\widehat{G}_{y/z}^{\mathrm{RLC}}$ in figure 6.19 and figure 6.16, all in $\mathrm{m/s^2/V}$, relative deviation in %

	experimental			numerical			relative deviation		
X	Σ_X	Δ_X	Q_X^{95}	Σ_X	Δ_X	Q_X^{95}	$\mathrm{err}(\Sigma_X)$	$\mathrm{err}(\Delta_X)$	$\mathrm{err}(Q_X^{95})$
$\widehat{G}_y^{\mathrm{RL}}$	9.50	0.65	11.43	9.71	0.64	11.64	−2.2	1.6	−1.8
$\widehat{G}_z^{\mathrm{RL}}$	8.97	0.49	10.43	8.94	0.56	10.60	0.4	−14.4	−1.7
$\widehat{G}_y^{\mathrm{RLC}}$	3.23	0.28	4.06	2.92	0.20	3.51	9.7	28.8	13.7
$\widehat{G}_z^{\mathrm{RLC}}$	3.23	0.31	4.15	2.83	0.22	3.48	12.5	29.0	16.2

6.3.5 Summary of results and conclusion of case II

Probabilistic uncertainty due to spring element manufacturing and system assembly variations affects the dynamic behavior of the beam-column system and, hence, represents an important source of uncertainty that reduces the vibration attenuation with RL- and RLC-shunt as it has been shown in section 6.3 by experiments and simulation.

A set of $S = 10$ different spring elements in support B and $A = 5$ iterations of system assembly for each spring element, in total 50 measurements, is used to quantify probabilistic uncertainty in the beam-column system's dynamic behavior without shunts. The experimental short circuited resonance frequencies $\omega_{y/z,\mathrm{exp}}^{\mathrm{sc}}$, the GEMCCs $\gamma_{y/z,\mathrm{exp}}$ and the static capacitances $C_{y/z,\mathrm{exp}}^{\mathrm{s}}$ show significant variations due to spring element manufacturing and system assembly variations, which are justified to be approximated by normal distributions. The experimentally observed variations are adequately represented by the beam-column system's model with the assumed parameter uncertainty in the support stiffness and geometric properties.

Results of a MCS with $I = 20000$ samples show that the numerical peak gains with RL-shunt $\widehat{G}^{\mathrm{RL}}$ and with RLC-shunts $\widehat{G}^{\mathrm{RLC}}$ vary with a right-skewed distribution due

to the assumed parameter uncertainty. The most likely peak gain value of the distribution Σ_X is close to the optimal peak gain value, whereas the maximum peak gain value Q_X^{95} is significantly increased. The peak gains with RLC-shunts are always smaller than with RL-shunts. However, uncertainty due to spring element manufacturing and system assembly, as represented by the assumed parameter uncertainty, has the same relative effect on vibration attenuation with RL- and RLC-shunts. The experimentally observed and the numerically predicted variations in the peak gains match adequately with a maximal relative deviation of 16.2 %.

The experimental and numerical variations in the beam-column system's dynamic behavior without and with shunts caused by spring element manufacturing and system assembly variations are similar in y- and z-direction. The same was observed for static load variations in section 6.1.2. Since uncertainty assumed from literature will also have similar effects on the vibration attenuation in y- and z-direction, the investigation of cases III, IV, V and VI is only performed for the lateral beam-column y-direction.

6.4 Cases III and IV: Effect of shunt and transducer manufacturing variations

This section presents numerical results to quantify probabilistic uncertainty in the vibration attenuation in y-direction due to shunt component and transducer manufacturing variations as introduced by cases III and IV in table 6.1.

6.4.1 Parameter uncertainty assumed from literature

For transducer $P_{y,B}$ in support B in figure 3.2, which is made of lead zirconate titanate (PZT) as explained in section 2.2, the properties d_3, k^{sc} and C may vary up to ±20 %, [82] and data sheet by PHYSIK INSTRUMENTE [75]. However, tighter manufacturing tolerances are available with d_3 and k^{sc} varying up to ±5 % and C varying up to ±10 % as indicated in data sheets by THORLABS, NOLIAC and APC, [5, 67, 90]. The tighter manufacturing tolerances are used in this work.

For the resistors in the RL- and RLC-shunts circuits in figures 3.8b and 3.9b, standard resistor tolerances from ±0.10 % to ±20 % deviation are available, [43, 98]. Usually, tighter tolerances also mean higher component costs. In this work, values R of resistors in the shunt circuits are assumed to vary by ±1 %. For the capacitors in the RL- and RLC-shunts circuits, standard capacitor tolerances from ±1 % to ±20 % deviation are available, [43, 46]. In this work, values C of capacitors in the shunts circuits are assumed to vary by ±2 %.

Table 6.14: Case III: normally distributed shunt circuit parameter uncertainty with mean μ_X and standard deviation σ_X

		RL-shunt		RLC-shunt		
property	X	μ_X	σ_X	μ_X	σ_X	unit
resistance	R^{D}	55.27	0.18	13.51	0.05	Ohm
	R^{L1}	23.14	0.07	2.32	0.01	Ohm
	R^{L2}	1000	3.33	1000	3.33	Ohm
	R^{L3}	1000	3.33	1000	3.33	Ohm
	R^{L5}	20064	66.88	20064	66.88	Ohm
	R^{N1}	–	–	1160.97	3.87	Ohm
	R^{N2}	–	–	1000.00	3.33	Ohm
	R^{N3}	–	–	994000	3313.33	Ohm
capacitance	C^{L4}	–	–	1.00	0.006	µF
	C^{N4}	–	–	1.54	0.01	µF

Based on the lower and upper ranges of the tolerances, the standard deviations of the assumed normally distributed variations of the transducer and shunt properties are derived, section 6.1.2 , and summarized in tables 6.14 and 6.15. The mean values of the transducer properties correspond to those from table 5.3. For the shunts, the mean values of optimal resistances are taken from table 6.11, and the mean values of the constant circuit values are taken from tables 4.2 and 4.3.

Table 6.15: Case IV: normally distributed transducer parameter uncertainty with mean μ_X and standard deviation σ_X

property	X	μ_X	σ_X	unit
transducer stiffness	$k_{y,\mathrm{B}}^{\mathrm{sc}}$	$32.4 \cdot 10^{6}$	$0.54 \cdot 10^{6}$	N/m
transducer const.	$d_{3,y,\mathrm{B}}$	$3.10 \cdot 10^{-10}$	$5.12 \cdot 10^{-12}$	m/V
transducer capacitance	$C_{y,\mathrm{B}}$	$1.43 \cdot 10^{-6}$	$0.05 \cdot 10^{-6}$	F

6.4.2 Prediction of uncertainty by model with shunts

For each of the cases III and IV, the numerical peak gains with RL-shunt $\widehat{G}_{y,\mathrm{num}}^{\mathrm{RL}}$ (3.96) and with RLC-shunt $\widehat{G}_{y,\mathrm{num}}^{\mathrm{RLC}}$ (3.98) are calculated $I = 20000$ times via MCS with I samples of normally distributed and independently varying parameter values in $\boldsymbol{P}_i$. For cases III and IV, $\boldsymbol{P}_i$ contains values from normally distributed parameters in tables 6.14 or 6.15.

The variations of the numerical peak gains $\widehat{G}_{y,\mathrm{num}}^{\mathrm{RL}}$ and $\widehat{G}_{y,\mathrm{num}}^{\mathrm{RLC}}$ obtained from MCS for cases III and IV are shown with normalized histograms in figure 6.20. To quantify uncertainty in the vibration attenuation with RL- and RLC-shunts, section 2.3.1, the most likely peak gain values $\Sigma_{\widehat{G}_y^{\mathrm{RL}}}$ and $\Sigma_{\widehat{G}_y^{\mathrm{RLC}}}$ as well as the maximum peak gain values $Q_{\widehat{G}_y^{\mathrm{RL}}}^{95}$ and $Q_{\widehat{G}_y^{\mathrm{RLC}}}^{95}$ of the histograms in figure 6.20 are summarized in table 6.16 together with their respective optimal values opt_X. The values are directly obtained from the histograms, because the use of the GUMBEL distribution is not valid for distributions in figure 6.20.

In case III, uncertainty due to manufacturing variations of the shunt resistors and capacitors has bigger influence on vibration attenuation with RLC-shunts, because Q_{RLC}^{95} increases more than Q_{RL}^{95} in relative terms, table 6.16. This is attributed to the fact that the RLC-shunt comprises more uncertain components than the RL-shunt, compare figure 3.8 and figure 3.9.

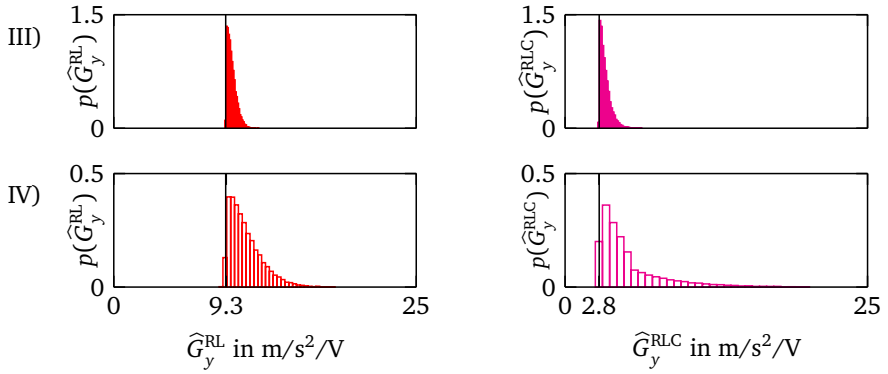

Figure 6.20: Cases III and IV: num. histograms with $I = 20000$ MCS of peak gains with RL-shunts and RLC-shunts
left: $\widehat{G}_{y,\mathrm{num}}^{\mathrm{RL}}$ (——), opt (——) right: $\widehat{G}_{y,\mathrm{num}}^{\mathrm{RLC}}$ (——), opt (——)

According to case IV, uncertainty due to transducer manufacturing variations has the biggest influence on vibration attenuation with RLC-shunts, compared to case III and II in table 6.12. This could be attributed to a high sensitivity of vibration attenuation with RLC-shunts to changes in the transducer capacitance, and the relatively high manufacturing tolerance of ±10 %, [56]. Comparing the absolute peak gains with RL- and RLC-shunts of cases III and IV, it becomes evident that the RLC-shunt still achieves higher vibration attenuation.

Table 6.16: Cases III and IV: most likely peak gain values Σ_X and maximum peak gain values Q_X^{95} of histograms in figure 6.20, for comparison: optimal peak gain value opt_X, all in $\mathrm{m/s^2/V}$

		absolute values			relative change	
Case	X	opt_X	Σ_X	Q_X^{95}	Σ_X/opt_X	Q_X^{95}/opt_X
III	$\widehat{G}_y^{\mathrm{RL}}$	9.25	9.39	10.48	1.02	1.13
	$\widehat{G}_y^{\mathrm{RLC}}$	2.82	2.95	4.21	1.05	1.49
IV	$\widehat{G}_y^{\mathrm{RL}}$	9.25	9.71	13.56	1.05	1.47
	$\widehat{G}_y^{\mathrm{RLC}}$	2.82	3.26	11.21	1.16	3.98

6.5 Cases V and VI: Effect of static load, manufacturing and system assembly variations

This section presents numerical results to quantify probabilistic uncertainty in the vibration attenuation in y-direction due to combined static load, manufacturing and system assembly variations as introduced by cases V and VI in table 6.1.

6.5.1 Combined probabilistic parameter uncertainty

Probabilistic parameter uncertainty from cases II, III and IV is combined to investigate uncertainty in the vibration attenuation according to cases V and VI. Table 6.17 summarizes the beam-column system parameters with probabilistic parameter uncertainty due to spring element manufacturing and system assembly from case II, table 6.9, and due to transducer manufacturing from case IV, table 6.14. Table 6.18 summarizes the RL-shunt parameters with probabilistic parameter uncertainty due to shunt component manufacturing from case IV, table 6.14.

In order to guarantee stable lateral beam-column vibrations for all parameter combinations in the uncertainty analysis in cases V and VI when transducer $\mathrm{P}_{y,\mathrm{B}}$ is connected to the RLC-shunt, the RLC-shunt must be newly tuned with negative capacitance ratio $\delta = -0.84$ (3.103). As defined in section 3.5.2, the vibration attenuation becomes unstable for $\delta < \delta_{\mathrm{crit}} = -0.95$. For the RLC-shunt with shunt resistances in table 6.11 from case II, which is tuned with $\delta = -0.9$, the probabilistic uncertainty from case V leads to variations in δ that exceed δ_{crit} as demonstrated in figure 6.21a. For the RLC-shunt with shunt resistances from table 6.18, which is tuned with $\delta = -0.84$, the limit δ_{crit} is not being exceeded and the vibrations remain stable as shown by figure 6.21b.

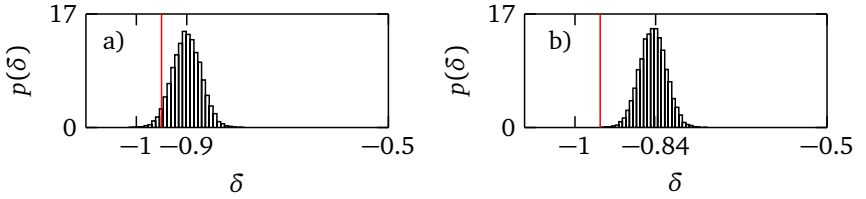

Figure 6.21: Case V: histograms of negative capacitance ratio δ, a) δ exceeds stability limit δ_{crit} (——) due to parameter uncertainty, b) δ does not exceed the stability limit δ_{crit} (——)

Table 6.17: Case V: normally distributed beam-column system parameter uncertainty with mean μ_X and standard deviation σ_X

property	X	μ_X	σ_X	unit
lateral stiffness	$k_{y,\mathrm{A/}B}$	$30.1 \cdot 10^6$	$3.80 \cdot 10^6$	N/m
rotational stiffness	$k_{\varphi_z,\mathrm{A/B}}$	123.0	15.37	N/m
axial extension	$l_{\mathrm{ext,A/B}}$	$6.7 \cdot 10^{-3}$	$0.08 \cdot 10^{-3}$	mm
transducer stiffness	$k^{\mathrm{sc}}_{y,\mathrm{B}}$	$32.4 \cdot 10^6$	$0.54 \cdot 10^6$	N/m
transducer const.	$d_{3,y,\mathrm{B}}$	$3.10 \cdot 10^{-10}$	$5.12 \cdot 10^{-12}$	m/V
transducer capacitance	$C_{y,\mathrm{B}}$	$1.43 \cdot 10^{-6}$	$0.05 \cdot 10^{-6}$	F

Table 6.18: Case V: normally distributed electrical RL- and RLC-shunt parameter uncertainty with mean μ_X and standard deviation σ_X, $\delta = -0.84$

		RL-shunt		RLC-shunt		
property	X	μ_X	σ_X	μ_X	σ_X	unit
resistance	R^{D}	55.27	0.18	18.58	0.06	Ohm
	R^{L1}	23.14	0.07	3.75	0.01	Ohm
	R^{L2}	1000	3.33	1000	3.33	Ohm
	R^{L3}	1000	3.33	1000	3.33	Ohm
	R^{L5}	20064	66.88	20064	66.88	Ohm
	R^{N1}	–	–	1243.89	4.14	Ohm
	R^{N2}	–	–	1000.00	3.33	Ohm
	R^{N3}	–	–	994000	3313.33	Ohm
capacitance	C^{L4}	–	–	1.00	0.006	µF
	C^{N4}	–	–	1.54	0.01	µF

6.5.2 Prediction of uncertainty by model with shunts

For case V, the numerical peak gains with RL-shunt $\widehat{G}^{\mathrm{RL}}_{y,\mathrm{num}}$ (3.96) and with RLC-shunt $\widehat{G}^{\mathrm{RLC}}_{y,\mathrm{num}}$ (3.98) are calculated $I = 20000$ times via MCS with I samples of normally distributed and independently varying parameter values in $\boldsymbol{P}_i$ from normally distributed parameters in tables 6.17 and 6.18. For case VI, the MCS from case V is repeated with tensile force $F_x = F_x^- = -1200\,\mathrm{N}$, indicated by VI$^-$, and the compressive force $F_x = F_x^+ = 1200\,\mathrm{N}$, indicated by VI$^+$, section 6.2.

The variations of the numerical peak gains $\widehat{G}^{\mathrm{RL}}_{y,\mathrm{num}}$ and $\widehat{G}^{\mathrm{RLC}}_{y,\mathrm{num}}$ obtained from MCS for cases V and VI are shown with normalized histograms in figure 6.22. Again, the most likely peak gain values $\Sigma_{\widehat{G}^{\mathrm{RL}}_y}$ and $\Sigma_{\widehat{G}^{\mathrm{RLC}}_y}$ as well as the maximum peak gain values $Q^{95}_{\widehat{G}^{\mathrm{RL}}_y}$ and $Q^{95}_{\widehat{G}^{\mathrm{RLC}}_y}$ together with their respective optimal values opt_X are used to quantify uncertainty in the peak gains in figure 6.22. The values are summarized in table 6.19.

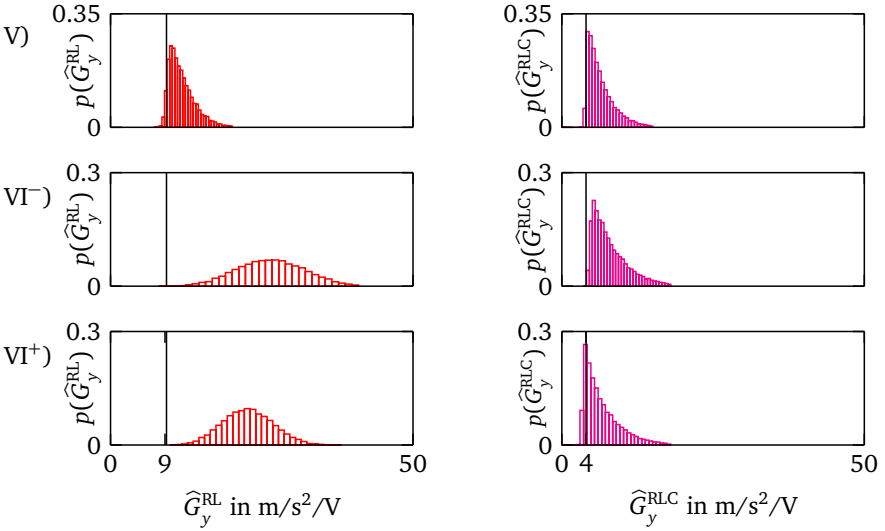

Figure 6.22: Cases V and VI (tensile VI$^-$ and compressive VI$^+$): num. histograms with $I = 20000$ MCS of peak gains with RL-shunts and RLC-shunts
left: $\widehat{G}^{\mathrm{RL}}_{y,\mathrm{num}}$ (——), opt (——) right: $\widehat{G}^{\mathrm{RLC}}_{y,\mathrm{num}}$ (——), opt (——)

In case V, uncertainty due to combined manufacturing and system assembly variations has bigger influence on vibration attenuation with RLC-shunts, because $Q^{95}_{\widehat{G}^{\mathrm{RLC}}_y}$ increases more than $Q^{95}_{\widehat{G}^{\mathrm{RL}}_y}$ in relative terms. This observation is consistent with results from cases II, III and VI in tables 6.12 and 6.16, and suggests that vibration attenuation with the RLC-shunt in general is more sensitive to manufacturing and assembly variations than with the RL-shunt.

Case VI$^-$ has the highest effect on vibration attenuation with the RL-shunt, as seen by the relative changes of $\Sigma_{\widehat{G}^{\mathrm{RC}}_y}$ and $Q^{95}_{\widehat{G}^{\mathrm{RL}}_y}$. So far, $\Sigma_{\widehat{G}^{\mathrm{RL}}_y}$ usually remained close to the optimal value, but the static force significantly shifts the most likely value

upwards, which leads to increased uncertainty. Case VI$^+$ has a smaller influence on uncertainty in the vibration attenuation, which is in agreement with observations from case I. In general, case VI shows that uncertainty in the vibration attenuation with RLC-shunts is mainly caused by manufacturing and assembly variations and less by static load variations.

Table 6.19: Results of cases V, VI$^-$ and VI$^+$: most likely peak gain values Σ_X and maximum peak gain values Q_X^{95} of histograms in figure 6.22, for comparison: optimal peak gain value opt_X, all in $\mathrm{m/s^2/V}$

		absolute values			relative change	
Case	X	opt_X	Σ_X	Q_X^{95}	Σ_X/opt_X	Q_X^{95}/opt_X
V	$\widehat{G}_y^{\mathrm{RL}}$	9.25	10.16	16.14	1.10	1.74
	$\widehat{G}_y^{\mathrm{RLC}}$	4.00	4.53	11.33	1.13	2.83
VI$^-$	$\widehat{G}_y^{\mathrm{RL}}$	9.25	26.77	35.80	2.89	3.87
	$\widehat{G}_y^{\mathrm{RLC}}$	4.00	5.42	14.42	1.35	3.60
VI$^+$	$\widehat{G}_y^{\mathrm{RL}}$	9.25	22.63	29.67	2.45	3.21
	$\widehat{G}_y^{\mathrm{RLC}}$	4.00	4.12	13.01	1.03	3.25

6.6 Summary of results and conclusion of cases I to VI

Sections 6.2.5 and 6.3.5 provide the individual results for the effects of uncertainty from own experiments (cases I and II). In the following, the effects of additional uncertainty from literature (cases III and IV) and the combined uncertainty (cases V and VI) are summarized and compared.

The main results of the case study are:

- Cases II, III and IV: Uncertainty in vibration attenuation with RL- and RLC-shunts caused by manufacturing variations is dominated by manufacturing variations of the piezoelectric transducer. This also shows that the assembly and the manufacturing of the piezo-elastic support is not excessively adding new uncertainty to the vibration attenuation.
- Case VI: Uncertainty in vibration attenuation with RL-shunts due to static load, manufacturing and system assembly variations is dominated by the

static axial load. In contrast, uncertainty in vibration attenuation with RLC-shunts is dominated by manufacturing and system assembly variations

- Cases III to VI: For probabilistic uncertainty, e.g. uncertainty due to transducer manufacturing variations, the shape of the observed peak gain distributions is not constant for all investigated cases and depends on the parameters that are assumed to be uncertain. Thus, no parametric distribution functions are used to describe uncertainty.

Overall, the vibration attenuation with shunted piezoelectric transducers in piezoelastic support B for all sources of uncertainty still achieves reasonable vibration attenuation of 65 % with RL-shunt and 86 % with RLC-shunt compared to vibrations with short circuited transducers, i.e. no attenuation by shunts.

7 Conclusion and outlook

In this work, a novel technical concept called the piezo-elastic support is investigated for lateral vibration attenuation of beam-columns with circular cross-section by using piezoelectric stack transducers connected to RL- and RLC-shunts. Furthermore, uncertainty in the vibration attenuation with RL- and RLC-shunts due to static axial beam-column load, manufacturing and system assembly variations is investigated in order to compare the influence of uncertainty in varying properties on the vibration attenuation and to evaluate the vibration attenuation capability of the piezo-elastic support.

The method of vibration attenuation with shunted piezoelectric transducers in general has been subject of research for several decades and there is a large variety of available shunt concepts. A comprehensive literature review showed that most previous studies are applied to beams with rectangular cross-section or plates, and patch transducers are used for vibration attenuation in one lateral direction. The piezo-elastic support investigated in this work attenuates lateral vibrations of a beam-column with circular cross-section in various lateral directions by use of PZT stack transducers.

Although the RL- and RLC-shunts allow precise vibration attenuation adjustment, uncertainty sources, such as structural loads or manufacturing variations, can significantly reduce the vibration attenuation potential. So far, research studies mainly focused on model-based uncertainty investigations with assumptions only made from literature. In this work, uncertainty caused by static axial beam-column load variations, manufacturing variations and system assembly variations is assumed from own experiments. In this context, it should be noted that the influence of a static axial load on the vibration attenuation has not been considered in literature. For a holistic uncertainty investigation of the vibration attenuation with the piezo-elastic support and shunts, parameter uncertainty assumed from own experiments and literature is combined in a model-based uncertainty analysis.

The investigated beam-column system consists of a beam-column with circular cross-section embedded in two piezo-elastic supports. One support is used to apply lateral vibration excitation at an oblique angle, and the other support is used

for vibration attenuation with shunted transducers. The piezo-elastic support features a rotational elastic spring element that allows the transformation of lateral beam-column displacements into the axial deformation of two stack transducers, and vice versa. The transducers are arranged orthogonally to each other in the lateral beam-column directions and the shunts are optimized separately for both directions. Thus, lateral vibrations in arbitrary lateral directions are attenuated evenly.

In experiments with optimally tuned shunts, lateral beam-column vibrations on average were reduced by 89 % with RL-shunts and by 96 % with RLC-shunts, compared to vibrations without shunts connected. This shows that the piezo-elastic support is well suited to attenuate vibrations of beam-columns with circular cross-section and, therefore, offers a new possibility to attenuate vibrations in truss-type structures.

For the model-based uncertainty analysis, non-probabilistic and probabilistic uncertainty in the vibration attenuation is investigated and quantified by the peak gain variations in the beam-column's attenuated amplitude response. Uncertainty in the vibration attenuation with RL- and RLC-shunts is compared by lower and upper peak gain values, in case of non-probabilistic uncertainty, and by the most likely and maximum occurring peak gain values in case of probabilistic uncertainty.

Non-probabilistic uncertainty due to static tensile and compressive axial load variations and probabilistic uncertainty due to spring element manufacturing and system assembly variations is obtained from own experiments. To quantify uncertainty in vibration attenuation with RL- and RLC-shunts from own experiments, experiments and numerical models without and with shunts connected are used. First, uncertainty is experimentally observed when no shunts are connected. Afterwards, the model without shunts is calibrated to adequately represent the observed uncertainty. Finally, numerically predicted and experimentally observed uncertainty in the vibration attenuation are compared in order to validate the model used for numerical uncertainty investigations and to evaluate the effect of uncertainty. Additionally, probabilistic uncertainty due to shunt component and piezoelectric transducer manufacturing variations is assumed from literature.

The main results of the model-based uncertainty analysis are:

- Uncertainty in vibration attenuation with RL- and RLC-shunts caused by manufacturing variations is dominated by manufacturing variations of the piezoelectric transducer. The assembly and the manufacturing of the piezo-lastic support is not excessively adding new uncertainty to the vibration attenuation.

- Uncertainty in vibration attenuation with RL-shunts due to static tensile and compressive load variations, manufacturing and system assembly variations is dominated by the static axial load variation. In contrast, uncertainty in vibration attenuation with RLC-shunts is dominated by manufacturing and system assembly variations and robust against a varying static axial beam-column load.
- The vibration attenuation with the piezo-elastic support and shunted piezoelectric transducers still achieves reasonable vibration attenuation of 65 % with RL-shunt and 86 % with RLC-shunt for all sources of uncertainty, compared to vibrations with short circuited transducers and no attenuation by shunts.

With respect to the model-based uncertainty analysis and vibration attenuation with the piezo-elastic support and shunted transducers, the following future objectives can be derived from the results of this work:

- Quantification and evaluation of uncertainty for more realistic excitation levels that exceed the small signal levels assumed in this work.
- Integration of multiple piezo-elastic supports with shunted transducers in a larger truss-structure and subsequent application of the model-based uncertainty analysis to identify the interactions of various sources of uncertainty.

A Appendix

Probability plots

Probability plots are a graphical tool used to assess if a set of data plausibly came from an assumed theoretical distribution. The experimental values in figure A.1 shown with circles and the assumed normal distributions in straight lines are in good accordance. Thus, the assumed distributions can be assumed as the underlying distributions. The same goes for figure A.2

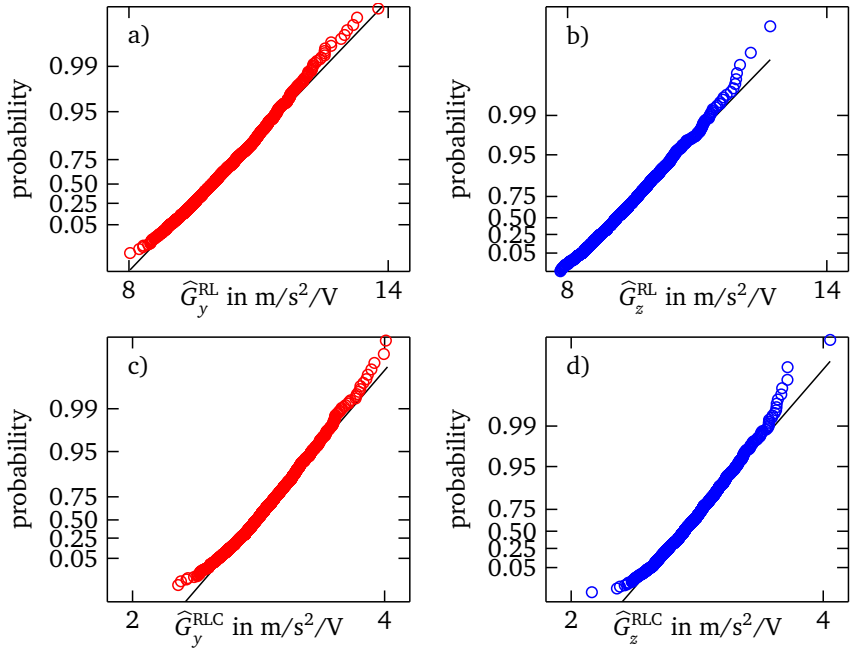

Figure A.1: Probability plots of numerical peak gain variations, 20000 samples obtained from MONTE-CARLO-Simulation in y-direction (○) and z-direction (○) and assumed GUMBEL distributions (——) with RL-shunts a) $\widehat{G}_y^{\mathrm{RL}}$ and b) $\widehat{G}_z^{\mathrm{RL}}$, with RLC-shunts c) $\widehat{G}_y^{\mathrm{RLC}}$ and d) $\widehat{G}_z^{\mathrm{RLC}}$

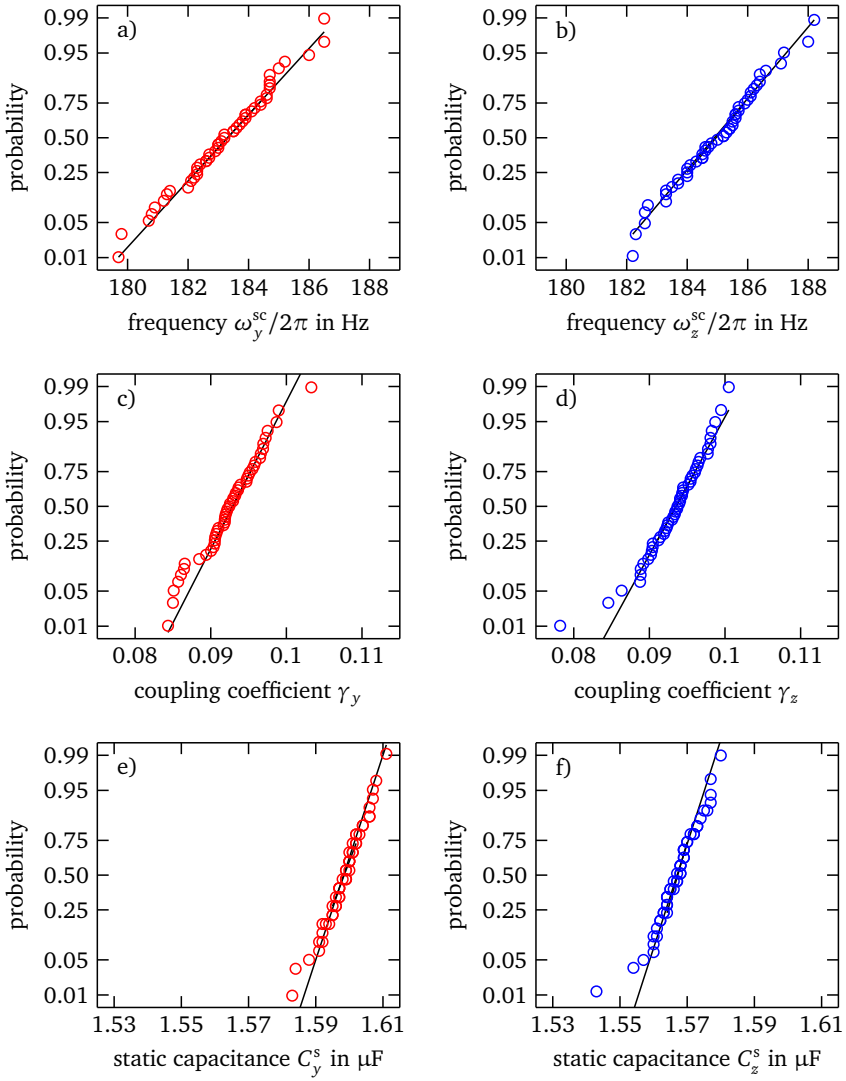

Figure A.2: Probability plots of 50 experimental samples in y-direction (○) and z-direction (○) and assumed normal distributions (——) for short circuited frequencies a) ω_y^{sc} and b) ω_z^{sc}, GEMCCs c) γ_y and d) γ_z, static capacitances e) C_y^s and f) C_z^s

List of Literature

[1] Adams, M. L. *Rotating machinery vibration: From analysis to troubleshooting*. CRC Press, 2001.

[2] Aldrich, J. B. *Design of passive piezoelectric damping for space structures*. Master's Thesis. Massachusetts Institute of Technology, 1993.

[3] Andreaus, U. and Porfiri, M. *Effect of electrical uncertainties on resonant piezoelectric shunting*. In: *Journal of Intelligent Material Systems and Structures* 18.5 (2006), pp. 477–485.

[4] Antoniou, A. *Realisation of gyrators using operational amplifiers, and their use in RC-active-network synthesis*. In: *Proceedings of IEEE*. Vol. 116. 1969, pp. 1838–1850.

[5] APC. *Data sheet piezoelectric material*. accessed March 15, 2018. URL: https://www.americanpiezo.com/apc-materials/piezoelectric-properties.html.

[6] Beck, B. S. *Negative capacitance shunting of piezoelectric patches for vibration control of continuous systems*. Dissertation. Georgia Institute of Technology, 2012.

[7] Behrens, S., Fleming, A. J., and Moheimani, S. O. R. *A broadband controller for shunt piezoelectric damping of structural vibration*. In: *Smart Materials and Structures* 12 (2003), pp. 18–28.

[8] Brandt, A. *Noise and vibration analysis: Signal analysis and experimental procedures*. Wiley, 2011.

[9] Casadei, F. et al. *Broadband vibration control through periodic arrays of resonant shunts: Experimental investigation on plates*. In: *Smart Materials and Structures* 19.1 (2010), p. 015002.

[10] Choi, S.-K., Grandhi, R. V., and Canfield, R. A. *Reliability-based structural design*. Springer, 2007.

[11] Chopra, A. K. *Dynamics of structures: Theory and applications to earthquake engineering*. Prentice Hall, Inc, 1995.

[12] Date, M., Kutani, M., and Sakai, S. *Electrically controlled elasticity utilizing piezoelectric coupling*. In: *Journal of Applied Physics* 87.2 (2000), pp. 863–868.

[13] Ducarne, J., Thomas, O., and Deü, J.-F. *Placement and dimension optimization of shunted piezoelectric patches for vibration reduction*. In: *Journal of Sound and Vibration* 331.14 (2012), pp. 3286–3303.

[14] Eifler, T. et al. *Approach for a consistent description of uncertainty in process chains of load carrying mechanical systems*. In: *Applied Mechanics and Materials* 104 (2011), pp. 133–144.

[15] Engelhardt, R. A. *Uncertainty mode and effects analysis - heuristische Methodik zur Analyse und Beurteilung von Unsicherheiten in technischen Systemen des Maschinenbaus*. Dissertation. Technische Universität Darmstadt, 2013.

[16] Enss, G. C. et al. *Device for bearing design elements in lightweight structures (Festkörperlager)*. DE 10 2015 101 084 A1.

[17] Enss, G. C. et al. *Device for optimal load transmission and load distribution in lightweight structures (Kraftübertragungsvorrichtung)*. DE 10 2014 106 858 A1.

[18] Fleming, A. J. and Moheimani, S. O. R. *Control orientated synthesis of high-performance piezoelectric shunt impedances for structural vibration control*. In: *IEEE Transactions on Control Systems Technology*. Vol. 13. 2005.

[19] Forward, R. L. *Electronic damping of vibrations in optical structures*. In: *Applied optics* 18.5 (1979), pp. 690–697.

[20] Fuller, C. R., Elliott, S. J., and Nelson, P. A. *Active control of vibration*. 2. printing. Academic Press, Inc, 1997.

[21] Götz, B., Platz, R., and Melz, T. *Consistent approach to describe and evaluate uncertainty in vibration attenuation using resonant piezoelectric shunting and tuned mass dampers*. In: *Mechanics & Industry* 18.1 (2017), p. 108.

[22] Götz, B., Platz, R., and Melz, T. *Effect of static axial loads on the lateral vibration attenuation of a beam with piezo-elastic supports*. In: *Smart Materials and Structures* 27.3 (2018), p. 035011.

[23] Götz, B., Platz, R., and Melz, T. *Effect of uncertain boundary conditions and uncertain axial loading on lateral vibration attenuation of a beam with shunted piezoelectric transducers*. In: *Proceedings of ISMA2014 including USD2014 International Conference on Uncertainty in Structural Dynamics*. 2014, pp. 4495–4508.

[24] Götz, B., Platz, R., and Melz, T. *Lateral vibration attenuation of a beam with circular cross-section by supports with integrated resonantly shunted piezoelectric transducers*. In: *Proceedings of SMART2015*. 2015.

[25] Götz, B. et al. *Lateral vibration attenuation of a beam with circular cross-section by a support with integrated piezoelectric transducers shunted to negative capacitances*. In: *Smart Materials and Structures* 25.9 (2016), pp. 1–10.

[26] Götz, B. et al. *Model verification and validation of a piezo-elastic support for passive and active structural control of beams with circular cross-section*. In: *Applied Mechanics and Materials, Trans Tech Publications* 807 (2015), pp. 67–77.

[27] Graham, C. and Talay, D. *Stochastic simulation and monte carlo methods: Mathematical foundations of stochastic simulation*. Vol. 68. Stochastic Modelling and Applied Probability. Springer, 2013.

[28] Gripp, J. A. B. et al. *An adaptive piezoelectric vibration absorber enhanced by a negative capacitance applied to a shell structure*. In: *Smart Materials and Structures* 24.12 (2015), p. 125017.

[29] Groche, P. et al. *Increased total flexibility by 3D Servo Presses*. In: *CIRP Annals* 59.1 (2010), pp. 267–270.

[30] Guyomar, D., Mohammadi, S., and Richard, C. *Effect of boundary (support) conditions on piezoelectric damping in the case of SSDI vibration control technique*. In: *Mechanical Systems and Signal Processing* 23 (2009), pp. 501–513.

[31] Guyomar, D., Richard, C., and Mohammadi, S. *Damping behavior of semi-passive vibration control using shunted piezoelectric materials*. In: *Journal of Intelligent Material Systems and Structures* 19.8 (2008), pp. 977–985.

[32] Hagood, N. W. and Crawley, E. F. *Experimental investigation into passive damping enhancement for space structures*. In: *Journal of Guidance, Control, and Dynamics* 14.6 (1991), pp. 1100–1109.

[33] Hagood, N. W. and Flotow, A. H. von. *Damping of structural vibrations with piezoelectric materials and passive electrical networks*. In: *Journal of Sound and Vibration* 146.2 (1991), pp. 243–268.

[34] Han, X., Neubauer, M., and Wallaschek, J. *A review: The control strategies of synchronized switching damping technique*. In: *International Conference on Mechatronics and Automation (ICMA)*. 2011, pp. 1657–1663.

[35] Hanselka, H. and Platz, R. *Ansätze und Maßnahmen zur Beherrschung von Unsicherheit in lasttragenden Systemen des Maschinenbaus*. In: *VDI-Zeitschrift Konstruktion* 11/12-2010 (2010), pp. 55–62.

[36] Hartog, J. P. D. *Mechanical vibrations*. Courier Corporation, 1985.

[37] Hesse, D., Hoppe, F., and Groche, P. *Controlling product stiffness by an incremental sheet metal forming process*. In: *Procedia Manufacturing* 10 (2017), pp. 276–285.

[38] Heuss, O. *Eine Analyse des Anwendungspotenzials von piezoelektrischen Netzwerken im Maschinenbau*. Dissertation. Technische Universität Darmstadt, 2018.

[39] Høgsberg, J. and Krenk, S. *Balanced calibration of resonant piezoelectric RL shunts with quasi-static background flexibility correction*. In: *Journal of Sound and Vibration* 341 (2015), pp. 16–30.

[40] Holzmann, H. *Vibration attenuation of a truss structure with shunted piezoelectric transducers subject to varying static loads*. Master's Thesis. Technische Universität Darmstadt, 2018.

[41] Huelsman, L. P. *Active and passive analog filter design: An introduction*. McGraw-Hill series in electrical and computer engineering Electronics and VLSI circuits. McGraw-Hill, 1993.

[42] Inman, D. J. *Vibration with control*. Wiley, 2006.

[43] International Electrotechnical Commission. *Marking codes for resistors and capacitors*. Geneva, Switzerland, 2016.

[44] Jendritza, D. J. *Technischer Einsatz Neuer Aktoren: Grundlagen, Werkstoffe, Designregeln und Anwendungsbeispiele*. expert, 2017.

[45] Jungblut, T. *Ein Beitrag zur modellbasierten, hybriden Entwicklung elektromechanischer Systeme zur Schwingungsminderung*. Dissertation. Technische Universität Darmstadt, 2015.

[46] Kemet. *Data sheet SMD capacitors*. accessed March 15, 2018. URL: http://www.kemet.com/ProductCatalog%20Documents/F9000_GenInfo_WoundSMD.pdf.

[47] Kozlowski, M. V., Cole, D. G., and Clark, R. L. *A comprehensive study of the rl series resonant shunted piezoelectric: A feedback controls perspective*. In: *Journal of Vibration and Acoustics* 133.1 (2011), pp. 1–10.

[48] Kuttich, A., Götz, B., and Ulbrich, S. *Robust optimization of shunted piezoelectric transducers for vibration attenuation considering different values of electromechanical coupling*. In: *Proceedings of IMAC*. Conference proceedings of the Society for Experimental Mechanics. Springer, 2017.

[49] Lallart, M. et al. *Blind switch damping (BSD): A self-adaptive semi-active damping technique*. In: *Journal of Sound and Vibration* 328.1-2 (2009), pp. 29–41.

[50] Lefeuvre, E. et al. *Semi-passive piezoelectric structural damping by synchronized switching on voltage sources*. In: *Journal of Intelligent Material Systems and Structures* 17.8-9 (2006), pp. 653–660.

[51] Lesieutre, G. A. and Davis, C. L. *Can a coupling coefficient of a piezoelectric device be higher than those of its active material?* In: *Journal of Intelligent Material Systems and Structures* 8 (1997), pp. 859–867.

[52] Mallapur, S. and Platz, R. *Quantification and evaluation of uncertainty in the mathematical modelling of a suspension strut using bayesian model validation approach*. In: *Proceedings of IMAC*. Conference proceedings of the Society for Experimental Mechanics. Springer, 2017, pp. 113–124.

[53] Manzoni, S. et al. *Vibration attenuation by means of piezoelectric transducer shunted to synthetic negative capacitance*. In: *Journal of Sound and Vibration* 331.21 (2012), pp. 4644–4657.

[54] Markert, R. *Strukturdynamik*. Mechanik. Shaker, 2013.

[55] Marneffe, B. de and Preumont, A. *Vibration damping with negative capacitance shunts: Theory and experiment*. In: *Smart Materials and Structures* 17.3 (2008), pp. 1–9.

[56] Matten, G. et al. *Sensitivity analysis of beams controlled by shunted piezoelectric transducers*. In: *Proceedings of IMAC*. Conference proceedings of the Society for Experimental Mechanics. Springer, 2014.

[57] Mayer, D., Linz, C., and Krajenski, V. *Synthetic inductor for passive damping of structural vibrations*. In: *ADAMES Abschlusskolloquium 2001*.

[58] Mayer, D. et al. *Additive manufacturing of active struts for piezoelectric shunt damping*. In: *Journal of Intelligent Material Systems and Structures* 27.6 (2016), pp. 743–754.

[59] Moheimani, S. O. R. *A survey of recent innovations in vibration damping and control using shunted piezoelectric transducers*. In: *Control Systems Technology, IEEE Transactions on* 11.4 (2003), pp. 482–494.

[60] Moheimani, S. O. R. and Fleming, A. J. *Piezoelectric transducers for vibration control and damping*. Advances in Industrial Control. Springer, 2006.

[61] Mokrani, B. et al. *Adaptive inductor for vibration damping in presence of uncertainty*. In: *Proceedings of SMART2015*. 2015.

[62] Nambu, Y. et al. *Robustness of multiple piezoelectric vibration absorbers*. In: *25th International Conference on Adaptive Structures and Technologies 2014 (ICAST 2014)*. 2014, pp. 1–12.

[63] Neubauer, M., Oleskiewicz, R., and Popp, K. *Comparison of damping performance of tuned mass dampers and shunted piezo elements*. In: *PAMM - Proceedings in Applied Mathematics and Mechanics*. Vol. 5. Wiley, 2005, pp. 117–118.

[64] Neubauer, M. and Wallaschek, J. *Vibration damping with shunted piezoceramics: Fundamentals and technical applications*. In: *Mechanical Systems and Signal Processing* 36.1 (2011), pp. 36–52.

[65] Neubauer, M. et al. *Optimization of damping and absorbing performance of shunted piezo elements utilizing negative capacitance*. In: *Journal of Sound and Vibration* 298.1-2 (2006), pp. 84–107.

[66] Niederberger, D. et al. *Adaptive multi-mode resonant piezoelectric shunt damping*. In: *Smart Materials and Structures* 13.5 (2004), pp. 1025–1035.

[67] Noliac. *Data sheet piezoelectric material*. accessed March 15, 2018. URL: http://www.noliac.com/products/materials/nce51/.

[68] Oberkampf, W. L. et al. *Error and uncertainty in modeling and simulation*. In: *Reliability Engineering and System Safety* 75 (2002), pp. 333–357.

[69] Ondoua, S. *Unsicherheit in der Bewertung von Struktur-Eigenschaftsbeziehungen zwischen aktiven und passiven Systemelementen in aktiven lasttragenden Systemen*. Dissertation. Technische Universität Darmstadt, 2016.

[70] Pai, S. S. *Probabilistic structural analysis of a truss typical for space station*. In: *Third Air Force/NASA Symposium On Recent Advances in Multidisciplinary Analysis and Optimization*. 1990.

[71] Pai, S. S. and Chamis, C. C. *Probabilistic assessment of space trusses subjected to combined mechanical and thermal loads*. In: *33rd Structures, Structural Dynamics and Materials Conference cosponsored by the AIAA, ASME, ASCE, AHS, and ASC*. 1992.

[72] Papagiannopoulos, G. A. and Hatzigeorgiou, G. D. *On the use of the half-power bandwidth method to estimate damping in building structures*. In: *Soil Dynamics and Earthquake Engineering* 31 (2011), pp. 1075–1079.

[73] Park, J.-W. and Han, J.-H. *Sensitivity analysis of damping performances for passive shunted piezoelectrics*. In: *Aerospace Science and Technology* 33 (2014), pp. 16–25.

[74] Philbrick, G. A. *Applications manual for computing amplifiers for modelling, measuring, manupulating & much else*. 1966.

[75] Physik Instrumente. *Data sheet piezoelectric actuator P-882 - P-888*. accessed March 15, 2018. URL: https://static.physikinstrumente.com/fileadmin/user_upload/physik_instrumente/files/datasheets/P-882-Datasheet.pdf.

[76] Pohl, M. *Elektromechanische Netzwerke mit adaptiven negativen Kapazitäten zur breitbandigen Schall- und Schwingungsreduktion*. Dissertation. Technische Universität Carolo-Wilhelmina zu Braunschweig, 2014.

[77] Preumont, A. *Vibration control of active structures, an introduction*. Springer, 2011.

[78] Preumont, A. and Seto, K. *Active control of structures*. Wiley, 2008.

[79] Preumont, A. et al. *The damping of a truss structure with a piezoelectric transducer*. In: *Computers & Structures* 86.3-5 (2008), pp. 227–239.

[80] Przemieniecki, J. S. *Theory of matrix structural analysis*. McGraw-Hill, 1968.

[81] Roy, C. J. and Oberkampf, W. L. *A complete framework for verification, validation, and uncertainty quantification in scientific computing*. In: *48th AIAA Aerospace Sciences Meeting Including the New Horizons Forum and Aerospace Exposition, Orlando, Florida*. 2010.

[82] Rupitsch, S. J., Ilg, J., and Lerch, R. *Enhancement of the inverse method enabling the material parameter identification for piezoceramics*. In: *IEEE International Ultrasonics Symposium Proceedings*. 2011, pp. 357–360.

[83] Salloum, R. *Optimization of shunt damped composite structures using negative capacitances*. Dissertation. Technische Universität Darmstadt, 2016.

[84] Santos, H. F. L. d. and Trindade, M. A. *Structural vibration control using extension and shear active-passive piezoelectric networks including sensitivity to electrical uncertainties*. In: *Journal of the Brazilian Society of Mechanical Sciences and Engineering* 33.3 (2011), pp. 287–301.

[85] Schaeffner, M., Götz, B., and Platz, R. *Active buckling control of a beam-column with circular cross-section using piezo-elastic supports and integral LQR control*. In: *Smart Materials and Structures* 25.6 (2016), pp. 1–10.

[86] Schuëller, G. I. *On the treatment of uncertainties in structural mechanics and analysis*. In: *Computers & Structures* 85.5-6 (2007), pp. 235–243.

[87] Scinocca, F. and Nabarrete, A. *Stochastic modeling of uncertainties in the piezoelectric coupling coefficient in arbitrary shell structures*. In: *Proceedings of 3rd International Symposium on Uncertainty Quantification and Stochastic Modeling*. 2016.

[88] Skogestad, S. and Postlethwaite, I. *Multivariable feedback control*. Wiley, 2001.

[89] Sutherland, W. C. *The practical operational-amplifier gyratorgyrator for inductorless filter synthesis: NASA TM X-64995*. In: (1976).

[90] Thorlabs. *Data sheet piezoelectric material*. accessed March 15, 2018. URL: `https://www.thorlabs.com/images/Brochures/Thorlabs_Piezo_Brochure.pdf`.

[91] Timoshenko, S. P. *Theory of elastic stability*. 2nd Edition. 1985.

[92] Tsai, M. S. and Wang, K. W. *A coupled robust control/optimization approach for active-passive hybrid piezoelectric networks*. In: *Smart Materials and Structures* 11 (2002), pp. 389–395.

[93] Vasic, D., Liu, Y.-P., and Costa, F. *Comparison of piezoelectric structural damping based on velocity controlled switching and pulse width modulation switching circuits*. In: *Vibration, Acoustics and Wave Propagation*. Vol. 12. ASME, 2012, pp. 375–385.

[94] VDI Standard. *VDI 2064: Aktive Schwingungsisolierung*. 2010.

[95] VDI Standard. *VDI 3833 Blatt 2: Schwingungstilger und Schwingungstilgung*. 2006.

[96] Warnaar, D. B. and McGowan, P. E. *Effects of local vibrations on the dynamics of space truss structures*. In: *AIAA Dynamics Specialists Conference 1987*. American Institute of Aeronautics and Astronautics, 1987, pp. 868–875.

[97] Wiedemann, J. *Leichtbau: Elemente und Konstruktion*. Springer, 2007.

[98] Yageo. *Data sheet SMD resistors*. accessed March 15, 2018. URL: `http://www.yageo.com/documents/recent/PYu-RT_1-to-0.01_RoHS_L_9.pdf`.

[99] Yan, B. et al. *Shunt damping vibration control technology: A review*. In: *Applied Sciences* 7.5 (2017), pp. 1–31.

[100] Zimmermann, B. *Bewertung und Anpassung eines piezo-elastischen Balkenlagers zur Strukturkontrolle von Balken mit Kreisquerschnitt*. Master's Thesis. Technische Universität Darmstadt, 2016.

List of Figures

List of Tables